Two-phase flow and pressure drop in a horizontal, equal-sided combining tee junction

by

Gavin D. A. Joyce

A Thesis submitted to the Faculty of Graduate Studies of

The University of Manitoba

in partial fulfilment of the requirements of the degree of

DOCTOR OF PHILOSOPHY

Department of Mechanical Engineering

University of Manitoba

Winnipeg

Abstract

A careful review of the literature showed that there is a serious lack of information (experimental or analytical) on the pressure losses during two-phase flow in combining tee junctions. Pipe networks in industrial applications involve combining and dividing junctions and knowledge of the pressure losses at these junctions is essential for analysis of the flow distribution in the network. To this end, the pressure losses of air-water mixtures passing through a horizontal, combining tee junction with a 37.8 mm diameter were experimentally studied with annular, wavy, and slug flow regimes in the outlet. The test matrix independently varied the outlet flow rates, the outlet mixture qualities, the gas distribution between the inlets, and the liquid distribution between the inlets. All experiments were conducted at room temperature and a nominal absolute pressure at the centre of the junction of 150 kPa. The pressure distribution in all three legs of the tee was determined using up to 49 pressure taps distributed among the three sides and monitored using pressure transducers to produce accurate measurements of the pressure losses. Time-averaged pressure measurements with annular and wavy flows are reported, while pressure measurements with slug flows were not repeatable. A new model and empirical coefficients is presented that allows accurate prediction of pressure losses for flows with either an annular or wavy outlet. Time-varying pressure measurements are presented and analyzed using probability density functions. Different distributions were found for differential measurements depending on whether or not slugging was present in the system. The probability density functions for cases with annular or wavy flow in the outlet followed Gaussian distributions, while cases with slug flow had skewed distributions. Time-varying pressure signals showed a time lag between slug events based on pressure tap locations. A visual study with slug flow present in the system showed upstream travelling waves

induced in a stratified inlet when slug flow was present in the other, which led to unexpected slugging under certain flow conditions.

Acknowledgements

It has been a great privilege to work with, and learn from my advisor, Dr. Hassan Soliman. His perceptiveness and profound gift for teaching are an inspiration for me. He granted me autonomy to work through problems in my own way, but has always been ready with guidance when I needed it. He's the fulcrum I've been levering off of. Dr. Soliman: thank you.

For aiding in the apparatus' construction and for kindness when fixing things I broke, I'm grateful to Mr. John Finken, Mr. Zeev Kapitanker, Mr. Irwin Penner, and Mr. Dan Rossong.

For financial support, I'm grateful to the Natural Sciences and Engineering Research Council of Canada, and the University of Manitoba. Thank you.

For keeping me (passably?) sane I owe my friends, in particular, Lukas Thiessen, Winston Permanand, Jeremy Wiebe, Laura Theissen, Qianqiu Xun, Dwight Klassen, Derek Koop, and Richard Lozowy. Also my friends I've found on the pages of books: Anne Shirley, Roland Deschain, Harry Potter, Lizzy Bennett, Samwise Gamgee, Purun Dass, Lucy Pevensie, Jonathan Strange, Pipp, Peekay, Prabaker, . . . what's science without imagination?

For your prayers, generosity, laughter, music, late-night meals, and rides when I was too exhausted to walk or too miserable to be rained on, I'm forever grateful to my top-notch family: Dean Joyce and Helga Pepneck-Joyce, Dave and Essie Bergen, Kristin Bergen, Adrienna Joyce, and Matthew Joyce.

Finally, my wife, Carla Bergen: I'm wearing the smile you gave me. I love you. Thank you.

"Unless you love someone, nothing else makes any sense"

–E. E. Cummings

for Carla . . .

Contents

Page

Page

Conclusions

Page

List of Figures

Figure Page

Figure Page

Figure Page

Figure Page

List of Tables

Table Page

List of Symbols

		Page of first use
δ	Kronecker delta	17
γ	two-phase pressure multiplier	16
κ	heat capacity ratio	188
λ	fraction of the total outlet mass flowing in the branch	5
ν	kinematic viscosity, $\mathrm{m^2\,s^{-1}}$	16
ρ	density, $\mathrm{kg\,m^{-3}}$	11
ω	two-phase parameter	164

Subscripts

1ϕ	single phase	17
2ϕ	two phase	16
B	branch inlet	6
C	combined outlet	5
e	energy	91
G	gas	5
h	homogeneous	16
L	liquid	5
M	main inlet	6
m	momentum	17
R	relative to tap C1	43
S	superficial	11
std	at 21.1 °C and 101.3 kPa	37

Acronyms

AM( )	arithmetic mean	113
AMD( )	arithmetic mean deviation	62

		Page of first use
CCM	contraction coefficient model	22
ESFM	energy-based separated flow model	18
GM( )	Gaussian distribution's mean	211
HFM	homogeneous flow model	18
LCM	loss coefficient model	22
MCM	momentum coefficient model	22
MESFM	modified energy separated flow model	67
$\mathrm{MMT}_c^k(\,)$	statistical moment of order k about c	195
MSFM	momentum-based separated flow model	18
PDF	probability density function	113
RMSD( )	root-mean-square deviation	50
$\mathrm{SMA}_k(\,)$	simple moving average using k samples	113
VAR( )	variance	210

Part I

Background

Chapter 1

Introduction

1.1 Overview

Piping networks of all kinds, from oil extraction to nuclear power plants, use tee junctions in distributing fluids. Tee junctions can be used in various configurations as illustrated in Fig. 1.1. Dividing tee junctions split a single inlet stream into two outlets and can be either branching, where the two outlets are perpendicular to one another, or impacting, where both outlets are perpendicular to the inlet. Combining tee junctions serve to combine two inlet streams into a single outlet and again can be either branching, where the two inlets are perpendicular to one another, or impacting, where both inlets are perpendicular to the outlet. Impacting combining junctions are uncommon, and for the rest of this work reference to combining tee junctions pertains only to the branching type.

Single-phase flow in tees has been the subject of many experimental and numerical studies. Classic experimental works like [1–4] examined horizontal tees in combining

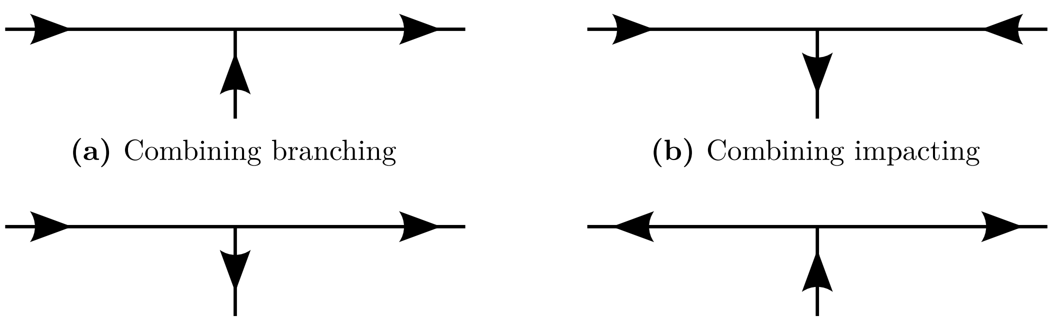

(a) Combining branching **(b)** Combining impacting

(c) Dividing branching **(d)** Dividing impacting

Figure 1.1 Various tee-junction configurations.

and dividing flows using rectangular and circular pipes with both sharp and curved edges, and also varying area ratios. More recent experimental studies have also been conducted with the aim of improving accuracy in pressure-loss predictions of unequal-sided tee junctions for small [5] and large area ratios [6, 7], examining compressible flows [8, 9], and specifically examining the effect of rounded edges at the junction [10]. Further studies have also been conducted with the intent of validating CFD techniques like [11–13], and currently interest in bioengineering and bifurcations in human anatomy has led to numeric works examining non-Newtonian fluid flows in simple tees [14, 15].

Gas-liquid flows through tee junctions have also been the subject of many studies, but for the most part only the dividing type. In heating and cooling applications, the presence or absence of one phase or the other can be catastrophic, and division of the flow does not necessarily lead to an even division of the phases. The importance of the phase redistribution problem has attracted research from many groups with several surveys of the topic available [16–19]. More recent studies looking at how the inclination of the outlets in a dividing impacting tee affects the phase redistribution [20], and the behaviour in a mini-size, dividing impacting tee [21]. Similarly, the pressure drop in dividing tee junctions has also been the subject of many studies, like [22–29], for both branching and impacting types for various diameter ratios and geometries. These studies have led to valuable insights and correlations, and also highlighted the need for further studies in the area of dividing flow.

Unlike these related topics, two-phase flow passing through combining tee junctions has had very little study. To the best of the author's knowledge, the only studies are [22, 30–32]. St. Pierre and Glastonbury [22] performed an experimental study using air-water mixtures combining in two different horizontal, unequal-sided tees.

They reported pressure-loss data and presented three models for the pressure losses across the tees, though they commented on difficulties in reading the manometers they used to measure the pressure distributions. Schmidt and Loth [30] performed an experimental study using refrigerant R12 with an equal-sided combining tee junction, but with a vertical up flow in the branch inlet. They presented three models for pressure losses across the tee. The studies of Belegratis [31, 32] experimentally examined air-water and various other oil-gas mixtures combining in two different horizontal, equal-sided tees. The primary focus was on flow interactions and the effects of mixing at the junction on the flow pattern (via visual observation and capacitance measurements) and while both the void fraction and pressure losses were measured, no pressure loss data were reported in tabular or graphical form. Belegratis [32] also compared the previous pressure-loss models from [22, 30] with both his own pressure loss data and the data from [22] finding deviations from the models ranging from (80–3 000) % with his own data, and (12–7 000) % with the data from [22].

These past works clearly show a serious lack of experimental data on two-phase flow in horizontal, equal sided combining tee junctions. There are no pressure loss data available for this configuration, and no model exists that can be used with confidence. Additionally, the physics of mixing at a tee and the flow interactions in each side of the junction has not been examined thoroughly.

1.2 Engineering significance of the present study

Piping networks consist of straight sections of pipe connected with various fittings, including both dividing and combining tee junctions. The normal procedure for an engineer to determine the flow rate and pressure throughout a piping network is to calculate the pressure drops assuming fully-developed conditions in the straight sections and then adjusting the pressures to account for reversible and irreversible losses at the fittings. The calculation procedure is almost always iterative, even for single-phase flow, and the pressure adjustments for fittings rely on empirical data. For two-phase flow there is some information about fully-developed pressure gradients in straight pipes resulting in many correlations and models, but with large variation among their predictions. On the other hand, there is very little information on the reversible and irreversible two-phase pressure losses associated with combining tees. The major objective of the present study is to provide engineers with practical information about the pressure losses for one particular combining tee junction by providing a quality experimental study.

1.3 Problem definition

Consider a simple horizontal, sharp-edged, equal-sided branching-combining tee of a given cross-sectional area, A, shown schematically in Fig. 1.1a. For a fixed geometry and fixed fluid properties, the case of incompressible single-phase flow may be completely described by the fraction of the total outlet mass flowing in the branch, λ, and the outlet (C) mass flow rate, W_{C}. For two-phase, gas-liquid flow through the same tee and assuming fixed fluid properties, four parameters are required to completely describe the flow: the fractions of the total outlet mass of gas and liquid flowing in the branch, λ_{G} and λ_{L}, respectively, the quality of the outlet flow, x_{C}, and the total outlet mass flow rate, W_{C}. Both inlets and the outlet can carry gas-liquid flow in any of its various regimes. For both single- and two-phase flow, the pressure losses due to the junction are defined by the illustration in Fig. 1.2 and calculated by extrapolating the fully-developed, linear pressure profiles to the junction's centre as if the tee had not perturbed the separate flows. The extrapolated pressures at the junction's centre for the main inlet (M), branch inlet (B), and outlet (C) are P_{M}, P_{B}, and P_{C}, respectively. The difference between P_{M} and P_{C} is the main to combined pressure loss, $\Delta P_{\text{M-C}}$, and the difference between P_{B} and P_{C} is the branch to combined pressure loss, $\Delta P_{\text{B-C}}$. The present study will experimentally examine the pressure losses that occur in a combining tee using a parametric study of W_{C}, x_{C}, λ_{G}, and λ_{L} using air and water. In addition to the pressure losses, visual observations and local-pressure data will also be obtained and the effects of mixing will be considered with particular interest in whether a simple tee can be used to induce flow regimes or other phenomenon in any of the legs that would otherwise not be present in undisturbed pipe flow.

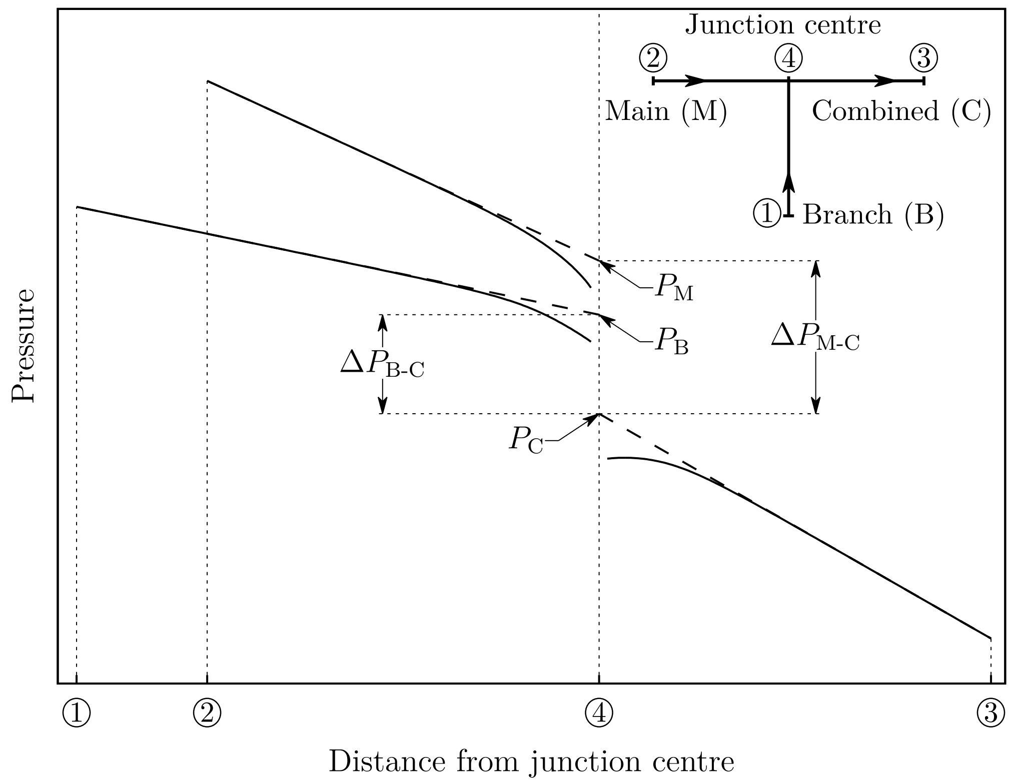

Figure 1.2 Illustration of the pressure distribution through a combining tee junction.

1.4 Objectives

1. Design and build an experimental facility capable of accurately measuring the time-averaged pressure distributions, the time variation of local pressure values, and visually examining the flow in all three sides of a horizontal, sharp-edged, equal-sided combining tee junction with air-water flow.

2. Design a data reduction method to minimize uncertainty and objectively analyze experimental pressure-loss data.

3. Run experiments for multiple test conditions, specifically with:

a. Annular flow in the outlet, and a combination of stratified, wavy, or annular flow in the inlets.

b. Wavy flow in the outlet, and a combination of stratified or wavy flow in the inlets.

c. Slug flow in the outlet, and a combination of stratified, wavy, or slug flow in the inlets.

This will encompass a full parametric study varying W_{C}, x_{C}, λ_{G}, and λ_{L}.

4. Analyze the experimental data and assess existing pressure-loss models.

5. Develop new models to predict the pressure losses for each outlet flow regime.

6. Identify any flow phenomenon caused by the presence of the tee. Specific attention will be paid to inducing flow regimes using the tee that would otherwise not be present in undisturbed pipe flow with the same conditions.

Chapter 2

Literature Review

2.1 Overview

This study draws upon several topics in both single-phase and two-phase flows. These will be looked at in the order of:

1. Single- and two-phase pipe flow
    - Gas-liquid flow regimes
    - Void fraction
    - Single-phase fully-developed pressure gradients
    - Two-phase fully-developed pressure gradients
2. Single- and two-phase flow in combining tee junctions
    - Single-phase pressure losses
    - Two-phase pressure losses
    - Two-phase mixing behaviour
3. Two-phase time-varying pressure measurement

2.2 Single- and two-phase pipe flow

Gas-liquid flow regimes

Gas-liquid flows are important in every day items like coffee perks, where steam and water form a 'bubble pump' mechanism to transport hot water, to large industrial systems like nuclear reactors, where cooling systems are essential components for safe functioning, and also oil extraction, where injection steam may be distributed throughout a complex pipe network to 'soften' oil before pumping it from reservoirs. One reason gas-liquid flows are of such practical importance is because of the different ways the phases can organize themselves within the flow. For example, a horizontal gas-liquid flow can form an annular flow structure, where a high velocity continuous gas core moves inside of a lower velocity liquid film surrounding it, or by reducing the gas velocity the same gas-liquid flow could form a slug flow structure, where intermittently segments of water fill the entire flow cross-section and are accelerated to the relatively high gas velocity and move at a much higher flow rate than the bulk of the liquid. Every mixture behaves differently based on the substance properties, flow orientation, tube diameter, and flow rates. The present study deals only with air-water mixtures flowing horizontally and further discussion of two-phase flow refers only to these conditions unless otherwise stated.

While several flow patterns are common in air-water flow, different authors used different names for the same regimes and also may subclassify flows in different ways. For example, the work of [33] refers to intermittent flow structure whereas [34] refers to plug and slug flow structures. This work generally follows the convention of [34] which identifies the different regimes as stratified, wavy, annular, plug, slug, and bubbly, but additionally includes annular-mist in some discussion. These different regimes are illustrated in Fig. 2.1. Stratified flow refers to relatively low gas and liquid flow rates with the gas flowing above the liquid and a flat and calm interface between the phases. As the gas flow rate is increased, the interface between the gas and liquid becomes disturbed by the higher level of shear and forms waves and sometimes droplets, and is aptly called the wavy regime. Further increase of the gas flow rate leads to the annular flow regime described above. With high enough gas flow rates annular flow changes to annular-mist flow where the liquid film covering the pipe wall is very thin and the bulk of the liquid is entrained in the gas flow in the form of a fine mist. If instead the liquid flow rate is increased from wavy flow, the liquid level is raised in the tube and the wavy interface becomes higher. At some point, the waves may become unstable and contact the upper part of the tube and consume the entire cross-section, which can form slugs and the slug flow regime described above. From stratified flow, if the liquid flow rate is increased the water will eventually fill the entire cross section similar to slug flow, but as the gas velocity is low no slugs are formed, and instead large bubbles of air coalesce in what are known as plugs forming the plug flow regime. At very high liquid flow rates, the bubbles largely do not coalesce and instead small diameter bubbles move through the liquid called the bubbly flow regime. By performing experiments at various flow rates and identifying the flow regime present, the different regimes can be mapped. For horizontal air-water flow, Mandhane et al. [34] suggested the map shown in Fig. 2.2 with the axes defined in terms of the superficial gas and liquid velocities:

$$V_{\mathrm{S}i} = \frac{W_i}{\rho_i A}, \quad i = \mathrm{G, L}, \tag{2.1}$$

where $V_{\mathrm{S}i}$ is the superficial velocity of phase i which can be either the gas (G) or liquid (L), W is the mass flow rate, ρ is the density, and A is the total cross-sectional

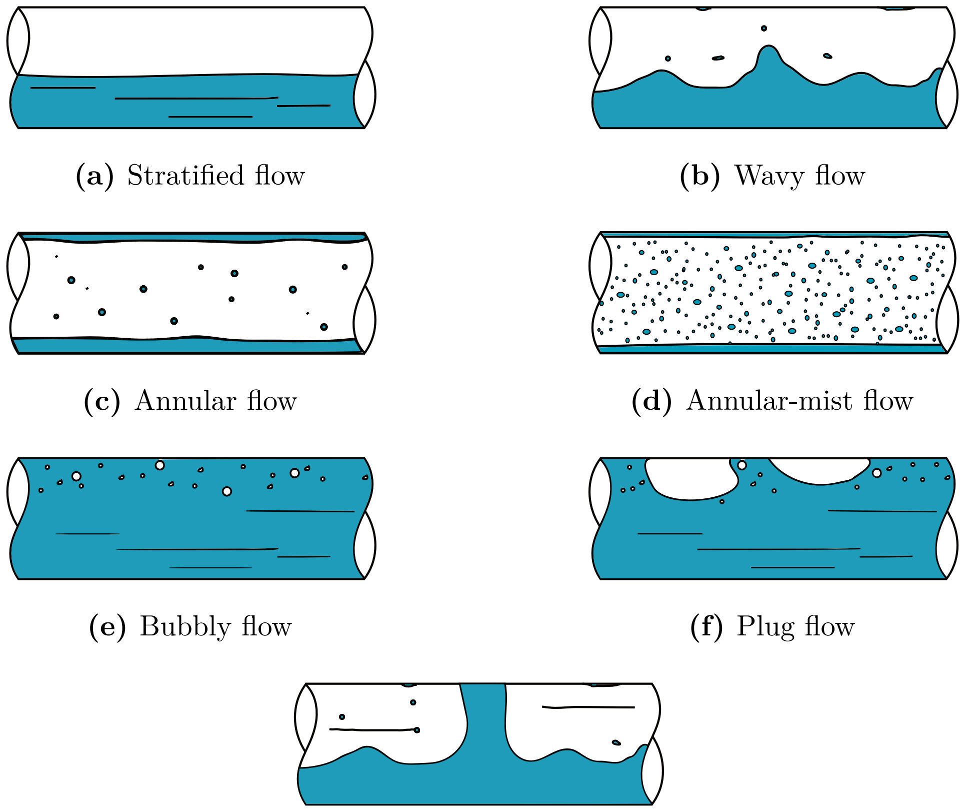

(a) Stratified flow
(b) Wavy flow
(c) Annular flow
(d) Annular-mist flow
(e) Bubbly flow
(f) Plug flow
(g) Slug flow

Figure 2.1 Flow regimes for horizontal two-phase flow.

area of the pipe. Similar to the laminar-turbulent transition in single-phase flows, the boundaries shown on the map are not definite and should be considered transition regions rather than sharp lines. There are several other maps, like [33, 35], which do not, in general, agree with one another owing to differing choices of parameter dependence and attempts at making a particular map more universal. This highlights one of the largest difficulties with two-phase flow: there are no dimensionless parameters that can be used to universally describe a particular flow. Most studies are particular to a set of fluids, pipe sizes, and orientation and cannot be extended with confidence beyond those parameters.

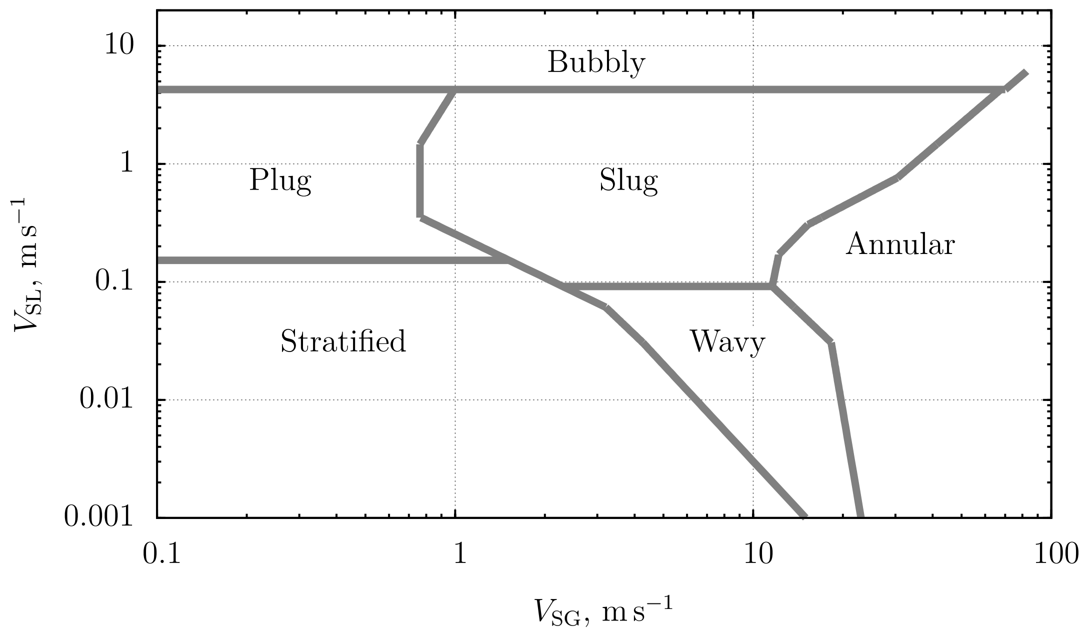

Figure 2.2 Horizontal air-water flow regime map of Mandhane et al. [34].

Since most pipes are opaque, the identification of flow regimes can be difficult in practice. When visual information is not available, liquid hold-up measurements from capacitance meters or gamma densitometers are sometimes used to aid in flow-pattern identification [31, 36, 37] as it can be shown that flow patterns may be identified by the signals fluctuation. Other researchers have shown that a time-varying pressure signal may also be used to identify flow regimes [38–44], which is quite attractive because of its low cost to implement. While no agreed upon signal analysis exists, and as flow regimes gradually transition from one to another making quantitative assessment of transition very difficult, these works have shown the pressure signal can provide valuable information on the flow structure.

Void fraction

A common parameter in two-phase flow is the void fraction, α. The definition of the void fraction is simply the ratio of area occupied by gas to the total area of the flow at a particular location in the pipe:

$$\alpha = A_{\mathrm{G}}/A, \tag{2.2a}$$

$$1 - \alpha = A_{\mathrm{L}}/A. \tag{2.2b}$$

Knowledge of the void fraction allows calculation of average phase velocities as:

$$V_{\mathrm{G}} = \frac{W_{\mathrm{G}}}{\rho_{\mathrm{G}} \alpha A}, \tag{2.3a}$$

$$V_{\mathrm{L}} = \frac{W_{\mathrm{L}}}{\rho_{\mathrm{L}} (1 - \alpha) A}. \tag{2.3b}$$

There are many correlations for the void fraction available in the literature. Quality assessments of these correlations have been ongoing since an early review by Dukler et al. [45]. More recently, a comparison of 68 correlations was performed by Woldesemayat and Ghajar [46] using a total of 2844 data points compiled from several sources using air-water, natural gas-water, or air-kerosene mixtures, diameters ranging from 12.7 mm to 102.26 mm, and various pipe inclinations, with 900 of those data points taken from horizontal flows. From their comparison, they recommended several correlations for each pipe orientation based on different criteria. Notably, the correlation of Rouhani and Axelsson [47] was able to predict 89.2 % of the horizontal data and 84.2 % of all of the flow data within 15 %.

Single-phase fully-developed pressure gradients

Fully-developed single-phase flow through a circular pipe has a linear pressure loss described by:

$$\frac{dP}{dz} = -\frac{f\rho V^2}{2D}, \tag{2.4}$$

where z is the axial flow direction, f is the Darcy friction factor, and D is the pipe diameter. For laminar flow it is well known that:

$$f = 64/\mathrm{Re}, \quad \mathrm{Re} \lesssim 2300, \tag{2.5}$$

but for the more complex turbulent flows empirical correlations must be used to define the friction factor. Several correlations exist; one common reference is the implicit equation from Colebrook [48]:

$$\frac{1}{f^{0.5}} = -2.0 \log\left(\frac{e/D}{3.7} + \frac{2.51}{\mathrm{Re} f^{0.5}}\right), \tag{2.6}$$

where e is the roughness height.

Two-phase fully-developed pressure gradients

Except for perfectly smooth stratified flows, gas-liquid flows are inherently unsteady with the interface between phases constantly in flux. Then, similar to turbulent single-phase flows, a fully-developed gas-liquid flow requires that the average pressure in the flow direction balances with the wall shear and results in a stable average velocity profile. With a long enough developing length the average pressure gradient, even for intermittent flows, is linear [49].

Ghajar and Bhagwat [50], and Elazhary [21] provide excellent summaries of the many available correlations and models. Generally, flows are analyzed as either homogeneous, where the two phases are assumed to flow at the same velocity, or separated, where the two phases move at different velocities with slip between them. The homogeneous assumption would be logical only for certain flows, such as bubbly and mist-annular, where the two phases have very little slip between them. Even so, the homogeneous flow assumption is often implemented to simplify formulations and correlations. If the flow is assumed homogeneous, then the pressure gradient can be calculated from Eq. (2.4) with the homogeneous density, ρ_{h}, defined as:

$$\rho_{\mathrm{h}} = \left(\frac{x}{\rho_{\mathrm{G}}} + \frac{1-x}{\rho_{\mathrm{L}}} \right)^{-1}, \tag{2.7}$$

and a homogeneous viscosity, ν_{h}. Correlations assuming homogeneous flow, like [45, 51], suggest different models for ν_{h}.

If the flow is assumed separated, correlations generally rely on the work of Lockhart and Martinelli [52] and their two-phase pressure multiplier, γ_{L}, defined as:

$$\gamma_{\mathrm{L}} = \left[\frac{(dP/dz)_{2\phi}}{(dP/dz)_{\mathrm{L}}} \right]^{1/2}, \tag{2.8}$$

where $(dP/dz)_{2\phi}$ is the two-phase fully-developed pressure gradient and $(dP/dz)_{\mathrm{L}}$ is the fully-developed pressure gradient if the liquid were flowing in the channel alone. Various models and correlations stemming from this work exist in the literature, like those of [33, 45, 51, 53–56].

Although there are many correlations, it is well documented that they are non-universal and have wide variation in their predictions [29, 50, 57, 58]. Often the correlations are phenomenologically based and flow-regime dependent, as expressed by [50, 59].

2.3 Single- and two-phase flow in combining tee junctions

Single-phase pressure losses

Previous works on single-phase pressure losses through tees have shown that for a given tee geometry, the pressure losses $\Delta P_{\text{M-C}}$ and $\Delta P_{\text{B-C}}$ are functions of W_{C} and λ, and that empirical correlations much better predict the data than theoretical attempts [1–4, 60–62].

For the horizontal, equal-sided, combining tee junction described in Fig. 1.1a, single-phase models use either a momentum or energy balance to describe the pressure losses. The momentum balance is valid only for $\Delta P_{\text{M-C}}$ since branch flows undergo a 90° bend. With the addition of a correction factor for the irreversible losses, $k_{1\phi,\text{m}}$, the momentum balance can be expressed as [2, 3, 63]:

$$\Delta P_{\text{M-C}} A = k_{1\phi,\text{m}}(W_{\text{C}} V_{\text{C}} - W_{\text{M}} V_{\text{M}}). \tag{2.9}$$

The value of $k_{1\phi,\text{m}}$ is generally determined empirically.

More commonly, both $\Delta P_{\text{M-C}}$ and $\Delta P_{\text{B-C}}$ are formulated with an energy balance. Assuming constant fluid properties and no change in internal energy, the energy balance from either inlet to the combined outlet with the addition of an irreversible term can be written as:

$$W_i\left(\frac{P_i}{\rho} + \frac{V_i^2}{2}\right) = W_i\left(\frac{P_{\text{C}}}{\rho} + \frac{V_{\text{C}}^2}{2}\right) + W_i \frac{V_{\text{C}}^2}{2} k_{1\phi,i\text{-C}}, \quad i = \text{B, M}, \tag{2.10}$$

where $k_{1\phi,i\text{-C}}$ is a single-phase loss coefficient. Solving for the pressure loss:

$$\Delta P_{i\text{-C}} = \frac{\rho V_{\text{C}}^2}{2}[1 - (\delta_{i\text{M}} - \lambda)^2] + \frac{\rho V_{\text{C}}^2}{2} k_{1\phi,i\text{-C}}, \quad i = \text{B, M}, \tag{2.11}$$

where $\delta_{i\text{M}}$ is the Kroenecker delta having a value of unity when $i = \text{M}$ and zero otherwise, and the value of $k_{1\phi,i\text{-C}}$ is generally determined empirically. For an equal-sided, horizontal, sharp edged combining tee, several correlations exist for $k_{1\phi,i\text{-C}}$; one such correlation from [63] gives the following:

$$k_{1\phi,\text{M-C}} = 1.55\lambda - \lambda^2, \tag{2.12a}$$

$$k_{1\phi,\text{B-C}} = 0.9(1-\lambda)(1+\lambda^2 - 2(1-\lambda)^2), \quad \lambda < 0.4, \tag{2.12b}$$

$$k_{1\phi,\text{B-C}} = 0.55(1+\lambda^2 - 2(1-\lambda)^2), \quad \lambda \geq 0.4. \tag{2.12c}$$

Two-phase pressure losses

As stated earlier, the only published studies on the topic of two-phase flow combing in a tee junction are [22, 30–32]. Detailed conditions for each of these studies are summarized in Table 2.1. The work of St. Pierre and Glastonbury [22] was performed in two horizontal, sharp-edged combining tee junctions but with branch sizes different than the main and combined. They measured the pressure distribution along all three sides of the tee using seven pressure taps in each of the three sides and reported their final values for $\Delta P_{i\text{-C}}$. However, their measurements were made using water and mercury manometers which they recognized as contributing significant error since the levels fluctuated and were difficult to read (particularly when slugging was present). Details of their data reduction procedure were not recorded and the uncertainty in curve fitting their results as in Fig. 1.2 is unknown. In addition to their experimental results, they also created three models to estimate to the pressure losses in a horizontal combining tee: the energy-based separated flow model (ESFM), the homogeneous flow model (HFM), and the momentum-based separated flow model (MSFM).

1. ESFM – This model was suggested for estimating either $\Delta P_{\text{B-C}}$ or $\Delta P_{\text{M-C}}$. St. Pierre and Glastonbury [22] derived the ESFM through a separated energy

Table 2.1 Summary of previous studies' test conditions. Flow regimes abbreviated as stratified (St), wavy (W), slug (Sl), and annular (A).

St. Pierre and Glastonbury [22]

Mixture	No. of Tests	W_C kg s^{-1}	x_C	λ_G	λ_L	P kPa	T °C	D mm	Outlet Regimes
Air-water	141	0.151–0.529	0.06–0.50	0.10–0.90	0.02–0.9	310	23–30	$D_C = 38.1$, $D_M = 38.1$, $D_B = 25.4$	A, Sl-A, Sl-W
Air-water	174	0.151–0.529	0.02–0.50	0.10–0.90	0.001–0.9	310	23–33	$D_C = 38.1$, $D_M = 38.1$, $D_B = 12.7$	A, W-A, Sl-W, Sl-A, W, St-W

Schmidt and Loth [30]

Mixture	No. of Tests	W_C kg s^{-1}	x_C	λ_G	λ_L	P kPa	T °C	D mm	Outlet Regimes
R-12	≈ 1000	–	–	–	–	826–3098	Near saturation	Vertical-up branch, 27.3	–

Belegratis [32]

Mixture	No. of Tests	W_C kg s^{-1}	x_C	λ_G	λ_L	P kPa	T °C	D mm	Outlet Regimes
SF_6-Exxsol D80	109	0.340–3.08	0.02–0.29	0.15–0.99	0.06–0.95	200, 470	Ambient	67	St, St-W, St-Sl, Sl
Air-Exxsol D80	22	0.533–2.68	0.00–0.05	0.08–0.80	0.09–0.74	100	Ambient	67	Sl
Air-Water	170	0.024–1.14	0.001–0.20	0.00–1.00	0.00–1.00	100	Ambient	38	St-W, W-Sl, Sl, Sl-A

balance on the mass entering from either inlet as it passed through the junction, and added an irreversible term based on the inlet's homogeneous velocity, $V_{\mathrm{h},i}$:

$$W_{\mathrm{G},i}\left(\frac{P_i}{\rho_\mathrm{G}}+\frac{V_{\mathrm{G},i}^2}{2}\right)+W_{\mathrm{L},i}\left(\frac{P_i}{\rho_\mathrm{L}}+\frac{V_{\mathrm{L},i}^2}{2}\right)= \tag{2.13}$$
$$W_{\mathrm{G},i}\left(\frac{P_\mathrm{C}}{\rho_\mathrm{G}}+\frac{V_{\mathrm{G,C}}^2}{2}\right)+W_{\mathrm{L},i}\left(\frac{P_\mathrm{C}}{\rho_\mathrm{L}}+\frac{V_{\mathrm{L,C}}^2}{2}\right)+$$
$$W_i\frac{V_{\mathrm{h},i}^2}{2}k_{\mathrm{ESFM},i\text{-C}},\quad i=\mathrm{B,\ M.}$$

Here, $k_{\mathrm{ESFM},i\text{-C}}$ is a two-phase loss coefficient and the homogeneous velocity is calculated from:

$$V_{\mathrm{h},i}=\frac{W_i}{A\rho_{\mathrm{h},i}},\quad i=\mathrm{B,\ M.} \tag{2.14}$$

Equation (2.13) can be reduced to:

$$\frac{2\Delta P_{i\text{-C}}}{\rho_{\mathrm{h},i}}=x_i(V_{\mathrm{G,C}}^2-V_{\mathrm{G},i}^2)+ \tag{2.15}$$
$$(1-x_i)(V_{\mathrm{L,C}}^2-V_{\mathrm{L},i}^2)+V_{\mathrm{h},i}^2k_{\mathrm{ESFM},i\text{-C}},\quad i=\mathrm{B,\ M.}$$

St. Pierre and Glastonbury [22] then applied a separated flow model to the reversible terms which allowed the gas and liquid components separate velocities calculated according to Eq. (2.3), and using the Turner and Wallis equation [64] for the void fraction, α. To close the model, St. Pierre and Glastonbury assumed the two-phase loss coefficient was equal to the single-phase loss coefficient defined in Eq. (2.11), and used their own experimental correlation for calculations.

2. HFM – This model was suggested for prediction of $\Delta P_{\text{B-C}}$ only, though it is unclear why the HFM was not used for prediction of $\Delta P_{\text{M-C}}$ as well. The HFM begins with the same energy balance as the ESFM, Eq. (2.13), but St. Pierre and Glastonbury assumed a homogeneous flow in each leg so that:

$$V_{\mathrm{G},i}=V_{\mathrm{L},i}=V_{\mathrm{h},i},\quad i=\mathrm{B,\ C.} \tag{2.16}$$

Again, the two-phase loss coefficient was assumed identical to the single-phase value defined in Eq. (2.11) and their own correlation was used in calculations.

3. MSFM – This model was derived from a momentum balance and is therefore only applicable for predicting $\Delta P_{\text{M-C}}$. Starting from a separated momentum balance, the basic equation with the addition of a two-phase correction factor for the irreversible losses, $k_{\text{MSFM,M-C}}$, can be written as:

$$\begin{aligned}\Delta P_{\text{M-C}} A = k_{\text{MSFM,M-C}}(&W_{\text{G,C}} V_{\text{G,C}} + W_{\text{L,C}} V_{\text{L,C}} \\ &- W_{\text{G,M}} V_{\text{G,M}} - W_{\text{L,M}} V_{\text{L,M}}).\end{aligned} \tag{2.17}$$

St. Pierre and Glastonbury then applied a separated flow assumption so that the gas and liquid velocities were calculated according to Eq. (2.3). To close the model, the two-phase correction factor was assumed to be equal to the single-phase value defined in Eq. (2.9) and their own correlation was used in calculations.

Schmidt and Loth [30] performed their experiments in a sharp-edged, equal-sided combining tee, but with a vertical-up branch and using refrigerant R-12. They measured the pressure distribution in each of the three sides using four pressure taps in each inlet and eight pressure taps in the outlet. The only pressure-drop results presented were graphically in comparison with models, however, in their presentation the value of $\Delta P_{i\text{-C}}$ and the corresponding independent parameters cannot be deciphered. In the body of their paper they cited a previous work, "Schmidt 1993", however this document was not listed within their reference list, and communications with the Technische Universität Darmstadt, where Schmidt's work was conducted, ended with confirmation that the university had no record, thesis, or report related to this work in their archives. In addition to their experimental work, they also created three models to estimate the pressure losses in a combining tee: the loss coefficient model (LCM), the contraction coefficient model (CCM), and the momentum coefficient model (MCM). These models are much more complicated than those of St. Pierre and Glastonbury [22], so only a brief outline of each model is given here with full derivations given in Appendix A.

1. LCM – This model was suggested for both $\Delta P_{\text{B-C}}$ and $\Delta P_{\text{M-C}}$. Schmidt and Loth assumed the flows from the main and branch inlets occupied separate stream tubes until some point downstream in the outlet where they mixed. Integral energy balances were then formed for the stream tubes and several additional terms were included such as mechanical energy exchange between the stream tubes, an additional pressure loss associated with development of the final outlet flow regime after the flows mixed, and streamline correction factors which allowed implementation of either homogeneous or separated flow models. The irreversible losses were included through means of two-phase loss coefficients similar to the single-phase energy analysis.

2. CCM – This model was suggested for prediction of both $\Delta P_{\text{B-C}}$ and $\Delta P_{\text{M-C}}$. For its derivation, Schmidt and Loth assumed a vena contracta immediately after the two inlets mixed and defined contraction coefficients for each inlet as the ratio of the minimum flow area at the constriction to the total area of the pipe. The pressure drop from either inlet up to the vena contracta was solved for with a control volume energy analysis as in the LCM including the same additional terms, and after the vena contracta a further pressure drop was added with a momentum balance as the flow settled to occupying the full pipe area.

To close the model, the contraction coefficients were solved for as functions of single-phase loss coefficients.

3. MCM – This model is suitable only for $\Delta P_{\text{M-C}}$ as it was based solely on a momentum balance. The MCM was derived similarly to the MSFM, but used a homogeneous model for the velocities and included an additional pressure loss associated with development of the final outlet flow regime. The two-phase correction factor was solved for in terms of the single-phase loss coefficient, $k_{1\phi,\text{M-C}}$.

Schmidt and Loth [30] provided some guidance on how to select the additional parameters involved in their models, but did not provide any conclusion about their models' predictive abilities or recommend one as more accurate.

Belegratis [32] performed his experiments in two horizontal, sharp-edged, equal-sided, combining tees, but did not explore a wide range of mixture qualities. In the test section with $D = 67\,\text{mm}$, the pressure distribution was measured with only two pressure taps in each of the three sides of the tee, while in the other test section, with $D = 38\,\text{mm}$, two pressure taps were used in each inlet and four pressure taps were used in the outlet. While no pressure loss data were reported, Belegratis [32] did compare the predictions of the models of both [22, 30] with both his and St. Pierre and Glastonbury's [22] experimental results and reported deviations ranging from (80–3 000) % with his own data, and (12–7 000) % with the data from [22].

Two-phase mixing behaviour

The only investigations on the effects of mixing in a horizontal combining tee junction, reporting something other than pressure loss information, were those of [31, 32]. The experimental conditions used in these studies are given in Table 2.1. One facility, with $D = 67\,\mathrm{mm}$, used one gamma densitometer and one capacitance probe in the branch, two gamma densitometers and two capacitance probes in the main, and two gamma densitometers and one capacitance probe in the combined side to measure the liquid hold-up. The other facility, with $D = 38\,\mathrm{mm}$, used two capacitance probes in each inlet, and four capacitance probes in the outlet to measure the liquid hold-up. From their measurements, they found that when slugging was present in one inlet and stratified flow present in the other inlet, a backflow could be induced in the stratified inlet. Under certain conditions, the backflow could be severe enough to trigger transition from stratified flow to slugging in that inlet. Further, under other conditions, a single slug passing through the main inlet could be broken into a chain of several shorter slugs by using a higher gas velocity in the branch inlet.

2.4 Two-phase time-varying pressure measurement

Several authors have investigated time varying pressure signals in gas-liquid flows in various systems: vertical pipes [38, 39, 42, 65–70], horizontal pipes [40, 71–78], vertical annulus [79, 80], a vertical impacting-dividing tee junction [81], and a small horizontal rectangular channel [41]. Generally, these studies used air-water mixtures but Matsui [39, 65] used nitrogen-water mixtures, others used R-113 [72, 73, 79], and Weisman et al. [72] included several other air-aqueous solutions. The objective of most of these studies was the development of an objective measure for use in flow regime identification. Several measurement methods and analysis techniques were used in the different studies. Some of the researchers measured and examined local pressure signals from individual taps [66, 71, 75, 77, 79, 80]. Others only measured differential pressure signals [39, 65, 67, 70, 72, 76, 81]. Others simultaneously measured pressures at multiple taps and examined both local and differential pressures [38, 40, 41, 68, 74]. Most of these studies measured the static pressure at the wall, but Kinoshita and Murasaki [69] used a pitot tube to measure the dynamic pressure, Lee et al. [73] measured the pressure drop across an orifice plate, and Elperin and Klochko [42] measured the differential pressure across a venturi.

The analysis techniques differed widely among the studies that aimed to develop an objective measure for use in flow regime identification with techniques such as:

- Examination of the time-varying pressure signal alone [40–42, 72, 74].
- Statistical analysis of the time-varying pressure measurements including histograms and statistical moments [38, 39, 65, 66, 68–70, 73, 76, 79].
- Statistical analysis of the time-varying pressure measurements including the use of cross-correlations [39, 65–67, 69, 74].
- Spectral analysis including power-spectrum density [41, 66, 70, 73, 76, 78].
- More advanced analysis including chaos theory and wavelet transforms [41, 42, 75, 76, 81].

There is little agreement between these works on a satisfactory method to categorize flow regimes based on their results.

On the other hand, Fan et al. [71] and Dukler and Hubbard [77] aimed to model the pressure variation caused by passing slugs. They examined time-varying pressure and liquid hold-up measurements at a single location with one observation of particular note for the current study described next. Consider a single pressure tap located flush in the bottom wall of a straight, long, horizontal pipe with an air-water mixture flowing in it. The pressure tap is located far downstream in the pipe and a short distance upstream of the pipe's outlet to the atmosphere. A single slug passes through the pipe and the pressure tap measures the local static pressure. The solid line on Fig. 2.3 shows an illustration of what the time-varying pressure measurements may look like. The time interval between points A and E in Fig. 2.3 is on the order of approximately 0.5 s [71, 77], but it varies with experimental conditions. Before time A the slug has not arrived at the pressure tap and the pressure variation is relatively small. From time A to B the slug passes directly over the pressure tap and a sharp pressure rise occurs as the slug scoops liquid from the flow and the gas blocked behind the slug accelerates it. From time B to D the slug is downstream of the pressure tap but not yet discharged, and the tap pressure remains high as the gas blockage remains. There is relatively small variation in pressure readings similar to those before the slug arrived, but at a higher overall pressure. At time D the slug exits the pipe and the pressure rapidly drops back to its initial level. The process repeats as more slugs pass through the pipe. This is shown in the pressure traces reported in [71, 74, 77, 78] with a more thorough explanation and models given in [71, 77].

Now consider the situation that occurs when two slugs pass over the pressure tap before the first is discharged, illustrated by the dashed line on Fig. 2.3. The same sequence of events described previously lead up to time C when a second slug passes over the pressure tap and cause a second rise in pressure. At time D, the first slug is discharged and the pressure drops, but remains higher than its initial pressure as the second slug is still in the system. At time F, the second slug exists the system and the pressure finally returns to its original level at time G. Bear in mind that slug velocity, slug length, pipe diameters, pipe lengths, and mixture properties all cause wide variation in pressure traces.

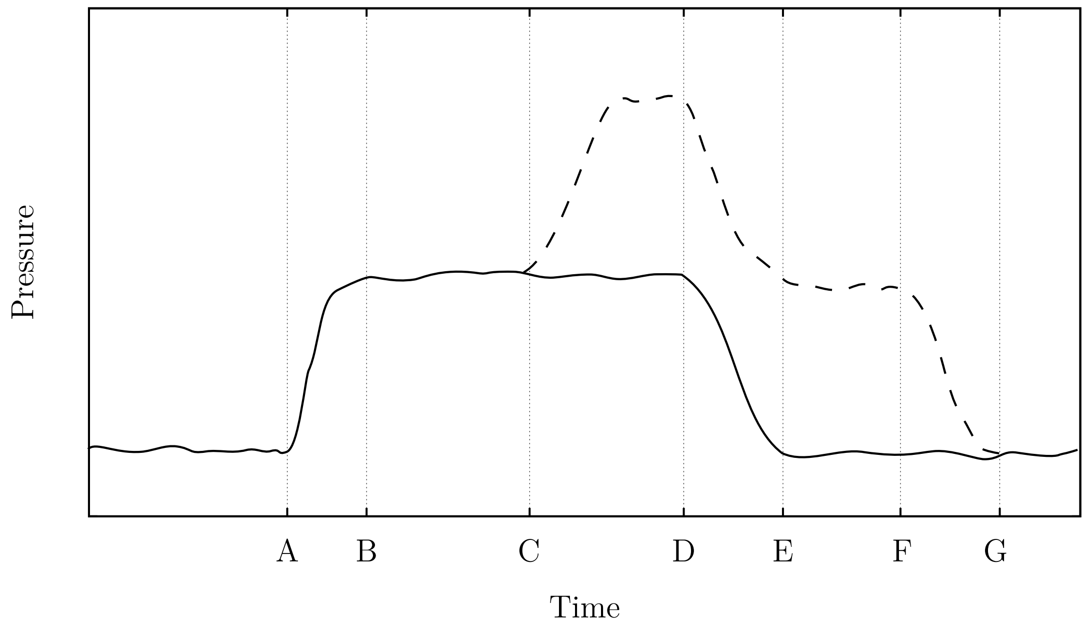

Figure 2.3 Illustration of idealized pressure traces during slug flow.

The case of a single slug, the solid line in Fig. 2.3, looks similar to a step function and results in two different pressure states for the pressure tap. The case of two slugs, shown by the dashed line in Fig. 2.3, has the features of two superimposed step functions and results in multiple pressure states. If more slugs pass over the pressure tap before any are discharged, more pressure states occur. These observations will be referred to later in Chapter 8.

Part II

The Rig and Analysis Techniques

Chapter 3

Apparatus

3.1 Overview

In order to fulfill the objectives laid out in Section 1.4 an apparatus was constructed capable of accurately monitoring static pressures at multiple locations around a horizontal combining tee junction. The next section provides a detailed description of the apparatus. The details of measuring devices and data acquisition follow.

3.2 The air-water loop

Figure 3.1 shows a schematic diagram of the apparatus, and Fig. 3.2 shows two photos of the apparatus. Several, but not all, items are labelled in the photo in Fig. 3.2a to help orient the reader. The facility was designed to operate using air-water mixtures at ambient temperature with an absolute static pressure of 150 kPa measured at the junction's centre. The test section was constructed from clear acrylic blocks and copper pipes of diameter (37.7 ± 0.2) mm. The lab's temperature and air pressure were monitored with a Control Company Traceable digital barometer which was factory calibrated with a National Institute of Standards and Technology traceable certificate to $\pm 1\,^{\circ}\mathrm{C}$ and ± 0.5 kPa, respectively.

Distilled water was pumped from a temperature controlled reservoir using a corrosion-resistant Berkely 3/4 hp shallow well pump. The amount of water sent to the test section was controlled using a bypass valve and passed through a 5 µm water filter before being split into the main and branch inlet streams. Each stream

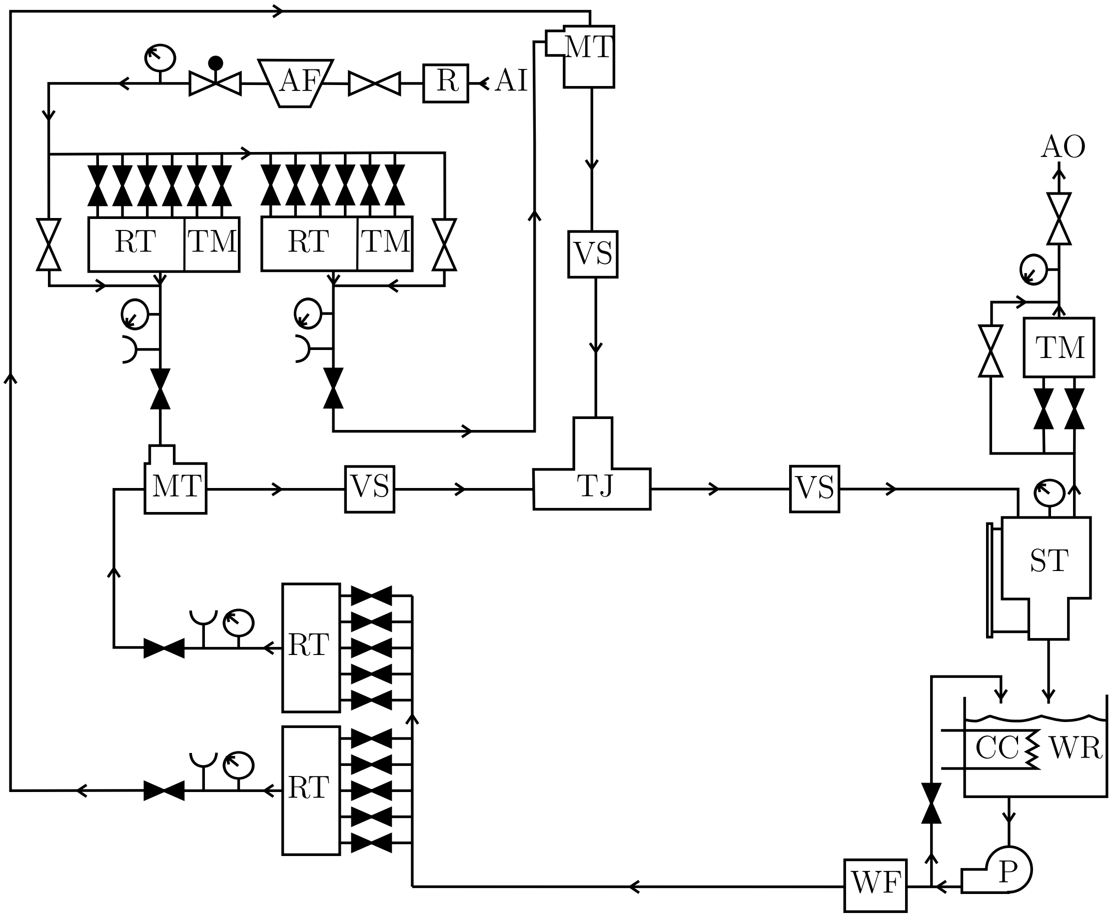

AF	Air filter	R	Air regulator	WF	Water filter
AI	Air inlet	RT	Rotameters	WR	Water reservoir
AO	Air outlet	ST	Separation tank		Control valve
CC	Cooling coil	TJ	Tee junction		Shut valve
MT	Mixing tee	TM	Turbine meters		Pressure controller
P	Pump	VS	Visual section		Thermocouple
					Pressure gauge

Figure 3.1 Schematic diagram of the experimental facility from Joyce and Soliman [82].

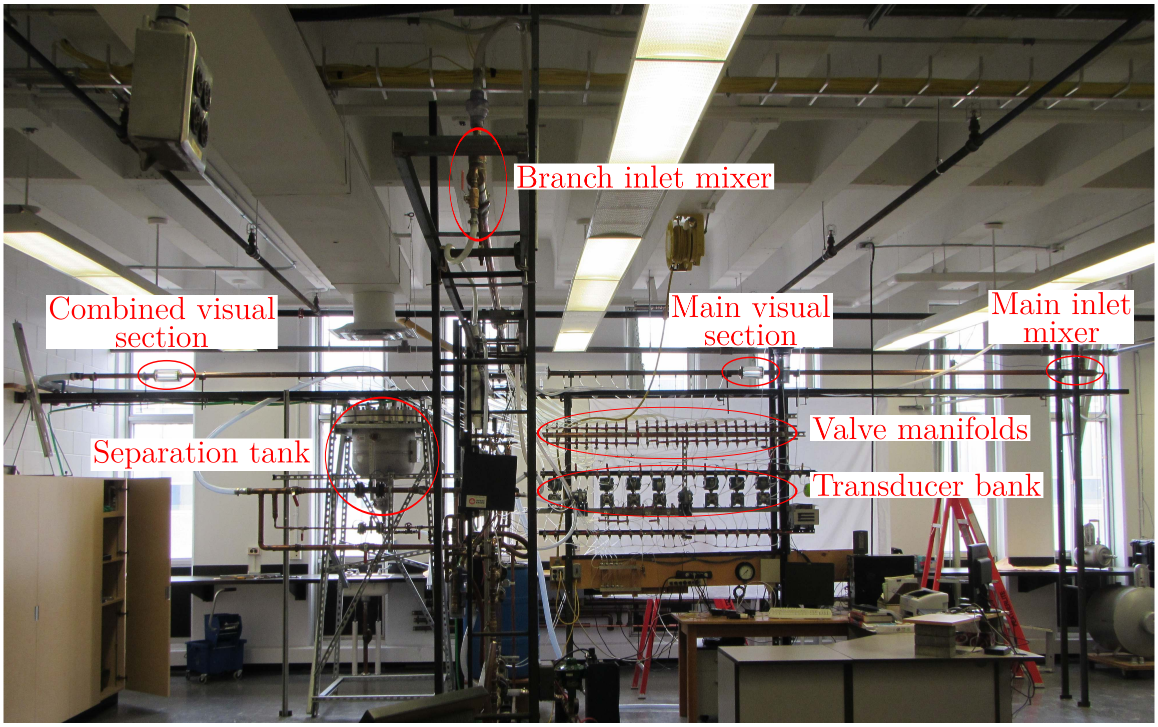

(a) View from under the branch inlet's mixer

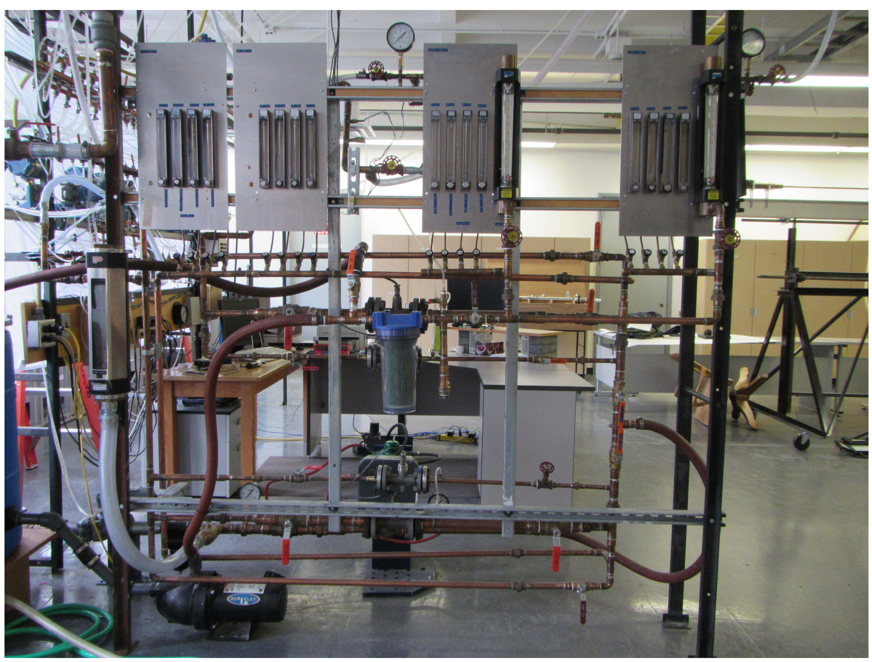

(b) View of the inlets' flow meters

Figure 3.2 Photos of the apparatus.

passed through its own metering station consisting of a bank of five rotameters with overlapping ranges configured in parallel, a thermocouple, and a pressure gauge. The flow rates were adjusted independently using needle valves with a maximum combined flow rate of $W_{\mathrm{L,C}} = 0.25\,\mathrm{kg\,s^{-1}}$ when the junction was at an absolute pressure of 150 kPa, corresponding to a superficial velocity of $V_{\mathrm{SL,C}} = 0.22\,\mathrm{m\,s^{-1}}$ at room temperature. With lower system pressures, as used in single-phase experiments, higher flow rates were possible. After metering, the water streams were directed to their corresponding inlet's air-water mixer.

Air from a central compressed-air line passed through a Fisher type 630 spring-loaded pressure regulator providing a first-stage of pressure control. The air passed through a 1 µm filter and then a Fisher type 4160k pressure controller providing a second-stage of pressure control. The air was then split into the two inlet streams and each stream passed through its own metering station consisting of a bank of four rotameters and two turbine meters with overlapping ranges configured in parallel, a thermocouple, and a pressure gauge. Each air stream's flow rate was controlled independently by needle valves with a maximum combined flow rate of $W_{\mathrm{G,C}} = 0.07\,\mathrm{kg\,s^{-1}}$ corresponding to a superficial velocity of $V_{\mathrm{SG,C}} = 35.6\,\mathrm{m\,s^{-1}}$ at room temperature and an absolute pressure of 150 kPa. After metering, the air streams were directed to their corresponding inlet's air-water mixer.

Figure 3.3 shows the details of the two identical air-water mixers constructed from standard copper fittings. The water mixed into the concentric air flow by spraying from an inner pipe perforated with 160 holes of 1.6 mm diameter. Each inlet's air-water mixture then entered a developing length of 60D, shown with dimensions in Fig. 3.5. Acrylic visual sections were installed in all three sides of the tee after the developing lengths, and the junction itself was manufactured out of a large acrylic block. The entire test section was levelled with a Wild Heerbrugg model NA20 automatic level with a standard deviation of 2.5 mm for 1 km double-run levelling. The test section discharged into a separation tank schematically shown in Fig. 3.4. Appendix B gives the full set of engineering drawings from Parr Metal Fabricators. The separation tank was designed with two sections: a small diameter lower section intended for low water flow rates where slight imbalances between the liquid flowing in and out corresponds to large interface movement in the sight glass, and; a large diameter upper section intended for high water flow rates where the interface movement is reasonably sensitive to liquid in and out flow imbalances necessary for intermittent regimes like slug flow. A perforated plastic baffle in the tank reduced splashing and improved separation. The separated air was then metered in a bank of two turbine meters with overlapping ranges configured in parallel, and discharged to the atmosphere through a muffler. The separated water was returned directly to the reservoir without metering.

Forty-nine pressure taps were distributed among the three sides of the junction as shown in Fig. 3.5: one tap at the centre of the junction, 18 taps in the branch, 15

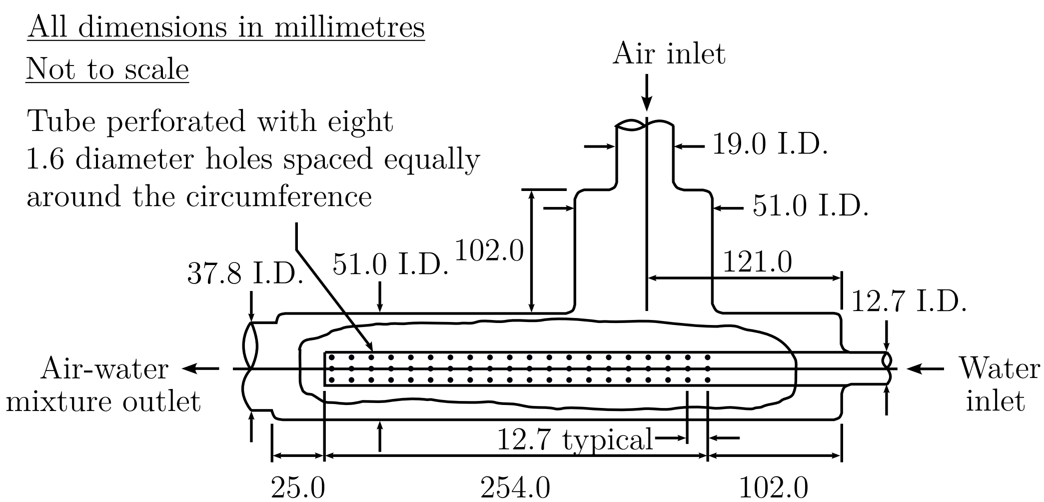

Figure 3.3 Details of the two-phase mixer from Van Gorp [83].

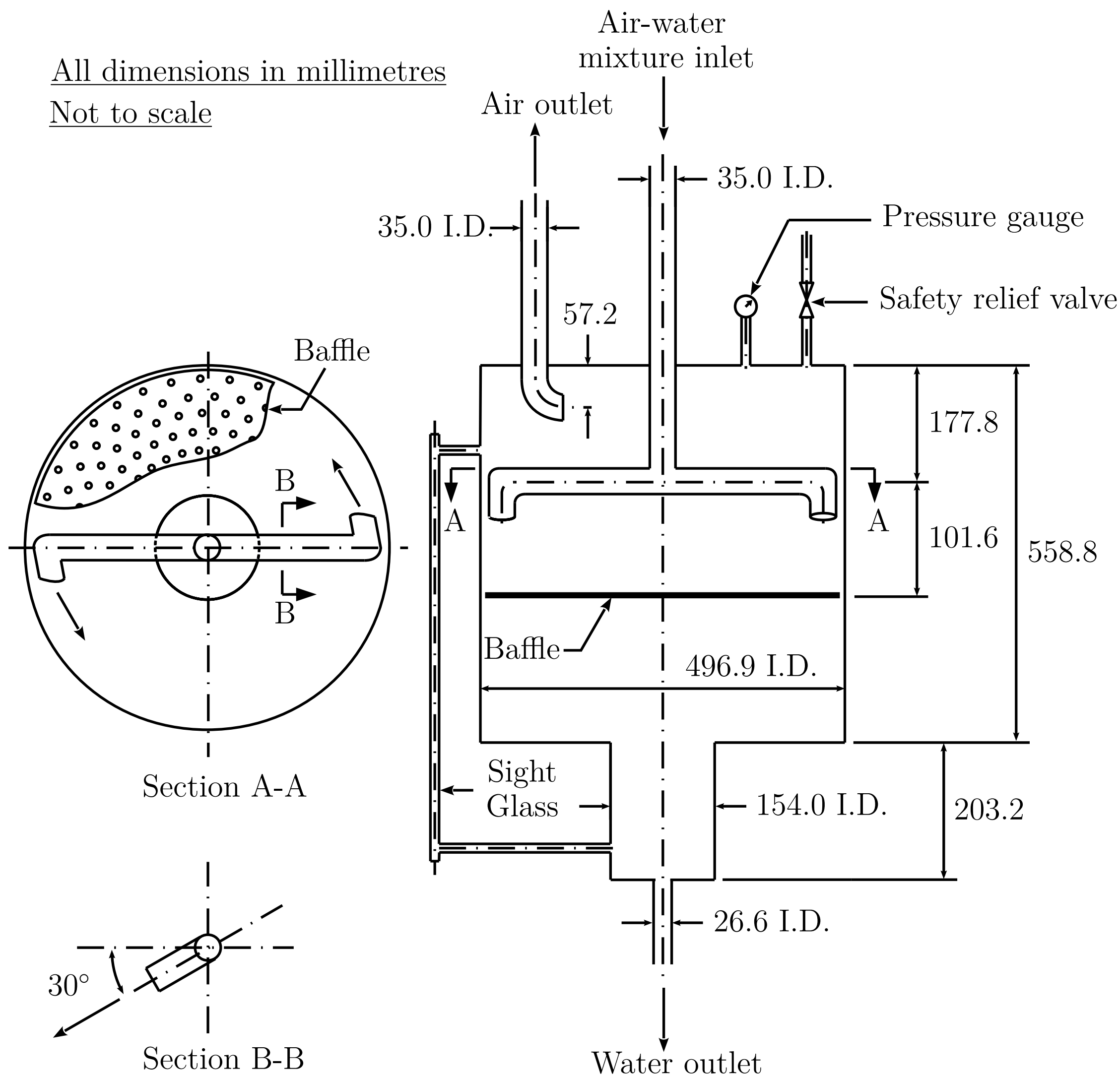

Figure 3.4 Details of the separation tank.

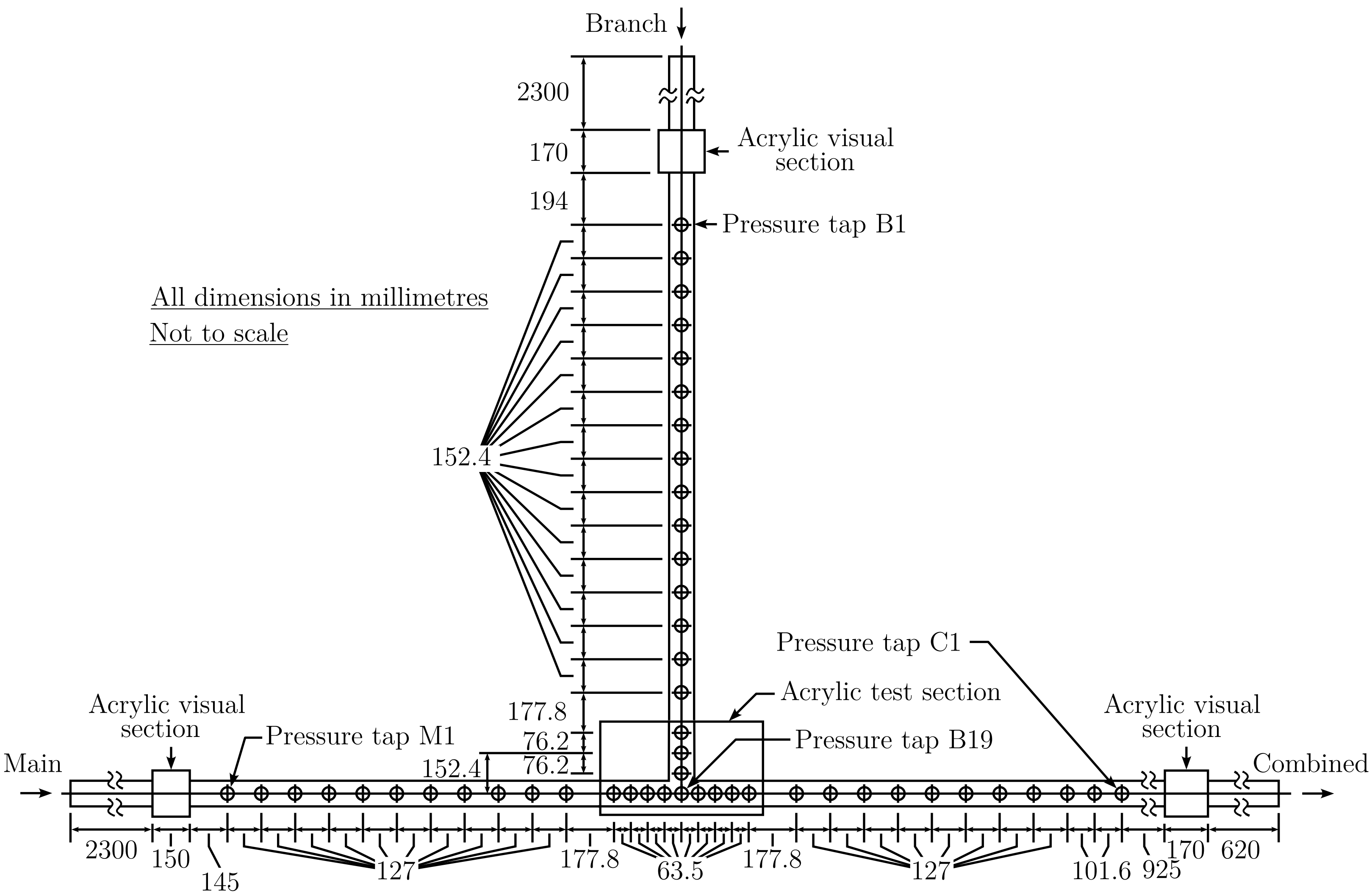

Figure 3.5 Details of the test section from Joyce and Soliman [84].

taps in the main, and 15 taps in the combined. For ease of reference the taps in each leg are numbered in ascending order starting at the tap furthest from the junction and labelled with the initial of the leg they are on. Taps B1, B19 (the junction's centre), M1, and C1 are labelled on Fig. 3.5. The taps in the copper pipes were drilled 1.6 mm holes in the bottom of the test section with 1/8 in barbed fittings soldered over them and connected to a bank of pressure transducers using 1/8 in clear, flexible Tygon tubing. Great care was taken to remove burs from the inside of the pipe as a result of drilling the taps, and also to clean any solder or flux from the taps after the barbed fittings were added. The taps in the acrylic test section were also 1.6 mm holes, but short pieces of acrylic tube with an outer diameter of 15.9 mm served as male fittings for connecting to the pressure transducers using 5/8 in clear, flexible Tygon tubing. For single-phase water and two-phase tests, the pressure transducers and connecting tubes were filled with water through a purge line and carefully monitored to ensure no air bubbles were present in the system. Eight of the 49 pressure taps were added part way through the experimental campaign: the four taps in the branch furthest from the junction, the two taps in the main furthest from the junction, and the two taps in the combined furthest from the junction. Pressure distributions of the experimental results will make clear which taps were installed at the time of the experiment. Operating procedures for single-phase and two-phase conditions can be found in Appendix C.

3.3 Measuring instrumentation

The measuring instruments were all calibrated in house. Calibration procedures and samples of typical calibration data compared with manufacturer calibrations can be found in Appendix D. The following sections give an overview of the various instruments and summarize their calibrated ranges.

Water meters

The water flow at each inlet was measured using separate banks of five rotameters. The largest rotameter in each inlet was manufactured by Fischer-Porter, while all other rotameters were manufactured by Cole-Parmer. Calibrations were done with weight and time measurements, and the rotameters' calibrated ranges in terms of the standard mass flow rates are listed in Table 3.1. Owing to the limitations of the pump, the combined flow rate could not exceed $W_{\mathrm{L,C}} = 0.25\,\mathrm{kg\,s^{-1}}$ when the junction's absolute pressure was 150 kPa, corresponding to a superficial velocity of $V_{\mathrm{SL,C}} = 0.22\,\mathrm{m\,s^{-1}}$. Higher flow rates were possible at lower pressures such as those used in the single-phase experiments.

Table 3.1 Water rotameters' calibrated ranges.

Model Number	$W_{\mathrm{std}} \times 10^4\,\mathrm{kg\,s^{-1}}$			
	Branch		Main	
	Lower	Upper	Lower	Upper
FM082-03	0.80	7.74	0.90	7.05
FM102-05	1.74	32.9	1.72	33.3
FM044-40-1	21.0	302	17.8	302
FM044-40-2	18.2	298	13.0	293
FP3/4-27-G-10/55	205	2010	226	1990

Air meters

The air flow at each inlet was measured using separate banks of four Cole-Parmer rotameters and two FTI Flow Technology turbine meters. The combined air flow was also measured after passing through the separation tank with a bank of two turbine meters. Accurate measurements from any of the various air meters relies on accurate pressure measurements at the instrument. As a result, each of the inlet rotameter banks and each individual turbine meter was connected by a manifold to an Omega PCL-200 pressure calibrator which was factory calibrated with a National Institute of Standards and Technology traceable certificate to ±0.5 kPa and confirmed against standards in house. Calibrations were done with wet test meters and venturi tubes as explained in Appendix D. The various meters' calibrated ranges, including representative values of the turbine meters calibrations, in terms of the standard mass flow rates are listed in Table 3.2. The combined flow rate could not exceed $W_{\mathrm{G,C}} = 0.07\,\mathrm{kg\,s^{-1}}$ corresponding to a superficial velocity of $V_{\mathrm{SG,C}} = 35.56\,\mathrm{m\,s^{-1}}$ at an absolute junction pressure of 150 kPa and a temperature of 20 °C.

The turbine meters required significant maintenance during the experimental

Table 3.2 Air meters' calibrated ranges.

Model Number	$W_{\mathrm{std}}\times10^6\,\mathrm{kg\,s^{-1}}$					
	Branch		Main		Combined	
	Lower	Upper	Lower	Upper	Lower	Upper
FM082-03	10.1	35.1	7.50	35.3	–	
FM102-05	17.5	175	15.4	175	–	
FM044-40-1	97.4	1210	117	1180	–	
FM044-40-2	84.5	1170	88.0	1190	–	
FT12-C1YA-PEA-1	3340	33200	3230	42700	2850	33400
FT24-C1Ya-GEA-1	20400	71300	16700	42100	15500	76900

campaign. The open bearing design used in the meters along with a large number of start-up and shut-down operations during the experimental campaign led to rapid degradation and failure of the bearings. Turbine meters are designed for continuous operation and each start-up and shut-down places stress on the bearings because of the associated acceleration. Eventually, the turbine meter will cease, but before that the calibration can drift significantly with increased bearing friction. The lifespan and accuracy of the turbine meters can be extended with gradual start-up and shut-down operations, but after prolonged use recalibration and possibly replacement of the bearings is necessary. After every approximately 24 hours of operation, the turbine meters were checked and recalibrated if necessary. During experiments requiring large air flow, it was not uncommon to have to replace bearings after every 6–8 hours of operation. An advantage of the turbine meters was their electronic output which was monitored with a data acquisition system.

Pressure transducers

Nine Rosemount pressure transducers were connected to the test section's pressure taps as shown in Fig. 3.6. This configuration allowed differential pressures to be measured in both of the inlets simultaneously against either a reference pressure or any of the taps in the outlet. The ability to measure against a reference pressure was necessary as the pressure transducers were calibrated to measure only positive differential pressures, while for some experiments (in the slug flow region) brief periods of negative differential pressure were possible if an inlet tap was measured against an outlet tap. The reference pressure was set using a high-precision hand pump and a 2 L reservoir. Transducer 0 was dedicated to measuring the junction's pressure at tap B19 (see Fig. 3.5, page 35) relative to the atmosphere. Tap B18 was also connected to transducer 0 in case flow conditions would not give stable readings at the junction's centre, tap B19, though this was never the case during the conducted experiments. When the rig was operating with either water or air-water mixtures the pressure read by transducer 0 had to be corrected by the height of the column of water connecting the tap to the transducer. The other eight transducers were calibrated as two sets, 1–4 and 5–8. Each set of transducers had overlapping ranges giving an extremely large measurement capacity with high accuracy. All of the transducers were monitored with a data acquisition system. The calibrated maximum pressure for each of the nine transducers is listed in Table 3.3. The pressure transducers' calibrations were done with various water and mercury manometers, details can be found in Appendix D. The Rosemount 1151 and 3051 transducers exhibit little to no drift, excellent calibration linearity, and high accuracy.

Data acquisition system

A data acquisition was constructed to process the analogue signals from the turbine meters and transducers, as well as to record all of the experimental data. The

Table 3.3 Pressure transducers' calibrated maximum pressures.

Transducer Number	Model Number	P_{maximum} kPa
0	1151DP 6E22B2C6	124
1, 5	3051DP CD0A02A1AH2B2C6L4	0.783
2, 6	1151DP 3E22B2C6	7.32
3, 7	1151DP 4E22B1C6	36.4
4	1151DP 5A22MB	184
8	1151DP 6E22B1C6	184

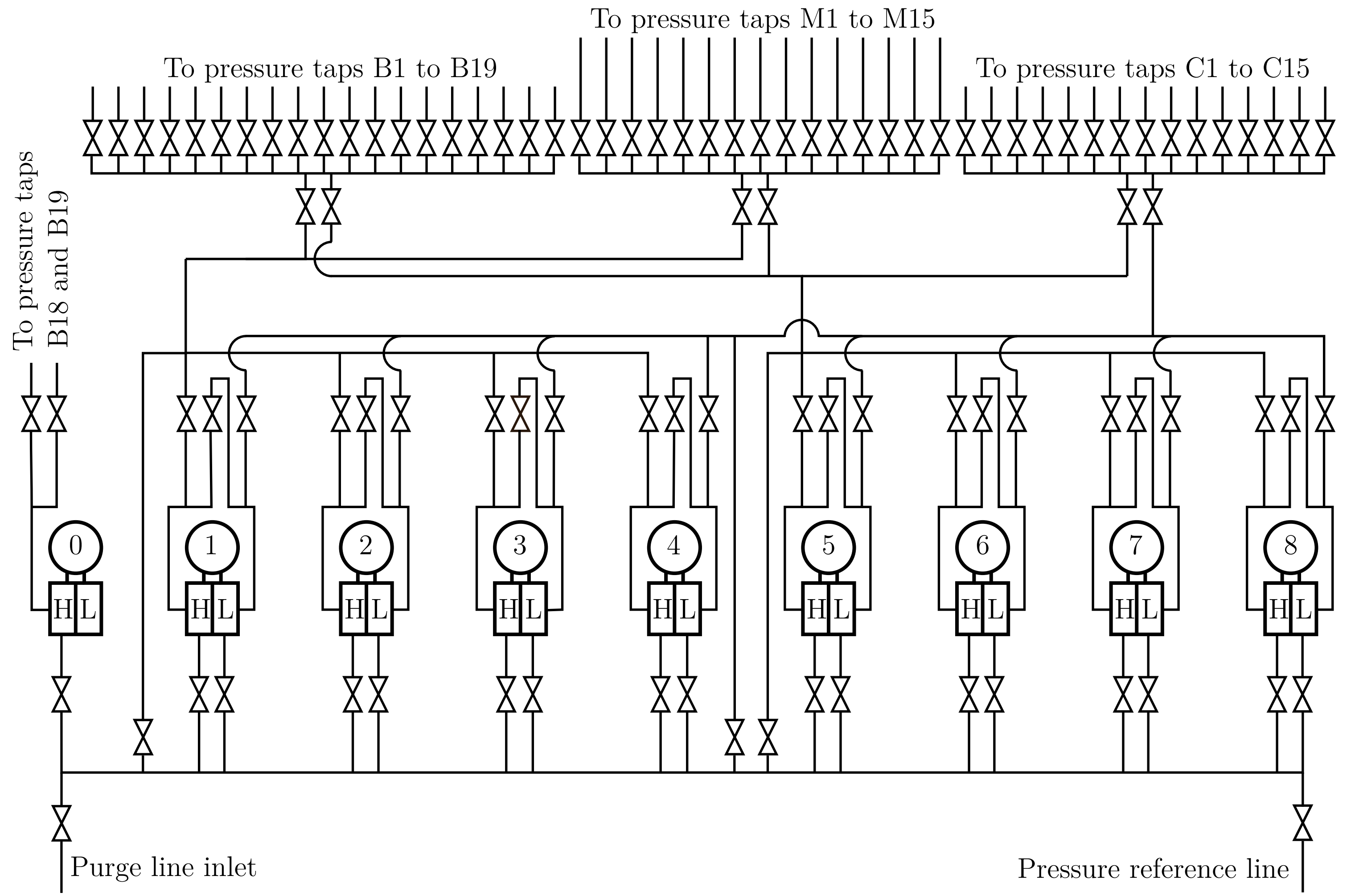

Figure 3.6 Pressure transducers' configuration.

data acquisition board was a 16 bit National Instruments PCI 6033E which accepted analogue (0–10) V signals from a National Instruments SCB 100 connector block. The turbine meters provided suitable output of (0–10) V directly, but the pressure transducers' output was an analogue current of (4–20) mA which had to be passed through high precision 500 Ω resistors to provide suitable voltage readings of (2–10) V. All of the experimental data, including rotameter readings, pressures, and temperatures, were recorded digitally using a custom instrument panel in National Instruments LabVIEW software.

Chapter 4

Analysis Calculations

4.1 Overview

For all experiments, the experimental data were reduced with the same analysis explained here. The measured data were generally recorded in terms of a time-averaged quantities and analysis performed on these values. The procedure for determining dP/dz and $\Delta P_{i\text{-C}}$ is discussed first, followed by statistical analysis used to objectively assess experimental repeatability, and finally a brief description of the uncertainty analysis (with further details in Appendix E).

4.2 Data reduction

Figure 4.1 shows a time-averaged pressure distribution relative tap C1, P_{R}, for $W_{\mathrm{C}} = 0.1009\,\mathrm{kg\,s^{-1}}$, $x_{\mathrm{C}} = 0.30$, $\lambda_{\mathrm{G}} = 0.50$, and $\lambda_{\mathrm{L}} = 0.20$. As explained in Appendix C.2, the pressures were measured in different ways depending whether the reference line was used or not. Accordingly, some minor manipulation of the measured data was done in order to reduce the data to the standard pressure distribution plots like Fig. 4.1. While not the most significant contribution, it does bear mentioning that these extra operations are considered in the uncertainty as discussed later.

For all experiments where the reference line was not in use the inlet pressure taps were measured relative to tap C1 directly.

$$P_{\mathrm{R}} = P_{\mathrm{measured}}. \tag{4.1}$$

The taps on the combined side were measured against the highest pressure tap so that they required an additional operation to calculate P_R:

$$P_\mathrm{measured} = P_i - \mathrm{MAX}(P_\mathrm{M1}, P_\mathrm{B1}),\ i = \mathrm{C1–C15}, \tag{4.2a}$$

$$P_\mathrm{R} = P_\mathrm{measured} - [P_\mathrm{C1} - \mathrm{MAX}(P_\mathrm{M1}, P_\mathrm{B1})]. \tag{4.2b}$$

For experiments using the reference line each inlet pressure tap was scanned simultaneously with C1. For experiments using 49 pressure taps the differential pressure relative the last tap in the outlet was calculated from the measurements as:

$$P_\mathrm{measured,1} = P_i - P_\mathrm{reference\ line},\ i = \mathrm{B1–B19,\ M1–M15}, \tag{4.3a}$$

$$P_\mathrm{measured,2} = P_\mathrm{C1} - P_\mathrm{reference\ line}, \tag{4.3b}$$

$$P_\mathrm{R} = P_\mathrm{measured,1} - P_\mathrm{measured,2}. \tag{4.3c}$$

The pressure taps on the combined side were similarly scanned simultaneously with the highest pressure tap so that the differential pressure relative to the last tap in the outlet was calculated as:

$$P_\mathrm{measured,1} = P_i - P_\mathrm{reference\ line},\ i = \mathrm{C1–C15}, \tag{4.4a}$$

$$P_\mathrm{measured,2} = \mathrm{MAX}(P_\mathrm{M1}, P_\mathrm{B1}) - P_\mathrm{reference\ line}, \tag{4.4b}$$

$$P_\mathrm{R} = P_\mathrm{measured,1} - P_\mathrm{measured,2} - [P_\mathrm{C1} - \mathrm{MAX}(P_\mathrm{M1}, P_\mathrm{B1})]. \tag{4.4c}$$

For each side of the junction the fully-developed pressure line was determined using a statistical method taken from Walpole and Myers [85]. As a first approximation, a line was generated with a least-squares analysis using the furthest three taps from the junction (either B1–B3, M1–M3, or C1–C3). An uncertainty in the curve fitting was then calculated with a 95 % confidence interval. The same curve fitting procedure was then repeated including another pressure tap's measurement and the uncertainty between the two regressions compared. If the uncertainty decreased with the additional pressure tap, it was assumed all of these pressure taps were within the fully developed region, and the procedure was repeated with the five furthest pressure taps and so on until the uncertainty increased, indicating an end of the fully developed region. Typically six to eleven pressure measurements were included in the final regression when wavy or annular flow was present in the combined side.

Rarely, this curve-fitting procedure creates a line of best fit based on very few data points that, although having an extremely low uncertainty, misrepresents the set of fully-developed data as a whole. This occurs when the first three or four points have an almost exact linear regression that is not aligned perfectly with the rest of the data, possibly as a result of a small change in operating conditions part way through the experiment or failure to allow the experiment to come to steady-state prior to taking measurements. As a precaution, if any of the regressions are based on less than five points the experiment was repeated since trying to 'correct' the regression by forcing the inclusion or removal of points is subjective and the intention of the procedure is to create an objective method to determining the 'best fit.'

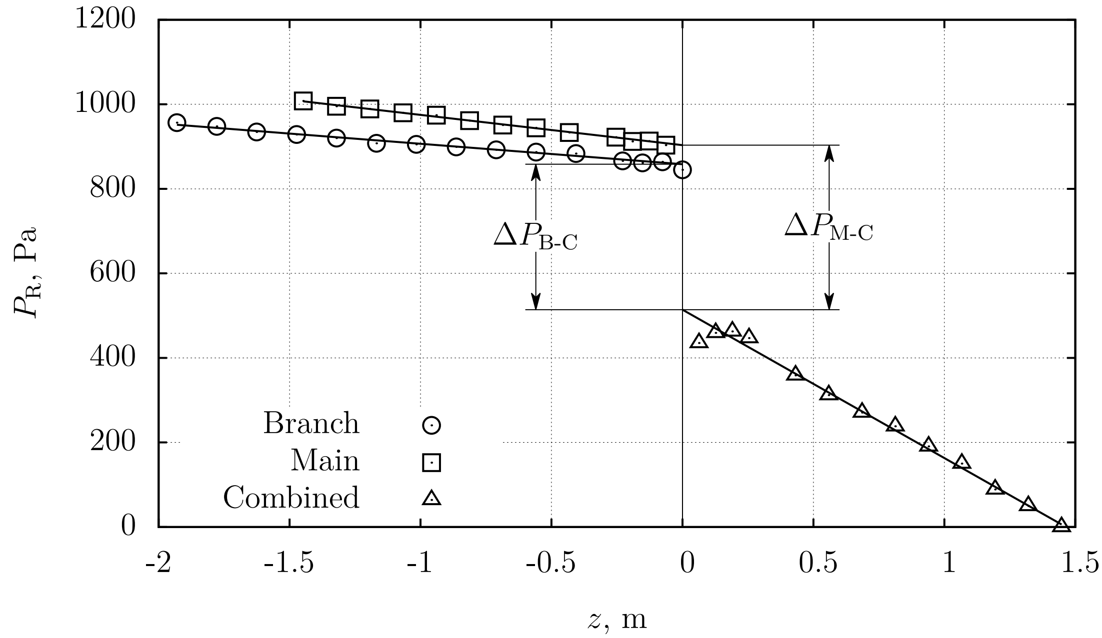

Figure 4.1 Sample time-averaged pressure distribution.

4.3 Repeatability and a note on fully-developed flow

Generally speaking, in order to show an experimental result is repeatable, simply conducting the experiment more than once and comparing the results suffices. The following sections use this method, with preliminary experiments to determine sufficient sampling times and sampling rates for each different outlet flow regime. Full experiments, samples of which are given later along with pressure loss values for comparison, were repeated for several conditions in order verify repeatability across the range of varied parameters.

Finally, the definition of $\Delta P_{i\text{-C}}$ requires that the measurements used to establish the lines in Fig. 4.1 come from a fully-developed pipe flow. It is not enough for the points to fit on a straight line well, but the value of dP/dz for a given combining flow experiment must also match the value of dP/dz for single-pipe flow (no combining) with the same flow conditions. Validation that the measurements come from fully-developed flow is accomplished in two ways: comparing measured dP/dz values from combining flow experiments with measured dP/dz values from single-pipe flow experiments (no combining) with the same flow conditions, and comparison of measured dP/dz values with different correlations available in the literature (see Section 2.2, page 15). Separate comparisons are made for each set of data.

4.4 Uncertainty

An uncertainty analysis was conducted for all results using the method of Moffat [86], described in detail in Appendix E. For all experiments, except those with slug flow or very low flow rates, the uncertainty in the pressure drop measurements was within 15 %. For all experiments, the liquid and gas mass flow rate uncertainties were always within ±3 %. The air mass balance from inlet to outlet was always within ±6 %. The uncertainty in dP/dz and $\Delta P_{i\text{-}C}$ for each experiment are reported in Appendix F.

Part III

Results

Chapter 5

Single-Phase Flow Results

A single-phase experimental campaign was completed using air and water. Comparison of the single-phase results with standard references provides validation of the rig, procedures, and analysis techniques. Before pressure-loss data was recorded, experiments were conducted to identify an appropriate sampling rate and time to ensure repeatable time-average pressure distributions. Using an air flow through only the main inlet with $V_G = 28.5\,\mathrm{m\,s^{-1}}$ and an absolute junction pressure of 150 kPa a differential measurement was taken between the pressure tap at the junction's centre and tap C1 using transducer 6. The results of various sampling time and frequency settings are listed in Table 5.1. Based on these results, a sampling frequency of 1 000 Hz and time of 120 s were used for all single-phase experiments as the difference between the resulting time-averaged pressures was within the instrument uncertainty.

A total of 37 single-phase experiments were carried out using air or water with various inlet mass distributions from $0 \leq \lambda \leq 1$. Air tests were conducted at room

Table 5.1 Single-phase repeatability tests for ΔP.

Sampling time s	Sampling frequency Hz	Time-averaged ΔP Pa
300	2 000	567.6
300	1 000	568.2
300	100	567.9
240	1 000	568.3
180	1 000	568.5
120	1 000	568.3
60	1 000	569.6

temperature with a nominal absolute pressure of 135 kPa and nominal outlet mass flow rates of 0.035 kg s^{-1} and 0.070 kg s^{-1} corresponding to Re = 64 400 and 128 800, respectively. Water tests were also conducted at room temperature but at a nominal absolute pressure of 108 kPa and nominal outlet mass flow rates of 0.265 kg s^{-1} and 0.400 kg s^{-1} corresponding to Re = 9 300 and 14 000, respectively. A full listing of experiment conditions and results are given in Appendix F. All measurements were taken without use of the reference line.

For the single-phase experiments, an analysis of the fully-developed pressure gradients and the pressure losses caused by the tee was conducted and the results compared to established values to prove the quality of the test facility and accuracy of the data acquisition and reduction processes. For each experiment, the values of the Darcy friction factor, f, were calculated using the measured dP/dz values in each side of the tee according to Eq. (2.4). Figure 5.1 shows the results along with Eqs. (2.5) and (2.6), the latter evaluated assuming smooth pipes ($e = 0$). Defining the root-mean-square deviation (RMSD) of the friction factor for n experiments as:

$$\mathrm{RMSD}(f) = 100\% \times \sqrt{\frac{1}{n}\sum_{j=1}^{n}\left(\frac{f_{\mathrm{crrltd},j} - f_{\mathrm{exp},j}}{f_{\mathrm{exp},j}}\right)^2}, \tag{5.1}$$

the RMSD for the friction factor was found to be 8.2 %, demonstrating good agreement with previous researchers and the high quality of the experimental facility and method of calculating the pressure gradient.

For single-phase flow, the values of $\Delta P_{i\text{-C}}$ are characterized by $k_{1\phi,i\text{-C}}$ defined by Eq. (2.11). Figure 5.2 graphically shows the experimental values of $k_{1\phi,i\text{-C}}$ compared with Idelchik's [63] correlation given by Eq. (2.12). There is some deviation between the water results and the air results in Fig. 5.2a. Elazhary [21] showed numerically that the single-phase loss coefficient is a function of Reynolds number when the value

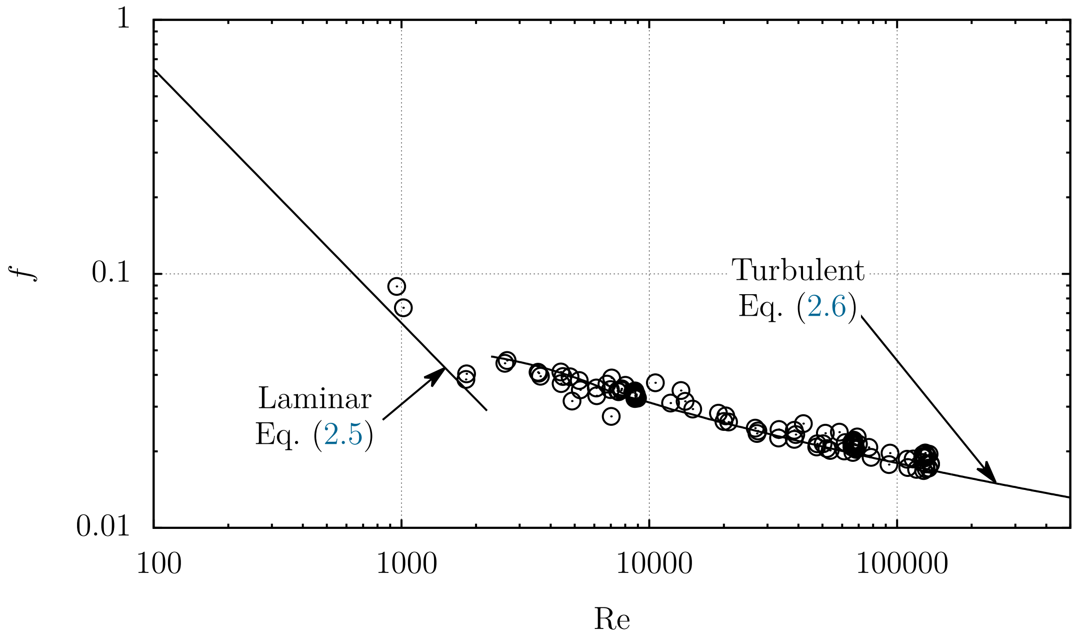

Figure 5.1 Experimental results for single-phase friction factor.

of Reynolds number is low; however at high Reynolds number, the loss coefficient becomes independent of Reynolds number. The deviation between the air and water results in Fig. 5.2a is attributed to the fact that $\mathrm{Re}_{\mathrm{water}}$ was relatively small (9 300 or 14 000) compared to $\mathrm{Re}_{\mathrm{air}}$ (64 000 or 128 800). The agreement with [63] is good, particularly for $k_{1\phi,\text{M-C}}$. A cubic polynomial fit of the experimental data resulted in the following equations:

$$k_{1\phi,\text{M-C}} = -0.009 + 1.528\lambda - 1.395\lambda^2 + 0.385\lambda^3, \tag{5.2a}$$

$$k_{1\phi,\text{B-C}} = -0.966 + 3.611\lambda - 2.510\lambda^2 + 0.838\lambda^3. \tag{5.2b}$$

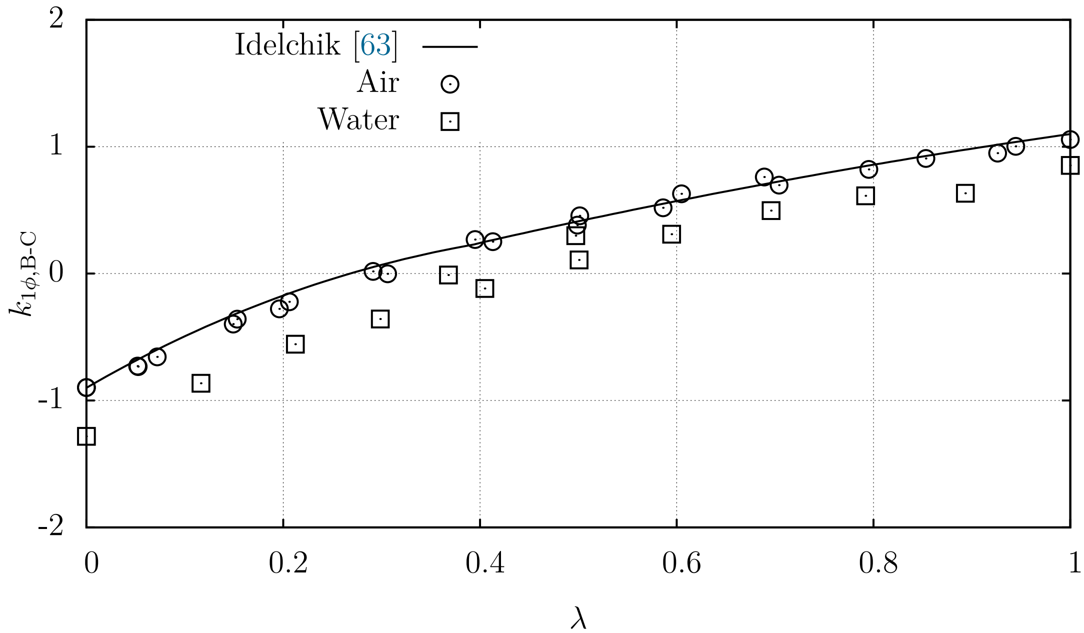

(a) Branch to combined

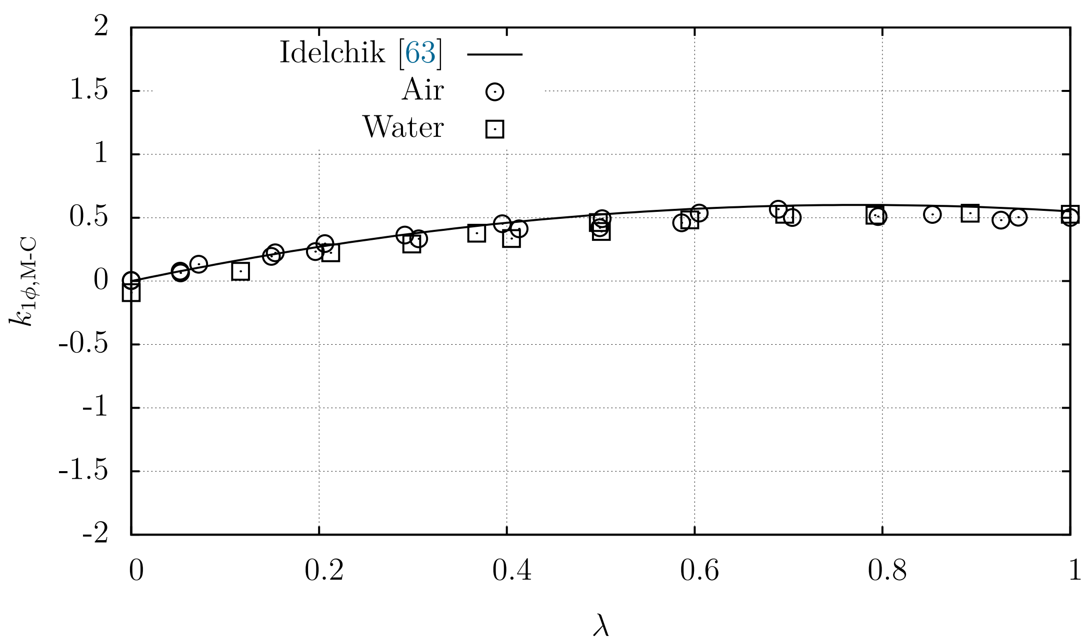

(b) Main to combined

Figure 5.2 Comparison of experimental values of $k_{1\phi,i\text{-C}}$ with Eq. (2.12) from [63].

Chapter 6

Annular Flow Results

6.1 Overview

Holding to the objectives of Section 1.4, an experimental campaign was completed with annular flow conditions in the combined side. As will be shown later (Section 7.4, page 90), $\Delta P_{i\text{-C}}$ varies with the square of W_C and was not initially considered for variation in the test matrix. Instead, a test matrix was designed to study the individual effects of x_C, λ_G, and λ_L by successively holding two parameters constant while varying the third. Later, a few tests varying the value of W_C were performed, but not independently (x_C also varied), for a total of 68 unique experiments. Table 6.1 summarizes the test conditions and Fig. 6.1 shows the combined flow conditions on Mandhane et al.'s [34] flow-regime map. The small variation in the mass flow between $W_\mathrm{C} = (0.101\text{–}0.114)\,\mathrm{kg\,s^{-1}}$ was not considered a variable. The flow regime in the combined side was annular in all cases except when $W_\mathrm{C} = 0.101\,\mathrm{kg\,s^{-1}}$ and $x_\mathrm{C} = 0.3$, or $W_\mathrm{C} = 0.056\,\mathrm{kg\,s^{-1}}$. In these cases the flow in the combined side was semi-annular, with only a partial annulus extending around approximately two-thirds of the pipe circumference when $W_\mathrm{C} = 0.101\,\mathrm{kg\,s^{-1}}$, and half of the pipe circumference

Table 6.1 Experiment conditions with annular flow in the combined side.

W_C $\mathrm{kg\,s^{-1}}$	x_C	λ_G	λ_L
0.056	0.9	0.3, 0.7	0.2, 0.8
0.101–0.114	0.3, 0.5, 0.7	0, 0.3, 0.5, 0.7, 1	0.2, 0.4, 0.6, 0.8
0.135	0.3	0.3, 0.7	0.2, 0.8

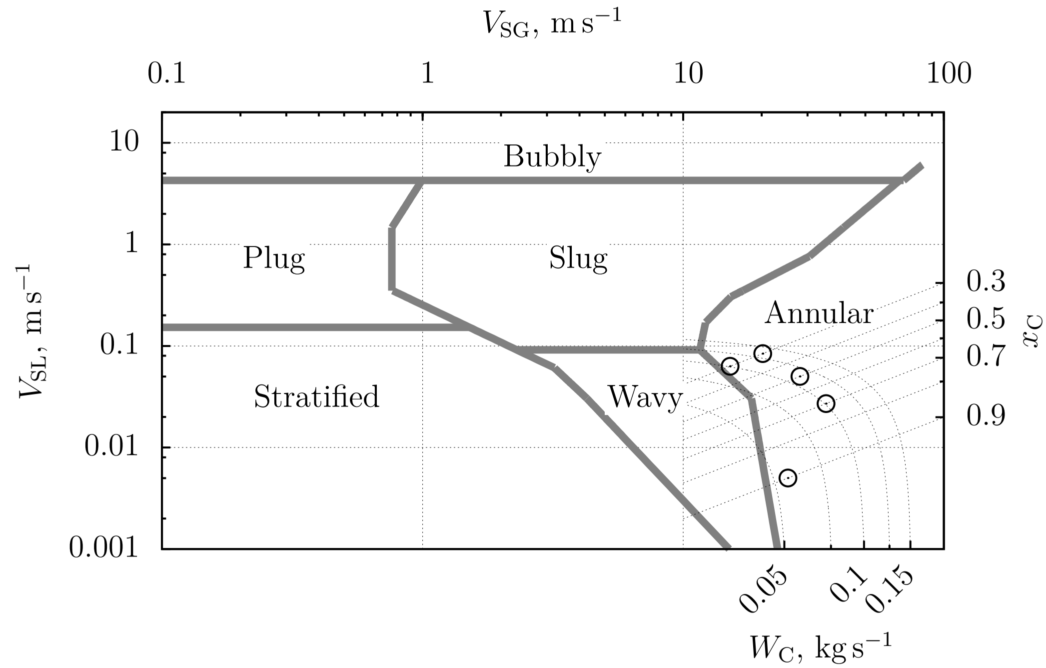

Figure 6.1 Annular flow conditions in the combined side on the flow-regime map of Mandhane et al. [34].

when $W_{\mathrm{C}} = 0.056\,\mathrm{kg\,s^{-1}}$. The flow regimes in the main and branch sides also included wavy and stratified flows.

The results of the experimental campaign are dealt with next. The first section verifies repeatability as laid out in Section 4.3. The second section shows the measured values of dP/dz are both accurate and correspond to fully-developed flow as explained in Section 4.3. Finally, the third section discusses the results for $\Delta P_{i\text{-C}}$, evaluates the performance of previous models, and introduces a new model.

6.2 Sampling rate and repeatability tests

Before pressure-loss data were recorded, an experiment was conducted to determine an appropriate sampling time for repeatable time-averaged pressure distributions. For a flow with $W_\mathrm{C} = 0.106\,\mathrm{kg\,s^{-1}}$, $x_\mathrm{C} = 0.54$, $\lambda_\mathrm{G} = 0.50$, and $\lambda_\mathrm{L} = 0.50$, the differential pressure between taps B1 and C1 was monitored with transducer 2 and the time-varying signal recorded over a period of 30 min at a sampling frequency of 1 000 Hz. The average pressure difference between the two taps was calculated after various amounts of time with the results summarized in Table 6.2. Variation of the sampling rate from (100–4 000) Hz did not affect the results, and so a conservative sampling time of 120 s with a sampling frequency of 1 000 Hz was selected for all experiments with annular flow in the outlet. Figure 6.2 and Table 6.3 show the results of repeating an experiment and confirm the sampling frequency and time experiments with annular flow in the combined side. Other experiments were also repeated with results given in Appendix F.

Table 6.2 Repeatability tests for $\Delta P_\text{B1-C1}$ in an experiment with annular flow in the outlet ($W_\mathrm{C} = 0.106\,\mathrm{kg\,s^{-1}}$, $x_\mathrm{C} = 0.54$, $\lambda_\mathrm{G} = 0.50$, $\lambda_\mathrm{L} = 0.50$).

Sampling time s	Time-averaged ΔP Pa
1 800	3 464.3
300	3 464.9
240	3 466.1
180	3 467.4
120	3 464.9
60	3 465.0

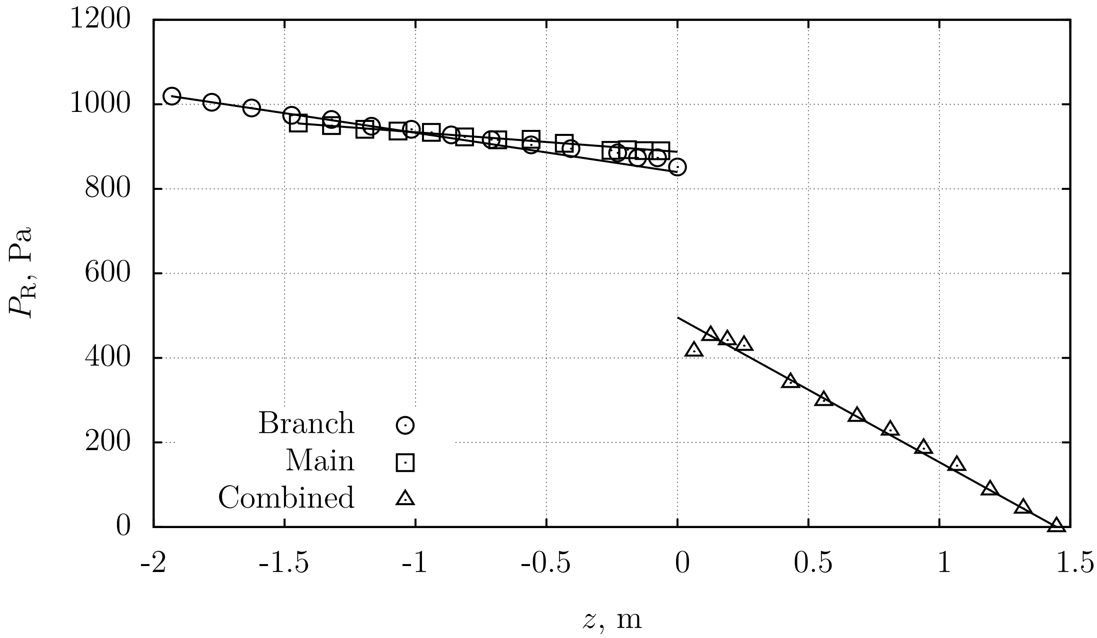

(a)

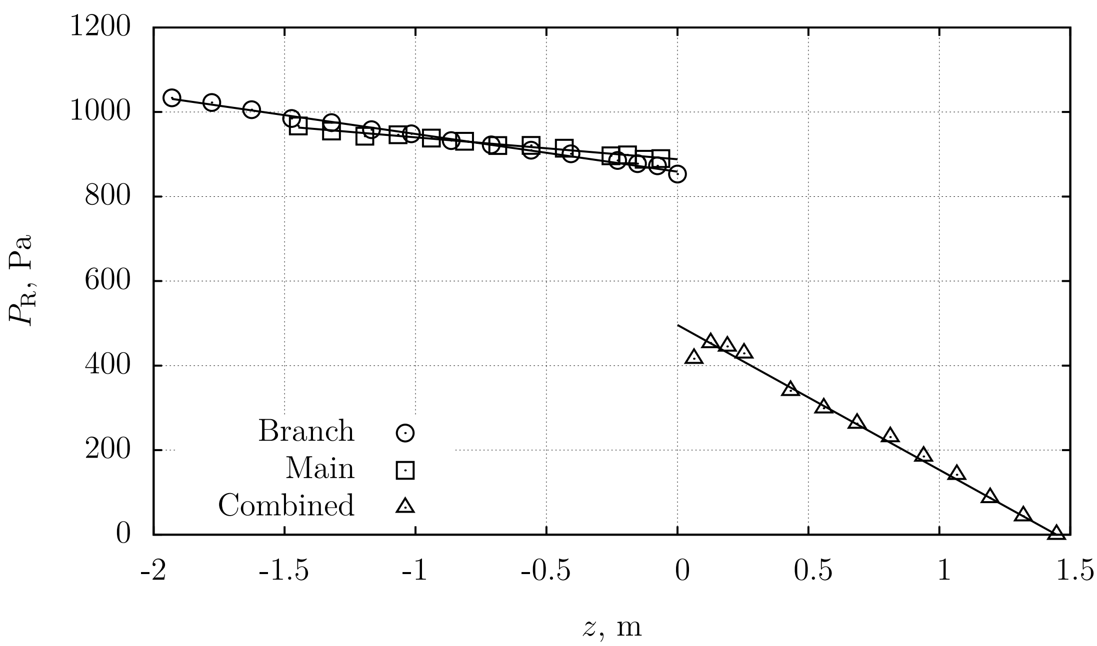

(b)

Figure 6.2 Pressure distributions for a repeated experiment with annular flow in the outlet ($W_C = 0.101\,\mathrm{kg\,s^{-1}}$, $x_C = 0.30$, $\lambda_G = 0.50$, $\lambda_L = 0.60$).

Table 6.3 Result summary for a repeated experiment with annular flow in the outlet.

W_{C}	x_{C}	λ_{G}	λ_{L}	$\Delta P_{\text{M-C}}$	$\Delta P_{\text{B-C}}$	dP/dz_{M}	dP/dz_{B}	dP/dz_{C}
$\mathrm{kg\,s^{-1}}$				Pa		$\mathrm{Pa\,m^{-1}}$		
0.101	0.30	0.50	0.60	384.1	355.2	52.2	89.1	346.4
0.101	0.30	0.50	0.60	380.7	355.1	49.9	81.4	345.6

6.3 Pressure gradients

The accuracy of the fully-developed dP/dz is crucial to determining the values of $\Delta P_{i\text{-C}}$. As a first confirmation of the dP/dz values a single experiment with an even flow distribution between the inlets was performed. Figure 6.3 shows the pressure distribution and Table 6.4 summarizes the values of dP/dz. Clearly the measurements for each inlet fit very well on the drawn lines, and $dP/dz_{\mathrm{B}} \approx dP/dz_{\mathrm{M}}$ within the measurement uncertainty.

Figure 6.4 shows the pressure distribution for a pipe flow experiment without any flow in the branch, and Table 6.4 lists the dP/dz values. The flow is slightly disturbed near the junction and $dP/dz_{\mathrm{M}} \approx dP/dz_{\mathrm{C}}$. Further, considering the small differences in flow rates between experiments, the dP/dz values agree very well between both the combining and pipe flow experiments and show that the gradients are from

Table 6.4 dP/dz results for a combining flow experiment with even flow distribution and annular flow in the combined, and a pipe flow experiment with the same inlet flow rate.

W_{C}	x_{C}	λ_{G}	λ_{L}	dP/dz_{M}	dP/dz_{B}	dP/dz_{C}
$\mathrm{kg\,s^{-1}}$				$\mathrm{Pa\,m^{-1}}$		
0.106	0.54	0.50	0.50	216.9	234.0	1 100.5
0.052	0.52	0.00	0.00	204.8	–	204.9

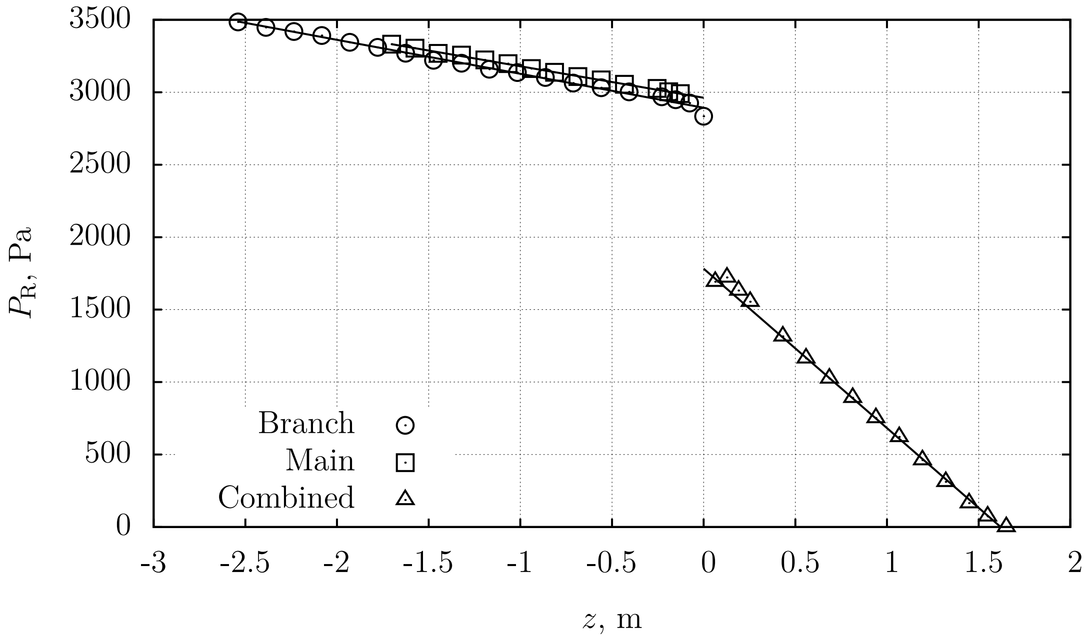

Figure 6.3 Pressure distribution for a combining flow experiment with an even flow distribution and annular flow in the combined side ($W_C = 0.106\,\mathrm{kg\,s^{-1}}$, $x_C = 0.54$, $\lambda_G = 0.50$, $\lambda_L = 0.50$).

fully-developed data in the combining case.

Validation of the measured dP/dz was also done by comparison with correlations in [33, 45, 51, 53–56]. Separated comparisons of stratified, wavy, and annular flow regimes were made as different correlations perform better for different flow patterns [50, 57, 59]. Generally, stratified and stratified-wavy flows had values of $dP/dz < 100\,\mathrm{Pa\,m^{-1}}$, wavy and semi-annular flows had values of $100\,\mathrm{Pa\,m^{-1}} \leq dP/dz \leq 800\,\mathrm{Pa\,m^{-1}}$, and annular flows had values of $dP/dz > 800\,\mathrm{Pa\,m^{-1}}$. Figure 6.5 shows the best comparisons for the three regions using the phenomenological model of Taitel and Dukler [33] for stratified flows, and the correlations of Sun and Mishima [56] and Müller-Steinhagen and Heck [54] for wavy and annular flows, respectively. The RMSD(dP/dz) values for the stratified, wavy, and annular results were 34.1 %, 15.9 %, and 9.9 %, respectively.

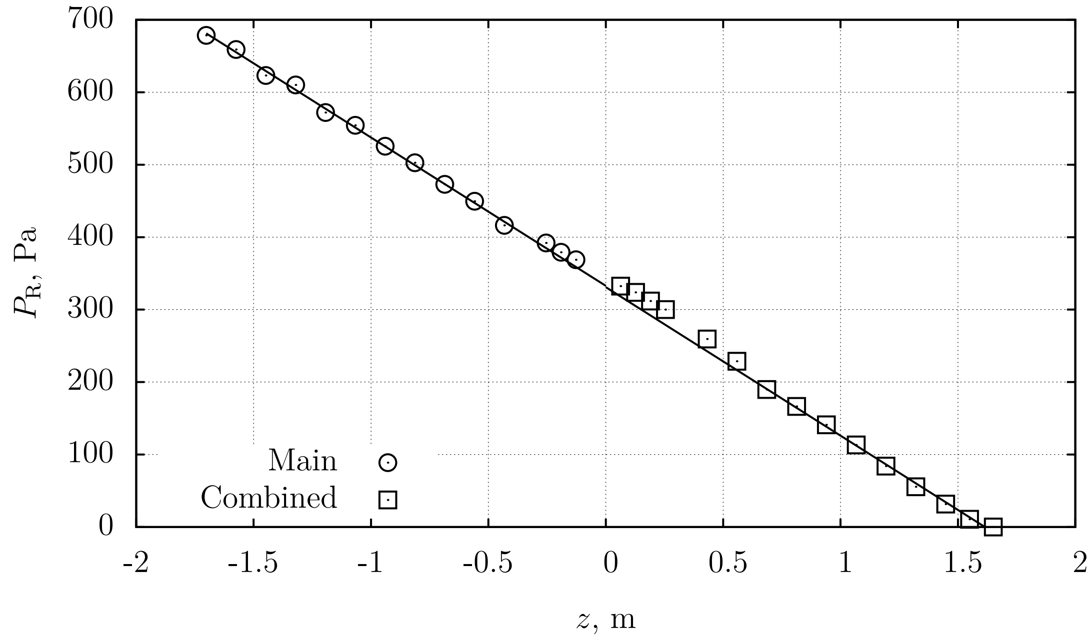

Figure 6.4 Pressure distribution for a pipe flow experiment with no flow entering through the branch ($W_C = 0.052\,\mathrm{kg\,s^{-1}}$, $x_C = 0.52$, $\lambda_G = 0.00$, $\lambda_L = 0.00$).

Tribbe and Müller-Steinhagen [59] have also noted that for stratified smooth flows accurate prediction is very difficult and small absolute errors appear large in relative measures, and similar behaviour was noted in [58] where the correlation accuracy was found to decrease as the mass flux (and thus the pressure gradient) decreased. Overall, the results indicate that the fully-developed slopes were accurately calculated.

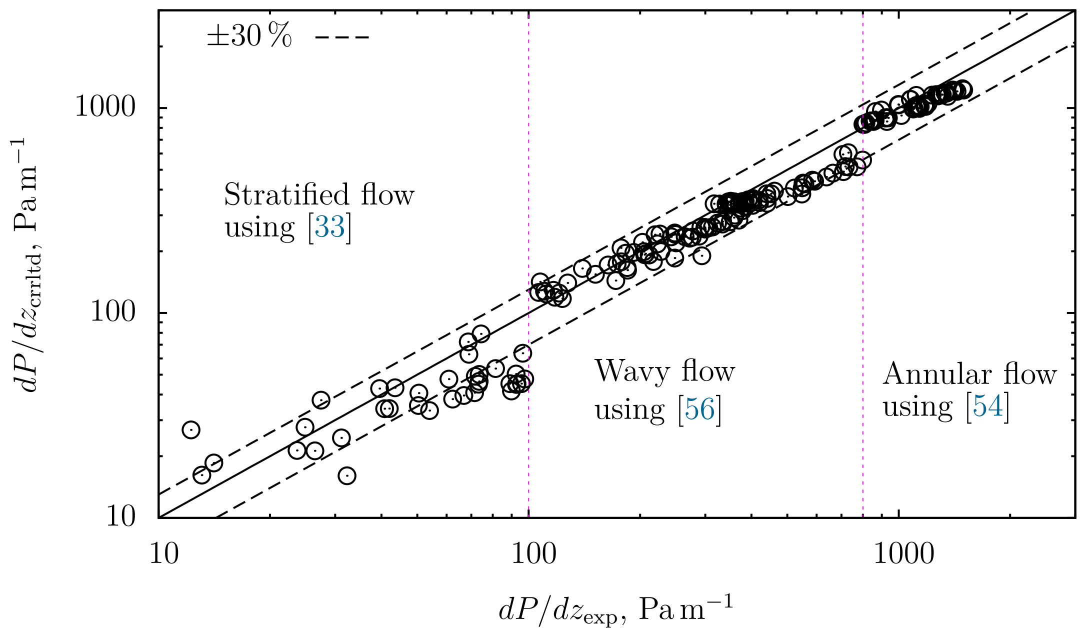

Figure 6.5 dP/dz results for experiments with annular flow in the combined side compared with correlations of [33, 54, 56].

6.4 Pressure drop

Experimental results

Figure 6.6 summarizes the results for $\Delta P_{i\text{-C}}$ with $W_{\mathrm{C}} = (0.101\text{–}0.114)\,\mathrm{kg\,s^{-1}}$. Dotted lines have been included on the plots to help differentiate the data. For this single mass flow rate, the dominant parameters are λ_{G} and x_{C}, with very little variation across the entire range of λ_{L}. The relatively high gas velocity compared to the liquid for these experiments explains the limited dependence on λ_{L}. For $x_{\mathrm{C}} = 0.5$ and 0.7 there appears to be a maximum value of $\Delta P_{\mathrm{B\text{-}C}}$ around $\lambda_{\mathrm{G}} = 0.7$, likely due to vigorous mixing at that flow distribution.

Figure 6.7 summarizes the results for $\Delta P_{i\text{-C}}$ with $W_{\mathrm{C}} = 0.056\,\mathrm{kg\,s^{-1}}$ and $0.135\,\mathrm{kg\,s^{-1}}$.

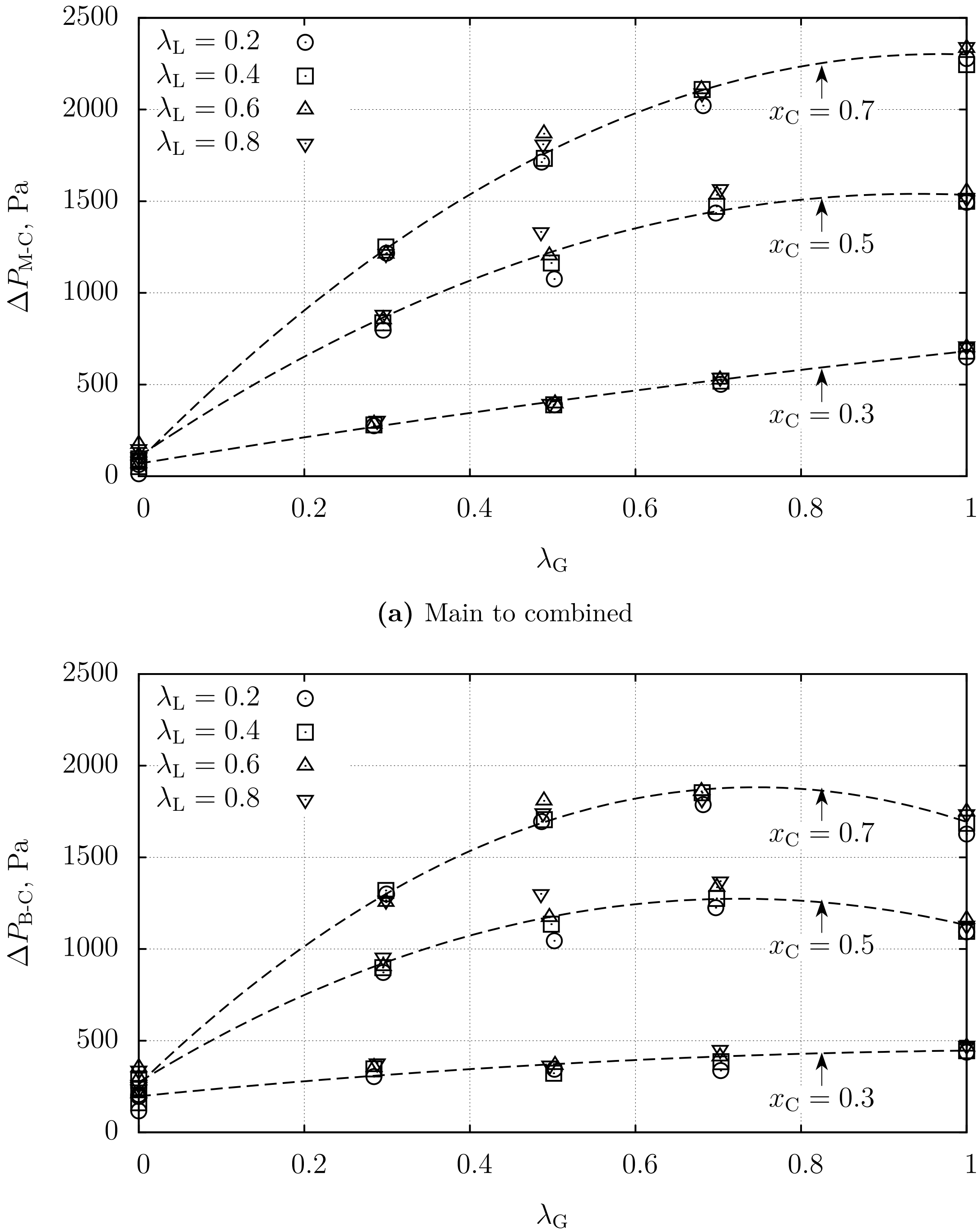

(a) Main to combined

(b) Branch to combined

Figure 6.6 Variation of $\Delta P_{i\text{-C}}$ with λ_G and x_C for $W_C = (0.101\text{–}0.114)\,\mathrm{kg\,s^{-1}}$.

Dotted lines have again been included on the plots to help differentiate the data. Consistent with the above reasoning, the data demonstrates little dependence on λ_L for $W_\mathrm{C} = 0.056\,\mathrm{kg\,s^{-1}}$ where $x_\mathrm{C} = 0.90$, and more significant dependence for $W_\mathrm{C} = 0.135\,\mathrm{kg\,s^{-1}}$ where $x_\mathrm{C} = 0.30$. Refer to Appendix F for a full set of experimental results.

Evaluation of previously published models

The previously published models for $\Delta P_{i\text{-C}}$ (see Section 2.3, page 18) were compared to the experimental results to demonstrate their predictive abilities. All of the experimental data except for those where $\lambda_\mathrm{G} = 0$ and $\lambda_\mathrm{G} = 1$ were included in the comparison. These data were excluded since the models were not intended for use with single-phase flow in either inlet. For implementation of the models, the void fraction was estimated by a semi-empirical correlation from [87]. For evaluation of the models, the arithmetic mean deviation (AMD) is defined as:

$$\mathrm{AMD}(\Delta P_{i\text{-C}}) = \frac{100\%}{n} \times \sum_{j=1}^{n} \left(\frac{(\Delta P_{i\text{-C}})_{\mathrm{crrltd},j} - (\Delta P_{i\text{-C}})_{\mathrm{exp},j}}{(\Delta P_{i\text{-C}})_{\mathrm{exp},j}} \right), \quad i = \mathrm{B},\ \mathrm{M}. \tag{6.1}$$

Table 6.5 summarizes the RMSD and AMD for each model. Based strictly on the RMSD, the poorest agreement was with the ESFM for $\Delta P_\text{M-C}$ and the HFM for $\Delta P_\text{B-C}$, both shown in Fig. 6.8. From these figures it is clear the ESFM underpredicts $\Delta P_\text{M-C}$ though it follows the overall trend in the data without much scatter in its predictions, while the HFM has a large amount of scatter and generally overpredicts $\Delta P_\text{B-C}$.

Conversely, the best agreement, based strictly on the RMSD, was with the LCM for both $\Delta P_\text{M-C}$ and $\Delta P_\text{B-C}$, both shown in Fig. 6.9. While the overall predictions of the LCM are reasonable, the model's predictions were less accurate when the outlet quality was $x_\mathrm{C} = 0.3$, corresponding to the data points with $\Delta P_{\text{M-C},\mathrm{exp}} < 700\,\mathrm{Pa}$. Isolating

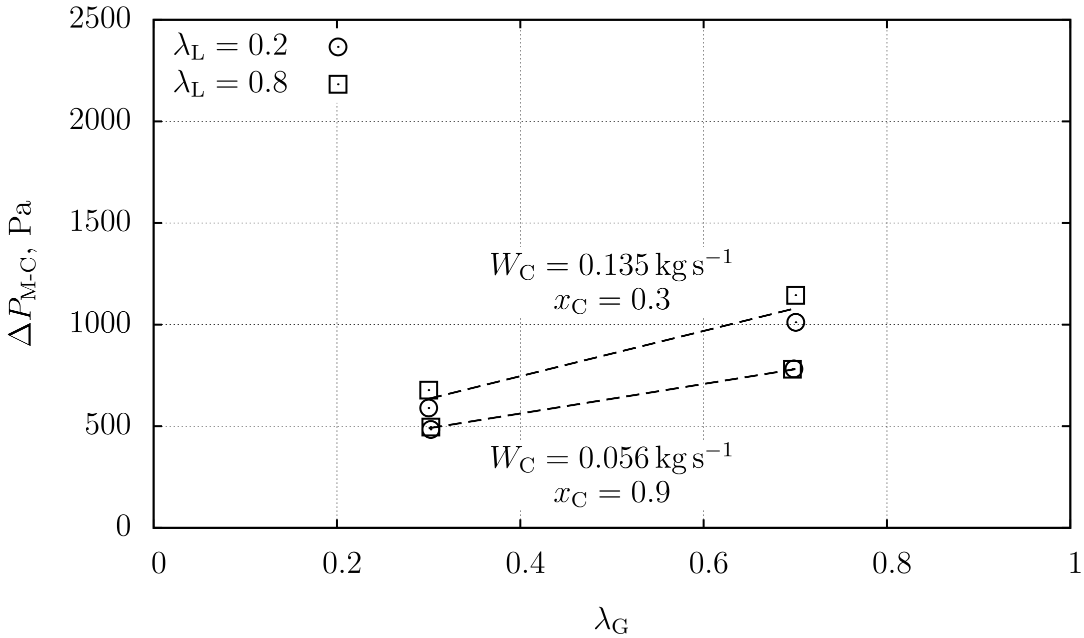

(a) Main to combined

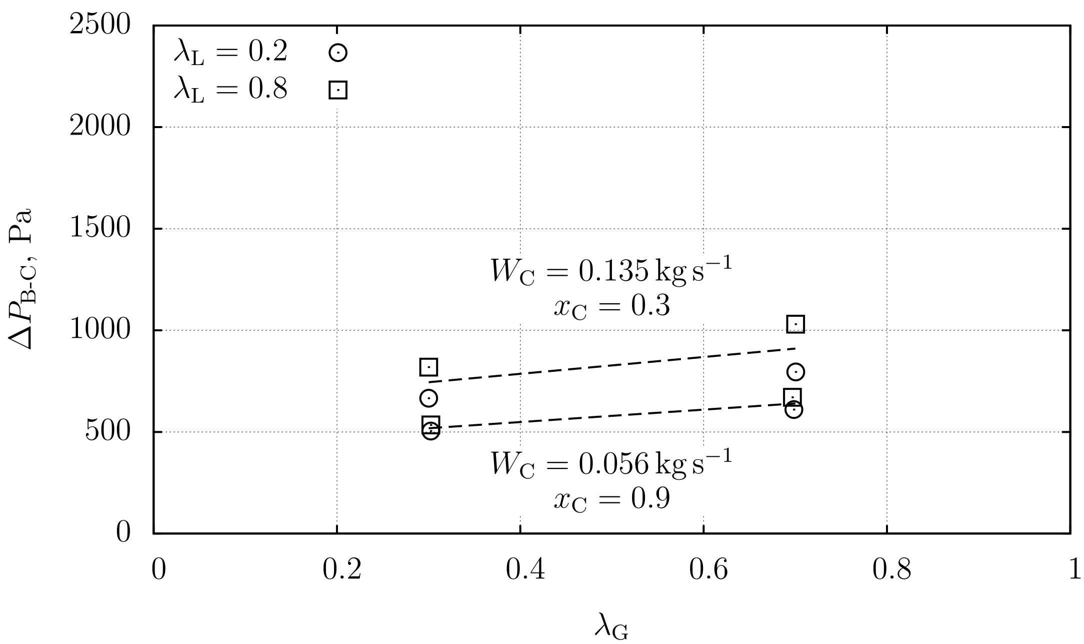

(b) Branch to combined

Figure 6.7 Variation of $\Delta P_{i\text{-C}}$ with λ_G for $W_C = 0.056\,\mathrm{kg\,s^{-1}}$ and $0.135\,\mathrm{kg\,s^{-1}}$.

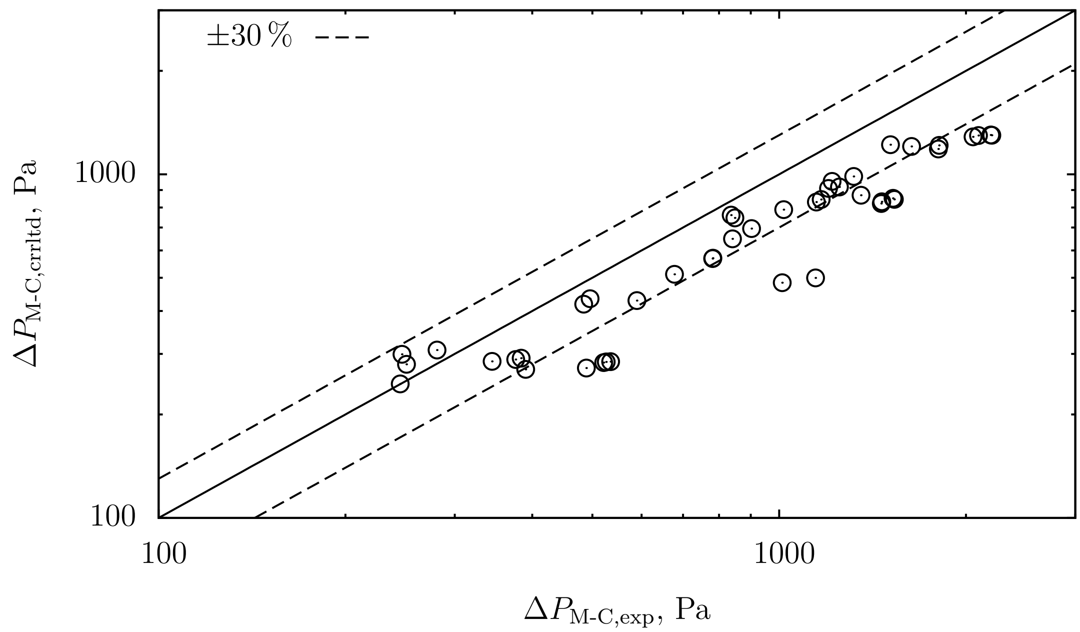

(a) $\Delta P_{\text{M-C}}$ compared with the ESFM's predictions

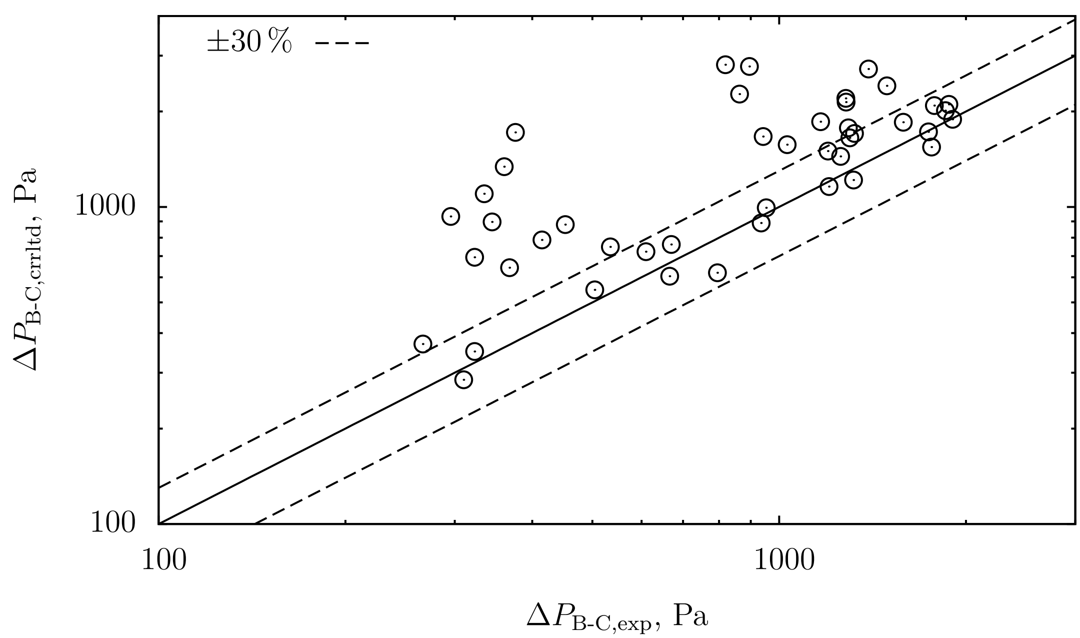

(b) $\Delta P_{\text{B-C}}$ compared with the HFM's predictions

Figure 6.8 Comparison of $\Delta P_{i\text{-C}}$ with published models: poorest prediction.

Table 6.5 Previous models' RMSDs and AMDs for data with annular flow in the combined.

Model	$\Delta P_{\text{M-C}}$		$\Delta P_{\text{B-C}}$	
	RMSD %	AMD %	RMSD %	AMD %
ESFM	31.5	−27.9	24.4	3.3
HFM	–	–	115.2	70.8
MSFM	22.8	−22.1	–	–
LCM	20.8	−10.9	23.5	4.1
CCM	20.9	−8.9	24.4	5.4
MCM	21.1	−10.2	–	–

only the tests with $x_{\text{C}} = 0.3$, the RMSD for predicting $\Delta P_{\text{M-C}}$ was 27.3 %, and for predicting $\Delta P_{\text{B-C}}$ was 37.6 %. Figure 6.9a shows the LCM consistently underpredicted $\Delta P_{\text{M-C}}$ for higher values of x_{C} corresponding to $\Delta P_{\text{M-C,exp}} > 700\,\text{Pa}$; however, given the difficulty in correlating two-phase flows, the LCM's prediction is considered adequate for this data set.

Despite the LCM's reasonable predictions of the present experimental data, [32] compared the LCM model against unpublished pressure-drop data for air-water as well as two-phase mixtures of Exxsol D80 oil with either air or SF_6 gas at system pressures ranging from (1–4) bar and pipe diameters of 38 mm and 67 mm, and reported RMSDs ranging from 72 % to 2 042 %. Further, all of the previously published models formulated their two-phase irreversible mechanical energy losses using single-phase loss coefficients. This implementation of the irreversible losses ignores all of the different regimes and phenomena associated with two-phase flow, and is not justified. As such, in the following section a new approach to modelling the pressure losses across a combining tee junction is proposed and an implementation correlated for the current data set.

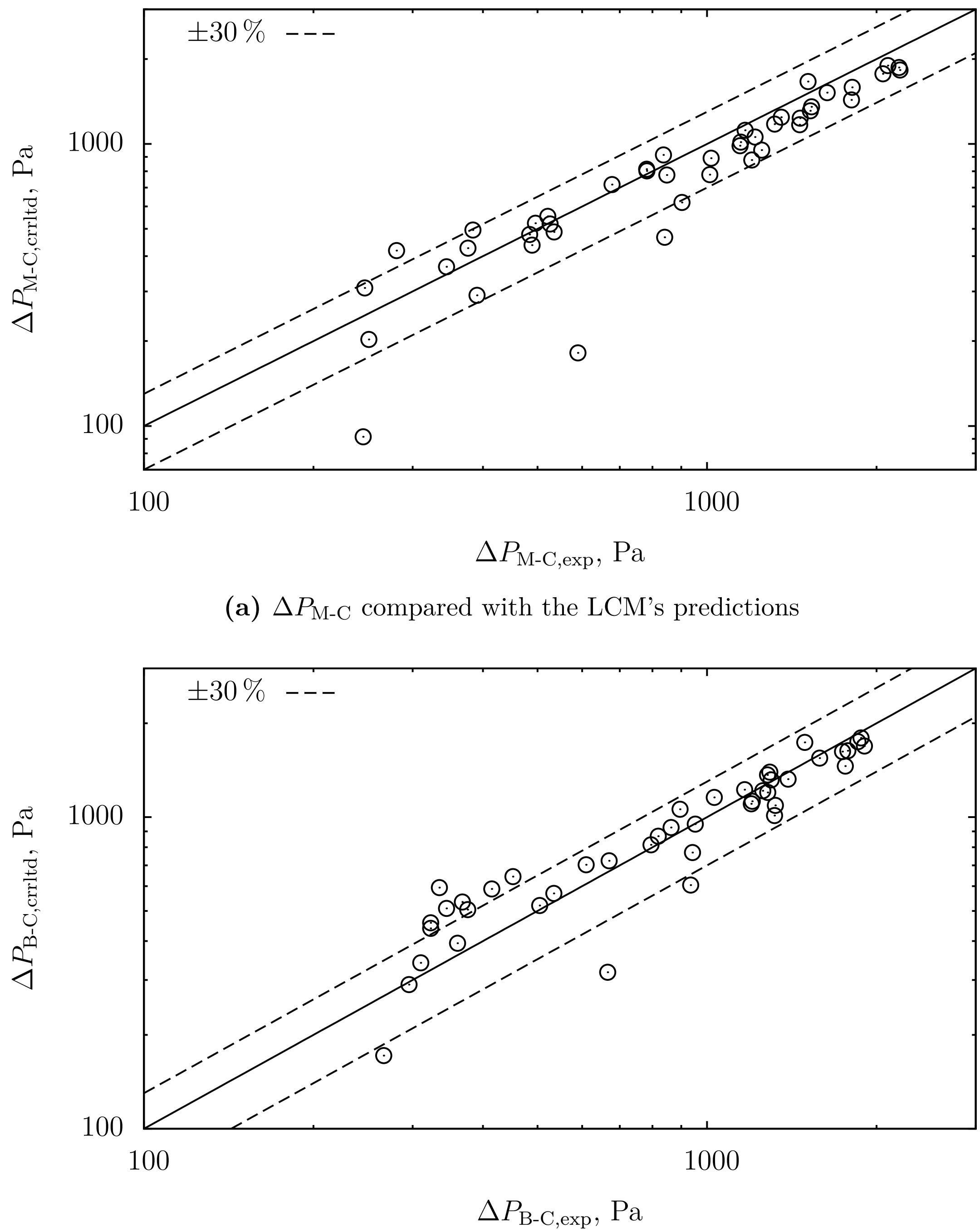

(a) $\Delta P_{\text{M-C}}$ compared with the LCM's predictions

(b) $\Delta P_{\text{B-C}}$ compared with the LCM's predictions

Figure 6.9 Comparison of $\Delta P_{i\text{-C}}$ with published models: best prediction.

New correlation

All of the previous two-phase $\Delta P_{i\text{-C}}$ models rely on single-phase loss coefficients correlated solely on the single-phase parameter λ (see Section 2.3, page 17). It is more reasonable to expect that the two-phase $\Delta P_{i\text{-C}}$ are functions of the two-phase parameters λ_{L}, λ_{G}, and x_{C}, and that a physically consistent model using these parameters will agree with single-phase values if taken to that limit. This is the basic idea for the correlating approach here.

The basic model for correlation is similar to the ESFM using a separated energy balance, but with the irreversible pressure losses accounted for with a loss-coefficient term based on a separated outlet velocity:

$$\begin{aligned} & W_{\mathrm{G},i}\left(\frac{P_i}{\rho_{\mathrm{G}}}+\frac{V_{\mathrm{G},i}^2}{2}\right)+W_{\mathrm{L},i}\left(\frac{P_i}{\rho_{\mathrm{L}}}+\frac{V_{\mathrm{L},i}^2}{2}\right)= \\ & W_{\mathrm{G},i}\left(\frac{P_{\mathrm{C}}}{\rho_{\mathrm{G}}}+\frac{V_{\mathrm{G,C}}^2}{2}\right)+W_{\mathrm{L},i}\left(\frac{P_{\mathrm{C}}}{\rho_{\mathrm{L}}}+\frac{V_{\mathrm{L,C}}^2}{2}\right)+ \\ & \left(W_{\mathrm{G,i}}\frac{V_{\mathrm{G,C}}^2}{2}+W_{\mathrm{L,i}}\frac{V_{\mathrm{L,C}}^2}{2}\right)k_{\mathrm{MESFM},i\text{-c}}, \quad i=\mathrm{B,\ M.} \end{aligned} \tag{6.2}$$

where $k_{\mathrm{MESFM},i\text{-c}}$ is the two-phase modified energy separated flow model (MESFM) loss coefficient. It seems somewhat counter-intuitive to base a new model on one of the poorest, as highlighted in Table 6.5, but the failing of the model was not in the basic model but rather in its use of single-phase data to try and predict two-phase results. The simple energy balance is physically grounded and a strong starting point for a model that can predict both $\Delta P_{\mathrm{B\text{-}C}}$ and $\Delta P_{\mathrm{M\text{-}C}}$. Equation (6.2) can be reduced to:

$$\frac{2\Delta P_{i\text{-C}}}{\rho_{\mathrm{h},i}} = x_i(V_{\mathrm{G,C}}^2 - V_{\mathrm{G},i}^2) + \\ (1-x_i)(V_{\mathrm{L,C}}^2 - V_{\mathrm{L},i}^2) + \\ \Big[x_i V_{\mathrm{G,C}}^2 + (1-x_i)V_{\mathrm{L,C}}^2\Big] k_{\mathrm{MESFM},i\text{-c}}, \quad i = \mathrm{B,\ M.} \tag{6.3}$$

The average phase velocities were calculated according to Eq. (2.3) using the void fraction correlation from [87] for semi-annular and annular flow conditions and the model from [33] for wavy and stratified flow conditions. The separated-flow approach is justified for the stratified, wavy, and annular regimes observed as the gas and the liquid flow in separate areas of the pipe cross-section.

Of particular importance is the behaviour of $k_{\mathrm{MESFM},i\text{-c}}$ at the limits of $\lambda_\mathrm{G} = 0$ and $\lambda_\mathrm{G} = 1$. Because of the large difference in the gas and liquid velocities for the annular experiments, $V_{\mathrm{G,C}}^2 >> V_{\mathrm{L,C}}^2$, and the coefficient of $k_{\mathrm{MESFM},i\text{-c}}$ in the last term of Eq. (6.3) is dominated by $V_{\mathrm{G,C}}^2$ until the inlet's gas flow is reduced to nearly zero. In order to demonstrate this behaviour, the values of $k_{\mathrm{MESFM,M\text{-}C}}$ over the whole range of $0 \leq \lambda_\mathrm{G} \leq 1$ were calculated from Eq. (6.3) using parabolic regressions for $\Delta P_{\mathrm{M\text{-}C}}$ fit to the data in Fig. 6.6a for each value of x_C and λ_L. Figure 6.10 shows a sample of the results where the dashed line between $0.7 < \lambda_\mathrm{G} < 1.0$ corresponds to the values calculated from the parabolic regression for $\Delta P_{\mathrm{M\text{-}C}}$. The value of $k_{\mathrm{MESFM,M\text{-}C}}$ only gradually changes over most of the range of λ_G because the value of $V_{\mathrm{G,C}}^2$ is large, but the value of $k_{\mathrm{MESFM,M\text{-}C}}$ very near to $\lambda_\mathrm{G} = 1$ rapidly increases as the value of $V_{\mathrm{L,C}}^2$ becomes significant. For this reason, $k_{\mathrm{MESFM,M\text{-}C}}$ was not correlated at $\lambda_\mathrm{G} = 1$ and instead, in the interest of correlating over as wide a range as possible, values at $\lambda_\mathrm{G} = 0.99$ calculated from parabolic regressions of $\Delta P_{\mathrm{M\text{-}C,exp}}$ were used. Similar results were obtained for the value of $k_{\mathrm{MESFM,B\text{-}C}}$ at the limit of $\lambda_\mathrm{G} = 0$, and so values at $\lambda_G = 0.01$ calculated from parabolic regressions of $\Delta P_{\text{B-C,exp}}$ were used.

For correlation, the experimental and interpolated values of $k_{\text{MESFM},i\text{-c}}$ for $W_C = (0.101\text{–}0.114)\,\text{kg}\,\text{s}^{-1}$ were plotted against each of the independent parameters: λ_G, λ_L, and x_C. Samples of these plots for $k_{\text{MESFM,M-C}}$ are given in Figs. 6.11 and 6.12. Two observations can be made from these graphs:

1. $k_{\text{MESFM,M-C}}$ has less dependence on λ_L than x_C or λ_G, as shown by the flat profiles in Fig. 6.11 and relatively small separation of data with λ_L in Fig. 6.12a.

2. The data were reasonably linear with x_C across the entire range of λ_L and λ_G, as shown in Fig. 6.12.

These same behaviours were confirmed for the branch coefficient from similar results for $k_{\text{MESFM,B-C}}$.

Based on these observations, the following simple correlation was proposed to fit the data:

$$k_{\text{MESFM},i\text{-c}} = a_i + b_i x_C, \quad i = \text{B, M}, \tag{6.4}$$

where a_i and b_i are correlation coefficients and functions of λ_G alone. Finally, by plotting the experimental and interpolated data for $k_{\text{MESFM},i\text{-c}}$ versus x_C for $W_C = (0.101\text{–}0.114)\,\text{kg}\,\text{s}^{-1}$, values of a_i and b_i were determined for the various λ_G and fit with parabolic regressions:

$$a_M = 0.252 + 0.853\lambda_G + 1.320\lambda_G^2, \tag{6.5a}$$

$$b_M = -0.246 + 0.781\lambda_G - 2.593\lambda_G^2, \tag{6.5b}$$

$$a_B = 0.165 + 0.610\lambda_G + 1.324\lambda_G^2, \tag{6.5c}$$

$$b_B = -1.322 + 3.866\lambda_G - 3.522\lambda_G^2. \tag{6.5d}$$

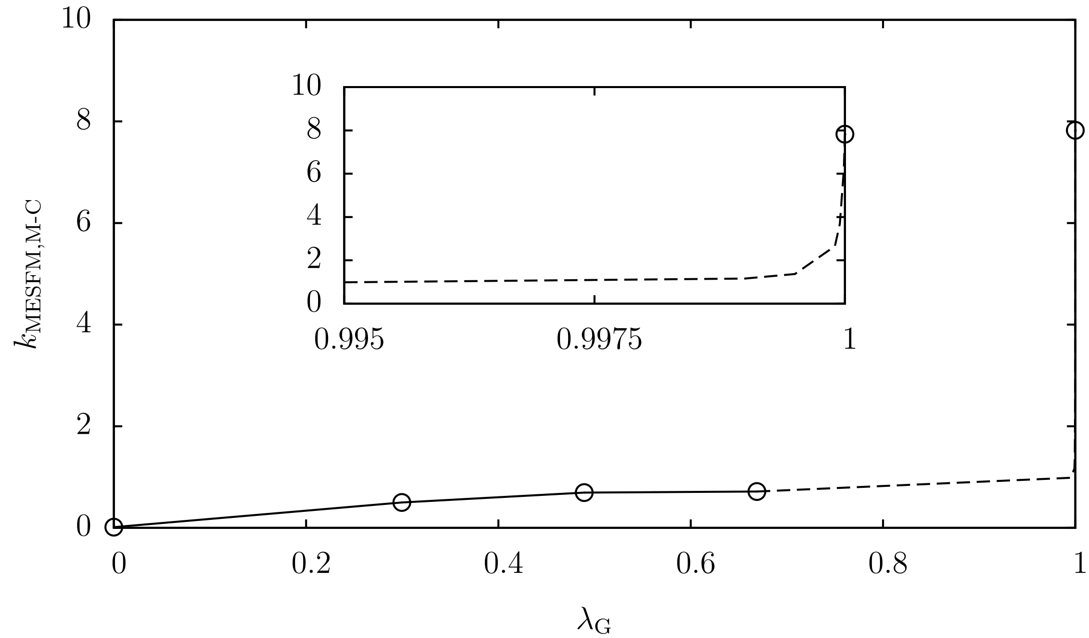

Figure 6.10 $k_{\text{MESFM,M-C}}$ versus λ_G for $W_C = (0.101–0.114)\,\text{kg}\,\text{s}^{-1}$, $\lambda_L = 0.8$, and $x_C = 0.7$. The dashed line was calculated from a parabolic regression of $\Delta P_{\text{M-C,exp}}$.

By using Eqs. (6.3) to (6.5) the pressure losses can be predicted as functions of λ_G and x_C.

Figure 6.13 shows the MESFM's predictive abilities for all of the experiments except those with $\lambda_G = 0$ and $\lambda_G = 1$, and Table 6.6 lists the AMDs and RMSDs for various ranges of the data. The small AMDs over the entire range of data shows the model tends to predict the centre of the data and the overall trend well. The RMSDs show little scatter except when the extrapolated data for $\lambda_G = 0.01$ and 0.99 is included. Notably, the RMSD slightly increases when $W_C = 0.135\,\text{kg}\,\text{s}^{-1}$ is included. As previously noted, semi-annular flow was observed in the combined for this data and the outlet condition falls close to the wavy-annular transition on Fig. 6.1. As the correlation was based on annular data, some difference is expected. Overall,

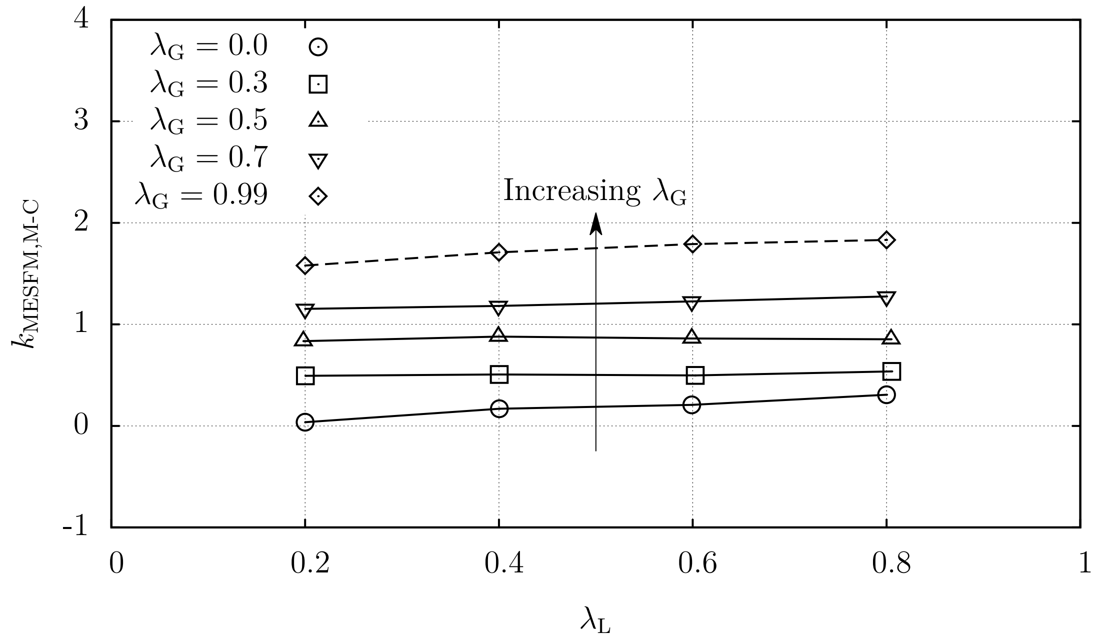

Figure 6.11 $k_{\text{MESFM,M-C}}$ versus λ_L for $W_C = (0.101\text{–}0.114)\,\text{kg}\,\text{s}^{-1}$ and $x_C = 0.3$

these results show excellent agreement between the MESFM's predictions and the experimental results.

In addition, the MESFM also compares very well with single-phase results if evaluated at the limit of pure gas flow, where $x_i = x_C = 1.0$ and $\lambda_G = \lambda$. Substituting

Table 6.6 The MESFM's RMSD and AMD for data with annular flow in the combined.

Interval	Mass Flow Range	$\Delta P_{\text{M-C}}$		$\Delta P_{\text{B-C}}$	
	$\text{kg}\,\text{s}^{-1}$	RMSD %	AMD %	RMSD %	AMD %
$0.3 \le \lambda_G \le 0.7$	0.101–0.114	6.8	1.4	10.0	2.0
	0.056–0.114	7.3	2.4	11.6	3.6
	0.056–0.135	9.4	−0.4	13.4	1.2
$0.01 \le \lambda_G \le 0.99$	0.056–0.135	16.3	2.3	28.1	−4.2

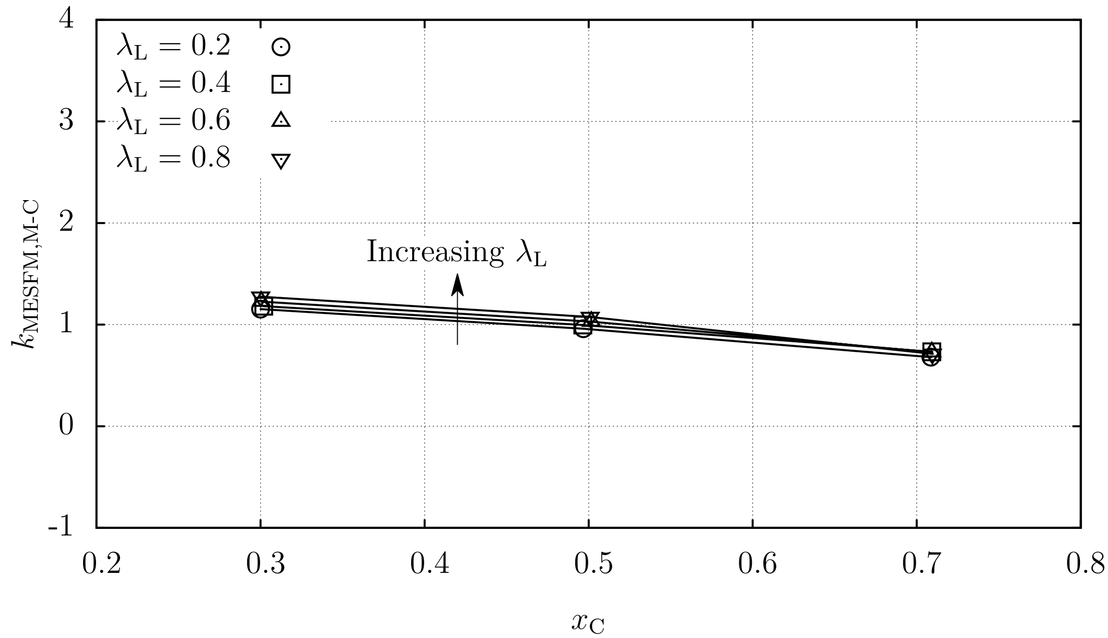

(a) $\lambda_G = 0.7$

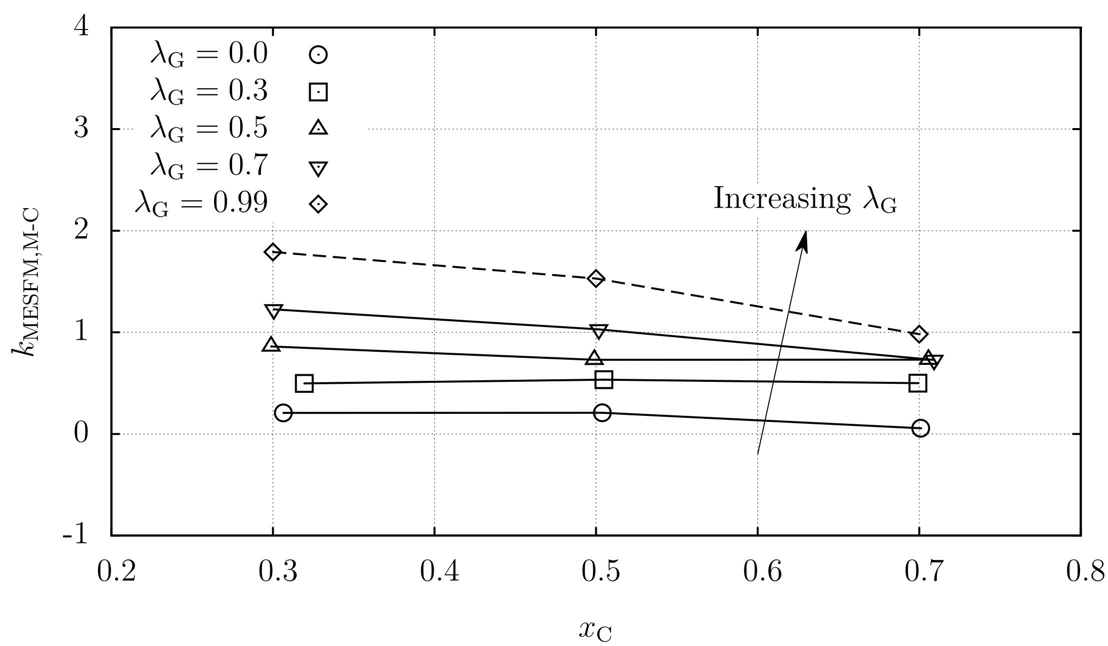

(b) $\lambda_L = 0.6$

Figure 6.12 Variation of $k_{MESFM,M-C}$ with x_C for $W_C = (0.101–0.114)\,\mathrm{kg\,s^{-1}}$.

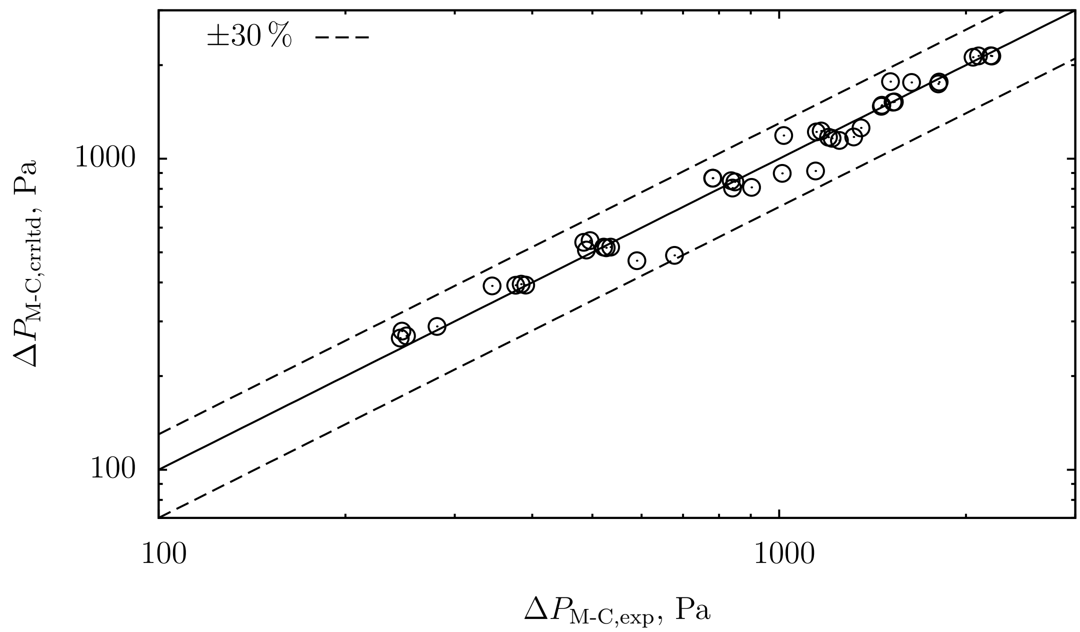

(a) Main to combined

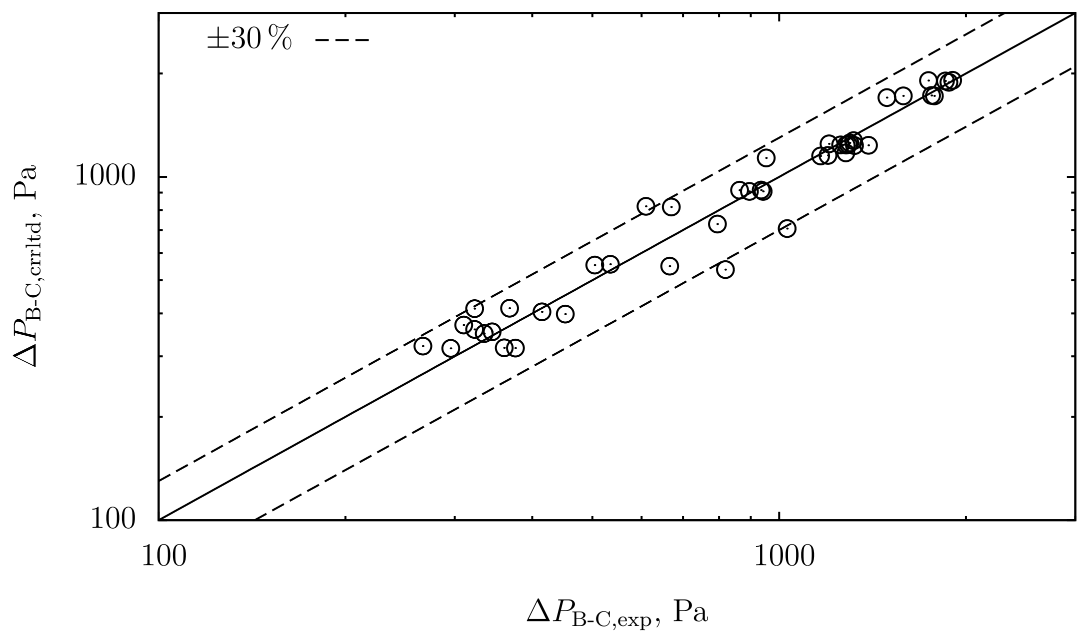

(b) Branch to combined

Figure 6.13 Experimental $\Delta P_{i\text{-C}}$ compared with the MESFM for experiments with annular flow in the combined side.

these values into Eqs. (6.4) to (6.5) yields:

$$\lim_{x_\mathrm{C}\to 1} k_{\mathrm{MESFM,M\text{-}C}} = \quad 0.006 + 1.634\lambda - 1.273\lambda^2, \tag{6.6a}$$

$$\lim_{x_\mathrm{C}\to 1} k_{\mathrm{MESFM,B\text{-}C}} = -1.157 + 4.476\lambda - 2.198\lambda^2. \tag{6.6b}$$

Figure 6.14 shows Eq. (6.6) and the single-phase Eq. (5.2). The agreement between the values is excellent and demonstrates the MESFM's capturing of the flow physics.

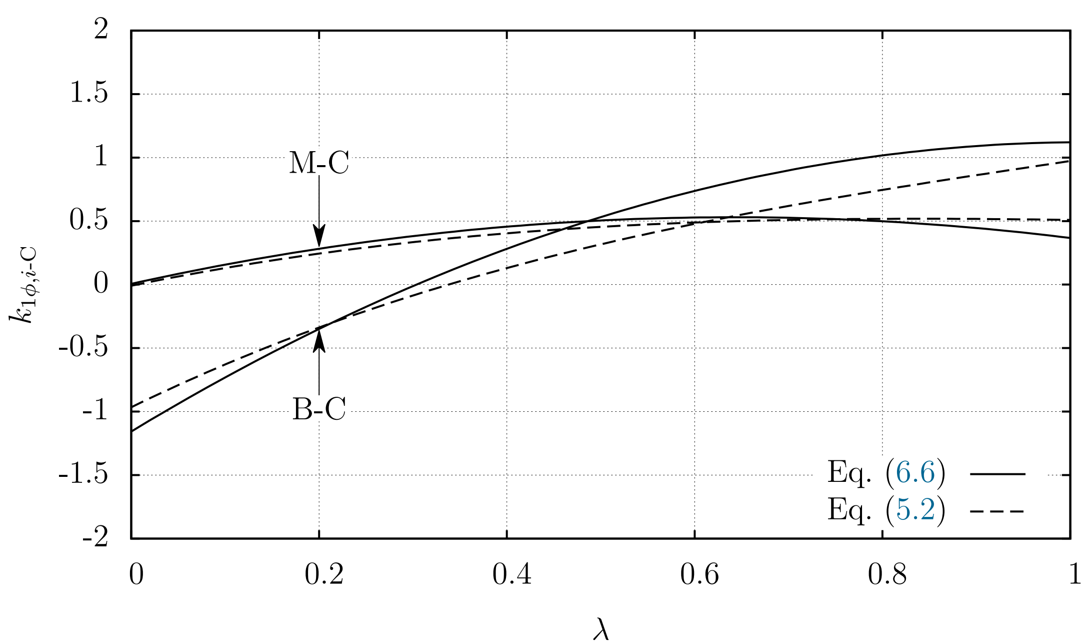

Figure 6.14 $k_{1\phi,i\text{-C}}$ correlated from experiments compared with the MESFM in the limit of single-phase gas flow.

Chapter 7

Wavy Flow Results

7.1 Overview

Holding to the objectives of Section 1.4, an experimental campaign was completed with wavy flow conditions in the combined side. The test matrix was designed to study the individual effects of the four independent parameters (W_{C}, x_{C}, λ_{G}, λ_{L}) by successively holding three parameters constant while varying the fourth. Table 7.1 summarizes the test conditions and Fig. 7.1 shows the combined flow conditions on Mandhane et al.'s [34] flow-regime map, along with those from Chapter 6 for reference. For each of the five (x_{C}, W_{C}) combinations, both λ_{G} and λ_{L} were varied independently between values of 0.2, 0.4, 0.6, and 0.8, totalling 80 unique experiments. The outlet flow regime was visually observed to be wavy except for at the highest mass flow rate or at the highest outlet quality, where the outlet condition was semi-annular with the annulus covering approximately half of the pipe circumference. These points are close to the wavy-annular transition boundary on Fig. 7.1. The flow regimes in the main and branch side included stratified and wavy flows.

The results of the experimental campaign are dealt with next in the same order

Table 7.1 Experiment conditions with wavy flow in the combined side.

W_{C} kg s^{-1}	x_{C}	λ_{G}	λ_{L}
0.045	0.5, 0.7, 0.9	0.2, 0.4, 0.6, 0.8	0.2, 0.4, 0.6, 0.8
0.056	0.5	0.2, 0.4, 0.6, 0.8	0.2, 0.4, 0.6, 0.8
0.067	0.5	0.2, 0.4, 0.6, 0.8	0.2, 0.4, 0.6, 0.8

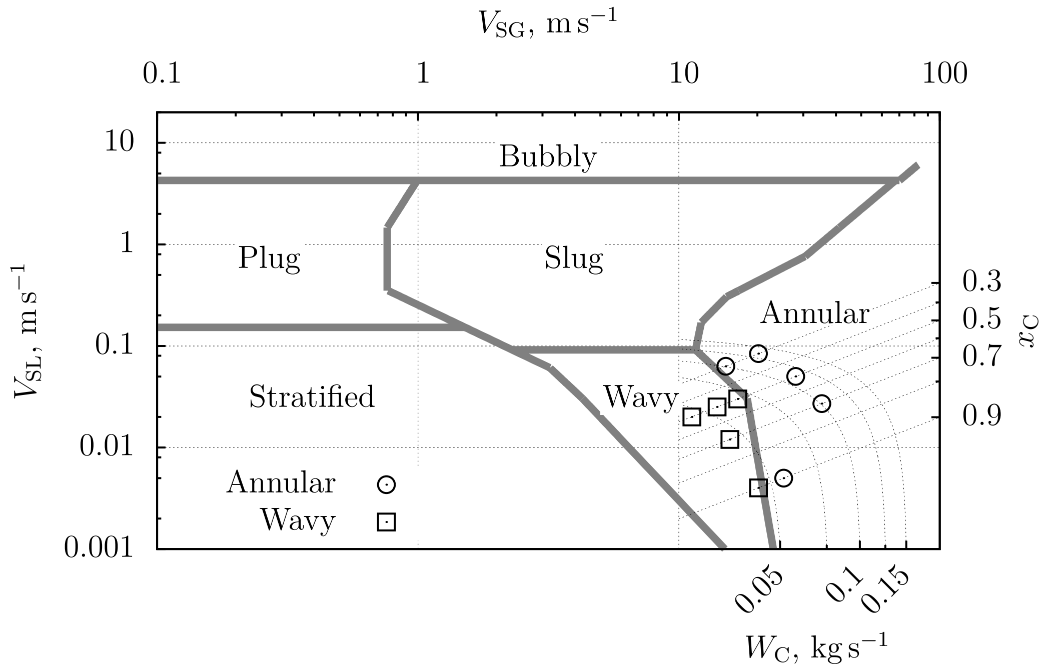

Figure 7.1 Wavy flow conditions in the combined side on the flow-regime map of Mandhane et al. [34].

as for annular flow in Chapter 6: the results of the repeatability analysis are discussed, the fully-developed dP/dz is compared with correlations, and, finally, results for $\Delta P_{i\text{-C}}$ are presented, discussed, and compared to previous models.

7.2 Sampling rate and repeatability tests

In the same manner as Chapter 6, before pressure-loss data were recorded an experiment was conducted to determine an appropriate sampling time for repeatable time-averaged pressure distributions. For a flow with $W_C = 0.051\,\mathrm{kg\,s^{-1}}$, $x_C = 0.50$, $\lambda_G = 0.50$, and $\lambda_L = 0.50$, the differential pressure between taps M1 and C1 was monitored with transducer 2 and the time-varying signal recorded continuously over a period of 30 min at a sampling frequency of 1 000 Hz. The average pressure difference between the two taps was then calculated over various amounts of time (e.g., 0–1 min, 0–2 min, ... etc.) with the results summarized in Table 7.2. Variation of the sampling rate from (100–4 000) Hz did not affect the results, and so a conservative sampling time of 120 s with a sampling frequency of 1 000 Hz was selected for all experiments with wavy flow in the combined side. Figure 7.2 and Table 7.3 show the results of repeating an experiment in order to confirm that the sampling frequency and time are adequate for experiments with wavy flow in the combined side. There appears to be some difference in the pressure results in the branch between Figs. 7.2a and 7.2b. The departure from fully-developed flow occurs because of a hydraulic jump near the junction (discussed later). The difference in pressure measurements in the branch may be attributed to slight differences in λ_G and λ_L; however, Table 7.3 shows that $\Delta P_{\text{B-C}}$ is within 3 % and dP/dz_B is within 10 %. Other experiments were also repeated with results given in Appendix F.

Table 7.2 Repeatability tests for $\Delta P_{\text{M1-C1}}$ in an experiment with wavy flow in the outlet ($W_C = 0.051\,\text{kg}\,\text{s}^{-1}$, $x_C = 0.50$, $\lambda_G = 0.50$, $\lambda_L = 0.50$).

Sampling time s	Time-averaged ΔP Pa
1 800	530.6
300	530.6
240	529.9
180	530.4
120	529.6
60	529.1

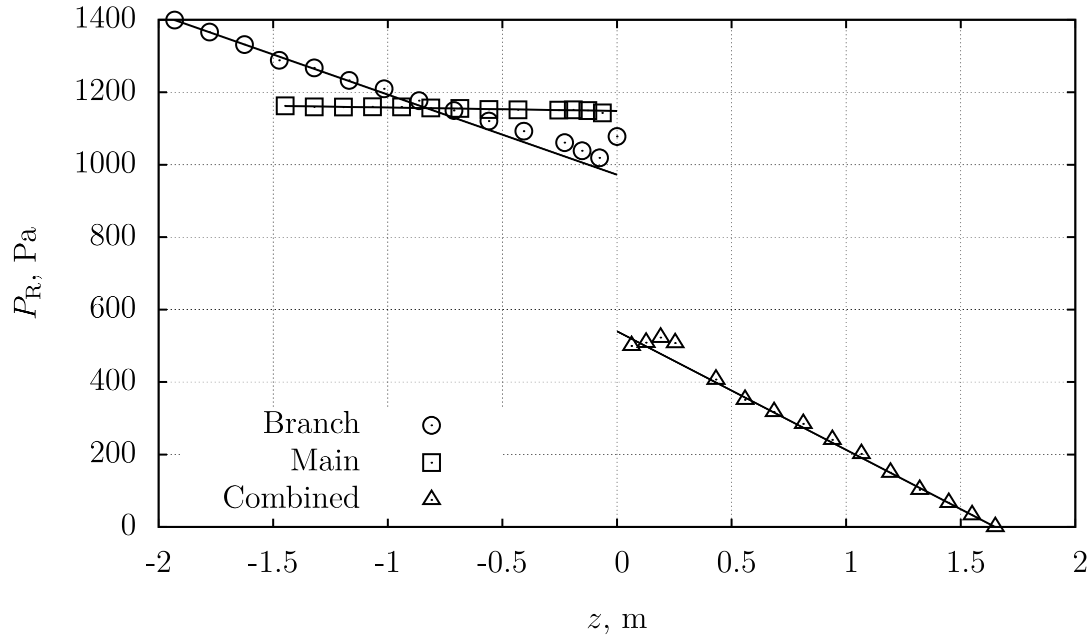

(a) $W_C = 0.067\,\mathrm{kg\,s^{-1}}$, $x_C = 0.50$, $\lambda_G = 0.79$, $\lambda_L = 0.60$

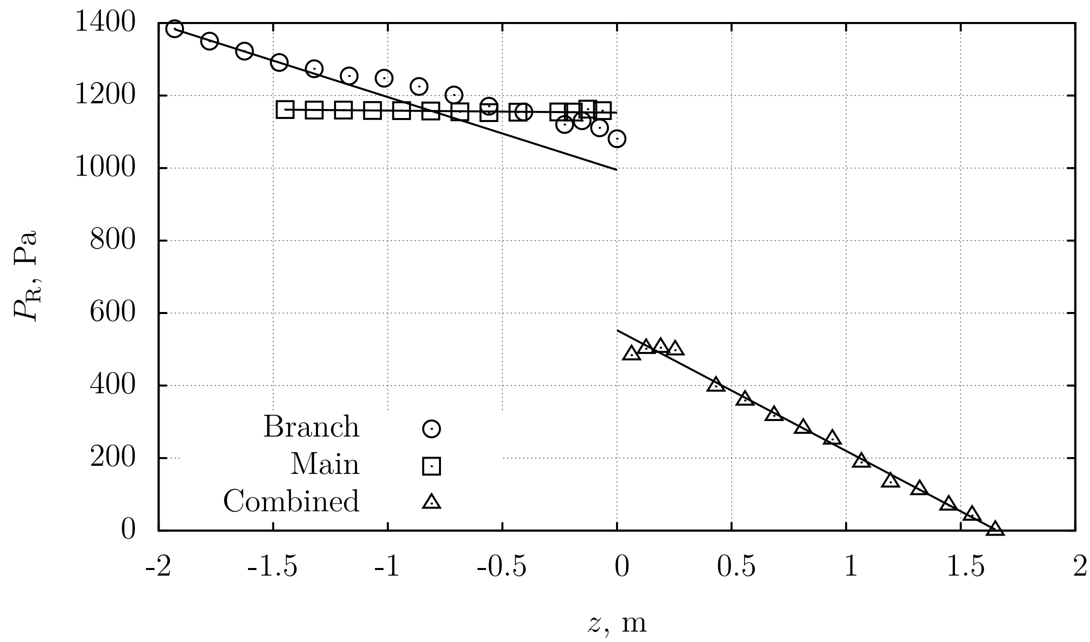

(b) $W_C = 0.068\,\mathrm{kg\,s^{-1}}$, $x_C = 0.49$, $\lambda_G = 0.80$, $\lambda_L = 0.59$

Figure 7.2 Pressure distributions for a repeated experiment with wavy flow in the outlet.

Table 7.3 Result summary for a repeated experiment with wavy flow in the outlet.

W_C	x_C	λ_G	λ_L	$\Delta P_{\text{M-C}}$	$\Delta P_{\text{B-C}}$	dP/dz_M	dP/dz_B	dP/dz_C
$\mathrm{kg\,s^{-1}}$				Pa		$\mathrm{Pa\,m^{-1}}$		
0.067	0.50	0.79	0.60	607.9	432.2	9.8	221.2	327.3
0.068	0.49	0.80	0.59	600.3	442.0	5.7	201.0	333.1

7.3 Pressure gradients

As a first check to ensure the pressure measurements correspond to fully-developed values, a single experiment with an even flow distribution between the inlets was performed. Figure 7.3 shows the pressure distribution and Table 7.4 summarizes the values of dP/dz. Clearly the measurements for each inlet fit very well on the drawn lines, and $dP/dz_B \approx dP/dz_M$ within the measurement uncertainty.

Figure 7.4 shows the pressure distribution for a pipe flow experiment without any flow in the branch, and Table 6.4 lists the dP/dz values. The flow is nearly undisturbed by the presence of the junction and $dP/dz_M \approx dP/dz_C$. Further, the dP/dz values agree very well between the combining and pipe flow experiments and show that the gradients are from fully-developed data in the combining case.

Table 7.4 dP/dz results for a combining flow experiment with even flow distribution and wavy flow in the combined side, and a pipe flow experiment with the same inlet flow rate.

W_C	x_C	λ_G	λ_L	dP/dz_M	dP/dz_B	dP/dz_C
$\mathrm{kg\,s^{-1}}$				$\mathrm{Pa\,m^{-1}}$		
0.051	0.50	0.50	0.50	33.0	32.3	148.1
0.026	0.50	0.00	0.00	29.2	–	26.9

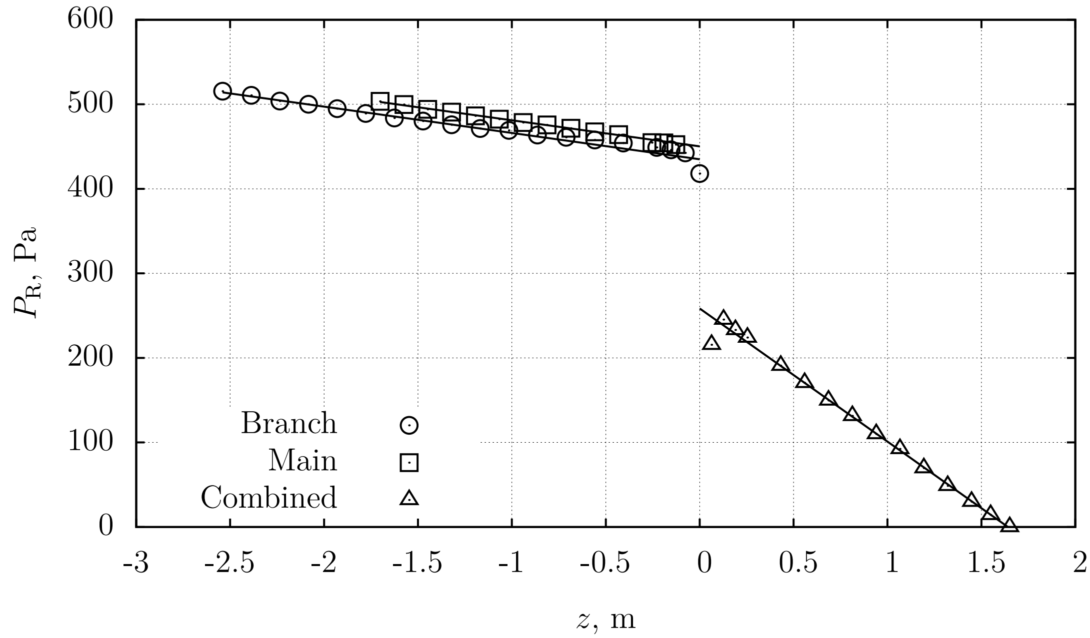

Figure 7.3 Pressure distribution for a combining flow experiment with an even flow distribution and wavy flow in the combined side ($W_C = 0.051\,\mathrm{kg\,s^{-1}}$, $x_C = 0.50$, $\lambda_G = 0.50$, $\lambda_L = 0.50$).

Just as in Chapter 6 for annular flow, the accuracy of dP/dz was validated by comparison with correlations in [33, 45, 51, 53–56]. Separate comparisons for the stratified and wavy flow regimes were made as different correlations perform better for different flow patterns [50, 57, 59]. Generally, stratified and stratified-wavy flows had values of $dP/dz < 100\,\mathrm{Pa\,m^{-1}}$ while wavy and semi-annular flows had values of $dP/dz > 100\,\mathrm{Pa\,m^{-1}}$. Figure 7.5 shows the best comparisons for the different regions using the phenomenological model of Taitel and Dukler [33] for stratified flows, and the correlation of Sun and Mishima [56] for wavy flows. The same correlations also had the best prediction for the data in the annular experiment campaign. The RMSD(dP/dz) for the wavy data and the correlation of [56] was 12.7 %. The RMSD(dP/dz) for stratified data above $10\,\mathrm{Pa\,m^{-1}}$ was 23.9 %. As mentioned

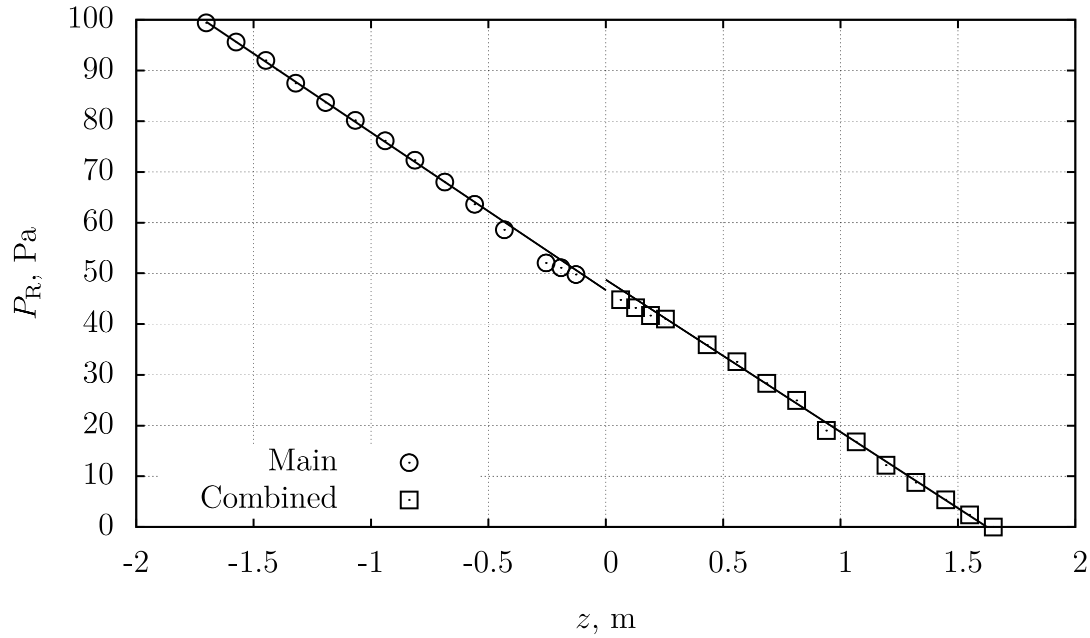

Figure 7.4 Pressure distribution for a pipe flow experiment with no flow entering through the branch ($W_C = 0.026\,\mathrm{kg\,s^{-1}}$, $x_C = 0.50$, $\lambda_G = 0.00$, $\lambda_L = 0.00$).

previously, the poor prediction of low gradients has been confirmed by others [58, 59]. Overall, the results are in excellent agreement and show the fully-developed slopes were accurately determined.

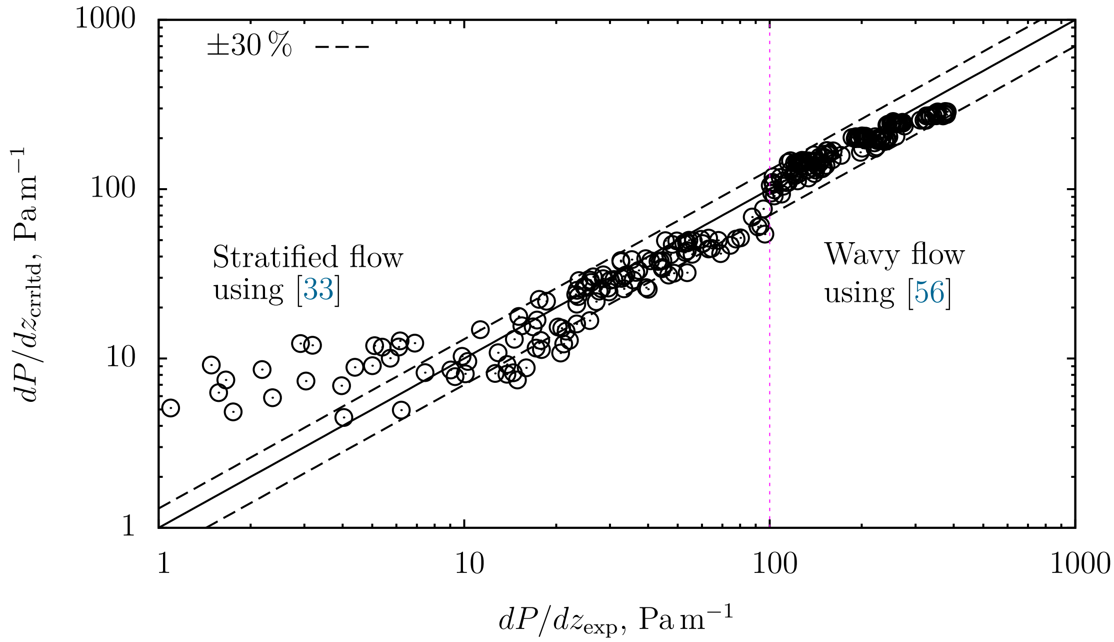

Figure 7.5 dP/dz results for experiments with wavy flow in the combined compared with correlations of [33, 56].

7.4 Pressure drop

Experimental results

Figure 7.6 summarizes the results for $\Delta P_{i\text{-C}}$ with $W_\mathrm{C} = 0.045\,\mathrm{kg\,s^{-1}}$. Dashed lines have been included on the plots to help differentiate the data. The value of $\Delta P_\text{M-C}$ shows a strong dependence on both λ_G and x_C, but is nearly independent of λ_L. The value of $\Delta P_\text{B-C}$ shows similar trends, but is less dependent on λ_G for $x_\mathrm{C} = 0.5$, and λ_L becomes modestly significant for small values of λ_G and $x_\mathrm{C} = 0.5$. While both $\Delta P_\text{M-C}$ and $\Delta P_\text{B-C}$ generally increase with λ_G, the effect on $\Delta P_\text{M-C}$ is more significant due to the branch flow increasingly impinging the main flow at the junction as λ_G grows.

Figure 7.7 summarizes the results for $\Delta P_{i\text{-C}}$ with $x_\mathrm{C} = 0.5$. Dashed lines have been included on the plots to help differentiate the data. Again, $\Delta P_\text{M-C}$ appears nearly

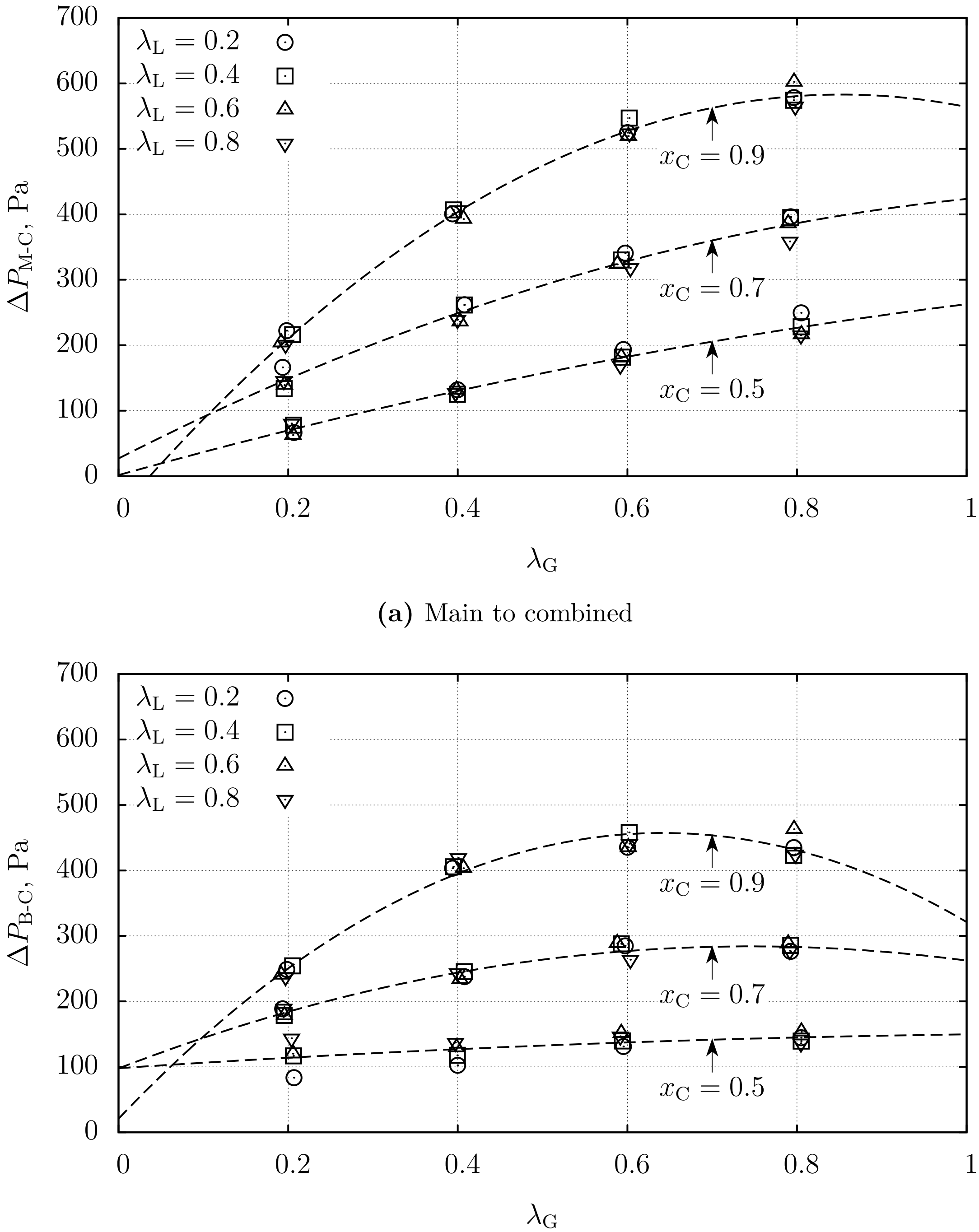

(a) Main to combined

(b) Branch to combined

Figure 7.6 Variation of $\Delta P_{i\text{-C}}$ with λ_{G} and x_{C} for $W_{\text{C}} = 0.045\,\text{kg}\,\text{s}^{-1}$.

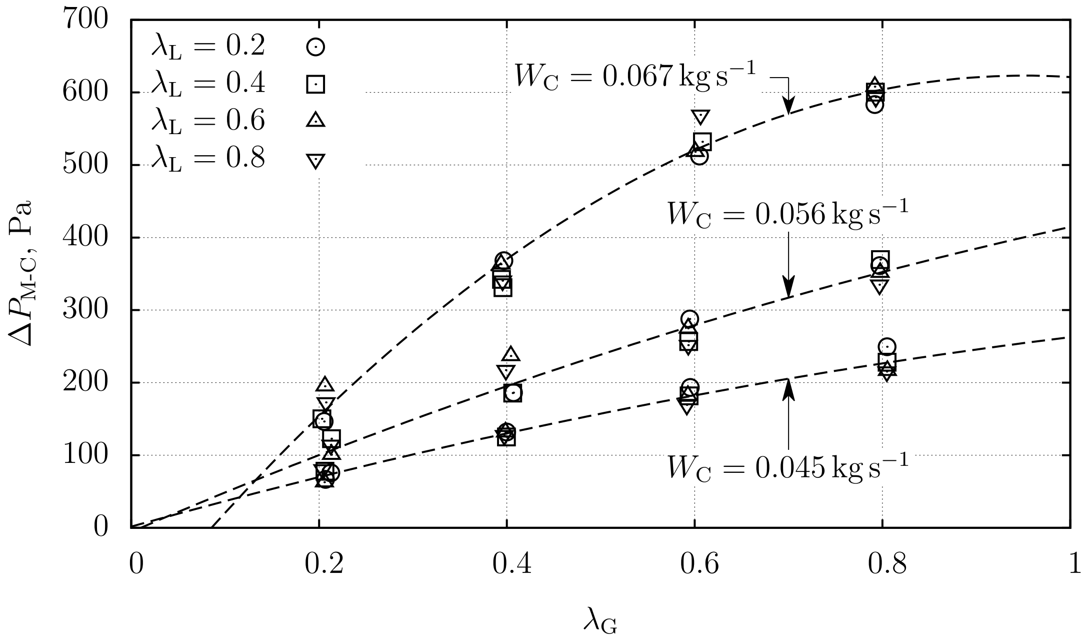

(a) Main to combined

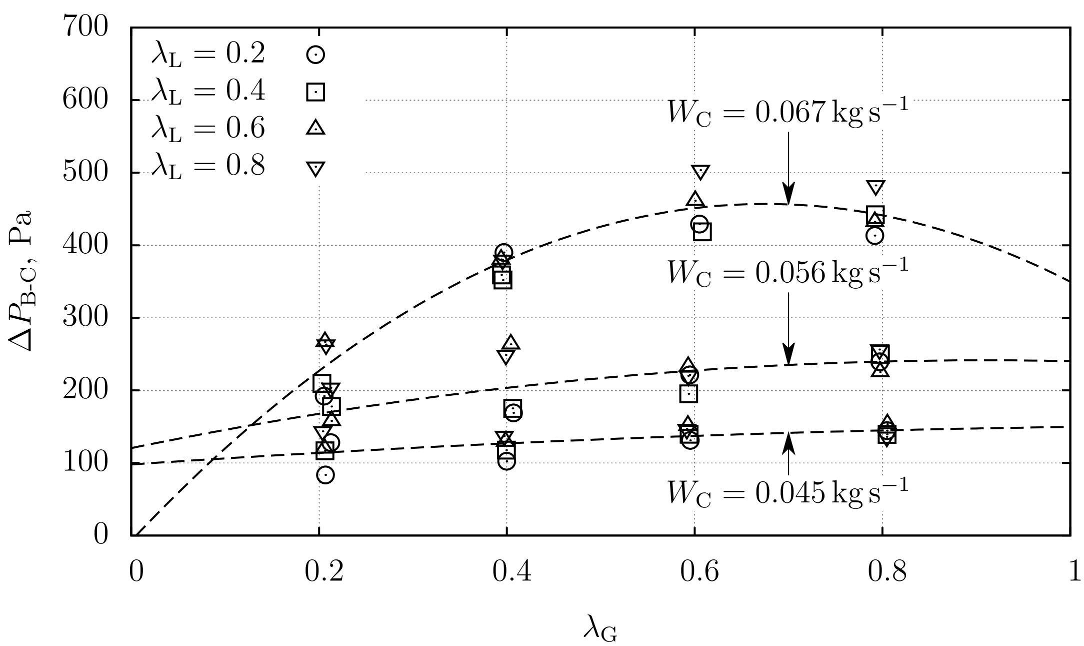

(b) Branch to combined

Figure 7.7 Variation of $\Delta P_{i\text{-C}}$ with λ_G and W_C for $x_C = 0.5$.

independent of λ_{L} with primary dependence on λ_{G} and W_{C}, while $\Delta P_{\text{B-C}}$ shows modest dependence on λ_{L} and increasing dependence on λ_{G} as W_{C} increases. Interestingly, the data has a more parabolic trend with λ_{G} when the gas flow rate is higher, as for the data with annular flow in the combined side. For the data sets with $x_{\mathrm{C}} = 0.9$ and $W_{\mathrm{C}} = 0.067\,\mathrm{kg\,s^{-1}}$, $\Delta P_{\text{B-C}}$ has a maximum value around $\lambda_{\mathrm{G}} = 0.6$ similar to the data with annular flow in the combined side (see Fig. 6.6b, page 61). From all of the data reported up to this point, it seems a parabolic trend occurs if the value of V_{SG} is greater than $16\,\mathrm{m\,s^{-1}}$. Refer to Appendix F for a full set of experimental results.

Evaluation of previously published models

The previously published models for $\Delta P_{i\text{-C}}$ (see Section 2.3, page 18) as well as the MESFM from Chapter 6 were compared to the experimental results to demonstrate their predictive abilities. For implementation of the models, estimates of the void fraction were made using [87] for semi-annular flow conditions and [33] for wavy and stratified flow conditions. Table 7.5 summarizes the RMSD and AMD for each model according to the flow regime in the combined side. For the full set of data the poorest agreement for $\Delta P_{\text{M-C}}$ and $\Delta P_{\text{B-C}}$ were with the ESFM and the HFM, respectively; these are the same models that gave the poorest predictions for the annular flow experiments. Figure 7.8 show these results. Notice that though the ESFM does not follow the trend in the data well, there is not much scatter in its predictions. The HFM, on the other hand, is poor in its predictions with a large amount of scatter and no identifiable trend. These observations are important: it suggests that the ESFM, which has a similar basis to the MESFM, is not necessarily a poor model of the phenomenon, but rather that its closure using single-phase results is inadequate.

On the other hand, the HFM, which attempts to use one homogeneous fluid to model the separated two-phase phenomena, fails outright.

Conversely, the best overall agreement among the previous models, excluding the MESFM which will be discussed later, was with the MSFM for $\Delta P_{\text{M-C}}$ and the LCM for $\Delta P_{\text{B-C}}$, both shown in Fig. 7.9. The MSFM does an adequate job for this data set, with nearly all of the data within $\pm 30\,\%$. The LCM, on the other hand, shows a significant amount of scatter, as it did for experiments with annular flow on the combined side at lower values of $\Delta P_{i\text{-C}}$ (see Figs. 6.9a and 6.9b). Scatter in the data shows inadequacy of the model to properly capture the flow physics.

Figure 7.10 shows the MESFM's predictions for $\Delta P_{\text{M-C}}$ and $\Delta P_{\text{B-C}}$. A general trend of over-prediction with an AMD $\geq 14\,\%$ is obvious, particularly for data with wavy flow in the combined side. Notice that for the data corresponding to semi-annular flow in the combined side the MESFM shows excellent overall agreement. This suggests the losses with wavy flow in the outlet are less severe than when annular flow is present in the combined side. This could be due to higher gas velocities causing more vigorous mixing, but also because the development of an annulus requires energy whereas wavy and stratified flows have similar structures. However, the separated structure in both wavy and annular regimes still justifies the same MESFM modelling approach but with new correlation coefficients to account for the smaller losses. The following analysis develops these new coefficients for the MESFM to include wavy outlet data.

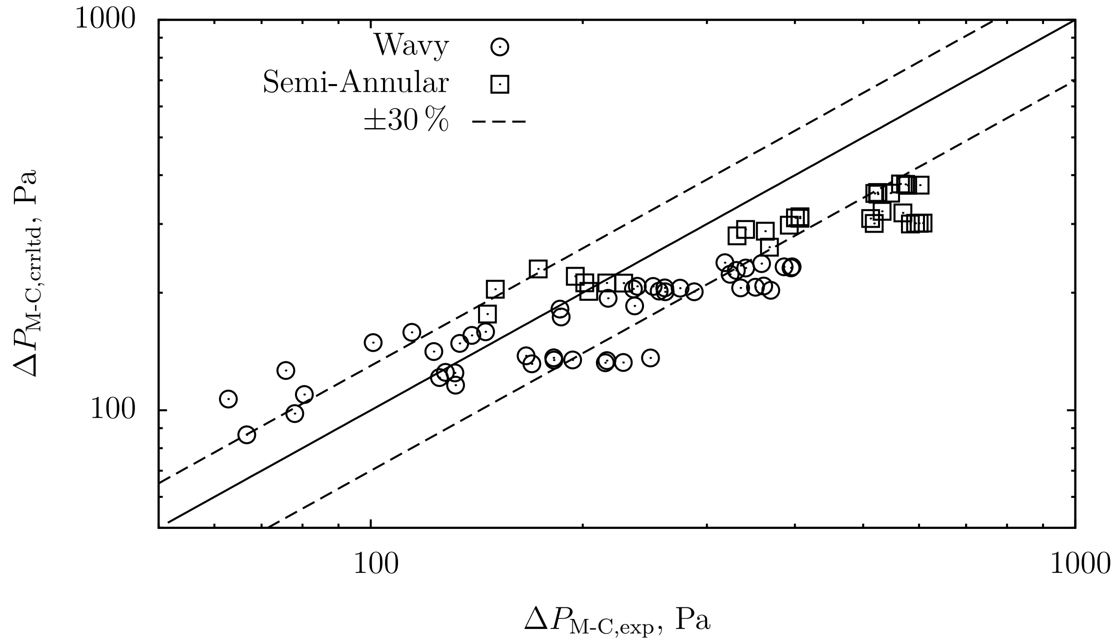

(a) $\Delta P_{\text{M-C}}$ compared with the ESFM's predictions

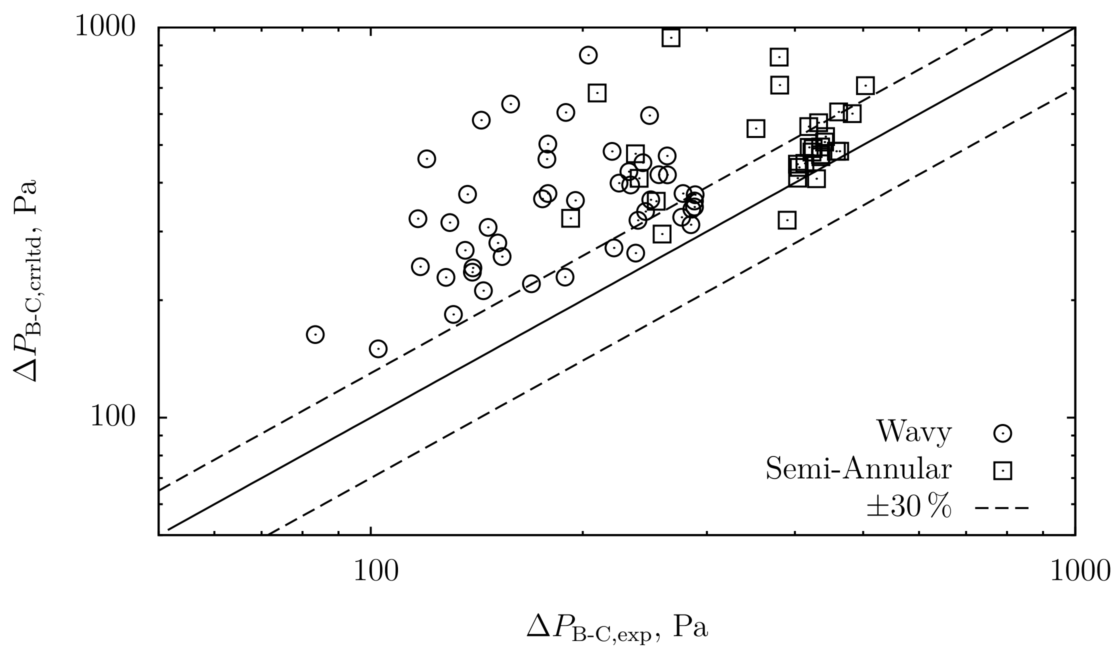

(b) $\Delta P_{\text{B-C}}$ compared with the HFM's predictions

Figure 7.8 Comparison of $\Delta P_{i\text{-C}}$ with published models: poorest prediction.

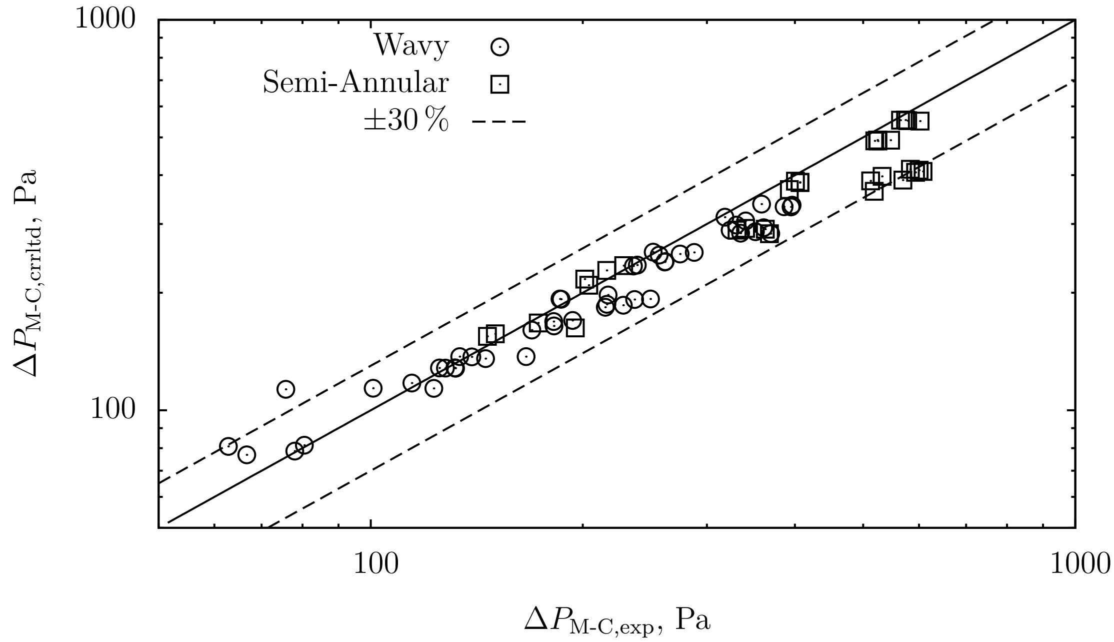

(a) $\Delta P_{\text{M-C}}$ compared with the MSFM's predictions.

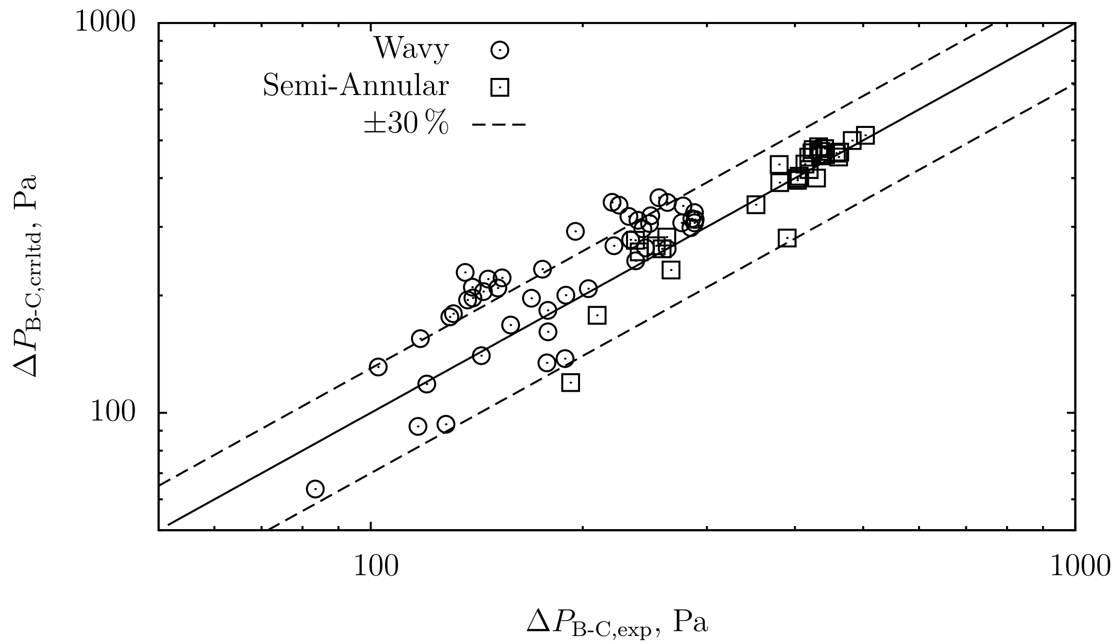

(b) $\Delta P_{\text{B-C}}$ compared with the LCM's predictions.

Figure 7.9 Comparison of $\Delta P_{i\text{-C}}$ with published models: best prediction.

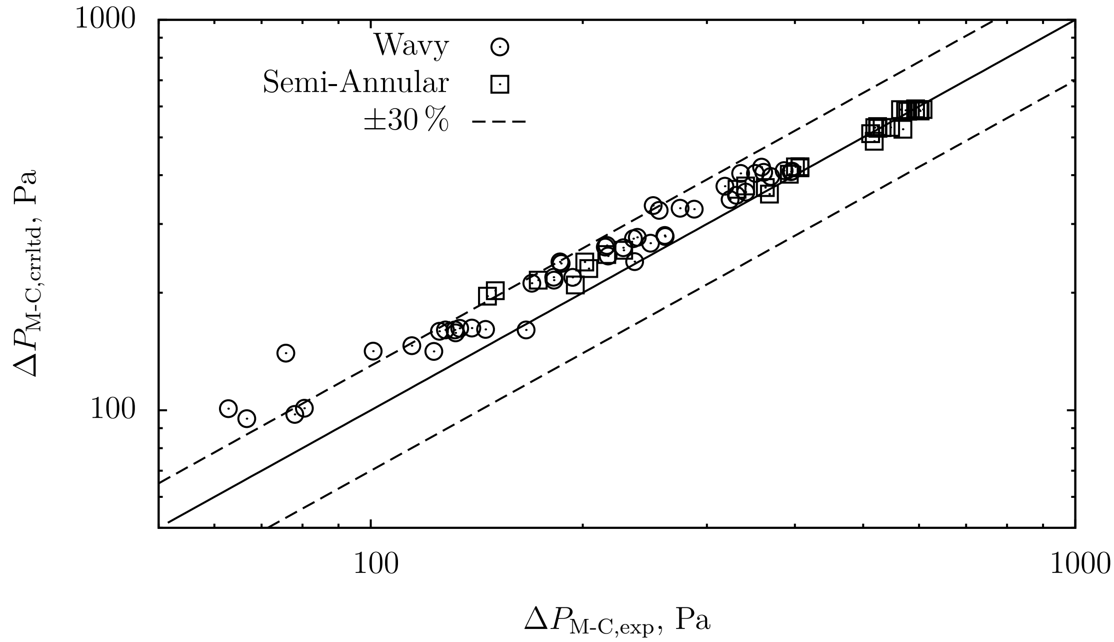

(a) Main to combined

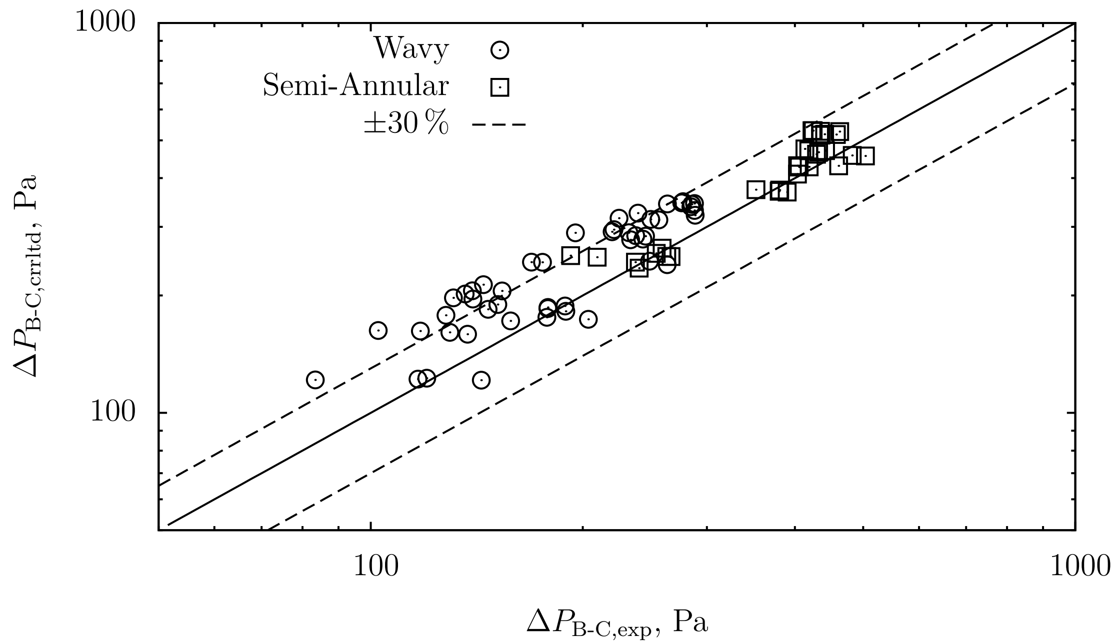

(b) Branch to combined

Figure 7.10 Comparison of $\Delta P_{i\text{-C}}$ with the MESFM.

Table 7.5 Models' RMSDs and AMDs for data with wavy and semi-annular flow in the combined side.

Outlet	Model	$\Delta P_{\text{M-C}}$		$\Delta P_{\text{B-C}}$	
Flow Regime		RMSD %	AMD %	RMSD %	AMD %
Wavy and semi-annular	ESFM	31.6	−16.3	27.2	17.6
	HFM	–	–	113.7	78.6
	MSFM	15.1	−7.7	–	–
	LCM	19.0	−0.7	24.6	12.1
	CCM	23.9	−2.1	25.1	14.9
	MCM	20.2	0.0	–	–
	MESFM	20.5	14.0	24.1	16.7
Wavy	ESFM	31.5	−12.4	32.8	24.8
	HFM	–	–	124.4	96.1
	MSFM	13.7	−5.2	–	–
	LCM	20.1	3.6	30.4	19.5
	CCM	25.5	2.6	31.0	22.5
	MCM	21.7	4.6	–	–
	MESFM	24.6	19.6	29.2	22.9
Semi-annular	ESFM	31.9	−22.0	15.3	6.9
	HFM	–	–	95.3	52.3
	MSFM	17.0	−11.4	–	–
	LCM	17.2	−7.3	11.1	1.0
	CCM	21.3	−9.2	11.8	3.6
	MCM	17.7	−6.7	–	–
	MESFM	11.7	5.7	13.0	7.4

Extending the MESFM

Further development of Eq. (6.3) casts the MESFM in a form that points out $\Delta P_{i\text{-C}}$'s dependence on W_C, x_C, λ_G, and λ_L:

$$\begin{aligned}\frac{2\rho_{\text{e},i}^2 \Delta P_{i\text{-C}} A^2}{W_\text{C}^2\, \rho_{\text{h},i}} =& \frac{\rho_{\text{e},i}^2}{|\delta_{i\text{M}} - \lambda_\text{G}| x_\text{C} + |\delta_{i\text{M}} - \lambda_\text{L}|(1 - x_\text{C})} \Bigg[|\delta_{i\text{M}} - \lambda_\text{G}| \frac{x_\text{C}^3}{\rho_\text{G}^2 \alpha_\text{C}^2} \\ &+ |\delta_{i\text{M}} - \lambda_\text{L}| \frac{(1 - x_\text{C})^3}{\rho_\text{L}^2 (1 - \alpha_\text{C})^2} \Bigg] (1 + k_{\text{MESFM},i\text{-c}}) \\ &- \Big[|\delta_{i\text{M}} - \lambda_\text{G}| x_\text{C} + |\delta_{i\text{M}} - \lambda_\text{L}|(1 - x_\text{C}) \Big]^2, \quad i = \text{B, M},\end{aligned} \tag{7.1}$$

where absolute values are denoted by || and ρ_{e} is the energy density defined as:

$$\rho_{\mathrm{e},i}^{-2} = \frac{x_i^3}{\rho_{\mathrm{G}}^2 \alpha_i^2} + \frac{(1-x_i)^3}{\rho_{\mathrm{L}}^2 (1-\alpha_i)^2}, \quad i = \mathrm{B, M, C}. \tag{7.2}$$

See Appendix A for details of the energy density's physical meaning and derivation.

Figure 7.11 shows the experimental values of the dimensionless group on the left-hand side of Eq. (7.1) for $x_{\mathrm{C}} = 0.5$ using the void fraction correlation from [87] for semi-annular flow conditions and the model from [33] for wavy and stratified flow conditions. The value of the dimensionless group collapses well with W_{C} confirming that the right-hand side of Eq. (7.1) is independent of W_{C} and therefore $k_{\mathrm{MESFM},i\text{-c}}$ is a function of λ_{L}, λ_{G}, and x_{C} only, as previously assumed in the MESFM.

While the importance of λ_{L} is not as insignificant as when the outlet flow condition was annular (compare Fig. 6.6b on page 61 with Fig. 7.7b on page 84 at low values of λ_{G}), it is still the least important parameter in determining $\Delta P_{i\text{-C}}$. Therefore, the same correlating approach was adopted using Eq. (6.4). From least squares regressions for the 48 experiments with $W_{\mathrm{C}} = 0.045\,\mathrm{kg\,s^{-1}}$, the following values of a and b were developed:

$$a_{\mathrm{M}} = \ 0.212 - 0.807\lambda_{\mathrm{G}} + 2.501\lambda_{\mathrm{G}}^2, \tag{7.3a}$$

$$b_{\mathrm{M}} = -0.340 + 3.022\lambda_{\mathrm{G}} - 4.195\lambda_{\mathrm{G}}^2, \tag{7.3b}$$

$$a_{\mathrm{B}} = \ 0.713 - 3.265\lambda_{\mathrm{G}} + 4.183\lambda_{\mathrm{G}}^2, \tag{7.3c}$$

$$b_{\mathrm{B}} = -1.853 + 7.824\lambda_{\mathrm{G}} - 6.792\lambda_{\mathrm{G}}^2. \tag{7.3d}$$

Table 7.6 and Fig. 7.12 compare the predictions using Eqs. (6.3), (6.4), and (7.3) with the experimental values. The experimental data agrees excellently with the correlation having an RMSD of 9.9% for $\Delta P_{\mathrm{M\text{-}C}}$ and 13.8% for $\Delta P_{\mathrm{B\text{-}C}}$. The agreement improves if only the data with wavy flow in the combined side is considered. The

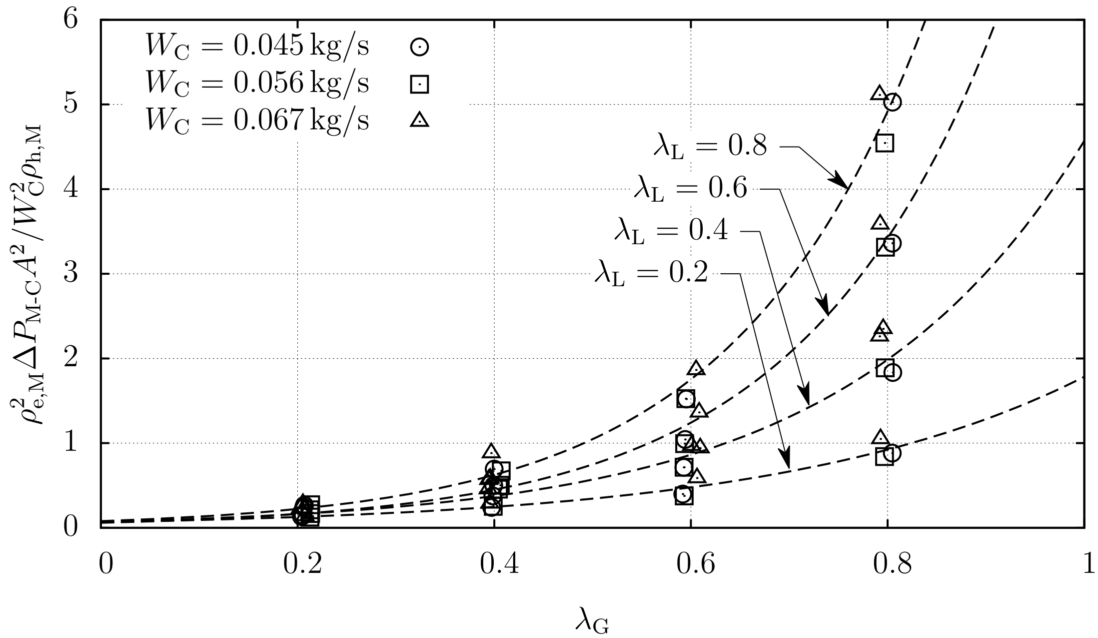

(a) Main to combined

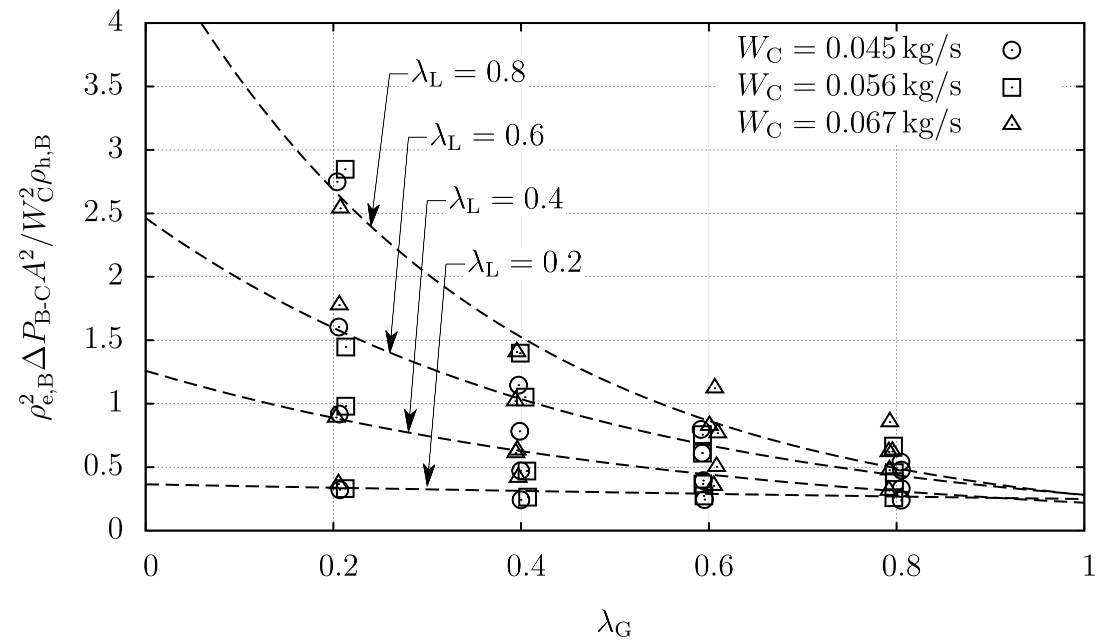

(b) Branch to combined

Figure 7.11 Experimental values of the dimensionless group on the left-hand-side of Eq. (7.1) for $x_C = 0.5$.

new coefficients for the MESFM under-predict the data with semi-annular flow in the combined side, however, these data are very well predicted by the MESFM using the annular coefficients from Eq. (6.5) as shown in Figs. 7.10a and 7.10b.

Again, it is an interesting exercise to observe the MESFM's behaviour with the coefficients of Eq. (7.3) for the limiting condition of single-phase gas flow in all sides of the tee where $x_i = x_\mathrm{C} = 1.0$ and $\lambda_\mathrm{G} = \lambda$. Equations (6.4) and (7.3) become the single-phase pressure loss relation:

$$\lim_{x_\mathrm{C}\to 1} k_{\mathrm{MESFM,M\text{-}C}} = -0.128 + 2.214\lambda - 1.694\lambda^2, \tag{7.4a}$$

$$\lim_{x_\mathrm{C}\to 1} k_{\mathrm{MESFM,B\text{-}C}} = -1.140 + 4.559\lambda - 2.609\lambda^2. \tag{7.4b}$$

Figure 7.13 shows a comparison of Eq. (7.4) and Eq. (5.2). The good agreement between the values supports the physics behind the MESFM's development.

Table 7.6 The MESFM's RMSD and AMD using Eq. (7.3) for data with wavy and semi-annular flow in the combined side.

Outlet	$\Delta P_{\mathrm{M\text{-}C}}$		$\Delta P_{\mathrm{B\text{-}C}}$	
Flow Regime	RMSD %	AMD %	RMSD %	AMD %
Wavy and semi-annular	9.9	−2.1	13.8	−3.7
Wavy	9.3	0.4	11.9	−1.0
Semi-annular	10.7	−5.8	16.2	−7.8

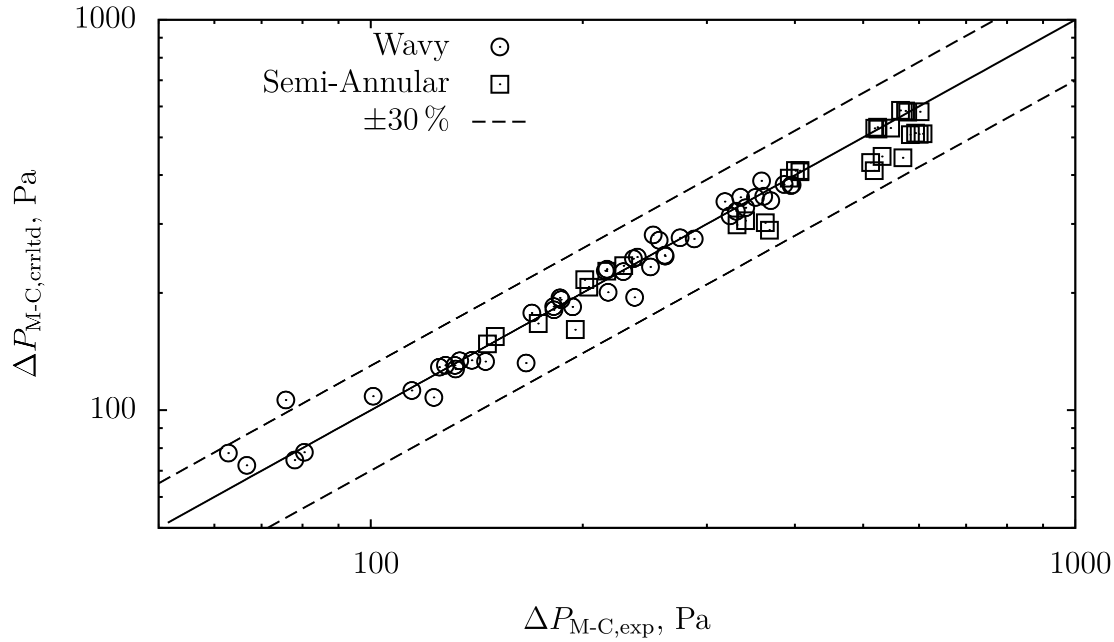

(a) Main to combined

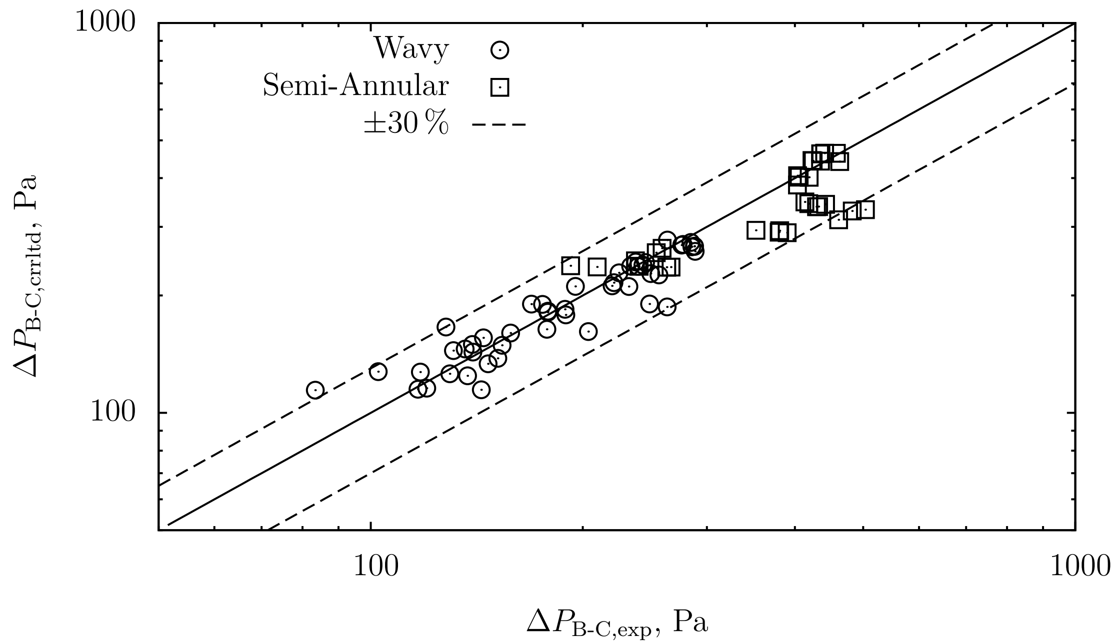

(b) Branch to combined

Figure 7.12 $\Delta P_{i\text{-C}}$ compared with the MESFM using Eq. (7.3) for experiments with wavy flow in the combined side.

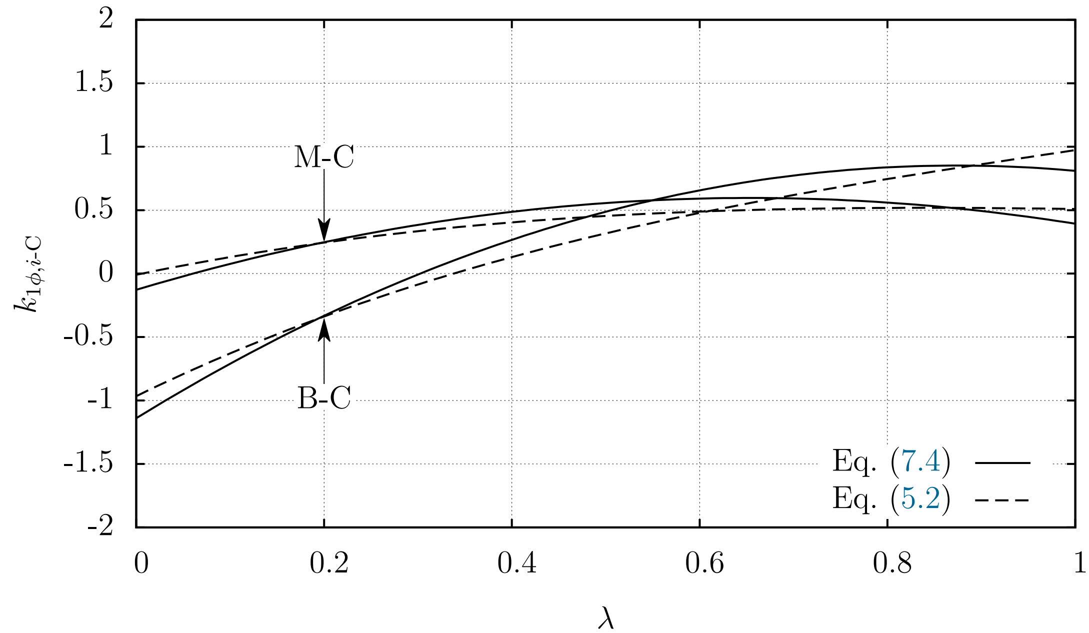

Figure 7.13 $k_{1\phi,i\text{-C}}$ correlated from experiments compared with the MESFM in the limit of single-phase gas flow.

7.5 Mixing behaviour at low gas velocities

Initially, a test matrix for experiments with wavy flow in the combined side was constructed to cover a range of gas velocities including lower gas velocities than the final test matrix shown in Fig. 7.1. However, a series of 36 experiments showed that the tee junction significantly affects the pressure distributions in all sides of the junction when mixtures were combined with $V_{\mathrm{SG,C}} \lesssim 10\,\mathrm{m\,s^{-1}}$, leading to less accuracy and poor repeatability in the results for $\Delta P_{i\text{-C}}$. As a result, the final test matrix was chosen such that $V_{\mathrm{SG,C}} > 10\,\mathrm{m\,s^{-1}}$. This section shows and discusses some of the experiments conducted with $V_{\mathrm{SG,C}} < 10\,\mathrm{m\,s^{-1}}$ that led to this restriction.

Figure 7.14 shows two examples of time-averaged pressure distributions for experiments with $V_{\mathrm{SG,C}} < 10\,\mathrm{m\,s^{-1}}$. At the junction, the flow swells due to mixing and the pressure in any of the three legs of the tee could deviate from the apparent fully-developed lines by a significant amount and for a significant distance away from the junction. Values above the presumed fully-developed line indicate an increase in the liquid level, referred to here as a ‘swell’ or a ‘hydraulic rise’. Figure 7.14 shows extreme examples of the phenomenon, with the ‘fully-developed’ lines not drawn with the normal algorithm but instead simply drawn through the first few points to highlight the extent of the deviation. Figure 7.14a shows a hydraulic rise in both the main and combined legs. The water in the branch under these conditions spills back into the main and causes a swell in the liquid level. While we have no evidence that any of the data in Fig. 7.14a is in the fully-developed region, if the drawn lines represent the fully-developed lines they suggest a negative $\Delta P_{\text{M-C}}$ with the present analysis methods, which is not possible. The swell continues in the combined side as the low overall gas flow rate cannot maintain a flat interface. Figure 7.14b shows a similar hydraulic rise, but in the branch inlet under different conditions. In both situations shown in Fig. 7.14, the combined flow takes a long distance to develop, particularly with the low gas flow in Fig. 7.14a.

Figure 7.15 shows the same experiment repeated for a case with a less extreme hydraulic rise and an even distribution of flow between the inlets ($\lambda_{\text{G}} = \lambda_{\text{L}} = 0.50$). The ‘fully-developed’ lines in these experiments were drawn according to the usual algorithm. In Fig. 7.15a, the apparent fully-developed slopes for the main and branch inlets are $dP/dz_{\text{M}} = 16.9\,\text{Pa}\,\text{m}^{-1}$ and $dP/dz_{\text{B}} = 29.6\,\text{Pa}\,\text{m}^{-1}$. In Fig. 7.15b, the apparent fully-developed slopes for the main and branch inlets are $dP/dz_{\text{M}} = 10.1\,\text{Pa}\,\text{m}^{-1}$, $dP/dz_{\text{B}} = 26.9\,\text{Pa}\,\text{m}^{-1}$. The experiments both have an even distribution of gas and liquid between the inlets, yet $dP/dz_{\text{B}} \neq dP/dz_{\text{M}}$, and therefore the data cannot be from the fully-developed region.

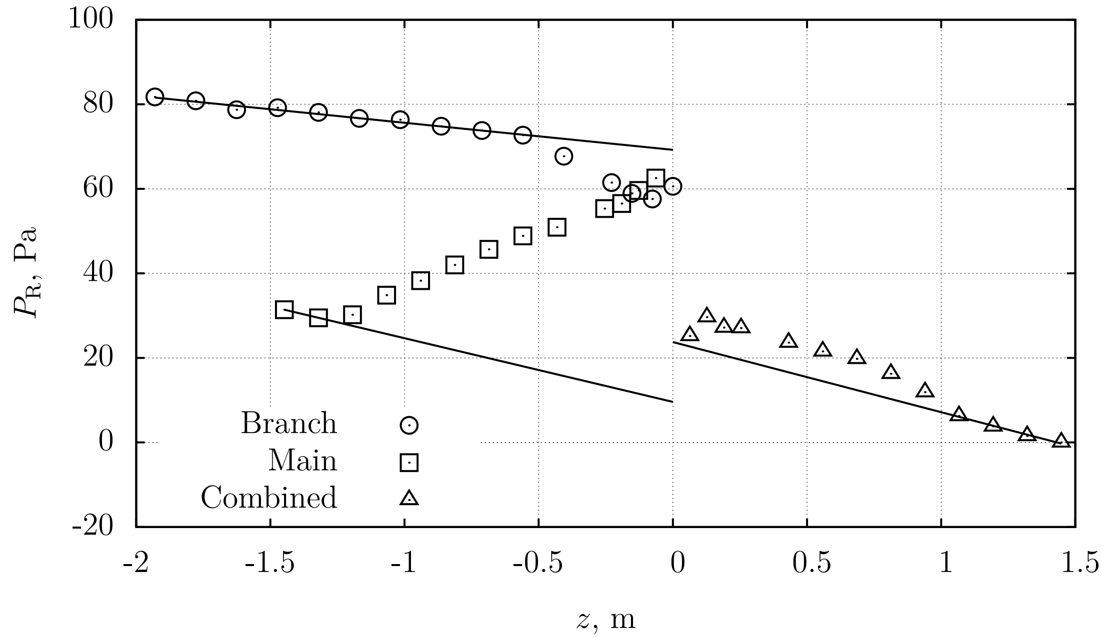

(a) $W_C = 0.050\,\mathrm{kg\,s^{-1}}$, $x_C = 0.20$, $\lambda_G = 0.20$, $\lambda_L = 0.80$, $V_{SG,C} = 5.0\,\mathrm{m\,s^{-1}}$

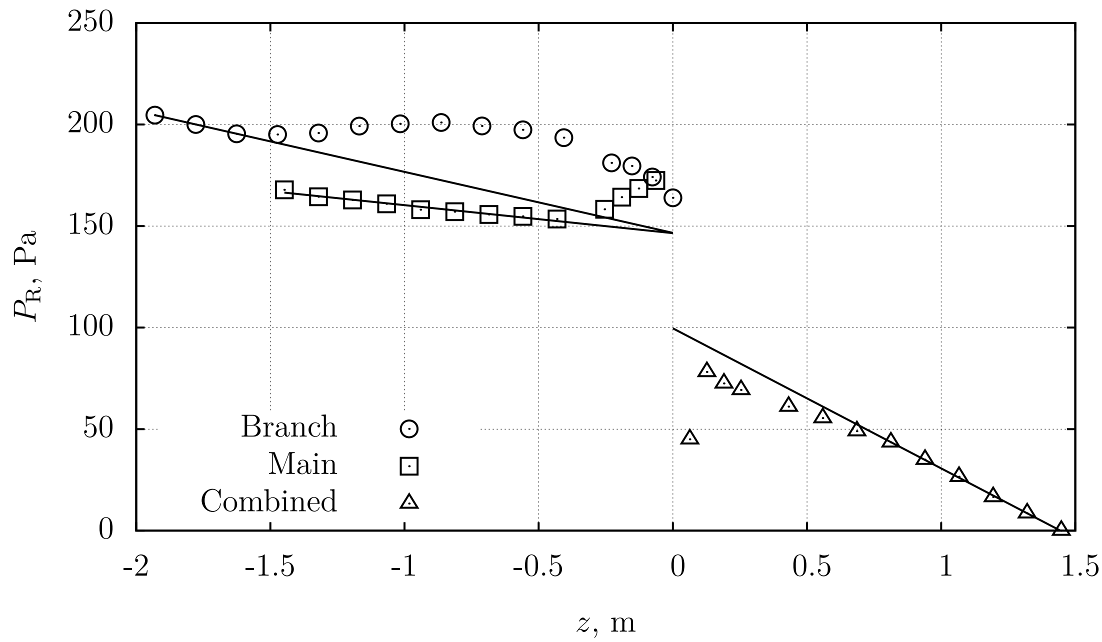

(b) $W_C = 0.052\,\mathrm{kg\,s^{-1}}$, $x_C = 0.30$, $\lambda_G = 0.40$, $\lambda_L = 0.80$, $V_{SG,C} = 7.5\,\mathrm{m\,s^{-1}}$

Figure 7.14 Examples of extreme hydraulic rise in the main, combined, and branch for different wavy experiments.

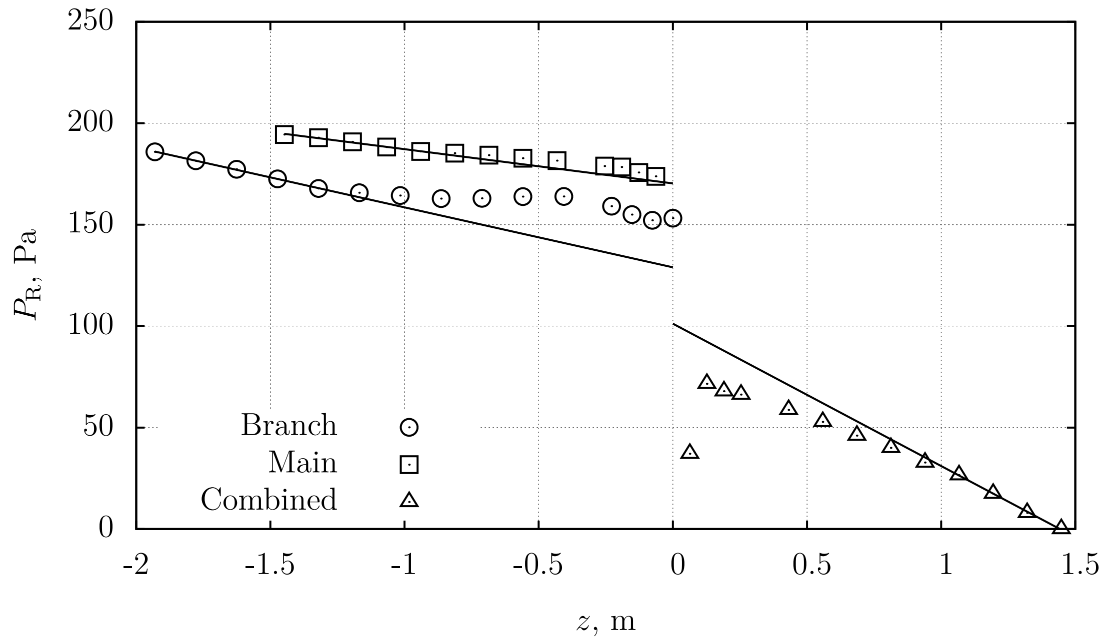

(a) $W_C = 0.050\,\mathrm{kg\,s^{-1}}$, $x_C = 0.31$, $\lambda_G = 0.50$, $\lambda_L = 0.50$, $dP/dz_M = 16.9\,\mathrm{Pa\,m^{-1}}$, $dP/dz_B = 29.6\,\mathrm{Pa\,m^{-1}}$

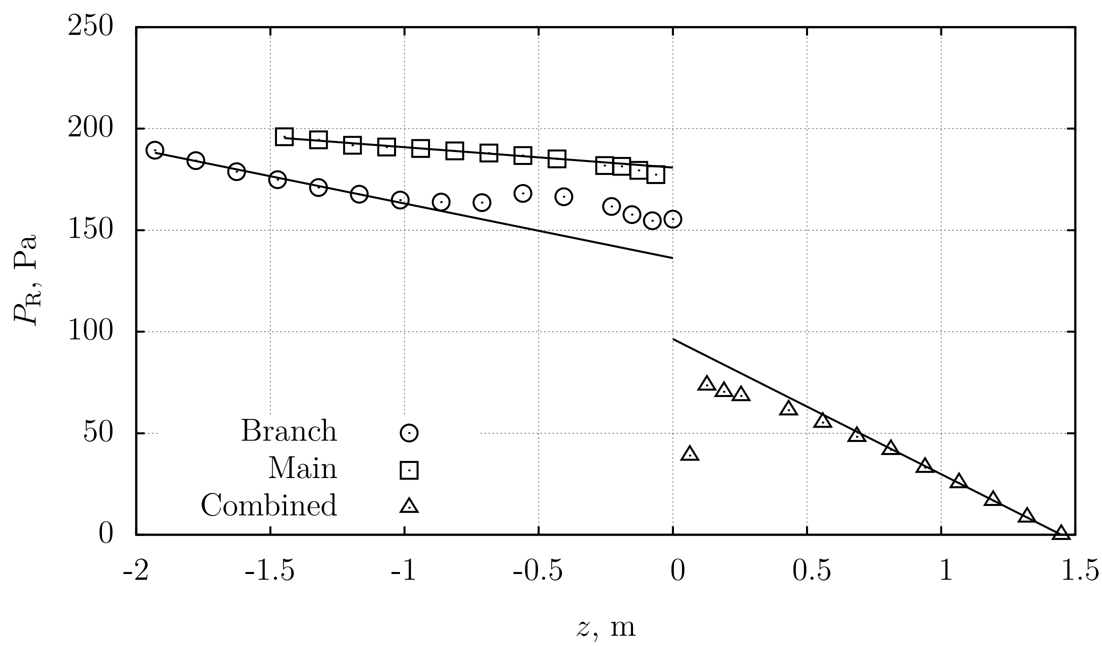

(b) $W_C = 0.051\,\mathrm{kg\,s^{-1}}$, $x_C = 0.30$, $\lambda_G = 0.50$, $\lambda_L = 0.50$, $dP/dz_M = 10.1\,\mathrm{Pa\,m^{-1}}$, $dP/dz_B = 26.9\,\mathrm{Pa\,m^{-1}}$

Figure 7.15 Repeated wavy flow experiments with a large hydraulic rise and an even flow distribution.

These experiments show that at low gas velocities great caution is required since the junction can perturb the flow a long distance upstream of the junction. Using data with only a few measurements to determine the slope of the fully-developed line leads to unacceptable uncertainty, and for study of mixtures with low gas velocity, a longer test section is recommended. Once again, for these reasons, the presented results for $\Delta P_{i\text{-C}}$ all had $V_{\mathrm{SG,C}} > 10\,\mathrm{m\,s^{-1}}$.

Chapter 8

Slug Flow Results

8.1 Overview

Previous results with a rig of similar design but a dividing impacting junction (see Fig. 1.1d, page 2) show a large amount of scatter in differential measurements of pressure for slug flow [88, page 137]; so much scatter, that no pressure loss results were reported for any slug flow experiments. Buell [88] explained that the scatter was a result of the large variation in pressure measurements, but this is at odds with theory that predicts linear gradients for fully-developed flow, even for intermittent regimes, if sufficient samples are taken and averaged over time. As such, objective 3c of Section 1.4 was set with the view that procedural and apparatus refinements would overcome difficulties with data-scatter and allow accurate measurements of the pressure distribution surrounding the junction. The discussion that follows gives evidence for why slug flow results are difficult to accurately measure, and also provides some suggestions for future investigation. The first section introduces the reference line and validates its accuracy by reproducing wavy and annular experimental results. The second section critically examines samples of initial results for time-averaged pressure distributions and shows the results are not repeatable. The third section presents and discusses time-varying pressure measurements in order to explain the difficulties with the presented time-averaged pressure distributions. The fourth section offers ideas for future investigation. Finally, a visual study of a single outlet slug flow condition while varying only λ_{L} highlights several slug flow mixing behaviours.

8.2 The reference line

Up to this point, all of the presented data was collected using differential measurements, and positive differentials were always measured. However, slug flow presents a problem because of its intermittent nature: when slugs pass they drastically increase local pressure readings. This means pressures downstream can momentarily have higher values than upstream and therefore, as the transducers are not capable of measuring negative differentials, the pressure distribution cannot be measured with the standard differential technique. For this reason the reference line, described in Section 3.2 and Appendix C.3, was installed. The reference line holds an adjustable, constant pressure and thereby allows positive differential measurements for each tap, regardless of local pressure changes. Accurate measurements of the differential pressure between two different taps requires the simultaneous measurement of both taps relative to the reference line, and then subtraction of their measured values (see Section 4.2).

Following the procedure given in Appendix C.3, experiments with wavy flow and annular flow in the combined side were repeated using the reference line and compared with results achieved without using the reference line. Table 8.1 and Figs. 8.1 and 8.2 summarize the results. The results obtained with and without the reference line agree excellently with each other.

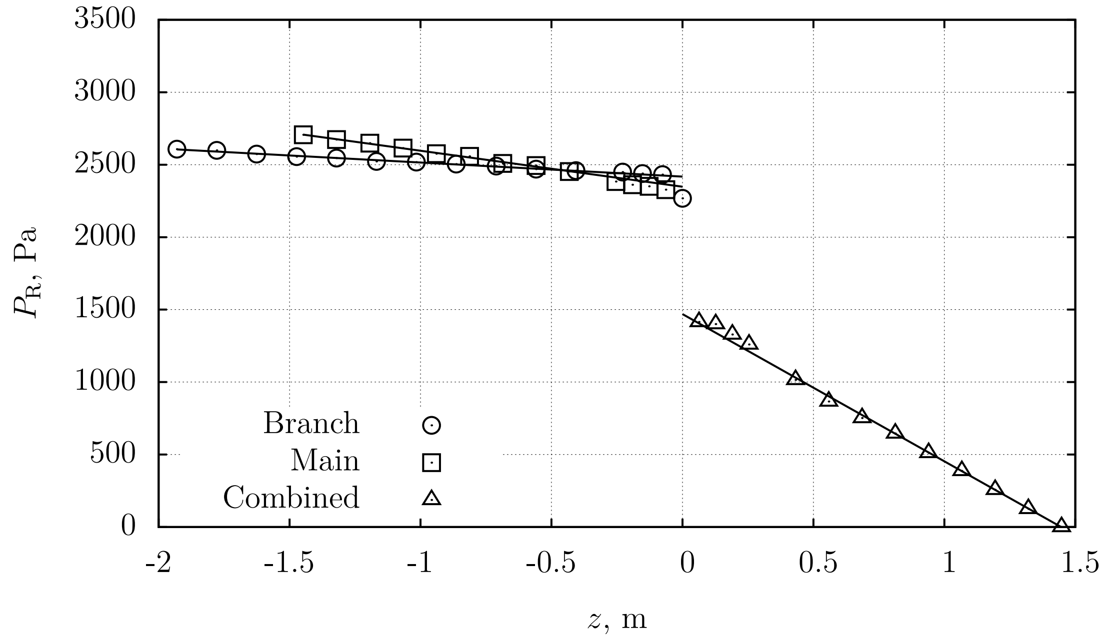

(a) Measurements with the reference line ($W_C = 0.113\,\mathrm{kg\,s^{-1}}$, $x_C = 0.51$)

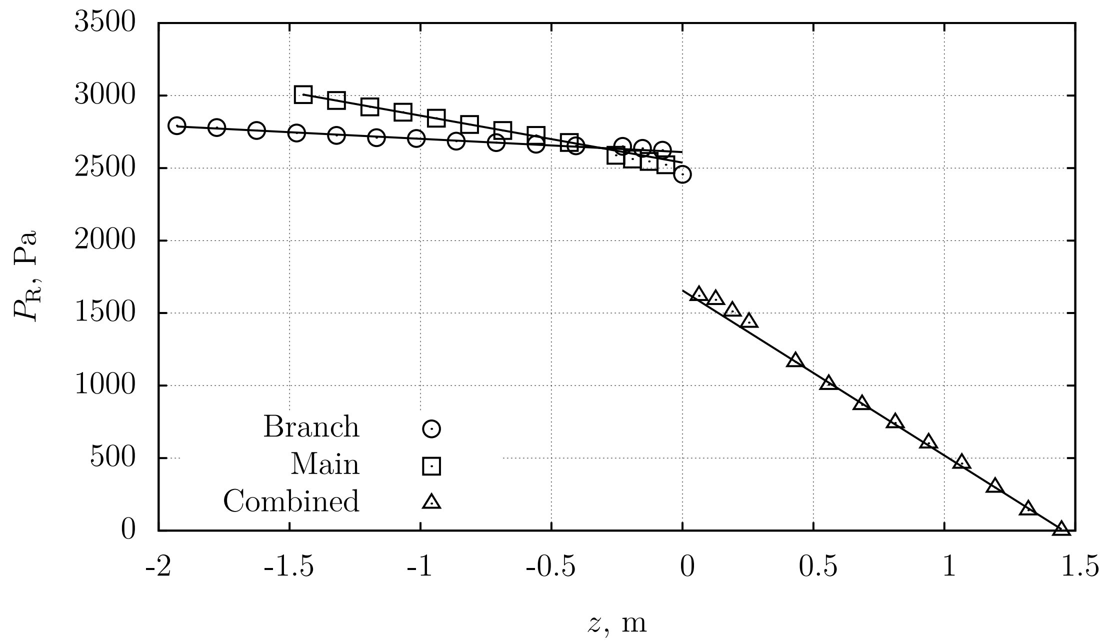

(b) Measurements without the reference line ($W_C = 0.107\,\mathrm{kg\,s^{-1}}$, $x_C = 0.49$)

Figure 8.1 Comparison of measurements taken with and without the reference line for an experiment with annular flow in the combined side ($\lambda_G = 0.30$, $\lambda_L = 0.80$).

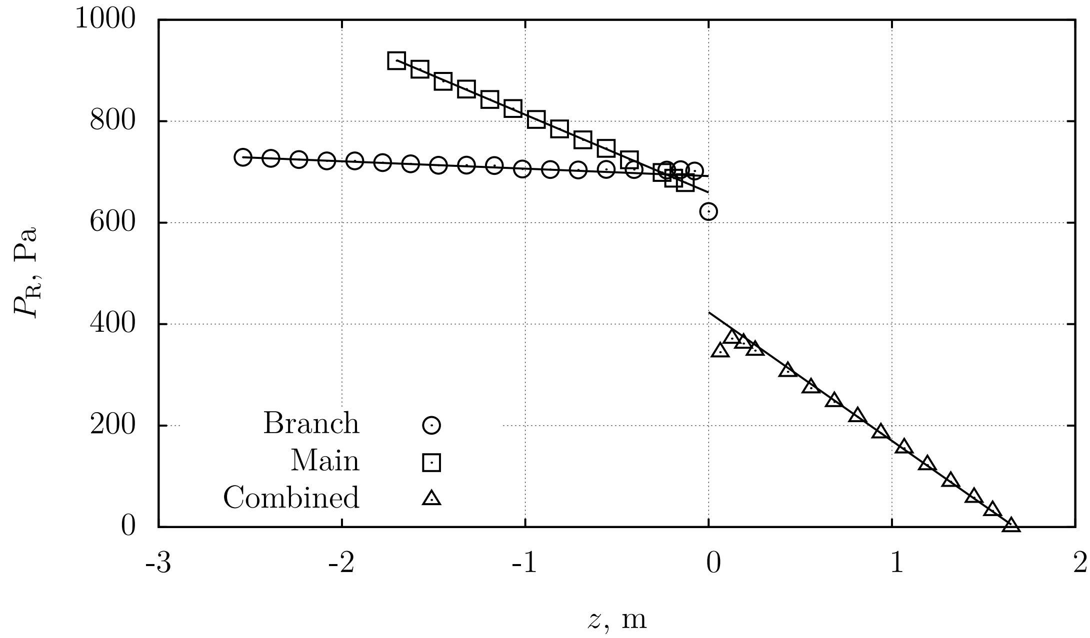

(a) Measurements with the reference line ($\lambda_G = 0.20$)

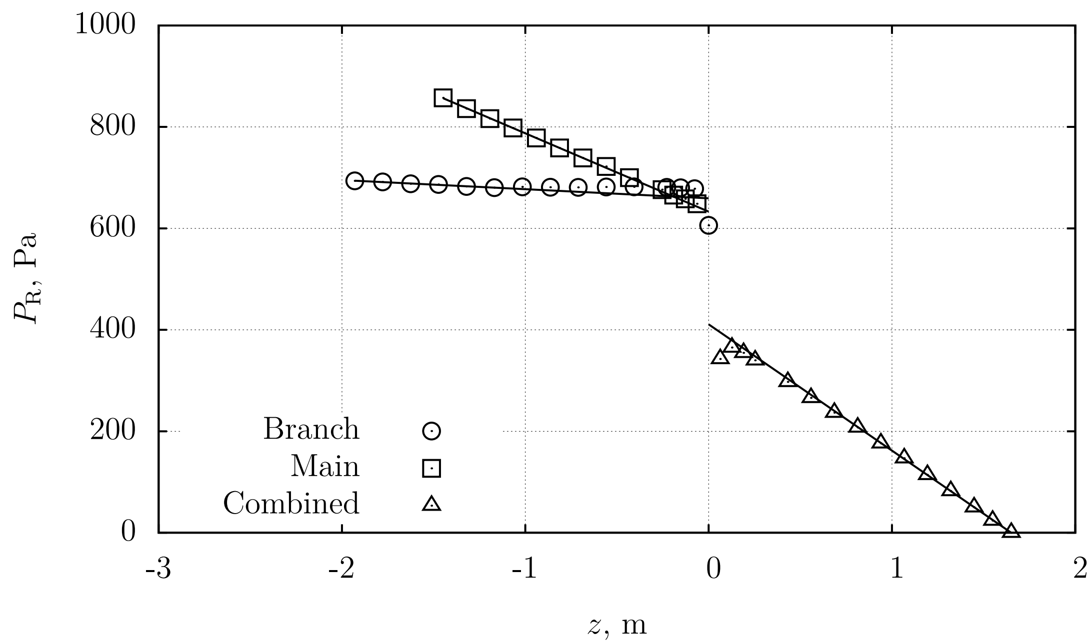

(b) Measurements without the reference line ($\lambda_G = 0.21$)

Figure 8.2 Comparison of measurements taken with and without the reference line for an experiment with wavy flow in the combined side ($W_C = 0.045\,\mathrm{kg\,s^{-1}}$, $x_C = 0.90$, $\lambda_L = 0.20$.

Table 8.1 Comparison of results obtained with and without the reference line.

Figure	W_C	x_C	λ_G	λ_L	$\Delta P_{M\text{-}C}$	$\Delta P_{B\text{-}C}$	dP/dz_M	dP/dz_B	dP/dz_C
	$\mathrm{kg\,s^{-1}}$				Pa		$\mathrm{Pa\,m^{-1}}$		
8.1a	0.113	0.51	0.30	0.80	882.1	954.7	323.9	91.6	1 137.1
8.1b	0.107	0.49	0.30	0.80	878.8	948.1	248.3	97.6	1 016.2
8.2a	0.045	0.90	0.20	0.20	222.3	248.7	154.3	17.9	248.9
8.2b	0.045	0.90	0.21	0.20	236.2	268.6	153.4	14.6	253.6

8.3 Initial (inaccurate) pressure distributions

Preliminary experiments with slug flow in the combined side were conducted for various conditions. A test matrix was designed for study of the individual effects of the four independent parameters (W_C, x_C, λ_G, λ_L) by successively holding three parameters constant while varying the fourth. Figure 8.3 shows the combined side's flow conditions on Mandhane et al.'s [34] flow-regime map, along with those from Chapters 6 and 7 for reference. Unlike experiments with annular flow and wavy flow in the combined side, repeatable results were not achieved. Before pressure-loss data were recorded, an experiment was conducted to determine an appropriate sampling time for repeatable time-averaged pressure distributions. For a flow with $W_C = 0.162\,\mathrm{kg\,s^{-1}}$, $x_C = 0.06$, $\lambda_G = 0.48$, and $\lambda_L = 0.50$, the pressure difference between taps B1 and C1 was measured with the reference line using transducers 3 and 7, and the time-varying signal recorded continuously over a period of 30 min at a sampling frequency of 1 000 Hz. The large measurement range of transducers 3 and 7 was necessary owing to the large pressure fluctuations caused by passing slugs. The average pressure difference between the two taps was calculated over various amounts of time (e.g., 0–1 min, 0–2 min, . . . etc.) with the results summarized in Table 8.2. Repeatability was not achieved within 10 Pa regardless of sampling time.

In spite of this difficulty, several experiments were conducted with an outlet flow rate of $W_\mathrm{C} = 0.31\,\mathrm{kg\,s^{-1}}$ and $x_\mathrm{C} = 0.03$ in order to examine the time-averaged pressure-distributions repeatability. Six experiments were conducted with a flow distribution of $\lambda_\mathrm{G} = 0.3$ and $\lambda_\mathrm{L} = 0.2$, and also three more experiments with an even flow distribution, $\lambda_\mathrm{G} = \lambda_\mathrm{L} = 0.5$. Figure 8.4 shows these conditions on Mandhane et al.'s [34] flow-regime map. Figures 8.5 to 8.7 and Table 8.3 summarize the results for the tests. A sampling rate of 1 000 Hz was used for all of these tests, but the sampling times varied between (4–12) min as indicated in the figures. Unlike repeatability tests when the combined side had annular or wavy flow (see Fig. 6.2 and Fig. 7.2), Figs. 8.5 to 8.7 show significant scatter in the main and branch sides for every test. As a result of the scatter in measured pressures, neither dP/dz_M nor dP/dz_B were repeatable, leading to, in the author's opinion, unacceptably large variation in $\Delta P_{i\text{-C}}$. The results for the experiments shown in Figs. 8.5 and 8.6 have $\mathrm{RMSD}(\Delta P_\text{M-C}) = 33\,\%$ and $\mathrm{RMSD}(\Delta P_\text{B-C}) = 45\,\%$ with respect to their average values.

More cause for concern is apparent in the experiments shown in Fig. 8.7. While

Table 8.2 Repeatability tests for $\Delta P_\text{B1-C1}$ in an experiment with slug flow in the outlet.

Sampling time s	Time-averaged ΔP Pa
1 800	599.7
900	605.6
600	610.0
300	611.5
240	609.9
120	603.9
60	616.7

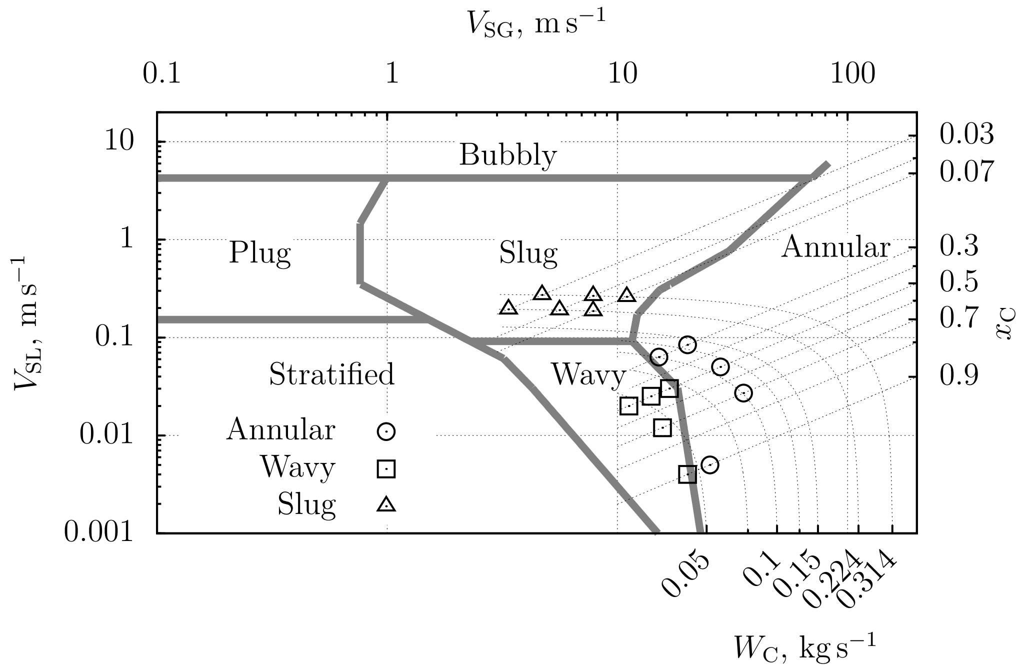

Figure 8.3 Intended region of study with slug flow conditions in the combined side on the flow-regime map of Mandhane et al. [34].

Table 8.3 Result summary for repeated experiments with slug flow in the combined side.

Figure	W_C	x_C	λ_G	λ_L	$\Delta P_{M\text{-}C}$	$\Delta P_{B\text{-}C}$	dP/dz_M	dP/dz_B	dP/dz_C
Figure	kg s^{-1}				Pa		Pa m^{-1}		
8.5a	0.309	0.03	0.29	0.20	145.0	24.5	127.4	71.2	371.1
8.5b	0.308	0.03	0.29	0.20	104.7	121.4	175.0	10.1	358.7
8.5c	0.308	0.03	0.29	0.20	144.0	155.5	173.9	17.0	351.0
8.6a	0.309	0.03	0.29	0.20	42.4	56.9	201.8	22.6	413.5
8.6b	0.309	0.03	0.29	0.20	147.0	131.1	176.0	34.7	352.0
8.6c	0.309	0.03	0.29	0.20	164.9	133.6	161.0	26.8	353.8
8.7a	0.314	0.03	0.51	0.50	640.7	179.9	15.2	204.1	352.8
8.7b	0.314	0.03	0.50	0.50	420.1	252.0	122.4	145.2	386.1
8.7c	0.315	0.03	0.50	0.50	464.9	169.7	117.6	209.5	356.0
–	0.158	0.03	1.00	1.00	–	–	–	99.7	–
–	0.157	0.03	0.00	0.00	–	–	97.2	–	–

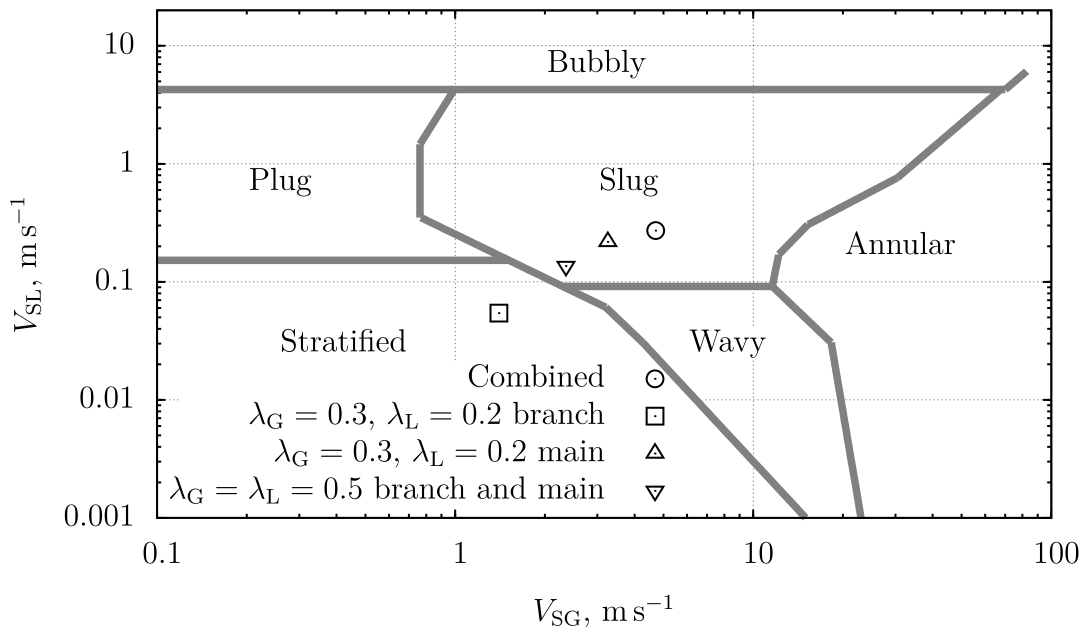

Figure 8.4 Flow conditions on Mandhane et al.'s [34] flow-regime map: $W_C = 0.31\,\mathrm{kg\,s^{-1}}$, $x_C = 0.03$ with either $\lambda_G = 0.3$ and $\lambda_L = 0.2$ (Figs. 8.5 and 8.6), or $\lambda_G = \lambda_L = 0.5$ (Fig. 8.7).

these experiments had an even mass distribution, the results given in Table 8.3 show $dP/dz_M \neq dP/dz_B$. Further, two experiments were conducted using the same inlet flow rate as Fig. 8.7 but only a single inlet with the inlet pressure gradients given on the last two lines of Table 8.3[1]. While the dP/dz values between these two experiments are in agreement, they differ significantly from the inlet dP/dz values in Fig. 8.7. Thinking that perhaps the method for determining the fully-developed lines was problematic when so much scatter was present, lines of best fit were drawn through the first 10 pressure taps in each side of the junction (not shown) rather than using the standard statistical method. Using this alternative procedure somewhat improved

[1]The pipe-flow experiments do not include dP/dz_C since the presence of the junction allowed a significant amount of water to spill into the inlet without any flow, and fully-developed flow was not established again in the combined side.

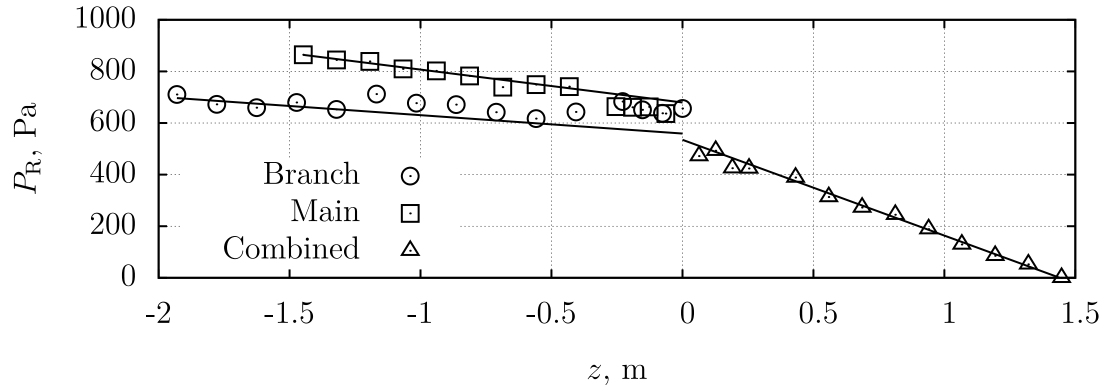

(a) 4 min sampling time ($W_C = 0.309\,\mathrm{kg\,s^{-1}}$)

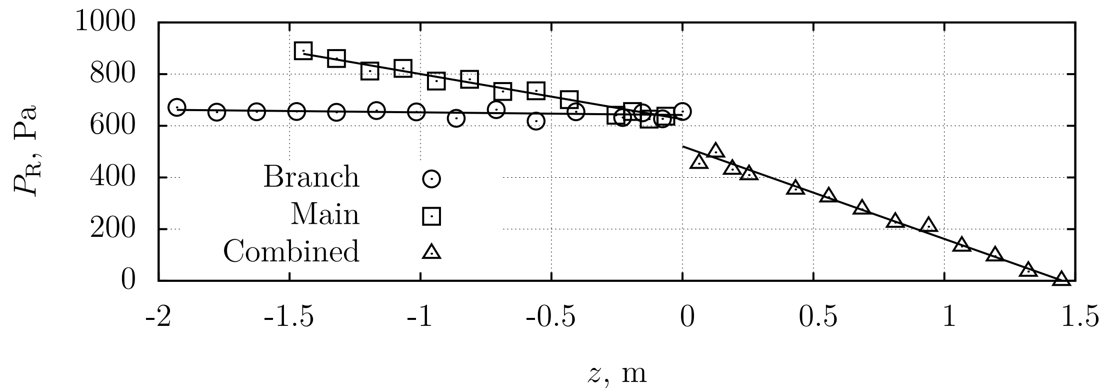

(b) 4 min sampling time ($W_C = 0.308\,\mathrm{kg\,s^{-1}}$)

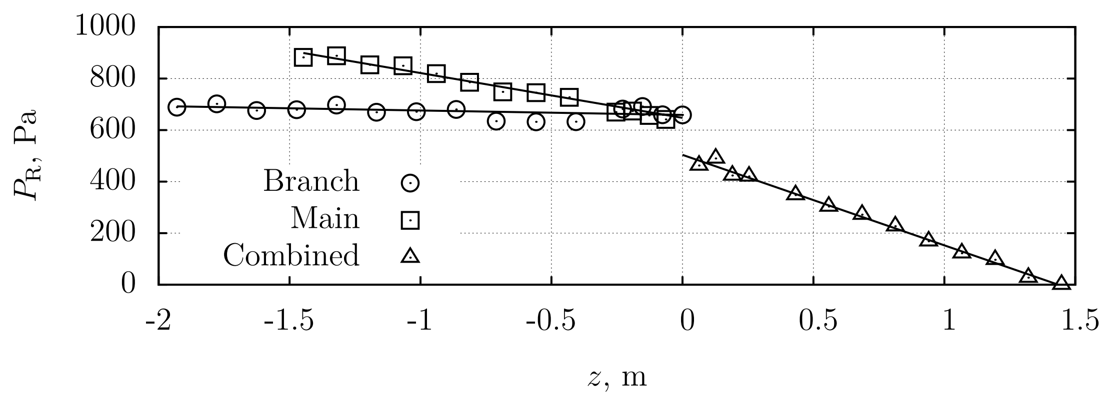

(c) 8 min sampling time ($W_C = 0.308\,\mathrm{kg\,s^{-1}}$)

Figure 8.5 Repeated experiments with slug flow in the combined side using different sampling times ($x_C = 0.03$, $\lambda_G = 0.29$, $\lambda_L = 0.20$).

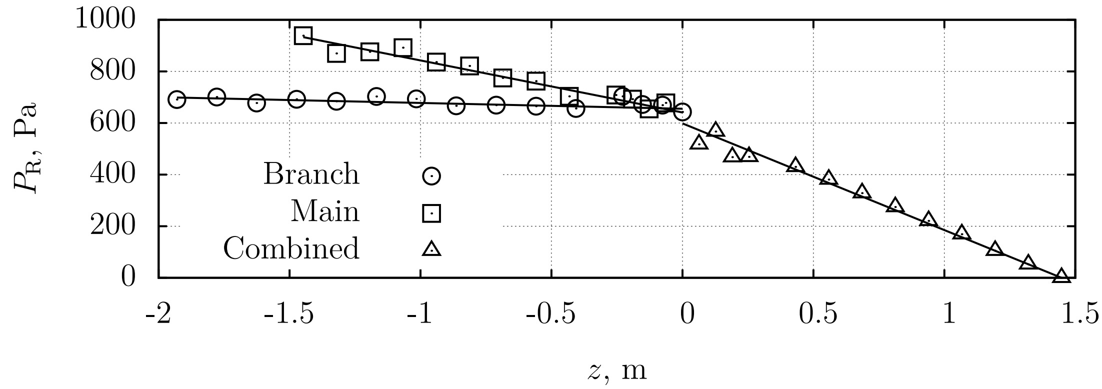

(a) 4 min sampling time

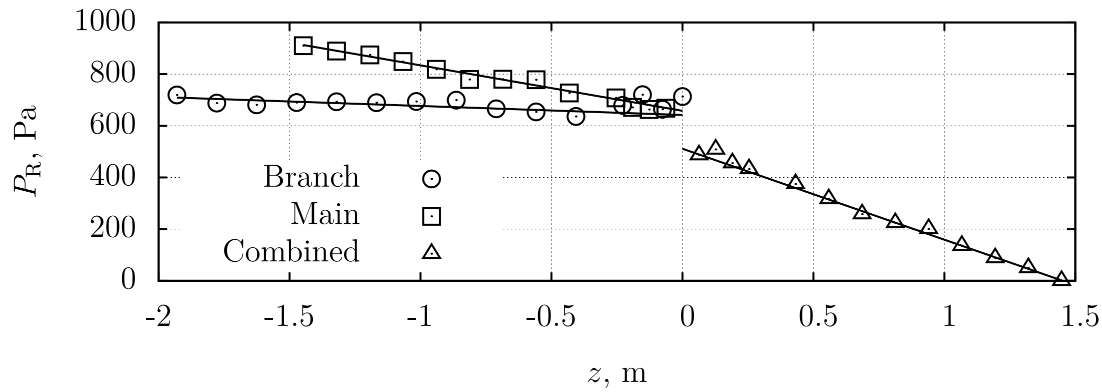

(b) 6 min sampling time

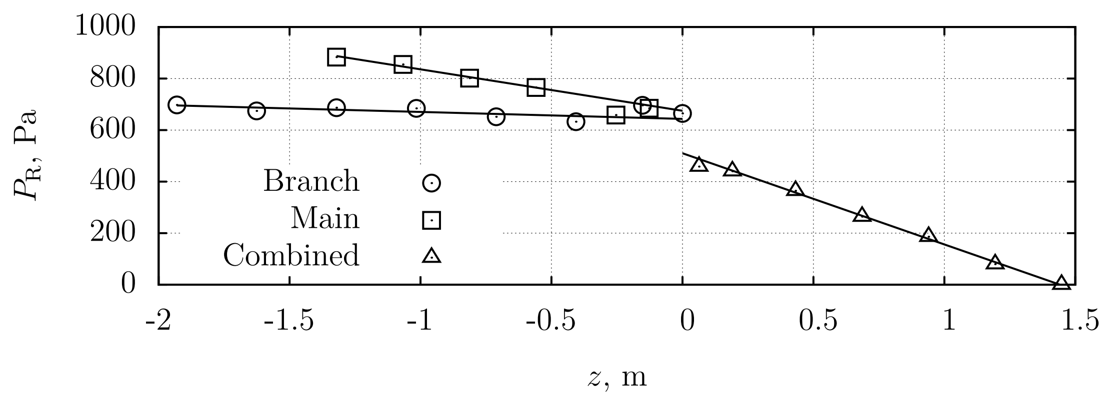

(c) 12 min sampling time

Figure 8.6 Repeated experiments with slug flow in the combined side using different sampling times ($W_{\mathrm{C}} = 0.309\,\mathrm{kg\,s^{-1}}$, $x_{\mathrm{C}} = 0.03$, $\lambda_{\mathrm{G}} = 0.29$, and $\lambda_{\mathrm{L}} = 0.20$).

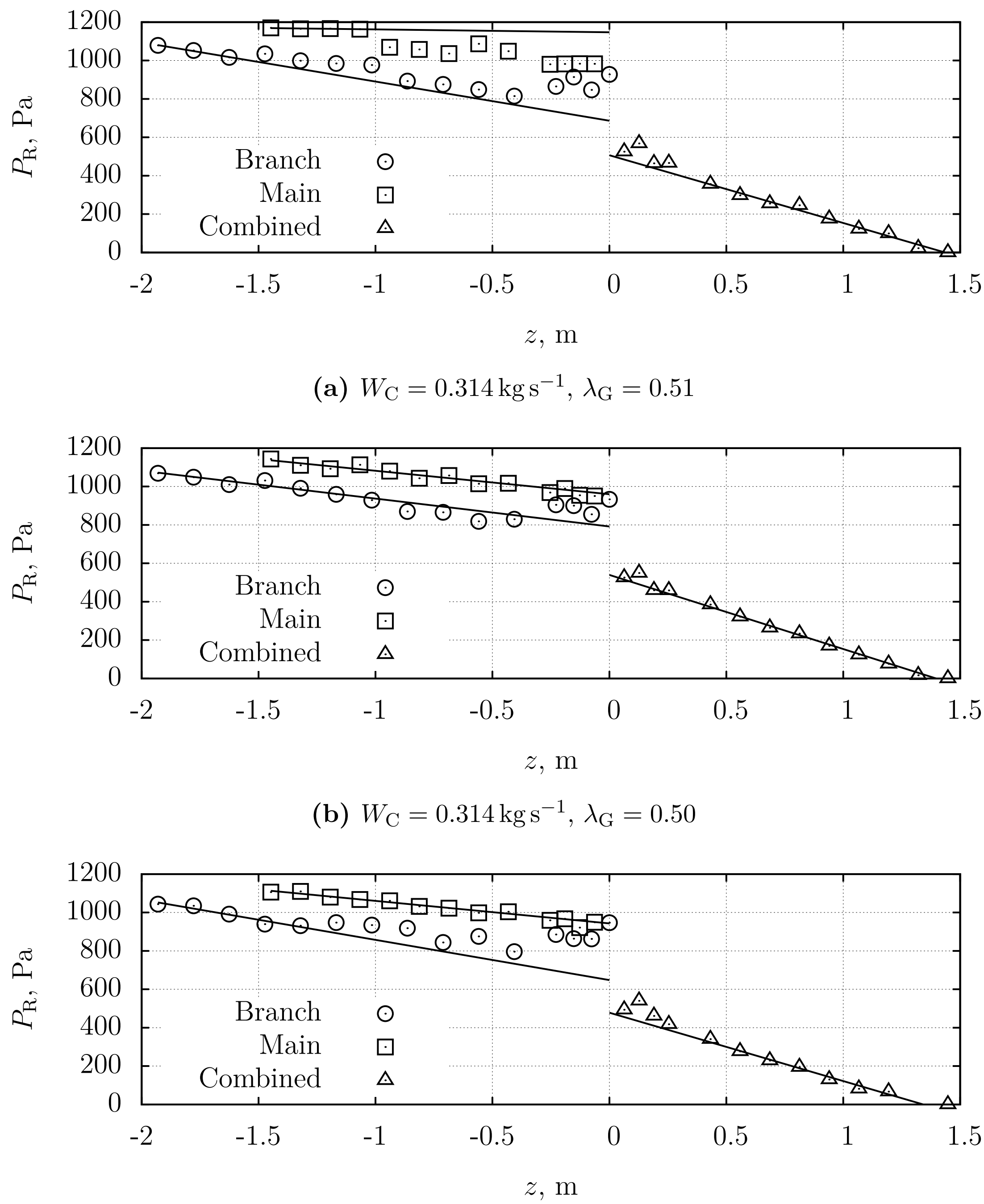

(a) $W_C = 0.314\,\mathrm{kg\,s^{-1}}$, $\lambda_G = 0.51$

(b) $W_C = 0.314\,\mathrm{kg\,s^{-1}}$, $\lambda_G = 0.50$

(c) $W_C = 0.315\,\mathrm{kg\,s^{-1}}$, $\lambda_G = 0.50$

Figure 8.7 Repeated experiments with slug flow in the combined side using a 4 min sampling time ($x_C = 0.03$, $\lambda_L = 0.50$).

the agreement between dP/dz_{M} and dP/dz_{B}, but not to anywhere near the level of consistency observed for experiments with annular flow in the combined side (see Fig. 6.3, page 58) or wavy flow in the combined side (see Fig. 7.3, page 80). Further, the dP/dz values calculated based on the first 10 pressure taps in each side of the junction ranged in value from (120–170) Pa, which still disagree with the single-inlet dP/dz values reported in the last two lines of Table 8.3.

These are only a sample of 48 experiments conducted at various conditions and with slight modifications between tests including disassembly and cleaning of the rig, repeated and thorough purging of air bubbles, checking and rechecking the horizontal level and alignment, pressure tests for leaks in the assembly and valves, variation of the sampling rate, variation of sampling time, increasing the number of pressure taps, and recalibration of the transducers, all with no improvement in the repeatability. The following section examines time-varying pressure measurements with the goal of identifying reasons for the lack of repeatability.

8.4 Time-varying pressure signals

The subject of time-varying pressure measurement and a measuring system's dynamic response is a complicated subject. Holman [89, ch. 6] explains that the measuring instrument, pressure transmitting fluid, and tubing connections all play important roles in the pressure measurements. The manufacturer of the pressure transducer states that they inherently damp the input pressure with a 0.2 s time constant. Significant lengths of water-filled tubing transmitted the pressure from the pressure taps to the pressure transducers and also imparted further damping. This is of no concern when acquiring time-averaged data, as presented earlier, but must be mentioned when examining time-varying signals. The time-varying measurements presented in the next section are damped wall pressure fluctuations and should not be compared directly to previous studies measuring the exact wall pressure fluctuations. Instead, the following sections identify differences between the acquired time-varying signals in experiments from previous chapters with wavy or annular flow in the combined side, and experiments with slug flow in the combined side. This comparison gives insight into why repeatability was not observed in experiments with slug flow in the combined side and also suggests

Time-varying pressure signals with wavy and annular flow in the outlet

For later comparison with experiments that involve slugging, time-varying pressure measurements were first acquired with annular flow ($W_{\mathrm{C}} = 0.105\,\mathrm{kg\,s^{-1}}$, $x_{\mathrm{C}} = 0.53$, $\lambda_{\mathrm{G}} = 0.50$, and $\lambda_{\mathrm{L}} = 0.50$) and then wavy flow ($W_{\mathrm{C}} = 0.500\,\mathrm{kg\,s^{-1}}$, $x_{\mathrm{C}} = 0.50$, $\lambda_{\mathrm{G}} = 0.50$, and $\lambda_{\mathrm{L}} = 0.49$) in the combined side. The experiment with annular flow in the combined side measured the pressure difference between taps B1 and C1 using transducer 2, while the experiment with wavy flow in the combined side measured the pressure difference between taps M1 and C1 using transducer 1. Both experiments used a sampling frequency of 1 000 Hz for a 30 min period. In order to reduce noise in the series of n time-varying pressure measurements, a new series of average values using subsets of $k < n$ samples was used:

$$\mathrm{SMA}_k(P) = \frac{1}{k}\left(P_i + \sum_{j=1}^{(k-1)/2} \left(P_{i-j} + P_{i+j}\right)\right), \qquad \text{for } (k-1)/2 < i < n-(k-1)/2. \tag{8.1}$$

This set of average values is called the simple moving average (SMA). Figure 8.8 shows samples of 30 s of $\mathrm{SMA}_{51}(\Delta P)$ for the experiments with annular and wavy flow in the combined side. The pressure traces look quite similar but the ranges of measurement differ by an order of magnitude.

Further insight into the characteristics of the signals was obtained from probability density functions (PDF), constructed as described in Appendix G with 100 bins. Figure 8.9 shows the PDFs for each of the experiments' time-varying pressure measurements along with a Gaussian distribution fit to the data using a nonlinear least-squares Marquardt-Levenberg algorithm. The Gaussian curves fit the data nearly perfectly and highlight the measurements' symmetry. The vertical dotted line marks the arithmetic mean (AM) of the measured data in each histogram and coincides with the Gaussian distributions' mean values. By examining the x-axis, the PDFs clearly show the range of pressure measurements $(\mathrm{MAX}(\Delta P) - \mathrm{MIN}(\Delta P))$ as within 700 Pa and 100 Pa for the experiments with annular flow and wavy flow in the combined side, respectively.

Time-varying pressure signals with slug flow in the outlet

Using the reference line, a single experiment was conducted with wavy flow in both inlets and slug flow in the combined side. The flow conditions were $W_\mathrm{C} = 0.225\,\mathrm{kg\,s^{-1}}$, $x_\mathrm{C} = 0.08$, and $\lambda_\mathrm{G} = \lambda_\mathrm{L} = 0.5$. Figure 8.10 shows both the inlet and outlet conditions on Mandhane et al.'s [34] flow-regime map. Pressures were measured at 1 000 Hz for 10 min using transducers 3 and 7. Observation showed slugs were only present in the combined side; large amplitude waves passed through both inlets' but never slugs. For reasons discussed later, the pressure signals were measured by connecting

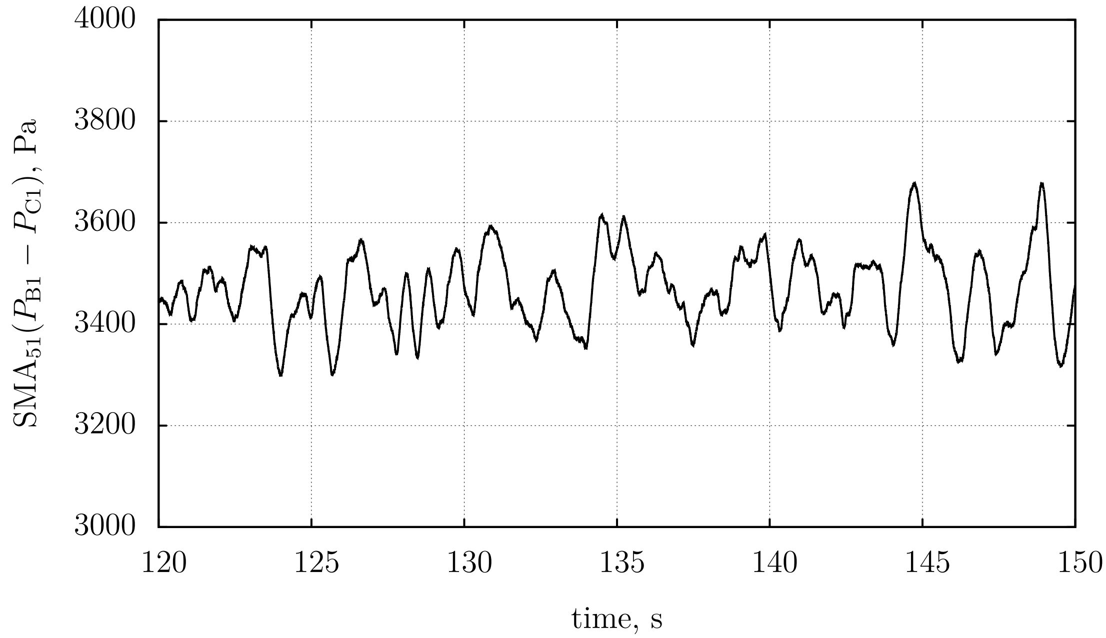

(a) Annular flow in the combined side

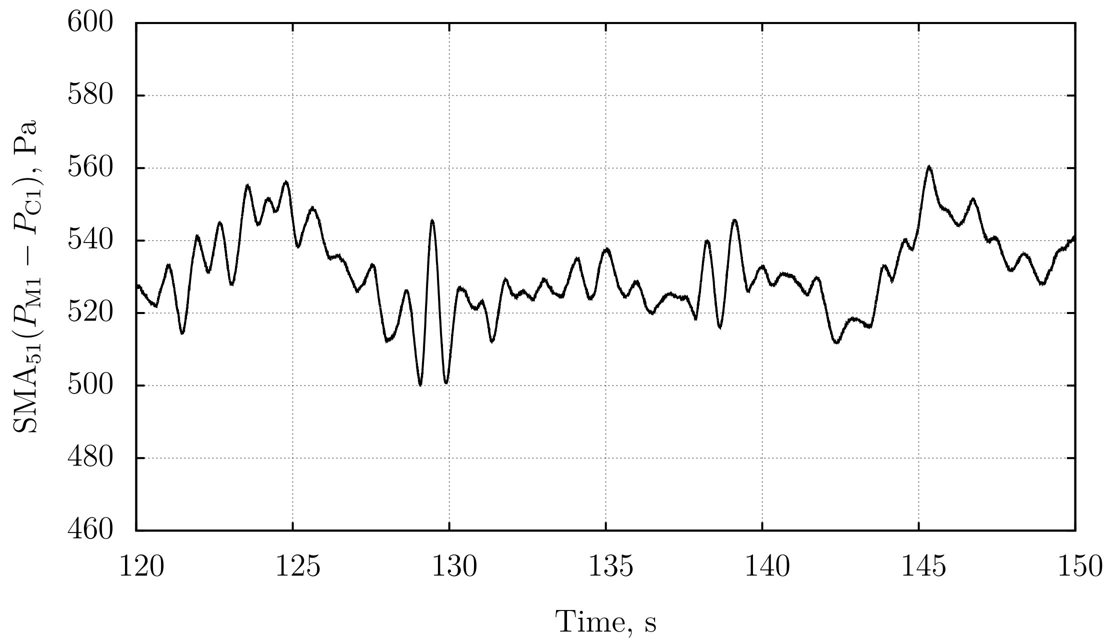

(b) Wavy flow in the combined side

Figure 8.8 Typical time-varying pressure signals for experiments with annular and wavy flow in the combined side (measured without the reference line).

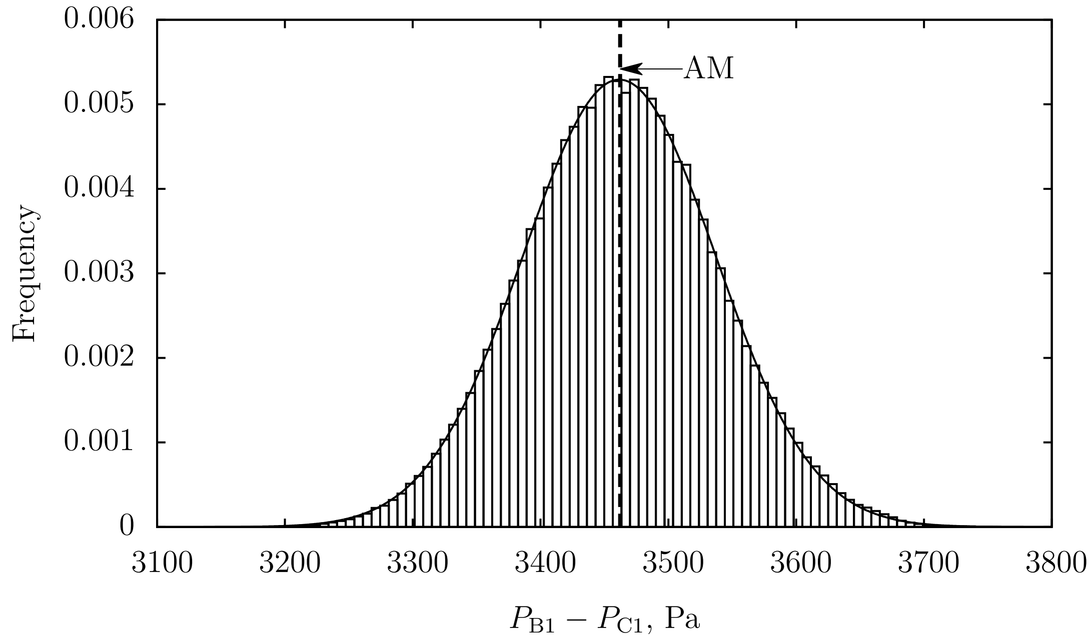

(a) Annular flow in the combined side

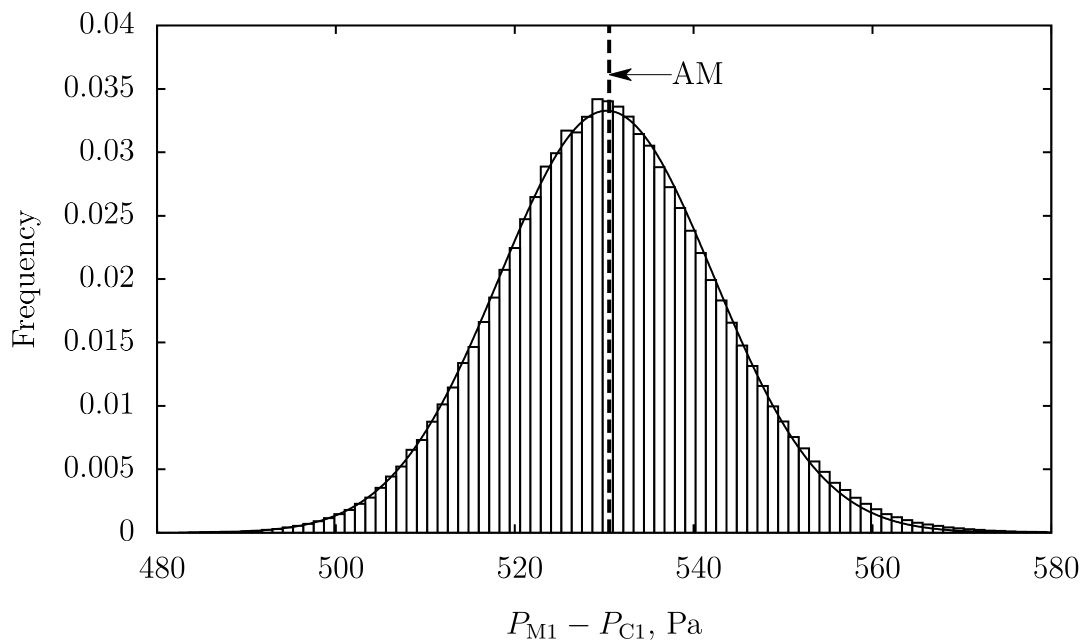

(b) Wavy flow in the combined side

Figure 8.9 Typical histograms of time-varying pressure measurements for experiments with annular and wavy flow in the combined side.

the pressure taps directly to the transducers using equal lengths of tubing. The discussion that follows shows representative measurements for simultaneous pressure measurements using taps B1 and C1. Measurements from pressure taps M1 and C1 were similar and are not presented here.

Figure 8.11 shows a sample of the pressure signal for simultaneous pressure measurements of taps B1 and C1 relative to the (constant) reference line pressure and the difference between the pressure measurements at the two taps for the same time period. Examination of $\mathrm{SMA}_{51}(P_{\mathrm{C1}} - P_{\text{reference line}})$, the black dashed line in Fig. 8.11, shows sharp peaks and valleys with a range of pressure measurements of over 10 000 Pa, which is largely expected for slug flow conditions. More interestingly, however, is $\mathrm{SMA}_{51}(P_{\mathrm{B1}} - P_{\text{reference line}})$, shown by the solid black line in Fig. 8.11, which largely has the same shape as the combined side's pressure measurements, even though the

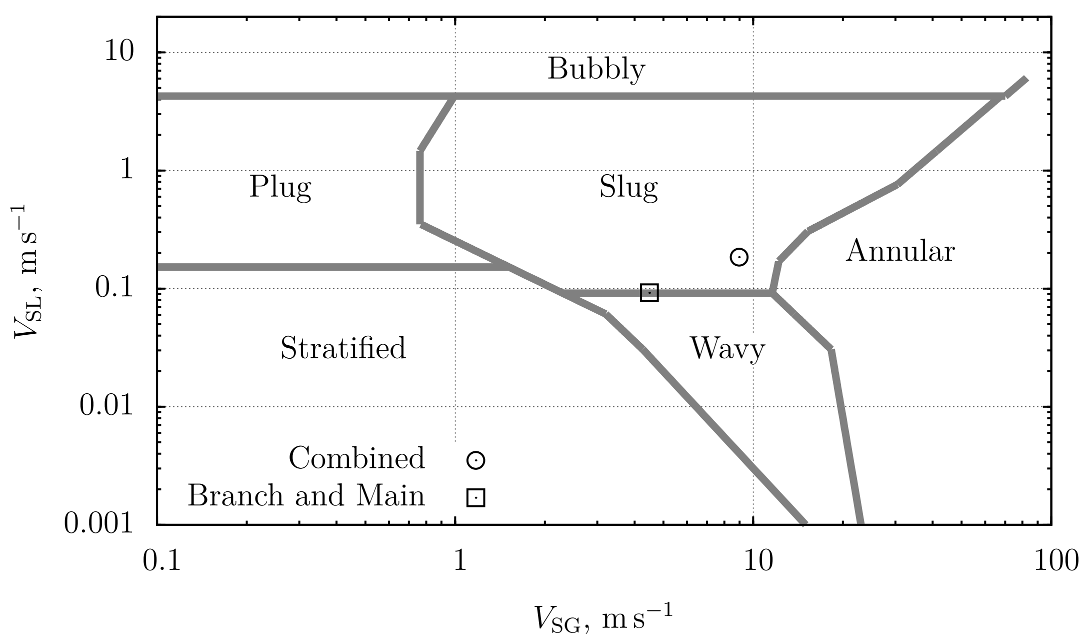

Figure 8.10 Flow conditions on Mandhane et al.'s [34] flow-regime map.

inlet's flow-regime is wavy. As a slug forms in the combined side it momentarily blocks the high-speed gas and pressure builds up everywhere upstream as the liquid slug accelerates. The pressure surge remains until the slug exits the test section. This was observed by Hubbard and Dukler [78] and applied to detect slugs in pipelines by Lin and Hanratty [74]. What effect, if any, the pressure variation caused by slugging in the combined side has on the wavy inlets' fully-developed dP/dz values is unknown. Careful examination shows that the branch signal leads the combined signal by a fraction of a second when the pressure increases, but generally lags the combined signal by a fraction of a second when the pressure drops, for example from (120–121) s in Fig. 8.11. This is consistent with slug events as slugs form upstream of pressure tap C1 and it does not have a pressure surge until the slug has passed, but the same slug forms downstream of pressure tap B1 and it experiences the pressure surge almost immediately. When the slugs discharge into the separation tank, the reverse order is true. This same phenomenon is also responsible for pressure tap B1's pressure consistently reaching higher levels than pressure tap C1. If the length of the pipe before the discharge were much longer and only single slug were in the system, both pressure signals would eventually reach similar levels and plateau, as explained in Section 2.4 and illustrated on Fig. 2.3 (page 27). A final observation can be made for times with large ΔP values where the pressure signals at tap B1 behave quite differently than tap C1, such as between 128.5 s and 129.5 s in Fig. 8.11. For such an event, it is conceivable that just as a slug is discharged into the separation tank a new slug developed upstream of tap C1. In this case, the pressure dropped at tap C1 once the first slug discharged and continued to drop until the next slug passed, while the pressure remained higher at tap B1. Other slug formation and discharge sequences could cause large deviation between the two signals.

Compared to the individual pressure taps' measurements relative to the reference line, the differential pressure $\text{SMA}_{51}(P_{\text{B1}} - P_{\text{C1}})$, shown by the red line in Fig. 8.11, and shows less extreme variation with a range of pressure measurements of approximately 5 000 Pa. However, compared to Figs. 8.8a and 8.8b with annular and wavy flow in the combined side, respectively, the variation is still very large. The large pressure deviations are a result of the time lag between slug events at the different pressure taps.

Further analysis of the time-varying signals was made by plotting PDFs using 100 bins. Figure 8.12 shows the PDFs of the measured pressures relative to the reference line as well as the difference between the two simultaneously acquired pressure signals for taps B1 and C1, corresponding to the signals shown in Fig. 8.11. Note that many measurements have very low frequency so that they are not discernible, but the range of the x-axis of each graph extends to near where the pressure measurement occurs. Each of the PDFs is skewed to the right, particularly for $P - P_{\text{reference line}}$, with asymmetric distributions unlike those for experiments without slugs shown in Figs. 8.9a and 8.9b. Based on the evidence of previous studies of time-varying static pressure fluctuations during slug flow (see Section 2.4, page 24), each skewed distribution was fit by superimposing two Gaussian distributions (shown by dashed red lines), one for each of two different pressure 'modes'. Each mode corresponds to a particular pressure state in the system as illustrated in Fig. 2.3: the lower Gaussian distribution represents measurements made when no slugs were present, the upper Gaussian distribution represents measurements made when a single slug was present between the pressure tap and the test-section's discharge. On both Figs. 8.12a and 8.12b at $P - P_{\text{reference line}} \approx 18000\,\text{Pa}$, a small peak can be seen that may indicate another pressure mode, possibly corresponding to two slugs being present between the pressure

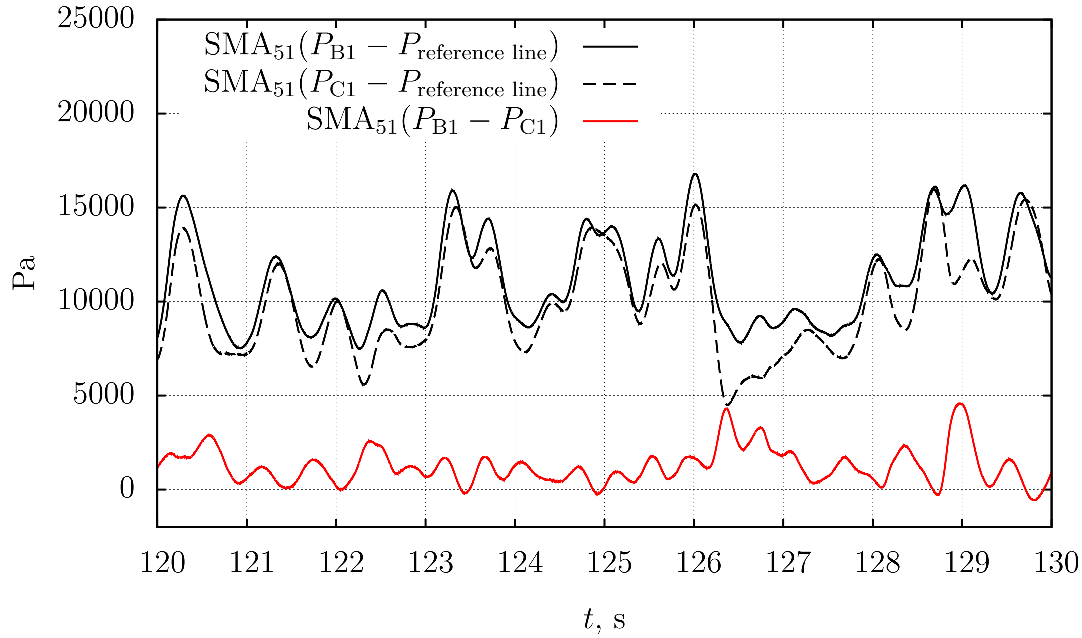

Figure 8.11 SMA of simultaneous pressure measurements between taps B1 and C1. Taps were connected directly to the transducers.

tap and the test-section's discharge at the time of measurement. Of course, even more pressure modes could be possible and so, rather than risk over-fitting the data, the fit was restricted to two superimposed Gaussian curves which overall represent the data quite well.

The PDF for ($P_{\mathrm{B1}} - P_{\mathrm{C1}}$), Fig. 8.12c, shows that differencing the measurements drastically reduces the range of pressure measurements from approximately 20 000 Pa in Figs. 8.12a and 8.12b to approximately 10 000 Pa in Fig. 8.12c. The shape of the distribution also appears more dependant on a single Gaussian curve than either Figs. 8.12a and 8.12b, but the result still clearly differs from the differential measurements taken without slugs in the system shown in Fig. 8.9. The presence of the tail is the result of the time lag between different pressure taps experiencing slug events,

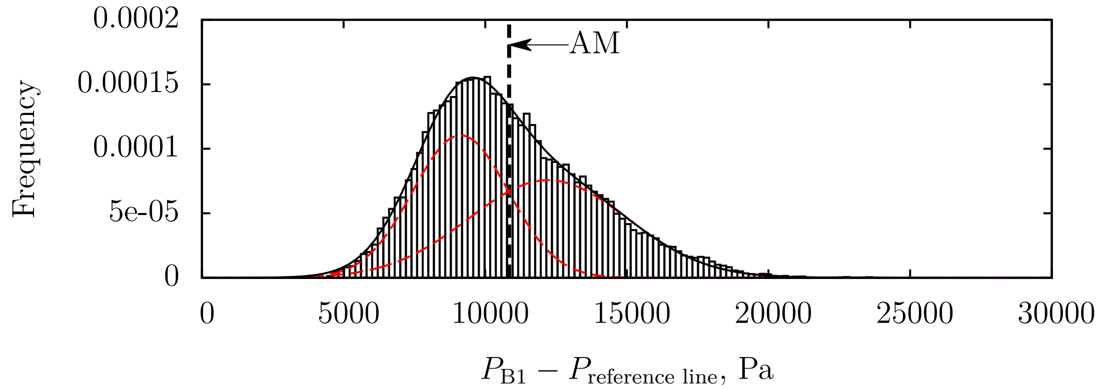

(a) Tap B1 relative to the reference line

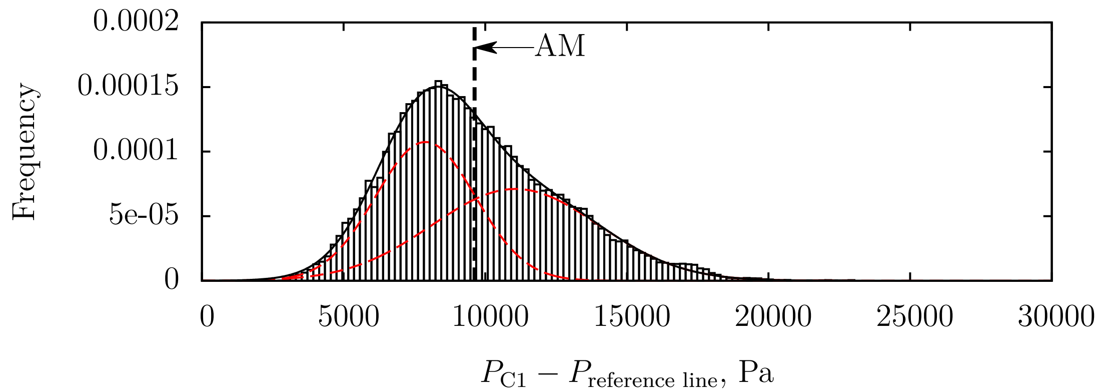

(b) Tap C1 relative to the reference line

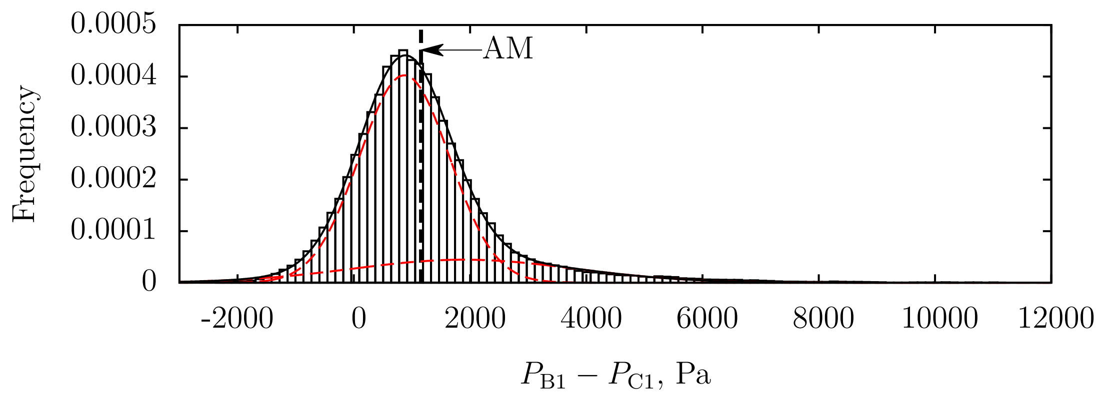

(c) Difference between taps B1 and C1

Figure 8.12 Histograms of the simultaneous pressure measurements at taps B1 and C1. Both pressure taps were connected directly to the transducers.

shown previously in the time-varying pressure measurements.

Several past studies using vertical pipes have shown results for differential pressure measurements in slug flow with pressure taps separated by varying distances [39, 65, 70]. Based on time-varying pressure measurements at four location separated by 0.1 m, 1.0 m, and 2.5 m in a 22 mm pipe with air-water mixtures, Akagawa et al. [70] stated that while mean values result in the same gradient, time-varying pressure drop signals are influenced by the separation between measuring locations. Their time-varying pressure measurements were accompanied by time-varying void fraction measurements that allowed an accurate description of pressure measurements based on slug location. Both slug length and the slug's position in the tube influenced their pressure signals; only small fluctuations in the differential pressure were measured if both taps were upstream of the same number of slug events, which was common with a short tap separation but uncommon at longer separation.

With these ideas in mind, several time-varying pressure measurements were made between consecutive taps in the current facility to compare with the pressure measurements between taps B1 and C1 already presented. Figure 8.13 shows samples of the pressure measurement signals for consecutive taps C2 and C1, and taps B1 and B2. While the time lag between measurements for each pair of consecutive pressure taps is small, as shown by the nearly identical paths of the solid black and dashed lines in Fig. 8.13, the time lag between pressure taps B1 and B2 is noticeably smaller with the two signals falling almost identically on top of one another. This is consistent with the time lag between taps B1 and B2 being caused by pressure surges through the wavy inlets as a result of slugs blocking the pipe downstream, and the time lag between taps C2 and C1 being caused by slugs moving (much more slowly than the upstream pressure surge) from one tap to the other. As a result, the differential pressure fluctuations between taps C2 and C1, shown by the red line in Fig. 8.13a, are significantly larger than the differential pressure fluctuations between taps B1 and B2, shown by the red line in Fig. 8.13b. However, the overall range of differential pressure measurements for consecutive taps in Fig. 8.13 is much smaller than that for taps separated by a longer distance, as shown in Fig. 8.11.

Figures 8.14 and 8.15 show the PDFs for simultaneous pressure measurements between consecutive taps C2 and C1, and taps B1 and B2, respectively. Figures 8.14a, 8.14b, 8.15a, and 8.15b shows PDFs for pressure measurements relative to the reference line, and these are similar in shape to distributions shown previously in Figs. 8.12a and 8.12b. However, the distributions of the differential pressure measurements between taps C2 and C1, shown in Fig. 8.14c, and between taps B1 and B2, shown in Fig. 8.15c, are both symmetric and fit well by a single Gaussian curve similar to those from experiments without slugs shown in Fig. 8.9. The range of differential pressure measurements between taps C2 and C1 is within 3 000 Pa, and between taps B1 and B2 is within 2 000 Pa, both only a fraction of the range of differential pressure measurements between taps B1 and C1 shown earlier as approximately 10 000 Pa. The slightly larger time lag between taps C1 and C2 than taps B1 and B2 seems to have only increased the range of pressure measurements, and not affected the shape of the PDFs distribution. Note that without the system's damping, larger pressure differences would occur since the pressure signals gradients would be larger.

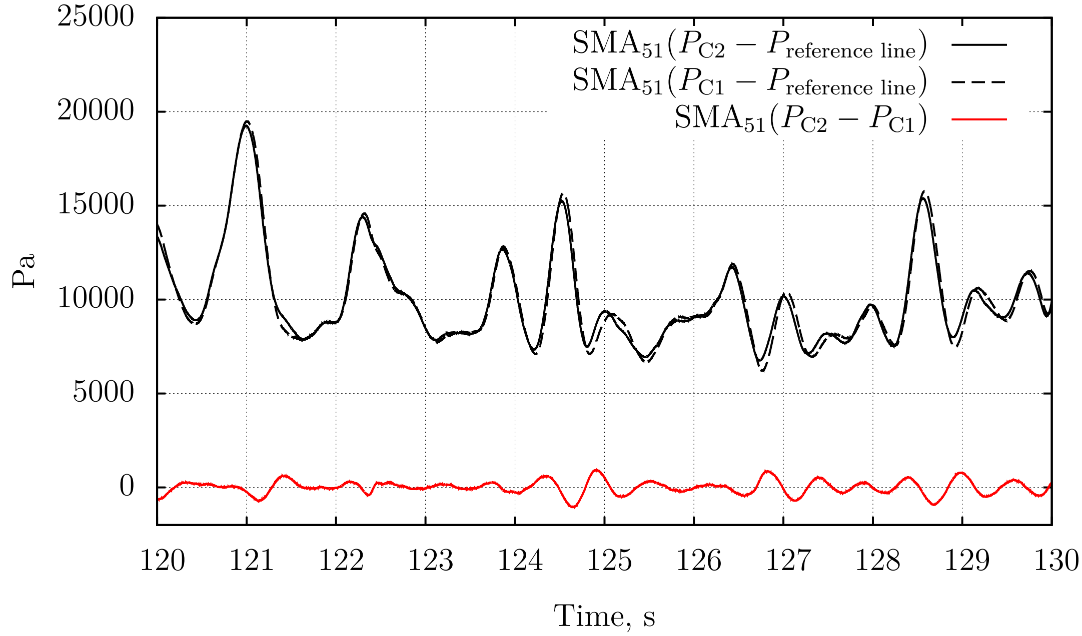

(a) Taps C2 and C1

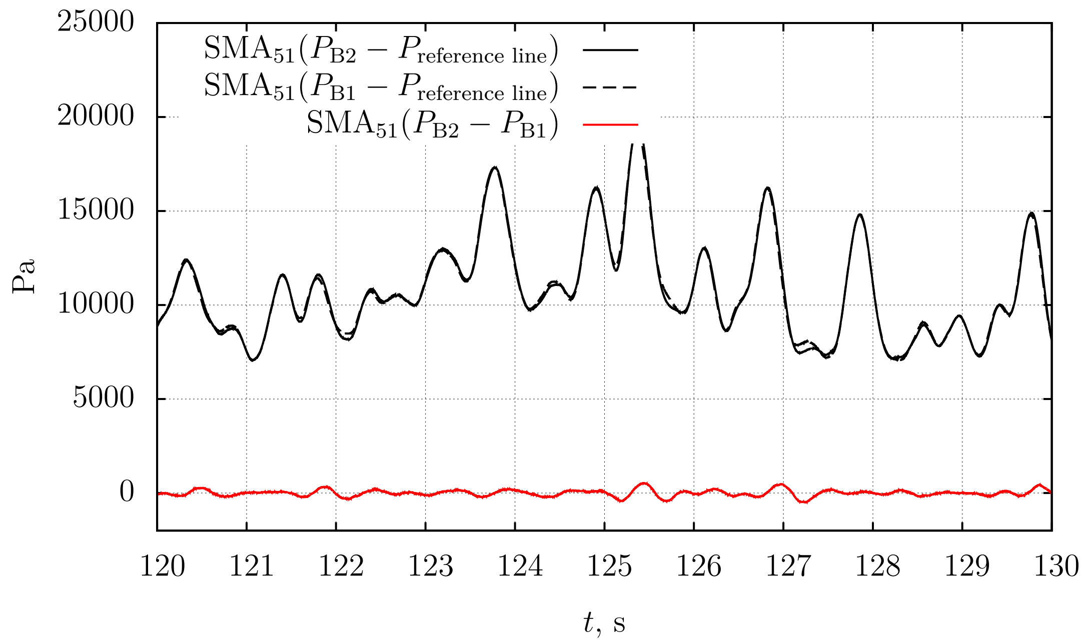

(b) Taps B2 and B1

Figure 8.13 SMAs of simultaneous measurements between taps C2 and C1, and taps B1 and B2. Taps were connected directly to the transducers.

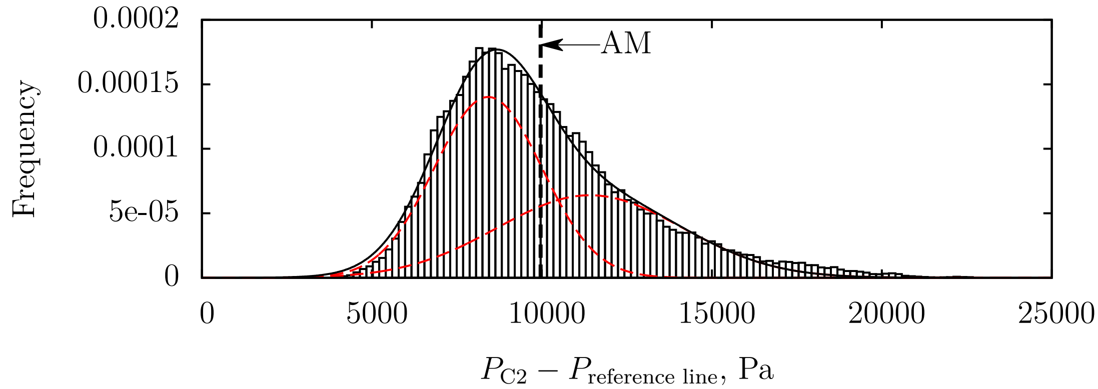

(a) Tap C2 relative to the reference line

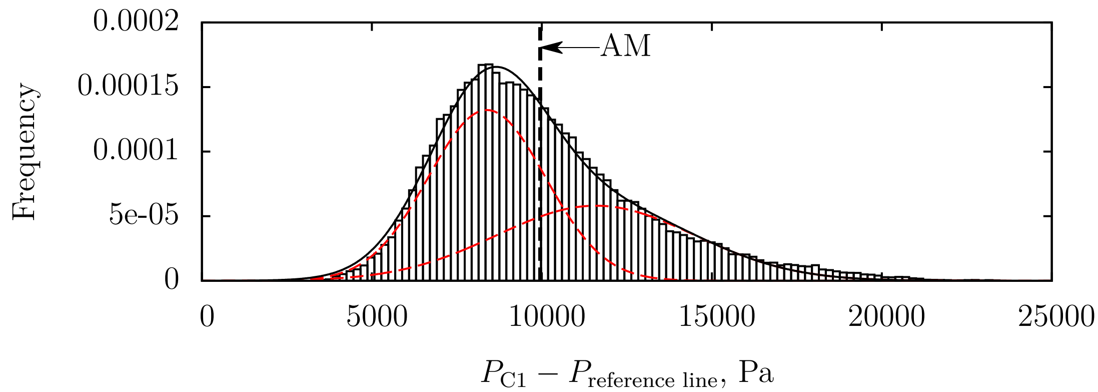

(b) Tap C1 relative to the reference line

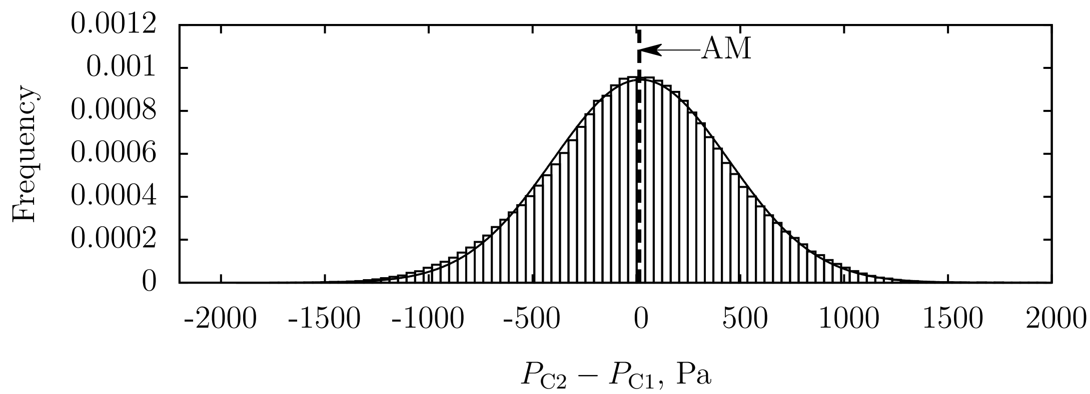

(c) Difference between taps C2 and C1

Figure 8.14 Histograms of the simultaneous pressure measurements at taps C2 and C1. Both pressure taps were connected directly to the transducers.

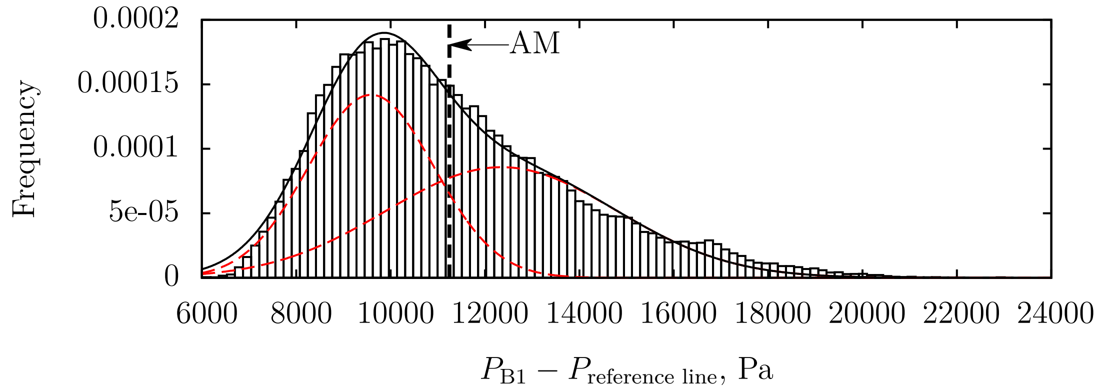

(a) Tap B1 relative to the reference line

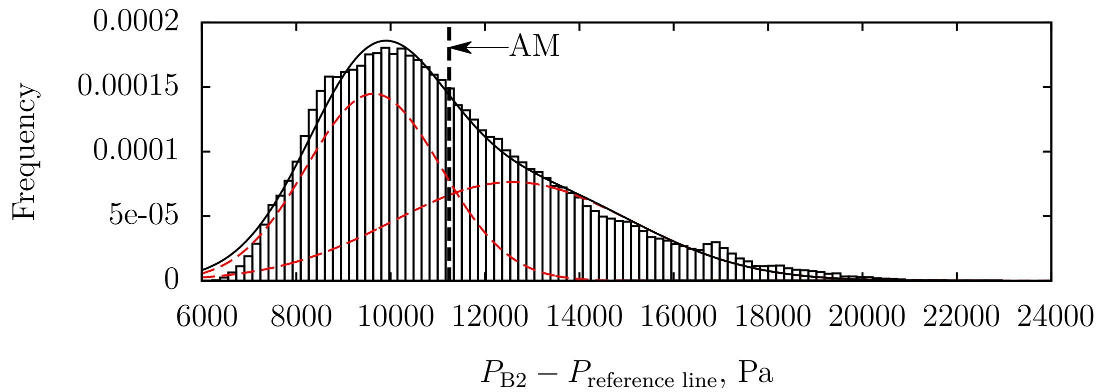

(b) Tap B2 relative to the reference line

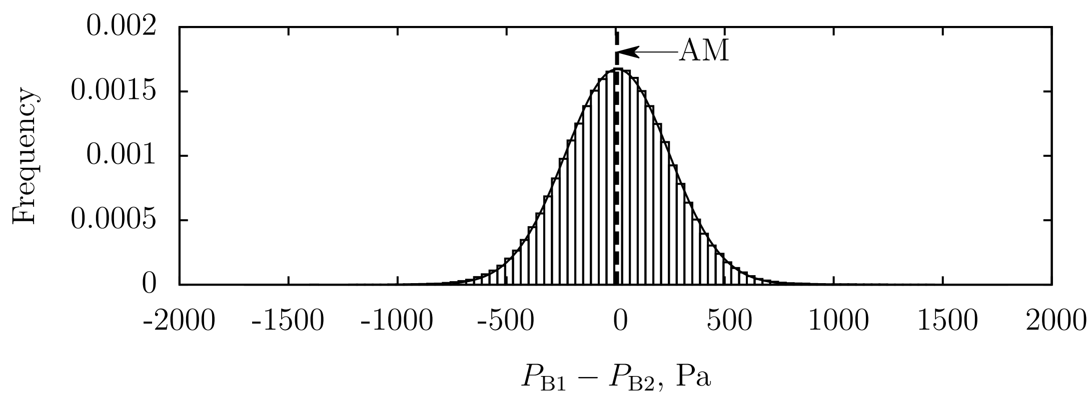

(c) Difference between taps B1 and B2

Figure 8.15 Histograms of the simultaneous pressure measurements at taps B2 and B1. Both pressure taps were connected directly to the transducers.

8.5 Recommendations for future investigation of slug flow

Obtaining repeatable time-averaged pressure signals (for which the current facility was designed) may not be possible if slugs are present in the test section. Before reaching a final conclusion, however, future investigation of pressure drop with slug flow in any of the sides of the tee should:

1. Modify the valve manifolds to allow measurements between any two pressure taps simultaneously, regardless of which leg of the tee they are in. Further, intentionally design the new manifolds and pressure leads with ease of purging in mind; both minimizing areas where air could be trapped and adding hinged mounting brackets to pressure transducers so that they may be easily rotated for purging and returned to their measuring orientation after. A large effort was required to purge bubbles in the current design and these changes would greatly improve the rig's operation.

2. Replace the Tygon tubing with stiff nylon tubing, as well as use equal lengths between all taps. The elasticity of the tubing adds an unwanted dynamic as it flexes under the high pressure changes in slug flow. Further, if unequal lengths of tubing are used the damping and time response of pressure measurements becomes unequal. To illustrate, Fig. 8.16 shows 10 s of pressure signals for the simultaneous measurements of tap C1, connected directly to transducer 3, and tap C2, connected through the valve manifold to transducer 7. Compared to the previously presented result where both pressure taps were connected directly to the transducers, Fig. 8.13a, there is substantial time lag that results from the unequal length of tubing used. Further, careful inspection shows that the signal from tap C2 lags tap C1 which is not physically possible: tap C2 is upstream of

tap C1 and therefore tap C2's pressure signal *must lead* tap C1's. For this reason, all of the results presented in the previous section bypassed the valve manifolds and used equal tubing lengths to connect pressure taps to the transducers.

3. Add transducers that can measure negative differentials. Figures 8.12, 8.14, and 8.15 all showed smaller ranges of pressures occurred in differential measurement between two pressure taps than against the reference line, so that smaller ranged transducers could be used for measurement than the current instrumentation allowed.

4. Try different measuring procedures and compare their results:

   a) Measuring B1-B2, B2-B3, B4-B5 and so on.

   b) Measuring i1-i2, i1-i3, i1-i4 and so on with i = B, M, C.

   c) The same procedure described in Appendix C.3.

5. Record time-varying signal data for every measurement rather than averages.

While the investigation reported herein provides some direction for further study, the ideas remain largely untested and do not by any means guarantee repeatable time-averaged pressure distributions, or pressure distributions without scatter. Particularly with regards to the measurement procedure caution is advised. The PDFs for pressure measurements in consecutive pressure taps with slug flow in the combined side had similar features to the PDFs for pressure measurements with wavy and annular flow in the combined side, but it would be premature to conclude this method will lead to repeatable results. Even though the range of pressure measurements was smaller when consecutive taps were examined, so to was the overall differential pressure between

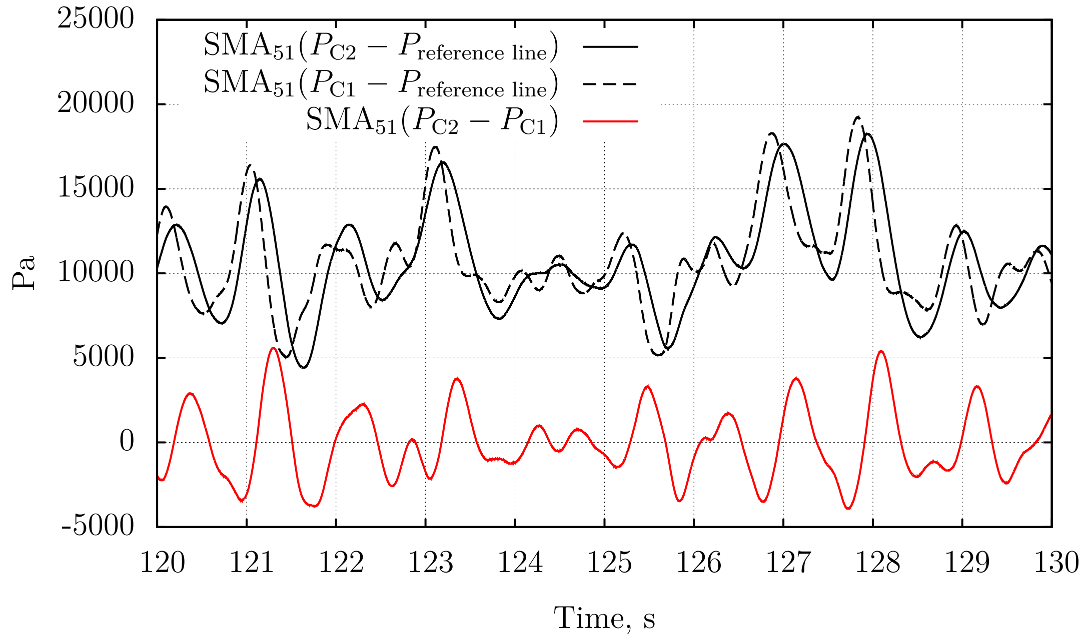

Figure 8.16 SMAs of the pressure signals at tap C2, connected to the transducer through the manifold, and tap C1, connected to the transducer directly.

the taps (in fact, it is very nearly zero in both Figs. 8.14c and 8.15c) and the same difficulties may persist regardless of the measuring technique.

8.6 Visual study

During the course of slug flow experiments, several sets of experiments were filmed with a high speed camera. The conditions for each of the experiments are listed in Table 8.4 and form four sets of experiments, labelled 1 through 4 in the table. The flow regimes indicated in Table 8.4 are those predicted by Mandhane et al.'s [34] flow-regime map (see Fig. 2.2, page 13) for the given flow conditions; visual observations will be discussed later. Each set consisted of a combining experiment, an experiment using only the main inlet, and an experiment using only the branch inlet, labelled 'C', 'M', and 'B', respectively, in Table 8.4. Experiments 1-C, 2-C, 3-C, and 4-C all had common flow conditions in the combined side and a common λ_{G}, while λ_{L} was varied independently. Experiment 1-M used the same flow conditions in the main inlet as experiments 1-C, but with no flow entering through the branch. Similarly, experiment 1-B used the same flow conditions in the branch inlet as experiment 1-C, but with no flow entering through the main. The same is true of experiments 2-M and 2-B with respect to experiment 2-C, and so on. Notable behaviours occurred particularly for experiment sets 1 and 4, so these conditions are focused on here.

Videos were taken at five different locations around the test section as shown on Fig. 8.17. The positions were chosen so that the flow direction was always left-to-right in the images. Labels were given to the various camera locations: position VS-B was of the branch visual section, VS-M was of the main visual section, VS-C was of the combined visual section, J-MC was of the tee junction in the same plane as the main and combined sides, and J-B was of the tee junction in the same plane as the branch. These labels will be used throughout the discussion.

The junction's presence significantly influenced the branch flow for experiment

Table 8.4 Experiment conditions for visual study with slug flow in the combined side. Flow regimes are those predicted by Mandhane et al.'s [34] flow-regime map (St=Stratified, W=Wavy, Sl=Slug).

Test	W_C kg s^{-1}	x_C	W_M kg s^{-1}	x_M	W_B kg s^{-1}	x_B	λ_G	λ_L	Flow regime M	B	C
1-C	0.225	0.08	0.181	0.09	0.043	0.04	0.10	0.20	Sl	St	Sl
1-M	0.181	0.09	0.181	0.09	—	—	0.00	0.00	Sl	—	Sl
1-B	0.043	0.04	—	—	0.043	0.04	1.00	1.00	—	St	St
2-C	0.227	0.08	0.142	0.11	0.085	0.02	0.10	0.40	Sl	St	Sl
2-M	0.142	0.11	0.142	0.11	—	—	0.00	0.00	Sl	—	Sl
2-B	0.085	0.02	—	—	0.085	0.02	1.00	1.00	—	St	St
3-C	0.225	0.08	0.099	0.17	0.127	0.01	0.10	0.60	W	St	Sl
3-M	0.099	0.17	0.099	0.17	—	—	0.00	0.00	W	—	W
3-B	0.127	0.01	—	—	0.127	0.01	1.00	1.00	—	St	St
4-C	0.227	0.08	0.057	0.28	0.170	0.01	0.10	0.80	W	St	Sl
4-M	0.057	0.28	0.057	0.28	—	—	0.00	0.00	W	—	W
4-B	0.170	0.01	—	—	0.170	0.01	1.00	1.00	—	St	St

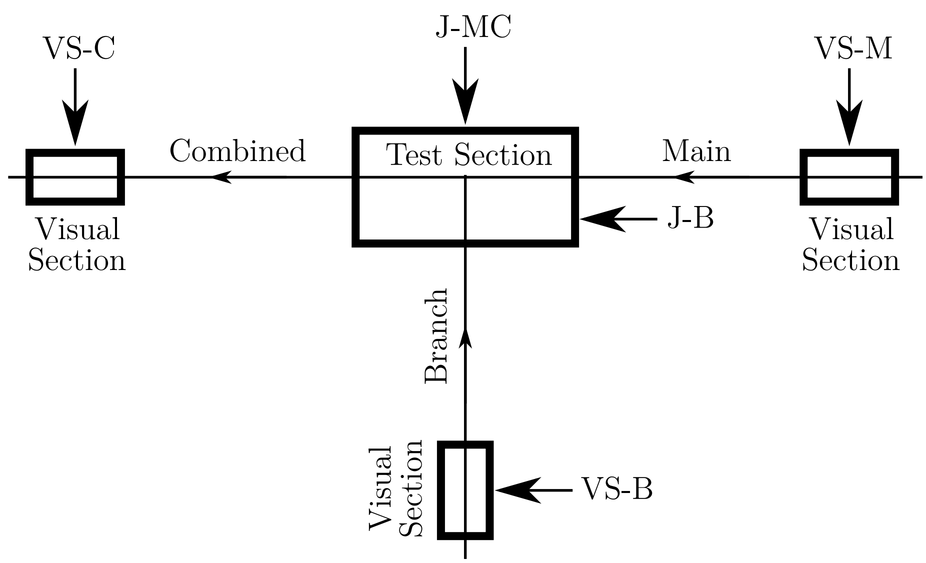

Figure 8.17 Camera positions around the test section.

set 1. For experiment 1-M, with flow only from the main inlet, slug flow was observed in VS-M, J-MC, and VS-C. Slugs remained coherent as they passed the junction, but each time a slug passed from the main into the combined side liquid would spill into the branch and waves propagated upstream. These waves generally dissipated before the branch visual section unless a particularly violent slug passed, in which case a small ripple could be seen. For experiment 1-B, with flow only from the branch inlet, the flow was stratified with a perfectly smooth interface in all sides of the tee and in all visual sections. For experiment 1-C, when the two flows were combined, the flow regimes viewed from VS-M and VS-B appeared exactly the same as when only their respective inlet was open. However, in J-B, upstream travelling waves could be seen as shown in Fig. 8.18, where the interface shows waves moving from right to left.

Experiment set 4 requires the most attention, as it had several unexpected behaviours. Experiment 4-M, with flow only from the main inlet, was as anticipated: wavy flow was observed in VS-M, J-MC, and VS-C. In J-B, there were observable ripples propagating upstream that dissipated before the branch's visual section, but these were small and of little note. On the other hand, experiment 4-B, with flow only from the branch inlet, had complex behaviour and requires consideration of observations from every viewing location.

VS-B The flow was stratified-wavy. Figure 8.19 shows a typical still frame of the interface.

J-B Slugs were present and the flow was visually very different from that observed in VS-B. Sometimes the slugs entered from upstream of the viewing location, while other times the slugs' formation could be observed in the acrylic. The series of images in Fig. 8.20 shows the formation of a slug very close to the

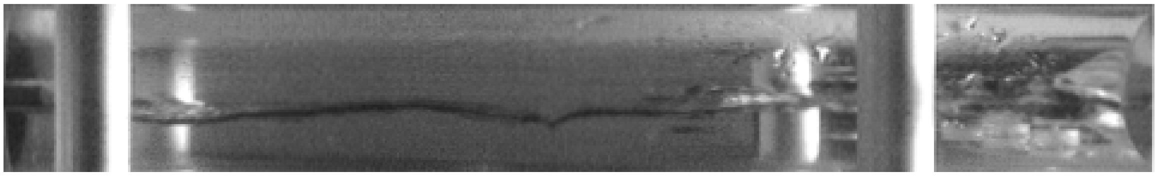

(a) Time 0

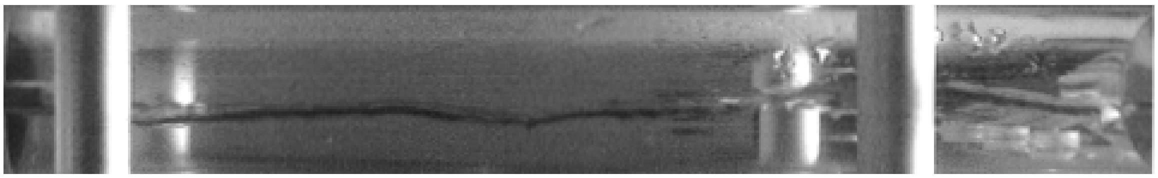

(b) Time 0.04 s

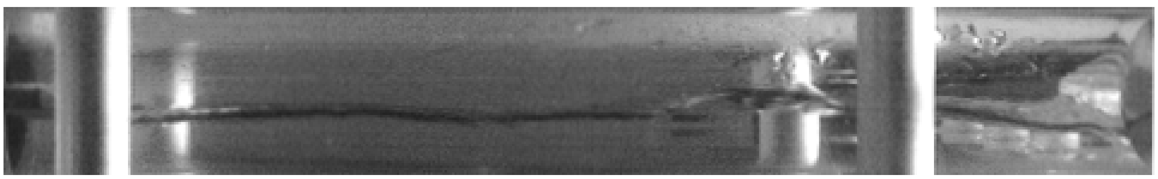

(c) Time 0.08 s

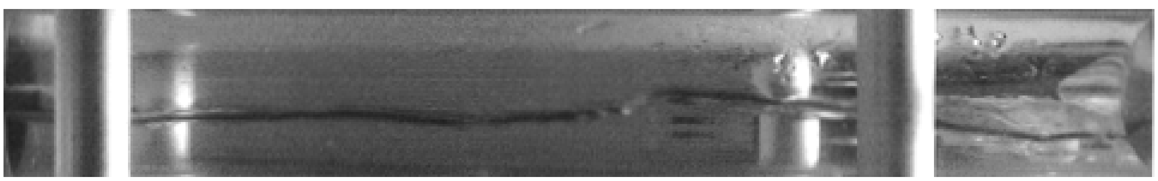

(d) Time 0.12 s

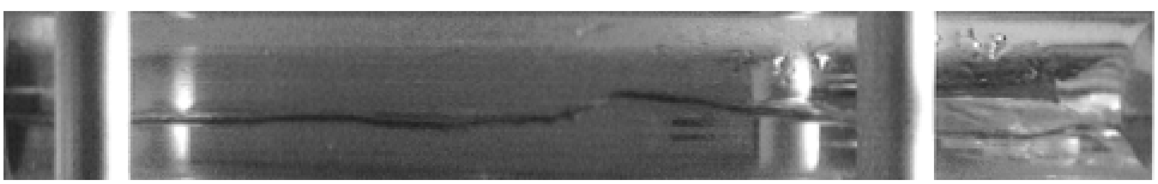

(e) Time 0.16 s

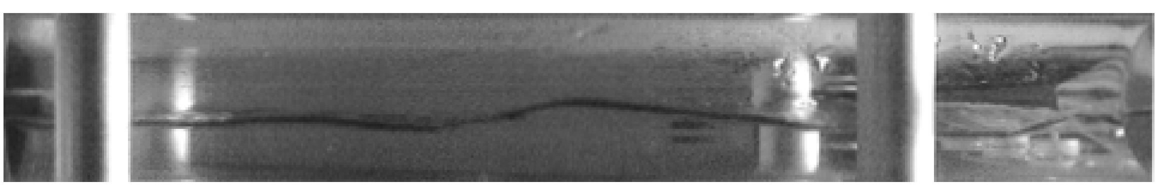

(f) Time 0.20 s

Figure 8.18 Upstream travelling waves in a stratified branch. Camera position J-B on Fig. 8.17. Experiment 1-C in Table 8.4: $W_\mathrm{C} = 0.225\,\mathrm{kg\,s^{-1}}$, $x_\mathrm{C} = 0.08$, $\lambda_\mathrm{G} = 0.10$, $\lambda_\mathrm{L} = 0.20$.

junction. Unfortunately, vertical posts used to secure the acrylic obscured some of the field of view where the slug began. In Fig. 8.20b the rightmost wave's crest contacts the top of the pipe, and in Figs. 8.20c to 8.20f the slug passes out of the branch.

J-MC Figure 8.21 shows the water level in the main side (with no flow) was much higher than the combined side. This was true for all times with the water level increasing to a maximum in the main side immediately after slugs passed the junction. When slugs entered from the branch and impacted on the back wall of the junction, water would move both upstream into the main side and also downstream in the combined side.

VS-M The interface was relatively flat, but the height of the water level oscillated up and down by approximately 1 cm.

VS-C Slugs were observed passing through the visual section, as shown in Fig. 8.22a, even though Mandhane et al.'s [34] flow-regime map predicted stratified flow. Between slugs the flow had a very flat interface as shown in Fig. 8.22b. The flow was visibly different from VS-B and J-B; generally the liquid level was lower and the air-water interface more flat.

As slugs were not anticipated at the given branch flow rate, a further experiment (not listed in Table 8.4) with the same flow rate as experiment 4-B was conducted, but using the main inlet instead of the branch in order to observe whether slugs still formed when the flow passed the junction. Once again, the behaviour of the flow passing the junction was complex and requires consideration of observations from every viewing location.

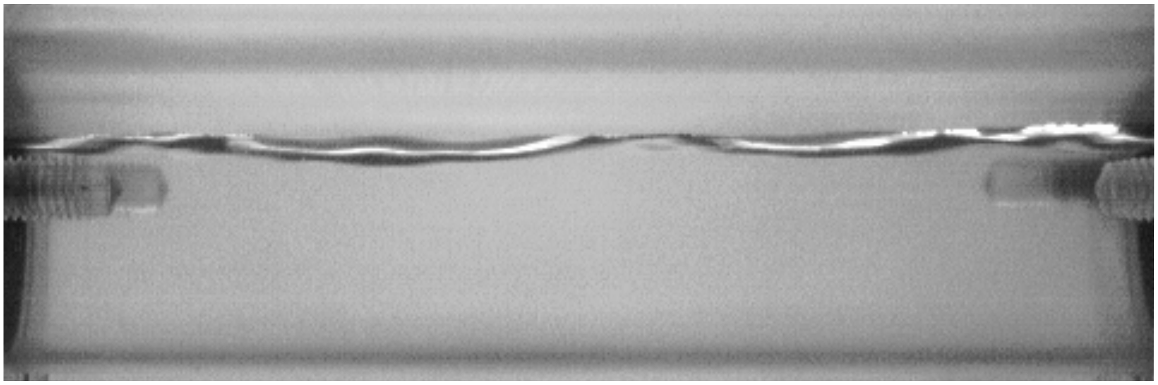

Figure 8.19 Sample of the flow seen from camera position VS-B on Fig. 8.17. Experiment 4-B in Table 8.4: $W_\mathrm{C} = 0.170\,\mathrm{kg\,s^{-1}}$, $x_\mathrm{C} = 0.01$, $\lambda_\mathrm{G} = 1.00$, $\lambda_\mathrm{L} = 1.00$.

VS-M The flow was identical to that observed in Fig. 8.19

J-MC Slugs were frequently observed entering from upstream of the viewing location, and occasionally forming in the acrylic. The slugs remained coherent as they passed the junction and left the viewing location. Figure 8.23 shows images of the events during (Figs. 8.23a and 8.23b) and after (Figs. 8.23c to 8.23h) a slug passed out of view. After the slug passes, Fig. 8.23c, the water level is very low as the slug pulls a lot of water, except immediately at the junction where the water swell as water spills into the pipe from the branch side. Over a period of several seconds, the water spilling from the branch pushes upstream into the main side.

J-B The air-water interface is wavy with large amounts of water spilling into the branch when slugs pass the junction as shown in Fig. 8.24.

VS-B The air-water interface is flat, but the water level varies (up and down) by approximately 0.5 cm.

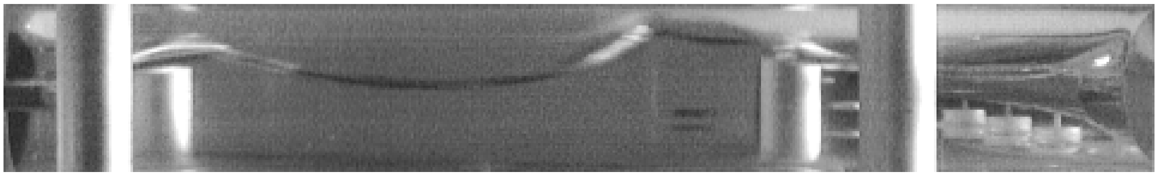

(a) Time 0

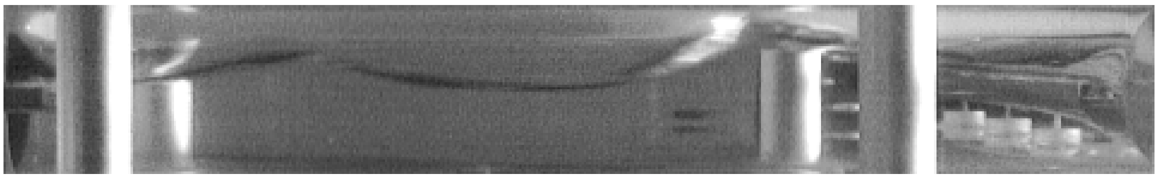

(b) Time 0.04 s

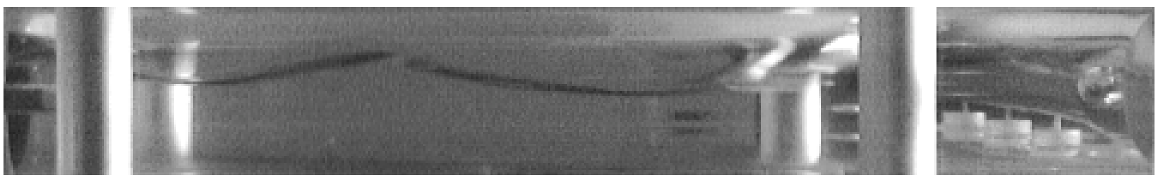

(c) Time 0.08 s

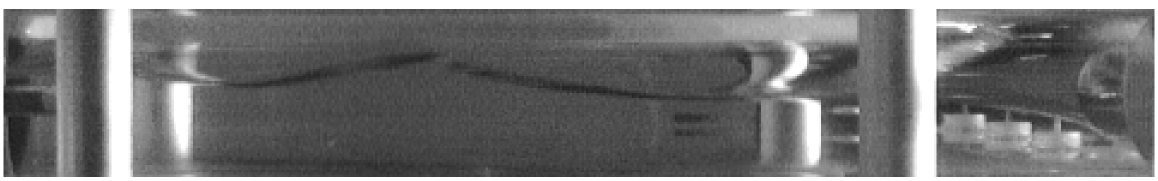

(d) Time 0.10 s

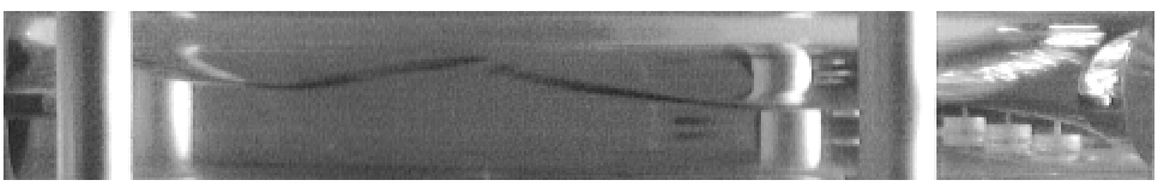

(e) Time 0.12 s

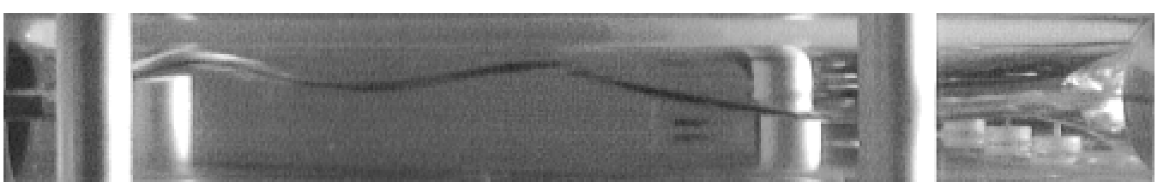

(f) Time 0.16 s

Figure 8.20 Formation of a slug near the tee junction at camera position J-B on Fig. 8.17. Experiment 4-B in Table 8.4: $W_\mathrm{C} = 0.170\,\mathrm{kg\,s^{-1}}$, $x_\mathrm{C} = 0.01$, $\lambda_\mathrm{G} = 1.00$, $\lambda_\mathrm{L} = 1.00$.

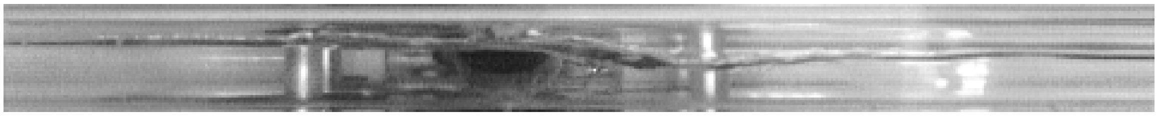

Figure 8.21 Sample of the flow seen from camera position J-MC on Fig. 8.17. Experiment 4-B in Table 8.4: $W_{\mathrm{C}} = 0.170\,\mathrm{kg\,s^{-1}}$, $x_{\mathrm{C}} = 0.01$, $\lambda_{\mathrm{G}} = 1.00$, $\lambda_{\mathrm{L}} = 1.00$.

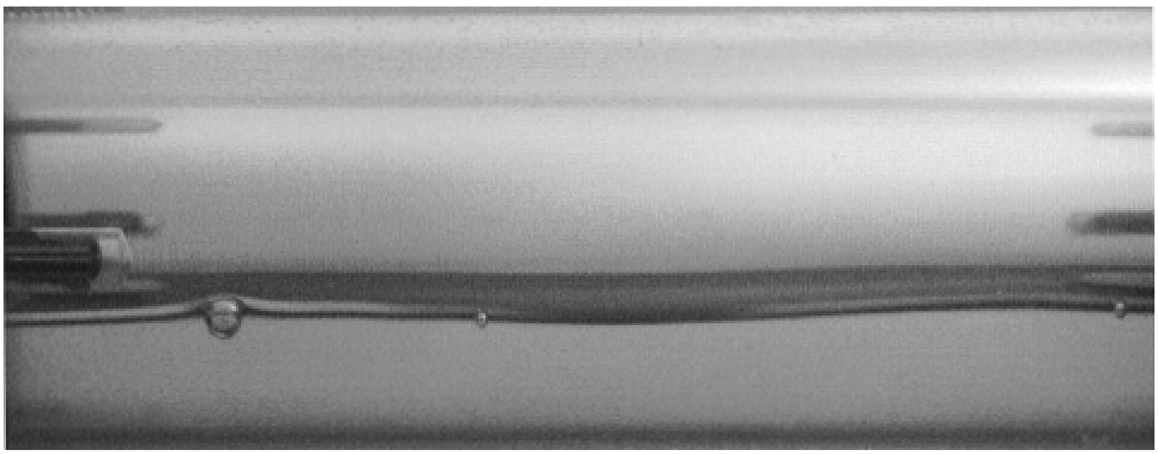

(a) Interface between slugs

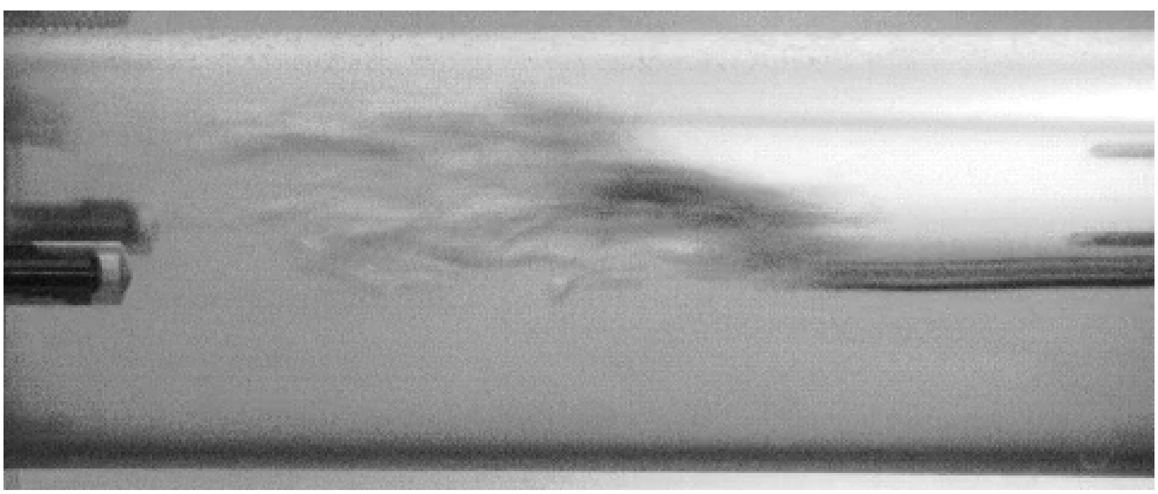

(b) The front of a slug passing through the visual section

Figure 8.22 Sample of the flow seen from camera position VS-C on Fig. 8.17. Experiment 4-B in Table 8.4: $W_{\mathrm{C}} = 0.170\,\mathrm{kg\,s^{-1}}$, $x_{\mathrm{C}} = 0.01$, $\lambda_{\mathrm{G}} = 1.00$, $\lambda_{\mathrm{L}} = 1.00$.

VS-C Slugs pass through the visual section and the flow was visibly different from both VS-M and also J-MC. Generally, between slugs, the liquid level was lower and the air-water interface more flat.

Finally, for experiment 4-C, the flow also had different behaviours. Again, each location's observations are discussed.

VS-M The flow was steady and wavy.

VS-B The flow varied between stratified and wavy as shown in Fig. 8.25. Stratified-smooth flow was much more common, and only for short periods would waves grow in the visual section, and then gradually fade. Occasionally a slug would form and pass through the visual section towards the junction, but infrequently (several minutes could pass between observed slugs).

J-B Slugs occurred more frequently than at VS-B, and between slugs the air-water interface was consistently wavy with large-amplitude rolling waves. Observed slugs always entered the viewing location from upstream. As slugs impacted the back wall of the junction, they sometimes 'stalled', as indicated in Figs. 8.26f to 8.26i and once more later for the same slug, as seen in Figs. 8.27e to 8.27g.

J-MC The high gas velocity and vigorous mixing made visual observation difficult from this viewing location. The flow appears highly aerated after the junction with an annulus around the entire pipe circumference. When slugs entered from the branch side they would accelerate rapidly and become highly aerated, but there was no visible effect on the flow in the main-side.

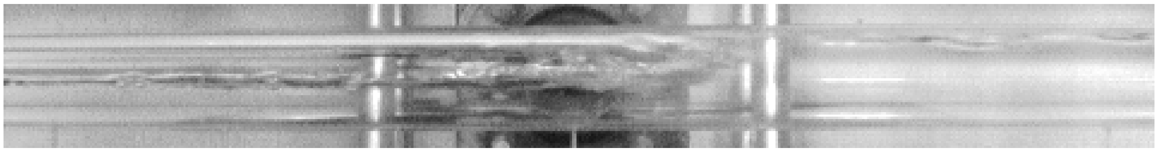

(a) Time 0

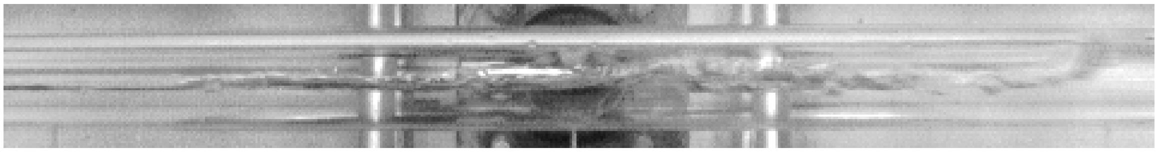

(b) Time 0.104 s

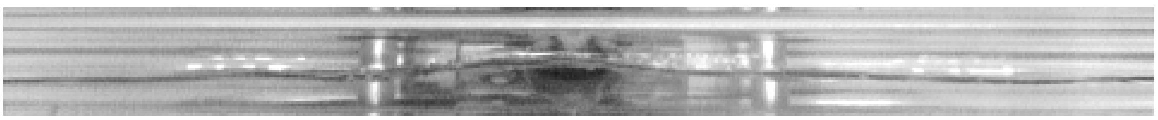

(c) Time 0.928 s

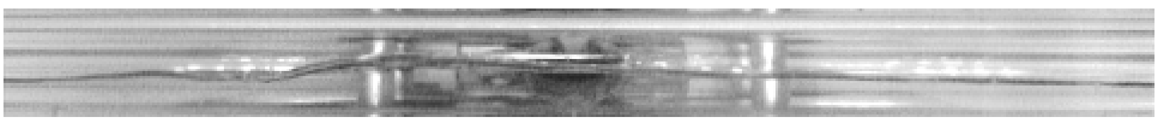

(d) Time 1.408 s

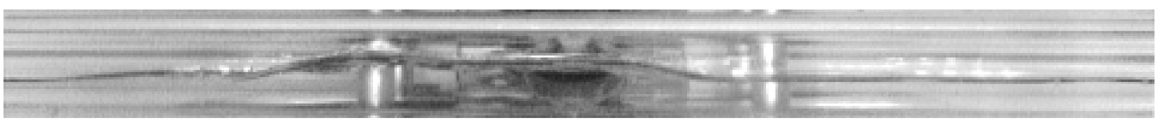

(e) Time 1.568 s

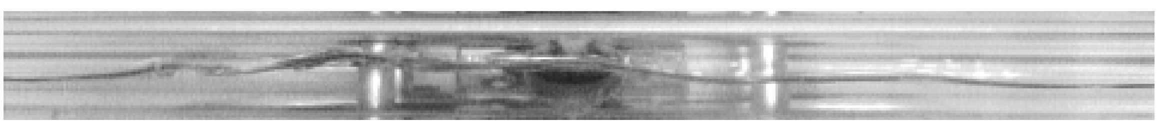

(f) Time 1.728 s

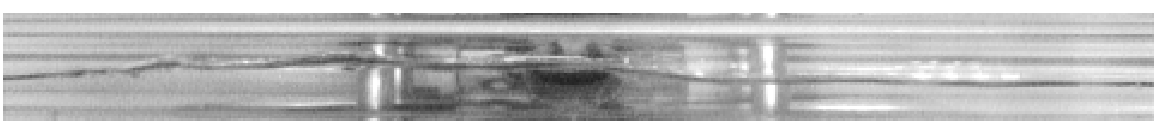

(g) Time 1.888 s

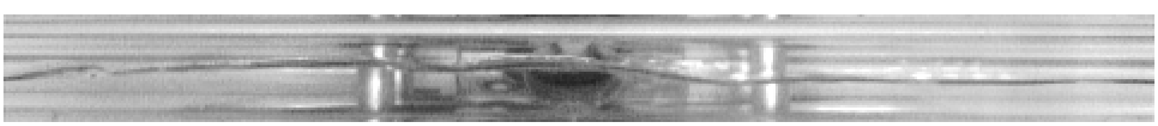

(h) Time 2.048 s

Figure 8.23 Water spilling into the junction from the branch after a slug passes at camera position J-MC on Fig. 8.17. $W_\mathrm{C} = 0.170\,\mathrm{kg\,s^{-1}}$, $x_\mathrm{C} = 0.01$, $\lambda_\mathrm{G} = 0.00$, $\lambda_\mathrm{L} = 0.00$.

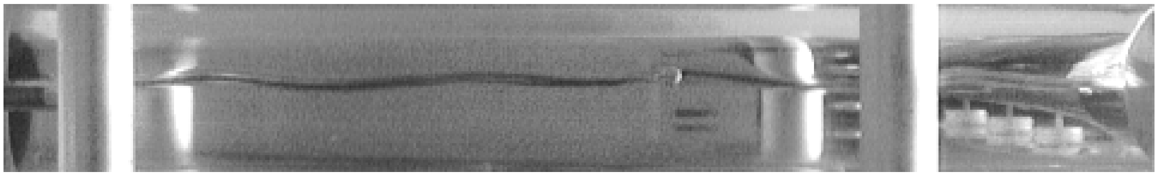

(a) Time 0

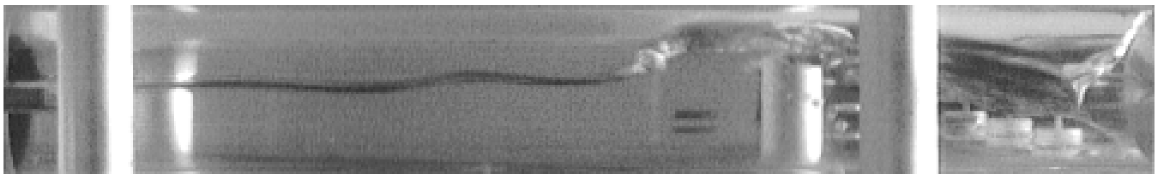

(b) Time 0.16 s

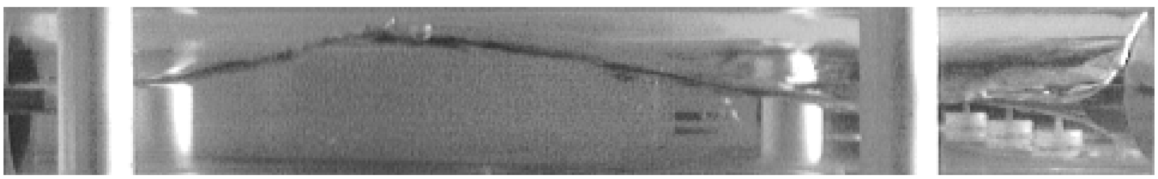

(c) Time 0.32 s

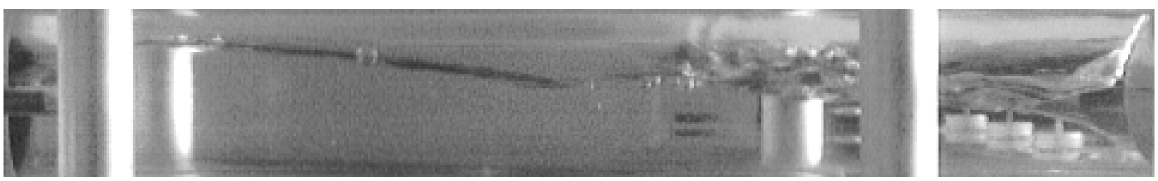

(d) Time 0.40 s

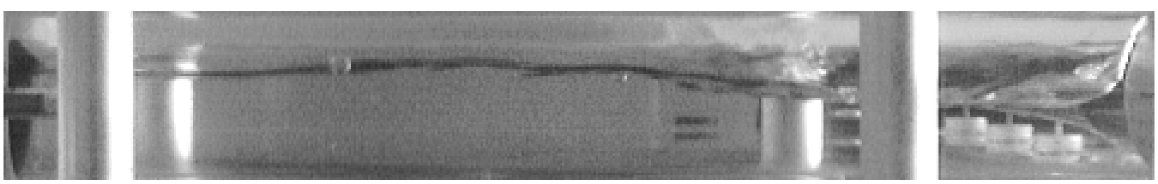

(e) Time 0.56 s

Figure 8.24 Water spilling into the branch after a slug passes. Camera position J-B on Fig. 8.17 ($W_C = 0.170\,\mathrm{kg\,s^{-1}}$, $x_C = 0.01$, $\lambda_G = 0.00$, $\lambda_L = 0.00$).

VS-C Slugs frequently passed (more slugs were observed here than entered from the branch), but they were highly aerated and had high velocity which made observing them difficult, even with the high-speed camera.

Study of mixing behaviour in a combining tee junction was done previously in [31, 32] and reviewed in Section 2.3. The current work confirms the presence of upstream travelling waves when slugging is present in one inlet and stratified flow present in the other. Belegratis et al. [31], Belegratis [32] also noted individual slugs being broken into chains of several shorter slugs, however, gamma densitometer and capacitance probe measurements of liquid hold-up in their work allowed accurate discrimination between consecutive slugs compared with visual observation where aeration and high velocities obscured identification in the present work. Even so, the observation of slugs entering from the branch and stalling periodically seems consistent with Belegratis observation. It must also be noted that Belegratis' work was at much lower gas flow rates than those observed in the current study (see Table 2.1, page 19), with the majority of tests also at considerably higher liquid flow rates than the present apparatus was capable of producing. The current study also found the junction's presence influenced flow from individual inlets and could induce slugging, observed visually as the developed flow viewed in the visual sections differed in several instances from the flow near the junction and in the combined side.

The above observations, which are unique to combining two-phase flow, may be a major reason for the difficulty in obtaining repeatable pressure-drop distributions with slug flows in the combined side. It is highly recommended for future investigators to pay particular attention to the high (and possibly unacceptable) uncertainty in measuring averaged values of the pressure gradients and the junction pressure drops, $\Delta P_{\text{M-C}}$ and $\Delta P_{\text{B-C}}$, when slugging occurs in the combined side.

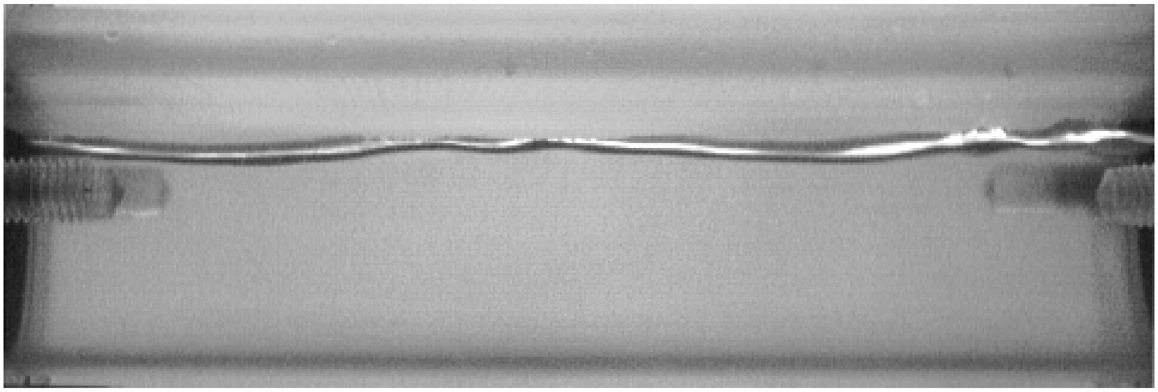

(a) Stratified flow

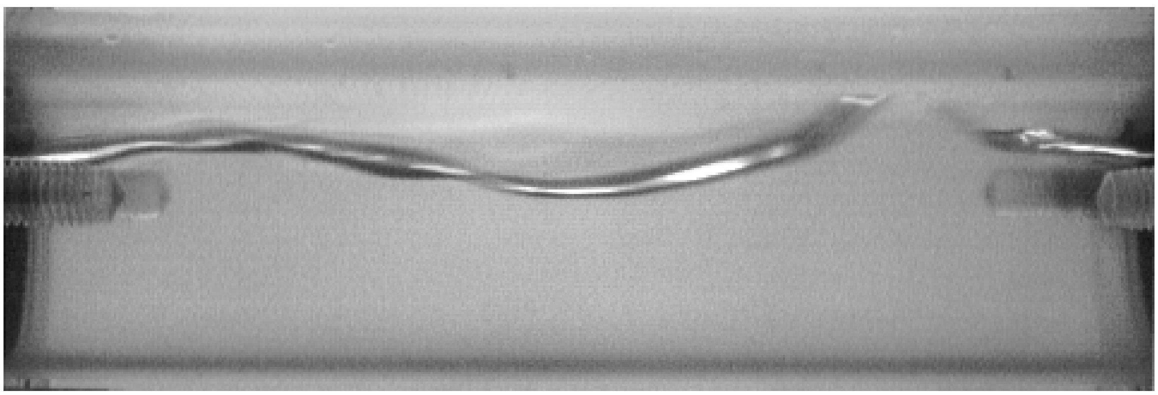

(b) Wavy flow

Figure 8.25 Different regimes viewed from position VS-B on Fig. 8.17. Experiment 4-C in Table 8.4: $W_{\mathrm{C}} = 0.227\,\mathrm{kg\,s^{-1}}$, $x_{\mathrm{C}} = 0.08$, $\lambda_{\mathrm{G}} = 0.10$, $\lambda_{\mathrm{L}} = 0.80$.

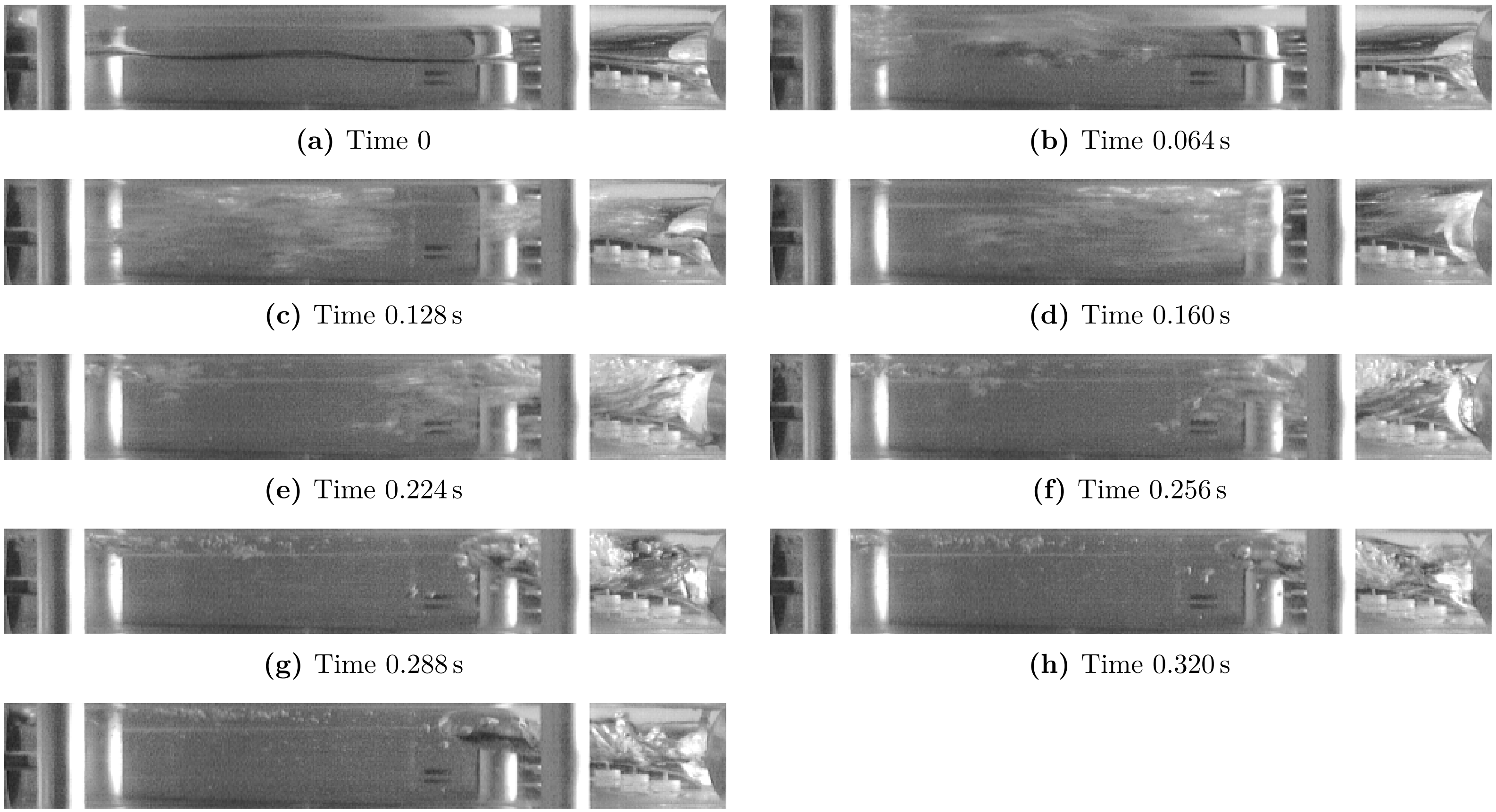

(a) Time 0
(b) Time 0.064 s
(c) Time 0.128 s
(d) Time 0.160 s
(e) Time 0.224 s
(f) Time 0.256 s
(g) Time 0.288 s
(h) Time 0.320 s
(i) Time 0.352 s

Figure 8.26 A slug moving into the junction from the branch viewed from location J-B on Fig. 8.17. Experiment 4-C in Table 8.4: $W_\mathrm{C} = 0.227\,\mathrm{kg\,s^{-1}}$, $x_\mathrm{C} = 0.08$, $\lambda_\mathrm{G} = 0.10$, $\lambda_\mathrm{L} = 0.80$.

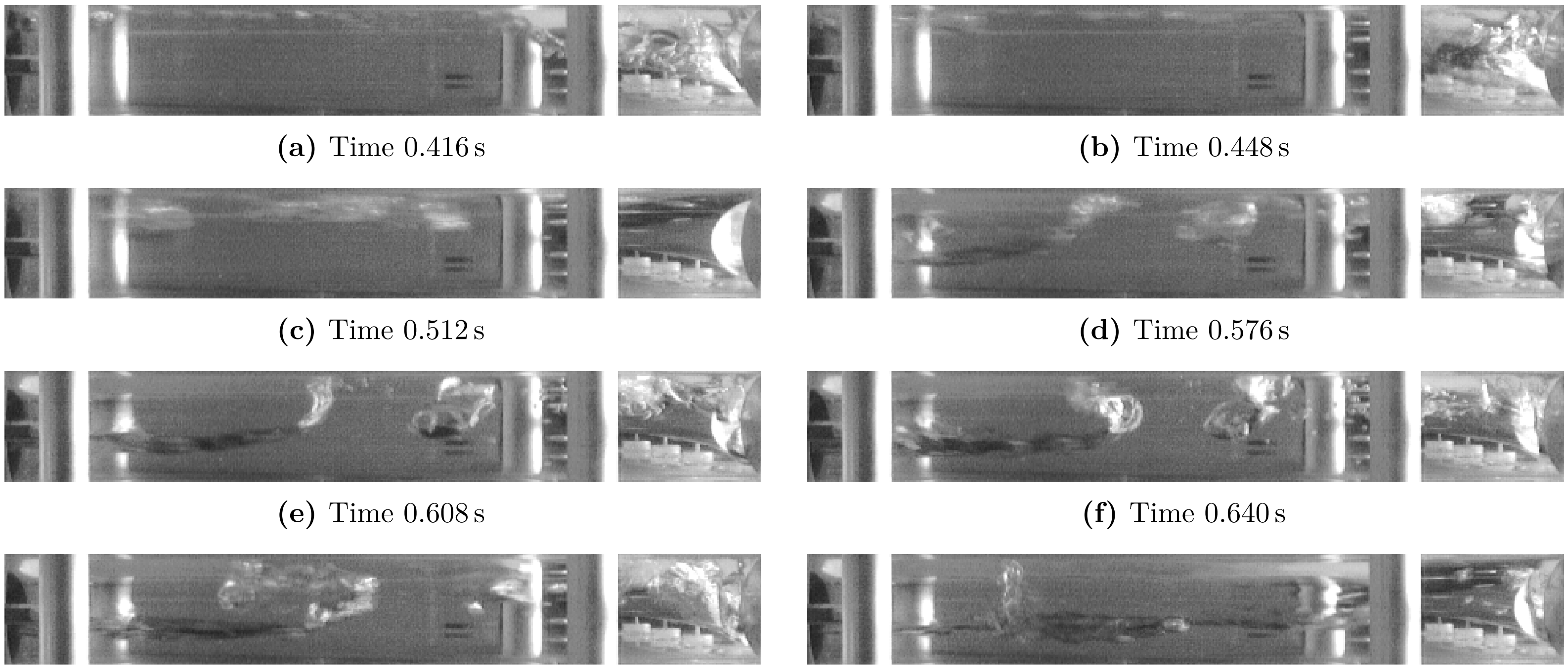

(a) Time 0.416 s

(b) Time 0.448 s

(c) Time 0.512 s

(d) Time 0.576 s

(e) Time 0.608 s

(f) Time 0.640 s

(g) Time 0.672 s

(h) Time 0.736 s

Figure 8.27 Continuation of stills of a slug moving into the junction from the branch viewed from location J-B on Fig. 8.17. Experiment 4-C in Table 8.4: $W_C = 0.227\,\mathrm{kg\,s^{-1}}$, $x_C = 0.08$, $\lambda_G = 0.10$, $\lambda_L = 0.80$.

Part IV

Conclusions

Chapter 9

Conclusions

This study presented results for experiments with air-water mixtures flowing in a 37.8 mm diameter, horizontal tee junction at an absolute pressure of 150 kPa. A wide range of conditions were studied with annular, wavy, and slug flow in the combined side, and additionally stratified flow in the inlets. Pressure measurements were made at 49 pressure taps distributed around the tee junction and reported values include single- and two-phase fully-developed pressure gradients, and pressure losses across the junction. Comparisons of the pressure-losses were made with previous models, but the data are unique and no other report exists in the literature with pressure loss data for the studied conditions. Mixing behaviours were reported based on both pressure measurements and visual observation made at three clear acrylic visual sections placed far from the tee in each side of the junction, and also at the tee junction which itself was also constructed of clear acrylic. From the presented results several conclusions can be drawn:

1. For single-phase flow experiments:

    - The measured friction factors had an overall RMSD of 8.2 % from the exact solution for laminar flow and Colebrook's [48] equation for turbulent flow.
    - The measured pressure losses agree well with established results from Idelchik [63] and correlations for the single-phase loss coefficient based on the present experiments are given.
    - These results confirmed the accuracy of the measurements and demonstrate the quality of the apparatus and methods.

2. For experiments with wavy and annular flow in the combined side of the tee junction:

   - Excellent repeatability was demonstrated in the measurements, and time-varying differential pressure measurement's PDFs were symmetric and fit well by Gaussian distributions.

   - Confirmation was made that all reported pressure gradients came from fully-developed flows.

   - Fully-developed pressure gradients were compared with seven correlations from the literature with wide variation found among the correlations predictions. The best agreement was with the phenomenological model of Taitel and Dukler [33] for stratified flows (RMSD(dP/dz) within 35 %), with the correlation of Sun and Mishima [56] for wavy flows (RMSD(dP/dz) within 16 %), and with the correlation of Müller-Steinhagen and Heck [54] for annular flows (RMSD(dP/dz) within 10 %).

   - It was shown that pressure losses are dependant on the outlet flow rate, the outlet quality, and the distribution of gas between the inlets, but nearly independent of the distribution of liquid between the inlets.

   - Pressure loss data was compared with predictions of the models of St. Pierre and Glastonbury [22] and Schmidt and Loth [30]. These models' predictions varied widely with accuracy dependant on the outlet flow regime.

   - A new model for pressure losses was proposed and predicts all of the reported two-phase pressure-loss data with $0.2 \leq \lambda_{\mathrm{G}} \leq 0.8$ with an of RMSD($\Delta P_{i\text{-C}}$) $\leq 14\%$. The model is closed by empirical correlation and has only been tested with the presented experimental conditions.

- For experiments with wavy flow in the combined side and $V_{\mathrm{SG,C}} < 10\,\mathrm{m\,s^{-1}}$, it was shown that the flow swells due to mixing, with an increase in the liquid level around the junction.

3. For experiments with slug flow in the combined side:

    - Time-averaged pressure distributions were not repeatable.
    - Time varying pressure signals showed pressure surges propagate rapidly upstream of slugs throughout the whole test section. Time-varying pressure signals upstream of slugging, regardless of whether slugs are present at the point of measurement or not, have wide variation.
    - Time-varying pressure signals showed a time lag between slug events based on pressure tap locations.
    - Time-varying pressure signals showed that not all locations in the test-section experience the slug events in the same way, as the location relative to slug formation (i.e. upstream or downstream of formation), proximity to slug formation, and proximity to the test-section's discharge affect the pressure signal. Multiple slugs can affect the pressure at one location while fewer or no slugs affect another depending on location.
    - Time-varying pressure measurements made relative to a constant pressure reference line had asymmetric PDFs skewed to the right and fit by multiple superimposed Gaussian distributions. Time-varying differential pressure measurements between inlet and outlet taps also had asymmetric PDFs skewed to the right and fit by multiple superimposed Gaussian distributions.
    - The cause of the pressure measurements PDFs' skewed shapes is the time lag between pressure taps experiencing slug events, and the effect of multiple

slugs present in the test-section.

- Time-varying differential pressure measurements between consecutive taps had symmetric PDFs fit well by Gaussian distributions.

Future work should include efforts to determine whether repeatable results are possible with slug flow in the combined side following the suggestions in Section 8.5. Further recommendations for future work are:

- Expand the test section so measurements may be taken farther upstream of the test-section, allowing study with lower flow rates, particularly wavy flows with low gas velocity and stratified flows, where the tee's presence was observed to cause deviation from fully-developed flow around the junction.

- Perform pressure loss experiments with pipe-flows (no tee). There is little agreement among published results and correlations, and this causes difficulty in validating two-phase experimental results. Careful experiments with many pressure taps similar to the method used in the present apparatus would greatly benefit other researchers in many areas.

- Investigate time-varying, static-wall pressure signals without damping. Several works in the literature have performed analysis on such measurements with the goals of flow-regime identification or modelling slug flow, but there is little agreement among them and further study would be of interest, particularly what effects tees may have on the signals.

- Further modelling efforts. While the presented model is in excellent agreement with the experimental results, it is empirically closed and flow-regime dependant. It would be beneficial to have a more complete physical model for the phenomenon.

- More orientations should be investigated. The effect of inclination has not been studied in combining tees.

- Try measurements with the pressure taps at the top of the pipe in order to avoid difficulties with the 'hydraulic rise' phenomenon, shown in Section 7.5 and possibly present in slug flow experiments as well. Of course, placing the pressure taps at the top of the pipe would introduce other difficulties such as using air as a pressure transmission fluid.

References

[1] J. S. McNown, Mechanics of manifold flow, ASCE Transactions 119 (1954) 1103–1142.

[2] A. Gardel, Les pertes de charge dans les écoulements au travers de branchements en te, Bulletin Technique de la Suisse Romande 83 (1957) 9, 123–130; 10, 143–148.

[3] F. W. Blaisdell, P. W. Manson, Loss of energy at sharp-edged pipe junctions in water conveyance systems, Technical Report 1283, U.S. Department of Agriculture, Minnesota Agricultural Experiment Station, and the University of Minnesota, 1963.

[4] H. Itō, K. Imai, Energy losses at 90° pipe junctions, Journal of the Hydraulics Division, ASCE 99 (HY9) (1973) 1353–1368.

[5] M. Serre, A. J. Odgaard, R. A. Elder, Energy loss at combining pipe junction, Journal of Hydraulic Engineering 120 (1994) 808–830.

[6] K. Oka, N. Takahito, H. Itō, Energy Losses Due to Combination of Flow at Tees, JSME International Journal Series B 39 (1996) 489–498.

[7] K. Oka, H. Itō, Energy Losses at Tees With Large Area Ratios, Journal of Fluids Engineering 127 (2005) 110–116.

[8] J. Pérez-García, E. Sanmiguel-Rojas, J. Hernández-Grau, A. Viedma, Numerical and experimental investigations on internal compressible flow at T-type junctions, Experimental Thermal and Fluid Science 31 (2006) 61–74.

[9] J. Pérez-García, E. Sanmiguel-Rojas, A. Viedma, New experimental correlations to characterize compressible flow losses at 90-degree T-junctions, Experimental Thermal and Fluid Science 33 (2009) 261–266.

[10] N. P. Costa, R. Maia, M. F. Proença, F. T. Pinho, Edge effects on the flow characteristics in a 90 deg tee junction, Journal of Fluids Engineering 128 (2006) 1204–1217.

[11] F. Z. Sierra-Espinosa, C. J. Bates, T. O'Doherty, Turbulent flow in a 90° pipe junction: Part 1 : Decay of fluctuations upstream the flow bifurcation, Computers and Fluids 29 (2000) 197–213.

[12] F. Z. Sierra-Espinosa, C. J. Bates, T. O'Doherty, Turbulent flow in a 90° pipe junction: Part 2 : Reverse flow at the branch exit, Computers and Fluids 29 (2000) 215–233.

[13] G. Gan, S. B. Riffat, Numerical determination of energy losses at duct junctions, Applied Energy 67 (2000) 331–340.

[14] H. Matos, P. Oliveira, Steady and unsteady non-Newtonian inelastic flows in a planar T-junction, International Journal of Heat and Fluid Flow 39 (2013) 102–126.

[15] P. Neofytou, C. Housiadas, S. G. Tsangaris, a. K. Stubos, D. I. Fotiadis, Newtonian and power-law fluid flow in a T-junction of rectangular ducts, Theoretical and Computational Fluid Dynamics (2013).

[16] U. Müller, J. Reimann, Redistribution of two-phase flow in branching conduits: A survey, in: Proceedings of the 1st International Conference on Multiphase Flow, Tsukuba, 1991, pp. 85–107.

[17] B. Azzopardi, E. Hervieu, Phase separation at junctions, Multiphase Science and Technology 8 (1994) 645–714.

[18] B. Azzopardi, Phase separation at T junctions, Multiphase Science and Technology 11 (1999) 223–329.

[19] A. El-Shaboury, H. Soliman, G. Sims, Current state of knowledge on two-phase flow in horizontal impacting tee junctions, Multiphase Science and Technology 13 (2001) 139–178.

[20] M. Mohamed, Phase redistribution and separation of gas-liquid flows in an equal-sided impacting tee junction with a horizontal inlet and inclined outlets, Ph.D. thesis, University of Manitoba, 2012.

[21] A. Elazhary, Two-phase flow in a mini-size impacting tee junction with a rectangular cross-section, Ph.D. thesis, University of Manitoba, 2012.

[22] C. C. St. Pierre, A. Glastonbury, Two-phase flow distribution and pressure changes for horizontal tee junctions, Technical Report AERE-R 7131, Chemical Engineering Division, U.K.A.E.A. Research Group, Atomic Energy Research Establishment, Harwell, 1972.

[23] J. Reimann, W. Seeger, Two-phase flow in a T-junction with a horizontal inlet part II: Pressure differences, International Journal of Multiphase Flow 12 (1986) 587–608.

[24] S. T. Hwang, R. T. Lahey Jr, A study on single- and two-phase pressure drop in branching conduits, Experimental Thermal and Fluid Science 1 (1988) 111–125.

[25] J. Buell, H. Soliman, G. Sims, Two-phase pressure drop and phase distribution of a horizontal tee junction, International Journal of Multiphase Flow 20 (1994) 819–836.

[26] L. Walters, H. Soliman, G. Sims, Two-phase pressure drop and phase distribution at reduced tee junctions, International Journal of Multiphase Flow 24 (1998) 775–792.

[27] A. El-Shaboury, H. Soliman, G. Sims, Two-phase flow in a horizontal equal-sided impacting tee junction, International Journal of Multiphase Flow 33 (2007) 411–431.

[28] A. P. Doherty, A. Murphy, P. L. Spedding, Fluid flow in an impacting symmetrical tee junction II : two-phase air / water flow, Asia-Pacific Journal of Chemical Engineering 4 (2009) 424–431.

[29] A. Elazhary, H. Soliman, Single- and two-phase pressure losses in a horizontal mini-size impacting tee junction with a rectangular cross-section, Experimental Thermal and Fluid Science 41 (2012) 67–76.

[30] H. Schmidt, R. Loth, Predictive methods for two-phase flow pressure loss in tee junctions with combining conduits, International Journal of Multiphase Flow 20 (1994) 703–720.

[31] V. Belegratis, B. J. Azzopardi, Y. Ladam, Interaction phenomena of two gas/liquid flows combining at a T-junction, in: 5th North American Conference on Multiphase Technology, Banff, AB, June 2006.

[32] V. Belegratis, Gas/liquid two-phase flow at a combining T-junction, Ph.D. thesis, University of Nottingham, 2007.

[33] Y. Taitel, A. E. Dukler, A model for predicting flow regime transitions in horizontal and near horizontal gas-liquid flow, AIChE Journal 22 (1976) 47–55.

[34] J. M. Mandhane, G. A. Gregory, K. Aziz, A flow pattern map for gas-liquid flow in horizontal pipes, International Journal of Multiphase Flow 1 (1974) 537–553.

[35] O. Baker, Simultaneous flow of oil and gas, Oil and Gas Journal 53 (1954) 185–195.

[36] F. Wang, Q. Marashdeh, L.-S. Fan, W. Warsito, Electrical Capacitance Volume Tomography: Design and Applications, Sensors (Basel, Switzerland) 10 (2010) 1890–917.

[37] N. A. Tsochatzidis, T. D. Karapantsios, M. V. Kostoglou, A. J. Karabelas, A conductance probe for measuring liquid fraction in pipes and packed beds, International Journal of Multiphase Flow 18 (1992) 653–667.

[38] N. K. Tutu, Pressure fluctuations and flow pattern recognition in vertical two phase gas-liquid flows, International Journal of Multiphase Flow 8 (1982) 443–447.

[39] G. Matsui, Identification of flow regimes in vertical gas-liquid two-phase flow using differential pressure fluctuations, International Journal of Multiphase Flow 10 (1984) 711–720.

[40] P. Spedding, D. Spence, Flow regimes in two-phase gas-liquid flow, International journal of multiphase flow 19 (1993) 245–280.

[41] Y. Cai, M. W. Wambsganss, J. A. Jendrzejczyk, Application of chaos theory in identification of two-phase flow patterns and transitions in a small, horizontal, rectangular channel, Journal of Fluids Engineering 118 (1996) 383–390.

[42] T. Elperin, M. Klochko, Flow regime identification in a two-phase flow using wavelet transform, Experiments in Fluids 32 (2002) 674–682.

[43] T. Xie, S. M. Ghiaasiaan, S. Karrila, Flow Regime Identification in Gas / Liquid / Pulp Fiber Slurry Flows Based on Pressure Fluctuations Using Artificial Neural Networks, Industrial and Engineering Chemistry Research 42 (2003) 7017–7024.

[44] B. Sun, H. Zhang, L. Cheng, Y. Zhao, Flow regime identification of gas-liquid two-phase flow based on HHT, Chinese Journal of Chemical Engineering 14 (2006) 24–30.

[45] A. E. Dukler, M. Wicks III, R. G. Cleveland, Frictional pressure drop in two-phase flow: A. A comparison of existing correlations for pressure loss and holdup, AIChE Journal 10 (1964) 38–43.

[46] M. A. Woldesemayat, A. J. Ghajar, Comparison of void fraction correlations for different flow patterns in horizontal and upward inclined pipes, International Journal of Multiphase Flow 33 (2007) 347–370.

[47] S. Z. Rouhani, E. Axelsson, Calculation of void volume fraction in the sub cooled and quality boiling regions, International Journal of Heat and Mass Transfer 13 (1970) 383–393.

[48] C. F. Colebrook, Turbulent flow in pipes, with particular reference to the transition region between the smooth and rough pipe laws, Journal of the Institution of Civil Engineers 11 (1939) 133–156.

[49] G. B. Wallis, One-Dimensional Two-Phase Flow, McGraw-Hill, 1969.

[50] A. J. Ghajar, S. M. Bhagwat, Flow Patterns, Void Fraction and Pressure Drop in Gas-Liquid Two Phase Flow at Different Pipe Orientations, in: L. Cheng (Ed.), Frontiers and Progress in Multiphase Flow, Springer International Publishing, 2014, pp. 157–212.

[51] D. Beattie, P. Whalley, Simple two-phase frictional pressure drop calculation method, International Journal of Multiphase Flow 8 (1982) 83–87.

[52] R. Lockhart, R. Martinelli, Proposed correlation of data for isothermal two-phase, two-component flow in pipes, Chemical Engineering Progress 45 (1949) 39–48.

[53] L. Friedel, Improved friction pressure drop correlation for horizontal and vertical two-phase pipe flow, in: Proceedings of the European Two-Phase Flow Group Meeting, Paper E2, Ispra, Italy, 1979.

[54] H. Müller-Steinhagen, K. Heck, A simple friction pressure drop correlation for two-phase flow in pipes, Chemical Engineering and Processing: Process Intensification 20 (1986) 297–308.

[55] K. Mishima, T. Hibiki, Some characteristics of air-water two-phase flow in small diameter vertical tubes, International Journal of Multiphase Flow 22 (1996) 703–712.

[56] L. Sun, K. Mishima, Evaluation analysis of prediction methods for two-phase pressure drop in mini-channels, International Journal of Multiphase Flow 34 (2009) 47–54.

[57] P. Spedding, E. Benard, G. Donnelly, Prediction of pressure drop in multiphase horizontal pipe flow, International Communications in Heat and Mass Transfer 33 (2006) 1053–1062.

[58] Y. Xu, X. Fang, X. Su, Z. Zhou, W. Chen, Evaluation of frictional pressure drop correlations for two-phase flow in pipes, Nuclear Engineering and Design 253 (2012) 86–97.

[59] C. Tribbe, H. Müller-Steinhagen, An evaluation of the performance of phenomenological models for predicting pressure gradient during gas-liquid flow in horizontal pipelines, International Journal of Multiphase Flow 26 (2000) 1019–1036.

[60] A. Vazsonyi, Pressure loss in elbows and duct branches, Transactions, American Society of Mechanical Engineers 66 (1944) 177–183.

[61] S. Katz, Mechanical potential drops at a fluid branch, Journal of Basic Engineering, Transactions, American Society of Mechanical Engineers, Series D 89 (1967) 732–736.

[62] R. A. Bajura, A model for flow distribution in manifolds, Journal of Engineering for Power, Transactions, American Society of Mechanical Engineers, Series A 93 (1971) 7–12.

[63] I. E. Idelchik, Resistance in the cases of merging of flow streams and division into flow streams: Resistance coefficients of wyes, tees, and manifolds, in: Handbook of Hydraulic Resistance, 1994, pp. 413–501.

[64] J. M. Turner, G. B. Wallis, The Separate-Cylinders Model of Two-Phase Flow, Technical Report NYO-3114-6, Thayer School of Engineering, Dartmouth College, Hanover, New Hampshire, 1965.

[65] G. Matsui, Automatic identification of flow regimes in vertical two-phase flow using differential pressure fluctuations, Nuclear Engineering and Design 95 (1986) 221–231.

[66] K. Nishikawa, K. Sekoguchi, T. Fukano, On the pulsation phenomena in gas-liquid two-phase flow, Bulletin of JSME 12 (1969) 1410–1416.

[67] A. L. Samways, L. J. S. Bradbury, H. H. Bruun, Pressure measurements and convection velocity evaluations in two-phase flow, International Journal of Multiphase Flow 23 (1997) 1007–1029.

[68] N. K. Tutu, Pressure drop fluctuations and bubble-slug transition in a vertical two phase air-water flow, International Journal of Multiphase Flow 10 (1984) 211–216.

[69] T. Kinoshita, T. Murasaki, On a stochastic approach to the pulsating phenomena in the two-phase flow, Bulletin of JSME 12 (1969) 819–826.

[70] K. Akagawa, H. Hamaguchi, T. Sakaguchi, T. Ikari, Studies on the fluctuation of pressure drop in two-phase slug flow, Bulletin of the JSME 14 (1971) 447–454.

[71] Z. Fan, Z. Ruder, T. Hanratty, Pressure profiles for slugs in horizontal pipelines, International Journal of Multiphase Flow 19 (1993) 421–437.

[72] J. Weisman, D. Duncan, J. Gibson, T. Crawford, Effects of fluid properties and pipe diameter on two-phase flow patterns in horizontal lines, International Journal of Multiphase Flow 5 (1979) 437–462.

[73] S. C. Lee, H. S. Shin, J. P. Lee, Statistical characteristics of instantaneous pressure drops through orifices for various two-phase flow regimes, in: G. F. Hewitt (Ed.), Proceedings of the 10th International Heat Transfer Conference, CRC Press, Brighton, UK, 1994, pp. 211–215.

[74] P. Y. Lin, T. J. Hanratty, Detection of slug flow from pressure measurements, International Journal of Multiphase Flow 13 (1987) 13–21.

[75] J. Drahoš, J. Tihon, C. Serio, A. Lübbert, Deterministic chaos analysis of pressure fluctuations in a horizontal pipe at intermittent flow regime, The Chemical Engineering Journal 64 (1996) 149–156.

[76] F. Franca, M. Acikgoz, R. Lahey, A. Clausse, The use of fractal techniques for flow regime identification, International Journal of Multiphase Flow 17 (1991) 545–552.

[77] A. E. Dukler, M. G. Hubbard, A model for gas-liquid slug flow in horizontal and near horizontal tubes, Industiral and Engineering Chemistry Fundamentals 14 (1975) 337–347.

[78] M. G. Hubbard, A. E. Dukler, The characterization of flow regimes for horizontal two-phase flow: I. statistical analysis of wall pressure fluctuations, in: M. A. Saad, J. A. Miller (Eds.), Proceedings of the 1966 Heat Transfer and Fluid Mechanics Institute, Stanford University Press, Santa Clara, California, 1966, pp. 100–121.

[79] P. K. Jain, R. P. Roy, Stochastic characteristics of vapor fraction and wall pressure fluctuations in boiling flows, International Journal of Multiphase Flow 9 (1983) 463–489.

[80] M. M. Sorour, M. S. El-Beshbeeshy, Void fraction and pressure fluctuations of bubbly flow in a vertical annular channel, Experiments in Fluids 4 (1986) 163–170.

[81] S. F. Wang, R. Mosdorf, M. Shoji, Nonlinear analysis on fluctuation feature of two-phase flow through a T-junction, International Journal of Heat and Mass Transfer 46 (2003) 1519–1528.

[82] G. Joyce, H. M. Soliman, Pressure drop in a horizontal, equal-sided, sharp-edged, combining tee junction with air-water flow, Experimental Thermal and Fluid Science 55 (2014) 140–149.

[83] C. A. Van Gorp, Two-phase pressure drop and phase distribution at a reduced horizontal tee junction: the effect of system pressure, Master's thesis, University of Manitoba, 1998.

[84] G. Joyce, H. M. Soliman, Pressure drop for two-phase mixtures combining in a tee junction with wavy flow in the combined side, Experimental Thermal and Fluid Science 70 (2016) 307–315.

[85] R. E. Walpole, R. H. Myers, Probability and Statistics for Engineers and Scientists, 4 ed., Macmillan, 1989.

[86] R. J. Moffat, Describing the Uncertainties in Experimental Results, Experimental Thermal and Fluid Science 1 (1988) 3–17.

[87] S. Z. Rouhani, Modified Correlations for Void and Two-Phase Pressure Drop, Technical Report AE-RTV 841, AB Atomenergi, Stockholm, Sweden, 1969.

[88] J. R. Buell, Two-phase pressure drop and phase distribution in a horizontal tee junction, Master's thesis, University of Manitoba, 1992.

[89] J. P. Holman, Experimental Methods for Engineers, 8 ed., Mcgraw-Hill College, 1994.

[90] N. H. Cook, E. Rabinowicz, Physical Measurement and Analysis, Addison-Wesley, 1963.

[91] J. Drahoš, J. Čermák, K. Selucký, Characterization of hydrodynamic regimes in horizontal two-phase flow part II: analysis of wall pressure fluctuations, Chemical Engineering and Processing: Process Intensification 22 (1987) 45–52.

Appendix A

The Models of Schmidt and Loth

A.1 Overview

Schmidt and Loth [30] presented three models for two-phase combining flow: the loss coefficient model (LCM), the contraction coefficient model (CCM), and the momentum coefficient model (MCM). For the derivation of all three models, Fig. A.1 will be used to help visualize the flow.

There are several 'open' parameters used in constructing Schmidt and Loth's models. The first is a two-phase flow streamline-correction factor used to solve the integral energy equation in both the LCM and CCM. The general definition of the factor is:

$$F_{<\rho^m V^n>i} = \frac{\frac{1}{A_i \Delta t} \int_{A_i} \int_0^{\Delta t} \rho^m V^n \,\mathrm{d}t \,\mathrm{d}A}{\rho_{\mathrm{h},i}^m V_{\mathrm{h},i}^n}, \;\; i = \mathrm{B,\ M,\ or\ C}. \tag{A.1}$$

This factor effectively implements either a homogeneous ($F_{<>} = 1$) or slip model in

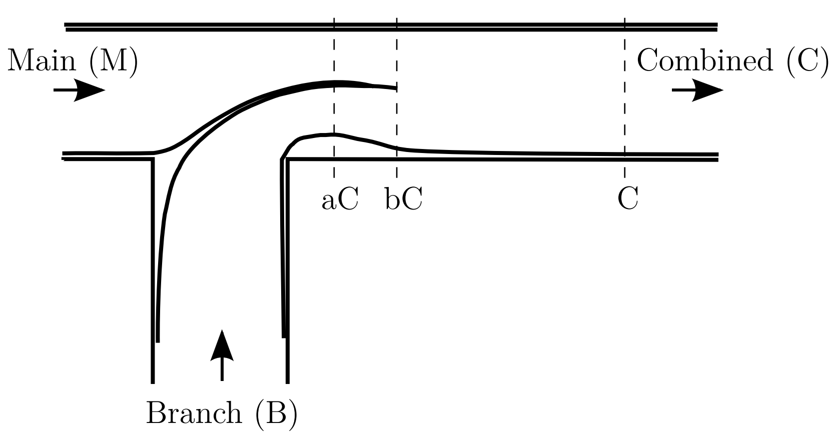

Figure A.1 Stream tubes used in the derivation of the models in [30].

order to evaluate the integral terms. With appropriate selection of dummy variables m and n, the streamline-correction factor allows use of average velocities which otherwise do not accurately represent kinetic energy or momentum.

The second open parameter is the additional pressure loss: the pressure loss incurred from immediately after the junction to further downstream where the just-mixed, chaotic flow organizes itself into its final flow regime. This open parameter is modelled by estimating the wall friction with a kinetic energy balance from slightly after the junction (position bC in Fig. A.1) to the fully developed flow further downstream (position C in Fig. A.1), and then performing a momentum balance including the frictional loss. The energy balance for estimating the friction is given by:

$$\Delta P_{\text{friction}} = \frac{W_{\text{C}}^2}{2A\rho_{\text{h,C}}}(F_{<\rho V^3>\text{bC}} - F_{<\rho V^3>\text{C}}). \tag{A.2}$$

The additional pressure loss can then be expressed as:

$$\Delta P_{\text{additional}} = \frac{W_{\text{C}}^2}{A\rho_{\text{h,C}}}(F_{<\rho V^2>\text{C}} - F_{<\rho V^2>\text{bC}}) + \Delta P_{\text{friction}}. \tag{A.3}$$

Schmidt and Loth recommended implementing this term for all models, otherwise the pressure loss estimates are too low based on their results.

The third open parameter is a mechanical energy exchange term that occurs in the LCM and CCM, referred to as L_i. The L-term is proposed to be proportional to the difference between the relative velocity and mass flow ratio of the inlet flow to the outlet, and also proportional to the kinetic energy flux at the outlet, leading to the expression:

$$L_i = \frac{W_i W_{\text{C}}^2}{2A^2\rho_{\text{h,C}}^2}\left(\frac{\rho_{\text{h,C}}}{\rho_{\text{h},i}} - 1\right). \tag{A.4}$$

Finally, the most significant open parameter for Schmidt and Loth is the term ω. This term is analogous to λ in single-phase flow: it is meant to be a single parameter capable of characterizing the loss coefficient. Schmidt and Loth argue:

> While the mass flow and the volume flow ratios stay unchanged for the two-phase flow, this is no longer valid for the momentum and the kinetic energy fluxes.

They tested several models for their new parameter but recommended implementing only the momentum flux ratio model:

$$\omega = \left(1 + \sqrt{\frac{\rho_{\mathrm{M}} V_{\mathrm{M}}^2}{\rho_{\mathrm{B}} V_{\mathrm{B}}^2}}\right)^{-1}. \tag{A.5}$$

Note that for single-phase conditions in an equal sided tee $\omega = \lambda$.

In addition to the homogeneous density, two other density forms can be written which will allow simplification of the models to follow. The momentum density is based on creating a fluid that would flow with the same total momentum of the two-phase flow instead of a common velocity:

$$WV = W_{\mathrm{L}} V_{\mathrm{L}} + W_{\mathrm{G}} V_{\mathrm{G}}. \tag{A.6}$$

Substituting for the velocities in terms of mass flow rates:

$$W \frac{W}{\rho_{\mathrm{m}} A} = W_{\mathrm{L}} \frac{W_{\mathrm{L}}}{\rho_{\mathrm{L}} A_{\mathrm{L}}} + W_{\mathrm{G}} \frac{W_{\mathrm{G}}}{\rho_{\mathrm{G}} A_{\mathrm{G}}}. \tag{A.7}$$

Using the definition of the void fraction from Eq. (2.2), and also the relations $W_{\mathrm{L}} = (1-x)W$ and $W_{\mathrm{G}} = xW$, the momentum density can be expressed as:

$$\rho_{\mathrm{m}} = \left(\frac{(1-x)^2}{(1-\alpha)\rho_{\mathrm{L}}} + \frac{x^2}{\alpha \rho_{\mathrm{G}}}.\right)^{-1}. \tag{A.8}$$

Similarly, the energy density is based on creating a fluid that would flow with the same total kinetic energy of the two-phase flow:

$$\frac{WV^2}{2} = \frac{W_{\mathrm{L}}V_{\mathrm{L}}^2}{2} + \frac{W_{\mathrm{G}}V_{\mathrm{G}}^2}{2}. \tag{A.9}$$

In a similar manner to the momentum density, the energy density can be written as:

$$\rho_{\mathrm{e}} = \left(\frac{(1-x)^3}{(1-\alpha)^2 \rho_{\mathrm{L}}^2} + \frac{x^3}{\alpha^2 \rho_{\mathrm{G}}^2} \right)^{-1/2}. \tag{A.10}$$

A.2 The loss coefficient model

The LCM subdivides the total tee-junction pressure drop from the branch or main to position bC, located just after the junction, where the two flows are first mixed and fill the total cross-section (see Fig. A.1, page 162), and then adds a further additional pressure drop to account for the flow coming to its final flow pattern further downstream.

$$\Delta P_{i\text{-C}} = \Delta P_{i\text{-bC}} + \Delta P_{\mathrm{ad}}. \tag{A.11}$$

Here, the additional pressure loss term is given by Eq. (A.3). The LCM then further subdivides the pressure drop occurring from the inlet legs to position bC into a reversible and irreversible pressure loss component:

$$\Delta P_{i\text{-C}} = (\Delta P_{i\text{-bC}})_{\mathrm{rev}} + (\Delta P_{i\text{-bC}})_{\mathrm{irrev}} + \Delta P_{\mathrm{ad}}. \tag{A.12}$$

Examining only the reversible component first, assume the combining flow occurs in separated stream tubes as shown in Fig. A.1. Further assumptions of steady flow, no heat transfer, and negligable gravitational effects reduces the general integral form of the energy equation for these stream-tube control-volumes to:

$$0 = \int_{\mathrm{CS}} \left(u + \frac{V^2}{2} + \frac{P}{\rho} \right) \rho V \, dA, \tag{A.13}$$

where u is the internal energy. Next, assuming constant properties, constant pressure across cross-sections, and forces on the stream tubes only affect the exchange of mechanical energy (L_i) between the stream tubes, we can expand Eq. (A.13) into:

$$0 = \int_{A_i} \frac{\rho V^3}{2} \, dA - \int_{A_{\mathrm{bC}}} \frac{\rho V^3}{2} \, dA + P_i \int_{A_i} V \, dA - P_{\mathrm{bC}} \int_{A_{\mathrm{bC}}} V \, dA - L_i. \tag{A.14}$$

Evaluation of the integrals requires the streamline-correction factor from Eq. (A.1). Performing the integrations with aid of $F_{<>}$ we arrive at:

$$(\Delta P_{i\text{-bC}})_{\mathrm{rev}} = \frac{\rho_{\mathrm{h},i} V_{\mathrm{h,C}}^2}{2} F_{<\rho V^3>\mathrm{bC}\text{-}i} - \frac{\rho_{\mathrm{h},i} V_{\mathrm{h},i}^2}{2} F_{<\rho V^3>i} + \frac{L_i}{V_{\mathrm{h},i} A}. \tag{A.15}$$

Next, the irreversible component of $\Delta P_{i\text{-bC}}$ is simply a correction factor, added in a similar fashion to the single-phase energy model of Eq. (2.11):

$$(\Delta P_{i\text{-bC}})_{\mathrm{irrev}} = \left(\frac{\rho_{\mathrm{h},i} V_{\mathrm{h,C}}^2}{2} F_{<\rho V^3>\mathrm{bC}\text{-}i} + \frac{L_i}{V_{\mathrm{h},i} A} \right) k_{\mathrm{LCM},i\text{-C}}. \tag{A.16}$$

In order to evaluate the two-phase loss coefficient, $k_{\mathrm{LCM},i\text{-C}}$, the model is evaluated at the limiting case of single-phase flow. Therefore, with $F_{<>} = 1$, $L_i = 0$, $\rho_i = \rho_{\mathrm{C}} = \rho$, and $\Delta P_{\mathrm{ad}} = 0$ we find Eq. (A.12) with Eqs. (A.15) and (A.16) substituted reduces exactly to the form of Eq. (2.11), which implies:

$$k_{\mathrm{LCM},i\text{-C}} = k_{1\phi,i\text{-C}}(\omega). \tag{A.17}$$

Note the two-phase coefficient adopts the form of the single-phase coefficient, but is *not* identical since it is in terms of the two-phase parameter ω defined by Eq. (A.5).

The tuned version of the LCM recommended by Schmidt and Loth uses a homogeneous model (which implies $F_{<>} = 1$) for Eqs. (A.15) and (A.16) in the main-to-combined pressure loss, and a slip model for the branch-to-combined pressure loss but with a homogeneous model at location bC ($F_{<>\mathrm{bC}} = 1$) in Eqs. (A.15) and (A.16). The mechanical energy exchange, L_i, should be evaluated according to Eq. (A.4), and the additional pressure loss according to Eq. (A.3) with a homogeneous model at position bC. The required estimates of the remaining streamline correction factors from the separated flow model are then given as:

$$F_{<\rho V^3>i} = \frac{\rho_{\mathrm{h},i}^2}{\rho_{\mathrm{e},i}^2}, \tag{A.18a}$$

$$F_{<\rho V^2>\mathrm{C}} = \frac{\rho_{\mathrm{h,C}}}{\rho_{\mathrm{m,C}}}. \tag{A.18b}$$

With these 'settings' applied, the final recommended equations for the 'tuned' LCM are:

$$\Delta P_{\text{M-C}} = \frac{W_{\mathrm{C}}^2}{2A^2\rho_{\mathrm{h,C}}}\left(\frac{2\rho_{\mathrm{h,C}}}{\rho_{\mathrm{m,C}}} - \frac{\rho_{\mathrm{h,C}}^2}{\rho_{\mathrm{e,C}}^2} - \frac{(1-\lambda)^2\rho_{\mathrm{h,C}}}{\rho_{\mathrm{h,M}}} + k_{\text{LCM,M-C}}\right), \tag{A.19a}$$

$$\Delta P_{\text{B-C}} = \frac{W_{\mathrm{C}}^2}{2A^2\rho_{\mathrm{h,C}}}\left(\frac{2\rho_{\mathrm{h,C}}}{\rho_{\mathrm{m,C}}} - \frac{\rho_{\mathrm{h,C}}^2}{\rho_{\mathrm{e,C}}^2} - \frac{\lambda^2\rho_{\mathrm{h,B}}\rho_{\mathrm{h,C}}}{\rho_{\mathrm{e,B}}^2} + k_{\text{LCM,B-C}}\right). \tag{A.19b}$$

A.3 The contraction coefficient model

For the contraction coefficient model, it is assumed there is a vena contracta immediately after the tee causing a flow restriction as shown in Fig. A.1. The point of maximum constriction in the vena contracta is referred to as position aC, and at this point the inlet flows are considered unmixed. Immediately after aC the flows mix and position bC is downstream of the junction where the flow again occupies the full pipe cross-section. The total pressure loss is then given by three separate terms:

$$\Delta P_{i\text{-C}} = \Delta P_{i\text{-a}i} + \Delta P_{\text{aC-bC}} + \Delta P_{\mathrm{ad}}. \tag{A.20}$$

Here, the notation in the subscripts ai implies component i's section of plane aC. Now define a contraction coefficient as:

$$V_{\mathrm{a}i}A_{\mathrm{a}i} = V_iA_i \implies \frac{V_{\mathrm{a}i}}{V_i} = \frac{A_i}{A_{\mathrm{a}i}} = \frac{1}{k_{\mathrm{CCM},i\text{-C}}}. \tag{A.21}$$

For simplicity, consider the single-phase case for the moment which serves to illustrate how the model originates. Writing Bernoulli's equation for single-phase flow from either inlet position to plane aC:

$$\Delta P_{i\text{-a}i} = \frac{\rho}{2}(V_{\mathrm{a}i}^2 - V_i^2). \tag{A.22}$$

Eliminating $V_{\mathrm{a}i}$ by use of Eq. (A.21) yields:

$$\Delta P_{i\text{-a}i} = \frac{\rho V_i^2}{2}\left(\frac{1}{k_{\mathrm{CCM},i\text{-C}}^2} - 1\right). \tag{A.23}$$

This is the single-phase version of Schmidt and Loth's [30] Eq. (17) in their paper. The two-phase form can be derived in a similar fashion to that used to derive the LCM, or may be deduced from Eq. (A.23) by adding the mechanical energy exchange term, L_i, and the streamline-correction factors, $F_{<>}$:

$$\Delta P_{i\text{-a}i} = \frac{W_i^2}{2A^2\rho_{\mathrm{h},i}}\left(\frac{F_{<\rho V^3>\mathrm{a}i}}{k_{\mathrm{CCM},i\text{-C}}^2} - F_{<\rho V^3>i}\right) + \frac{L_i}{V_{\mathrm{h},i}A}. \tag{A.24}$$

The losses from the flow constriction, aC, to the full cross-section, bC, are then solved with a momentum balance. Returning to the simplified single-phase case we can write the sum of forces must equal the momentum change from planes aC to bC as:

$$A_{\mathrm{C}}(P_{\mathrm{bC}} - P_{\mathrm{aC}}) = \rho A_{\mathrm{C}}V_{\mathrm{C}}^2 - \rho A_{\mathrm{aB}}V_{\mathrm{aB}}^2 - \rho A_{\mathrm{aM}}V_{\mathrm{aM}}^2. \tag{A.25}$$

Substituting for V_{aM}, V_{aB}, A_{aM}, and A_{aB} from Eq. (A.21) and assuming equal sizes in all three legs of the tee we arrive at:

$$\Delta P_{\mathrm{aC\text{-}bC}} = \rho V_{\mathrm{C}}^2 - \frac{\rho V_{\mathrm{B}}^2}{k_{\mathrm{CCM,B\text{-}C}}} - \frac{\rho V_{\mathrm{M}}^2}{k_{\mathrm{CCM,M\text{-}C}}}. \tag{A.26}$$

This corresponds directly to Schmidt and Loth's [30] Eq. (19) and we can deduce the two-phase equation simply by adding the streamline correction factors as:

$$\Delta P_{\text{aC-bC}} = \rho_{\text{h,C}} V_{\text{h,C}}^2 F_{<\rho V^2>\text{bC}} - \frac{\rho_{\text{h,B}} V_{\text{h,B}}^2 F_{<\rho V^2>\text{aB}}}{k_{\text{CCM,B-C}}} - \frac{\rho_{\text{h,M}} V_{\text{h,M}}^2 F_{<\rho V^2>\text{aM}}}{k_{\text{CCM,M-C}}}. \tag{A.27}$$

Again, the identical result is achieved if a two-phase analysis is followed.

The contraction coefficient, $k_{\text{CCM},i\text{-C}}$, is found by applying the CCM for the limiting case of single-phase flow ($F_{<>} = 1$, $L_i = 0$, and $\Delta P_{\text{ad}} = 0$) and equating the resulting pressure drop with the single phase model of Eq. (2.11). With some manipulation we can write:

$$\frac{1}{k_{\text{CCM},i\text{-C}}^2} - \frac{2}{k_{\text{CCM},i\text{-C}}} - \left(\frac{V_{\text{C}}^2}{V_i^2} (k_{1\phi,i\text{-C}} - 1) + \frac{2V_j^2}{V_i^2} \frac{1}{k_{\text{CCM},j\text{-C}}} \right) = 0. \tag{A.28}$$

Here, i represents either branch or main, and j represents its alternate so both the branch and main inlet equations are written with a single expression. This equation is a quadratic for $1/k_{\text{CCM},i\text{C}}^2$ with solutions:

$$\frac{1}{k_{\text{CCM},i\text{-C}}} = 1 \pm \sqrt{1 + \frac{V_{\text{C}}^2}{V_i^2} (k_{1\phi,i\text{-C}} - 1) + \frac{2V_j^2}{V_i^2} \frac{1}{k_{\text{CCM},j\text{-C}}}}. \tag{A.29}$$

Using this expression with Eq. (A.28) it is possible to eliminate one of the contraction coefficients and with some algebra find:

$$\begin{aligned} 0 = {} & \frac{1}{k_{\text{CCM},i\text{-C}}^4} - \frac{4}{k_{\text{CCM},i\text{-C}}^3} - \frac{2}{k_{\text{CCM},i\text{-C}}^2} \left(\frac{V_{\text{C}}^2}{V_i^2} (k_{1\phi,i\text{-C}} - 1) + \frac{2V_j^2}{V_i^2} - 2 \right) \\ & + \frac{4}{k_{\text{CCM},i\text{-C}}} \left(\frac{V_{\text{C}}^2}{V_i^2} (k_{1\phi,i\text{-C}} - 1) \right) + \frac{V_{\text{C}}^4}{V_i^4} (k_{1\phi,i\text{-C}} - 1)^2 \\ & + \frac{4V_j^2 V_{\text{C}}^2}{V_i^4} (k_{1\phi,i\text{-C}} - k_{1\phi,j\text{-C}}). \end{aligned} \tag{A.30}$$

For turbulent, incompressible single-phase flow with a constant area averaged density and equal sided tee, $\omega = \lambda = V_B/V_C$ so we can write implicit equations for the contraction coefficients in terms of the parameter ω.

$$
\begin{aligned}
0 = & \frac{1}{k_{\mathrm{CCM,B\text{-}C}}^4} - \frac{4}{k_{\mathrm{CCM,B\text{-}C}}^3} - \frac{2}{k_{\mathrm{CCM,B\text{-}C}}^2}\left(\frac{1}{\omega^2}(k_{1\phi,\mathrm{B\text{-}C}}-1) + \frac{2(1-\omega)^2}{\omega^2} - 2\right) \\
& + \frac{4}{k_{\mathrm{CCM,B\text{-}C}}}\left(\frac{1}{\omega^2}(k_{1\phi,\mathrm{B\text{-}C}}-1)\right) + \frac{1}{\omega^4}(k_{1\phi,\mathrm{B\text{-}C}}-1)^2 \\
& + \frac{4(1-\omega)^2}{\omega^4}(k_{1\phi,\mathrm{B\text{-}C}} - k_{1\phi,\mathrm{M\text{-}C}}), \\
0 = & \frac{1}{k_{\mathrm{CCM,M\text{-}C}}^4} - \frac{4}{k_{\mathrm{CCM,M\text{-}C}}^3} - \frac{2}{k_{\mathrm{CCM,M\text{-}C}}^2}\left(\frac{1}{(1-\omega)^2}(k_{1\phi,\mathrm{M\text{-}C}}-1)\right. \\
& \left. + \frac{2\omega^2}{(1-\omega)^2} - 2\right) + \frac{4}{k_{\mathrm{CCM,M\text{-}C}}}\left(\frac{1}{(1-\omega)^2}(k_{1\phi,\mathrm{M\text{-}C}}-1)\right) \\
& + \frac{1}{(1-\omega)^4}(k_{1\phi,\mathrm{M\text{-}C}}-1)^2 + \frac{4\omega^2}{(1-\omega)^4}(k_{1\phi,\mathrm{M\text{-}C}} - k_{1\phi,\mathrm{B\text{-}C}}).
\end{aligned}
$$

With empirical data for $k_{1\phi,i\text{-}\mathrm{C}}$ like Eq. (2.12), the zeros of these equations can then be found for $\omega = 0.1, 0.2, \ldots, 0.9$ and a cubic polynomial fit to find an approximate solution for the contraction coefficient.

The tuned version of the CCM recommended by Schmidt and Loth implements the same open parameters as the LCM, but the mechanical energy exchange should be set to zero, $L_i = 0$, giving the final form:

$$
\begin{aligned}
\Delta P_{\mathrm{M\text{-}C}} = \frac{W_{\mathrm{C}}^2}{2A^2\rho_{\mathrm{h,C}}} & \left(1 + \frac{2\rho_{\mathrm{h,C}}}{\rho_{\mathrm{m,C}}} - \frac{\rho_{\mathrm{h,C}}^2}{\rho_{\mathrm{e,C}}^2} - \frac{2\lambda^2\rho_{\mathrm{h,C}}}{\rho_{\mathrm{h,B}}k_{\mathrm{CCM,B\text{-}C}}} - \frac{2(1-\lambda)^2\rho_{\mathrm{h,C}}}{\rho_{\mathrm{h,M}}k_{\mathrm{CCM,M\text{-}C}}}\right. \\
& \left. + \frac{(1-\lambda)^2\rho_{\mathrm{h,C}}}{\rho_{\mathrm{h,M}}}\left(\frac{1}{k_{\mathrm{CCM,M\text{-}C}}^2} - 1\right)\right),
\end{aligned} \tag{A.32a}
$$

$$
\begin{aligned}
\Delta P_{\mathrm{B\text{-}C}} = \frac{W_{\mathrm{C}}^2}{2A^2\rho_{\mathrm{h,C}}} & \left(1 + \frac{2\rho_{\mathrm{h,C}}}{\rho_{\mathrm{m,C}}} - \frac{\rho_{\mathrm{h,C}}^2}{\rho_{\mathrm{e,C}}^2} - \frac{2(1-\lambda)^2\rho_{\mathrm{h,C}}}{\rho_{\mathrm{h,M}}k_{\mathrm{CCM,M\text{-}C}}} - \frac{2\lambda^2\rho_{\mathrm{h,C}}}{\rho_{\mathrm{h,B}}k_{\mathrm{CCM,B\text{-}C}}}\right. \\
& \left. + \frac{\lambda^2\rho_{\mathrm{h,C}}}{\rho_{\mathrm{h,B}}}\left(\frac{1}{k_{\mathrm{CCM,B\text{-}C}}^2} - \frac{\rho_{\mathrm{h,B}}^2}{\rho_{\mathrm{e,B}}^2}\right)\right).
\end{aligned} \tag{A.32b}
$$

A.4 The momentum coefficient model

The momentum coefficient model is suitable only for the main-to-combined pressure loss as it is based solely on a momentum balance. The MCM may be derived identically to the single phase method from Eq. (2.9) using the homogeneous densities for the main and combined legs, and incorporating the additional pressure change associated with the development of the outlet flow regime from Eq. (A.3).

$$\Delta P_{\text{M-C}} = \frac{W_{\text{C}}^2}{\rho_{\text{h,C}} A^2}\left[k_{\text{MCM,M-C}}\left(1 - \frac{(1-\lambda)^2 \rho_{\text{h,C}}}{\rho_{\text{h,M}}}\right) + \frac{\rho_{\text{h,C}}}{\rho_{\text{m,C}}} - \frac{\rho_{\text{h,C}}^2}{2\rho_{\text{e,C}}^2} - \frac{1}{2}\right] \tag{A.33}$$

Note that to achieve this form, the streamline correction factors have been replaced with the estimates from Eq. (A.18).

Similar to the LCM and CCM, the two-phase loss coefficient is solved for in terms of the single-phase coefficient with ω in place of λ. However, an oddity of the model is that the two-phase momentum coefficient is solved for in terms of $k_{1\phi,\text{M-C}}$ rather than $k_{1\phi,\text{m}}$. There also appears to be a publishing error in Schmidt and Loth's [30] paper as they omitted a factor of two in their coefficient. The correct form is:

$$k_{\text{MCM,M-C}} = \frac{1-(1-\omega)^2 + k_{1\phi,\text{M-C}}}{2[1-(1-\omega)^2]}, \tag{A.34}$$

with $k_{1\phi,\text{M-C}} = k_{1\phi,\text{m}}(\omega)$.

Appendix B

Separation Tank Engineering Drawings

The engineering drawings for the construction of the separation tank are included for reference in Fig. B.1.

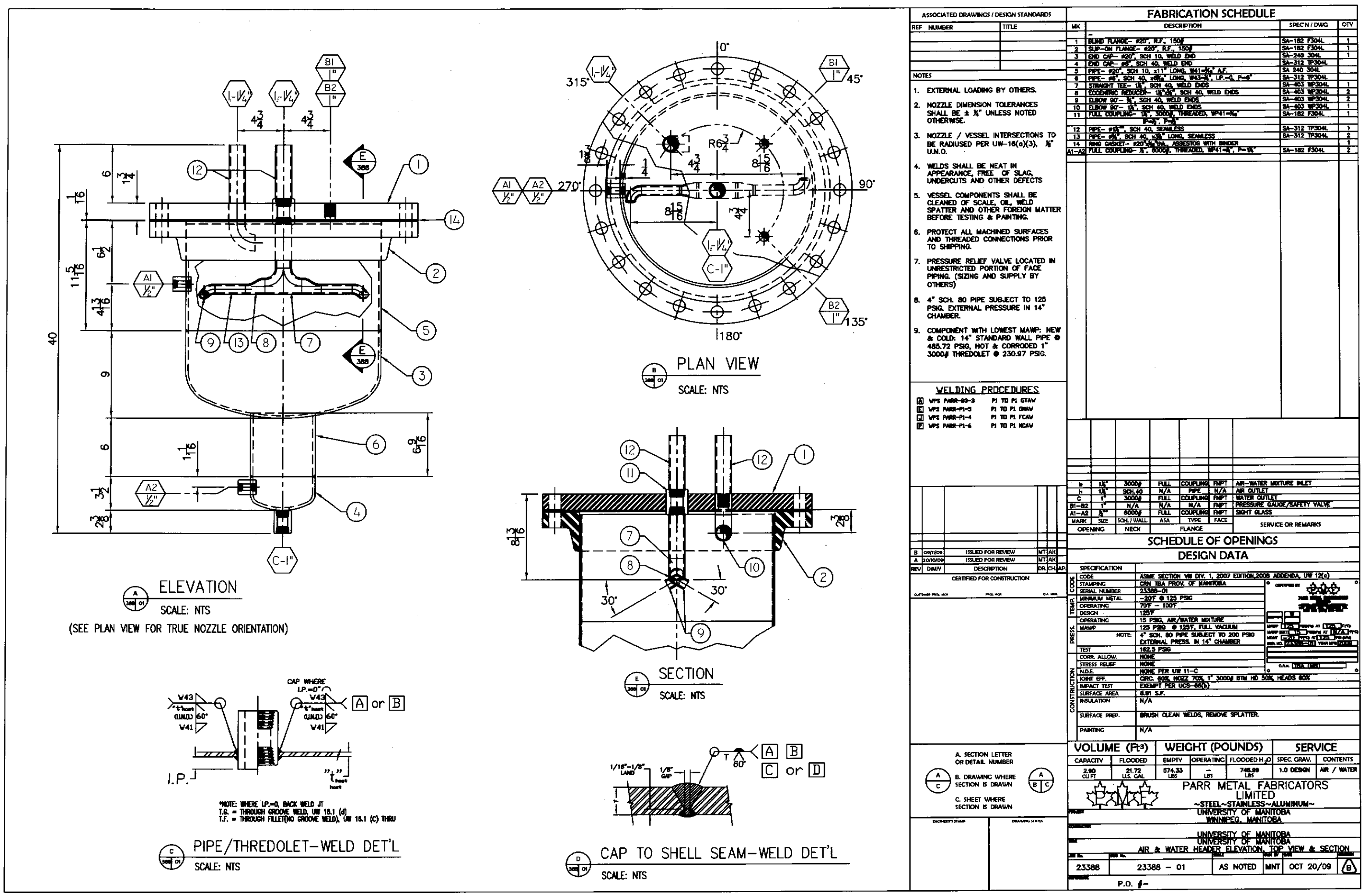

Figure B.1 Engineering drawings of the separation tank produced by Parr Metal Fabricators Limited.

Appendix C

Operating Procedures

C.1 Overview

Standard operating procedures help eliminate user errors and improve repeatability. Detailed procedures for attaining two-phase flow conditions are written here, followed by the method for measuring pressure-loss data and minor modifications to the procedure used in single-phase experiments.

C.2 Setting two-phase operating conditions

The following procedure was used to set the operating conditions for two-phase conditions.

1. Turn on the pressure transducers, turbine meters, thermocouples, PCL-200 pressure calibrator, and data acquisition computer.

2. Turn on the LabVIEW software to record flow rates and set the output path.

3. Record the barometric pressure and set the program for continuous operation at 2 second intervals.

4. Completely open the air outlet to bypass the turbine meters.

5. Set the pressure regulator to 20 psig by turning the handle in until it reaches the stop nut.

6. Set the pressure controller to its maximum.

7. Fully open the water outlet valve on the separation tank.

8. Purge the pressure transducers and their connections to the pressure taps as follows:

   a) Turn on the cooling water.

   b) Adjust the valves to allow water to recirculate in the reservoir without passing through the test section.

   c) Turn on the water pump.

   d) Open the purge line valve.

   e) Open and close valves to allow water to pass through each transducer to the test section, purging one transducer at a time.

   f) Once the transducers have been purged, open and close valves to allow the purge water to bypass the transducers and go through every connection in the test section, one at a time and carefully watching the tubing to see all bubbles have been removed.

   Alternatively, the reference line may be used to purge at very low pressures ensuring that there is no air dissolved in the water. In this case, the pressure reservoir will need to have water added periodically by opening the purge line to it and allowing the pump to fill it.

9. Open transducer 0 to pressure tap B19, the junction's centre.

10. Partially open the air and water control valves downstream of the inlet flow meters.

11. Open the control valves immediately upstream of the suitable inlet flow meters, close all other inlet flow meter control valves and the inlet bypass valves.

12. Gradually close the water recirculation valve which will force water to pass into the test section.

13. Gradually open the central air supply valve.

14. Enter temperature and pressure data into the LabVIEW instrument panel. If the water temperature changed significantly, adjust the cooling water accordingly.

15. Adjust the water and air flow by using the control valves downstream of the instruments.

16. Gradually open valves to the suitable outlet turbine meter and close the air outlet bypass valve.

17. Partially close the water outlet valve on the separation tank until air is no longer discharged into the water reservoir, and the liquid level is stable in the sight glass, preferably in the lower 20 cm of the separation tank.

18. While watching the junction pressure in the LabVIEW instrument panel, slightly close the outlet control to increase the junction pressure closer to the desired operating level.

19. In an iterative process repeat steps 14 to 18, increasing the regulator pressure as necessary to achieve the desired air flow rate and junction pressure.

20. Turn on the pressure controller by reducing its operating pressure valve until its alternate and controller loading gauges rise above their minimum marked operating levels, this will reduce the junction pressure.

21. Increase the pressure by iteratively adjusting the regulator and pressure controller until the desired pressure is reached. Ensure the alternate and controller loading gauges are above their minimum operating levels.

22. Adjust the pressure controller's proportional band and reset valves as desired. Higher proportional band settings mean the controller makes larger adjustments if the pressure changes. The reset control is a second feedback loop acting opposite the proportional band but at a time delay so that continuous oscillations induced by the proportional controller die out. In practice, the reset controller was never necessary as an appropriate proportional gain could be found where the outlet pressure remained very stable.

23. The experiment was considered at steady state when no changes were observed in the flow rates, liquid level in the separation tank, temperatures, or pressures. At this point, the desired sampling frequency and duration were entered into the LabVIEW instrument panel. The program was then run once to record all data pertaining to the mass flow rates.

C.3 Recording pressures

Depending on the flow characteristics, one of two different measuring techniques was used: measuring differential pressures between taps directly, or measuring differential pressures between taps and the reference line. In order to measure differential pressures directly the following steps were taken.

1. Set the LabVIEW instrument panel to record differential pressure data.

2. Close the equalization taps on pressure transducers 4 and 8 and turn on the appropriate transducers in the LabVIEW program.

3. Using the pressure tap manifolds, open taps B1 and M1 to the high side of pressure transducers 4 and 8, respectively, and enter the appropriate tap number in the LabVIEW program.

4. Using the pressure transducer manifolds, open tap C1 in the combined to the low side of both pressure transducers 4 and 8.

5. Run the LabVIEW program and observe the maximum and minimum transducer voltages. If the difference in voltages is greater than 1 V use these transducers for all pressure measurements, otherwise repeat steps 2 to 5 with the next largest transducers.

6. Once the appropriate transducers have been selected, sequentially record the differential pressures for taps B1–B19 and M1–M15 relative tap C1 by opening and closing the appropriate valves and updating the tap numbers in the LabVIEW program.

7. Similarly record taps C1–C15's differential pressures against either tap B1 or M1, whichever has the highest pressure.

In order to measure differential pressure against the reference line the following procedure was used instead.

1. Set the LabVIEW instrument panel to record pressures relative to the 'Reference Line'.

2. Close the equalization taps on pressure transducers 4 and 8 and turn on the appropriate transducers in the LabVIEW program, with transducer 8 as the reference transducer.

3. Using the pressure tap manifolds, open tap B1 to the high side of pressure transducer 4 and tap C1 to the high side of pressure transducer 8. Only enter tap B1 in the LabVIEW program for transducer 4 and enter tap 0 for pressure transducers 5–8.

4. Run the LabVIEW program for a few seconds and observe the pressure transducers' maximum and minimum values.

5. Add pressure to the reference line with the hand pump until the pressure transducers' voltages are in approximately the middle of their ranges.

6. Change the sampling time in the LabVIEW program to several minutes and run the program again. Note the difference between the maximum and minimum readings for the transducers.

7. Repeat steps 2 to 6 but with tap M1 instead of tap B1 connected to the high side of pressure transducer 4.

8. If the difference in voltages is greater than 1 V for any of the transducers use these transducers for all pressure measurements, otherwise repeat steps 2 to 7 with the next largest transducers.

9. Once the appropriate transducers have been selected, sequentially record the differential pressures between taps (B1–B19, M1–M15) and the reference line while simultaneously recording the differential pressure between tap C1 and the reference line.

10. Sequentially record the differential pressures between taps C1–C15 and the reference line while simultaneously recording the differential pressure between either tap B1 or M1 against the reference line, whichever is higher.

The procedure for recording time-varying pressure measurements is identical to that for the time-averaged pressure distribution, but using a separate LabVIEW program. The second program was necessary to handle the amount of data that could be generated by recording at high sampling rates for long periods of time.

C.4 Single-phase operating procedures

The operating procedures for single-phase experiments were nearly identical to those for two-phase flow conditions described in the previous section with the following exceptions.

1. The unused phase's outlet was completely closed.

2. For water flow experiments the rig was completely flooded, including the entire test section. In order to achieve this, the connection between the test section's outlet and the separation tank was elevated so that air could be pushed out with water flow and not reenter the test section.

3. For air flow experiments the rig was completely dry, including the transducers and their connections to the pressure taps.

Appendix D

Calibration

D.1 Overview

In total 10 water rotameters, 8 air rotameters, 6 air turbine meters, 9 pressure transducers, 8 pressure gauges, and 2 thermocouples were calibrated. The instruments used for calibrating, their use, and their ranges are listed in Table D.1.

Table D.1 Instruments used for calibration.

Measuring Instrument	Function	Range of Measurement at Standard Conditions
Small weigh scale	Weigh water for rotameter calibration	(0–35) kg (0.5 g increments)
Large weigh scale	Weigh water for rotameter calibration	(0–800) lbf (0.2 lbf increments)
Small wet test meter	Measure volume of air for rotameter calibration	(0.06–0.625) $m^3\,h^{-1}$
Large wet test meter	Measure volume of air for rotameter calibration	(0.15–15) $m^3\,h^{-1}$
Lab timer	Accurate timer for rotameter calibration	—
0.75 in venturi meter	Measure turbine meter air flow rates	(6–32) $ft^3\,min^{-1}$
1.25 in venturi meter	Measure turbine meter air flow rates	(14–90) $ft^3\,min^{-1}$
2 in venturi meter	Measure turbine meter air flow rates	(29.5–231) $ft^3\,min^{-1}$

Continued on next page

Table D.1 – continued from previous page

Measuring Instrument	Function	Range of Measurement at Standard Conditions
Voltmeter	Measure voltage output by turbine meters and check DAQ system accuracy	—
Omega PCL-200B	Measure local turbine meter pressure during TM calibration	—
Large mercury manometer	Pressure transducer calibration	100 inHg
Large water manometer	Pressure transducer calibration	200 Pa
Backlit small water manometer	Pressure transducer calibration	30 Pa
Hand pump and air cylinder	Set pressure level for transducer calibration	
Lab barometer	Local atmospheric pressure readings for all calibrations	1 mbar increments
Dead weight tester	Calibrate all pressure gauges	—
Lab thermometers	Used to calibrate thermocouples	—

All equipment in the experiment was calibrated in house and compared with previous calibrations from the manufacturer. The following sections document the process used to calibrate each instrument and also difficulties encountered. All equipment used to calibrate with was assumed exact.

D.2 Air rotameters

Calibrations were done at atmospheric pressure and 20 psig for the smaller two flow meters where an appreciable shift was observed. The 20 psig calibration was used for the analysis. Each rotameter's calibration data was plotted in terms of rotameter reading versus standard mass flow rate and compared with two sets of manufacturer's data from previous factory calibrations and also the matching rotameter from the alternate inlet. A sample of the calibration curve is shown in Fig. D.1. The calibrations were implemented through linear interpolations of the data: given a rotameter reading, the standard mass flow rate was linearly interpolated from the bracketing points.

Calibration was carried out using either of the wet test meters depending on the range of calibration. The calibrations were performed as depicted in Fig. D.2. The flow through the rotameter was controlled through a needle valve at the entrance

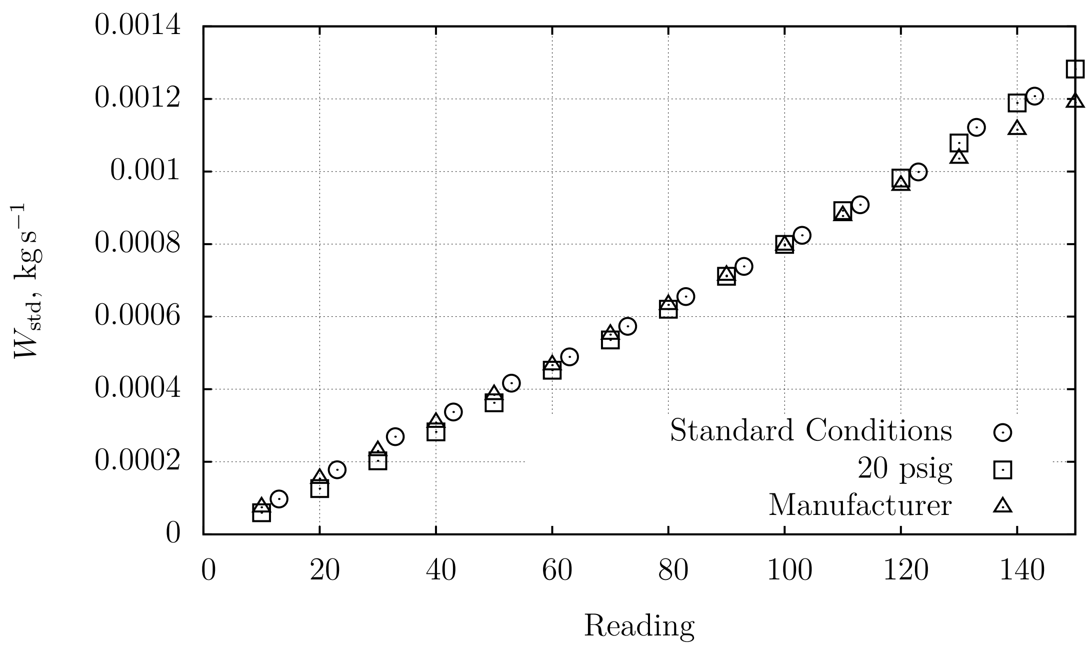

Figure D.1 Sample air rotameter calibration data.

to the rotameter. The pressure and temperature of the flow were measured using a thermocouple and appropriately ranged needle pressure gauge immediately after the rotameter. The wet test meters operate through turning an internal cylinder by buoyant force as air enters into a baffle within the meter. The wet test meters' water levels were checked daily and topped up as required to maintain the optimal value as indicated by the drain valve (filling the meter with the drain valve out, the water should just barely drip out when the meter is full). The gauge on the front of the wet test meter was then monitored and a timer started at a recorded reading. The dial could then be read after a period of time again to measure the volume of air, and then the average velocity calculated. The volume of air was assumed to be at atmospheric pressure since the exhaust port from the meters is of relatively large diameter. Although the air exiting the wet test meter is likely 100 % moist air, it was assumed dry as previous experience suggested correcting for evaporation makes negligible difference.

The atmospheric pressure, rotameter pressure, rotameter temperature, elapsed time, and measured volume were all recorded. The air density at the wet meter and rotameter were then calculated as:

$$\rho_{\text{rotameter}} = \frac{P_{\text{rotameter}}}{RT}. \tag{D.1}$$

The volume flow rate, Q, at the rotameter is then calculated as:

$$Q_{\text{rotameter}} = \frac{\forall\, \rho_{\text{wet test meter}}}{t\rho_{\text{rotameter}}}, \tag{D.2}$$

where $\forall$ is the volume measured by the wet test meter. The standard mass flow rate is then:

$$W_{\text{std}} = Q_{\text{wet test meter}} \sqrt{\frac{\rho_{\text{rotameter}}}{\rho_{\text{std}}}} \rho_{\text{std}}. \tag{D.3}$$

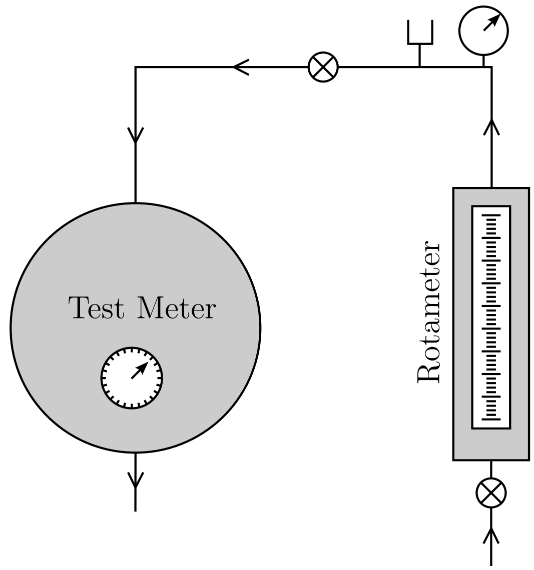

Figure D.2 Air rotameter calibration setup.

D.3 Turbine meters

The turbine meters are the most complicated and problematic equipment used for flow rate measurement. The meters consist of a cylindrical housing, an electronic pick-off, and an internal turbine assembly. As flow passes through the housing, it turns the turbine which creates the electronic signal that is amplified and then measured through the data acquisition system. The source of the main problem lies in the bearings that the turbine assembly spins on: they cannot withstand high loads associated with rapid start-up and shut down operations, and are not sealed so any particulates in the flow can cause failure. The health of the bearings can be monitored through the standard deviation of the output signal in the LabView data acquisition program: normal values are less than 0.04 V when sampled at 1 kHz. Bearing replacement is difficult as the internal parts are quite small and may not be handled by hand as the oils in skin can also degrade the bearings. Detailed instructions for bearing replacement including assembly diagrams are found in the turbine meters maintenance guide. A second problem is that for the higher flow rates the venturi tubes must be used for calibration. Although venturis are highly accurate and reliable, the calibration is more complicated than the simple process of measuring displacement. The procedure for calibration of the turbine meters is outlined below.

The calibration curves for the turbine meters are logistic in shape when plotted as the meter's K-factor versus the Reynolds number. A sample plot of a typical calibration curve is shown in Fig. D.3. It is notable that there is a clear plateau in the curve where the relation becomes strongly linear, in Fig. D.3 at $\mathrm{Re}_{\text{Turbine Meter}} \approx 20\,000$, and the turbine meters should not be used below their linear section to maintain accuracy as at lower flow rates the meter readings are not as repeatable. The calibrations were therefore implemented using a simple linear function.

$$K = a_0 + a_1 \mathrm{Re}_{\text{Turbine Meter}} \tag{D.4}$$

The turbine meter's K-factor is defined as:

$$K = \frac{\text{Voltage}}{Q}. \tag{D.5}$$

The required values to calibrate the turbine meters are the volumentric flow rate, voltage, and Reynolds number at the turbine meter. In order to define these values, the following data must be collected for each calibration point: the turbine meter gauge pressure, venturi inlet gauge pressure, venturi outlet gauge pressure, lab's barometric pressure, and temperature of the air flow (assumed constant). Figure D.4 shows the general setup for calibration. Note that various pressure gauges were required depending on the pressure drop and inlet pressure measured, which could be very small. Eventually, after using several measuring instruments, the transducer bank was employed to provide better results and it is recommended that they should be used

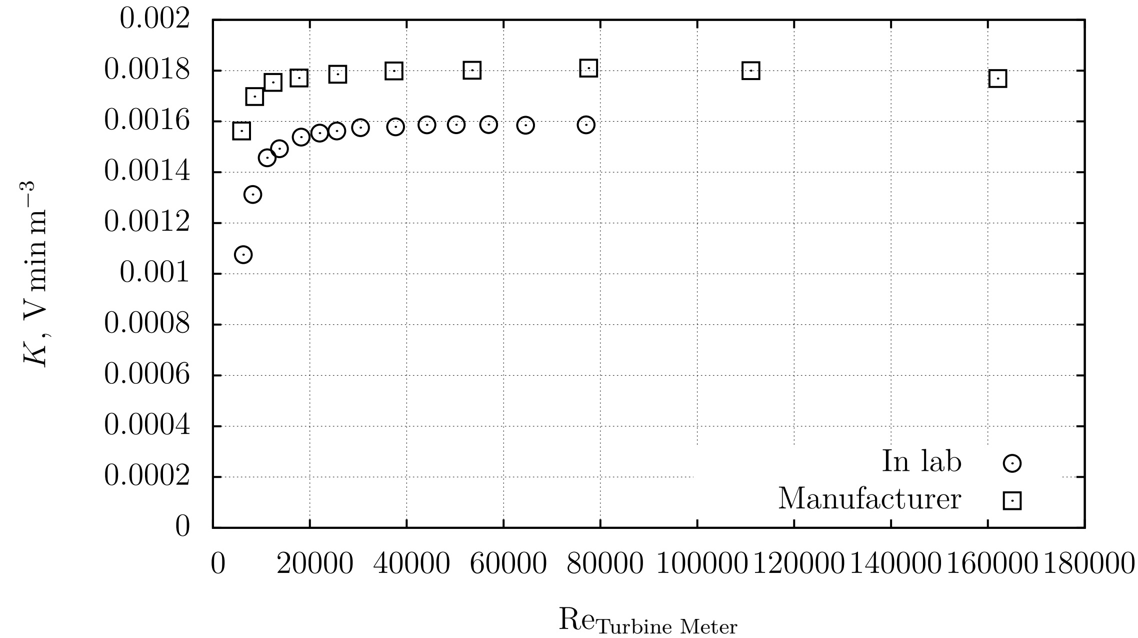

Figure D.3 Sample turbine meter calibration curve with manufacturer data.

for all calibrations with the venturis in the future. The other constant values required for calculations are the turbine meter diameters, which are 0.038 10 m, 0.020 32 m, and the venturi diameters and coefficients which are listed in Table D.2. Note that the coefficients given for the venturi meters are calculated from a line of best fit for the coefficient of discharge as a function of the Reynolds number from the venturis' calibration certificates. The line of best fit was taken as a cubic polynomial:

$$a_{\mathrm{D}} = a_{\mathrm{D0}} + a_{\mathrm{D1}}\mathrm{Re}_{\text{Venturi, throat}} + a_{\mathrm{D2}}\mathrm{Re}^2_{\text{Venturi, throat}} + a_{\mathrm{D3}}\mathrm{Re}^3_{\text{Venturi, throat}}. \tag{D.6}$$

The flow rate calculations for the venturis were made using the method in [89] and outlined below. The actual mass flow rate is defined as:

$$W_{\text{actual}} = YC_{\mathrm{D}}MA_{\text{Venturi,throat}}\sqrt{2\rho_{\text{Venturi,inlet}}(P_{\text{Venturi,inlet}-P_{\text{Venturi,throat}}})}, \tag{D.7}$$

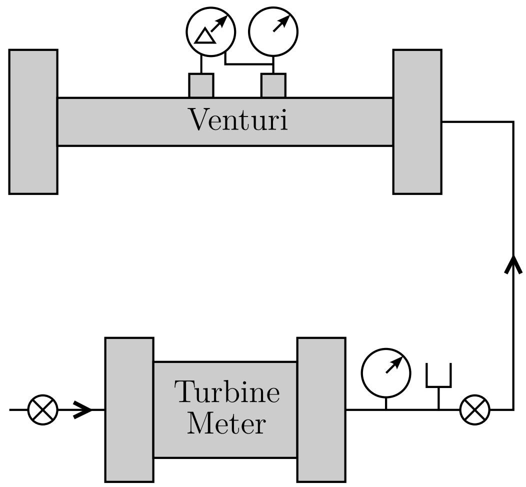

Figure D.4 Turbine meter calibration setup.

where Y is the expansion factor, and M is the velocity of approach factor. The expansion factor is calculated as:

$$Y = \left[\left(\frac{P_{\text{Venturi,throat}}}{P_{\text{Venturi,inlet}}}\right)^{2/\kappa} \frac{\kappa}{\kappa-1} \frac{1-\left(\frac{P_{\text{Venturi,throat}}}{P_{\text{Venturi,inlet}}}\right)^{(\kappa-1)/\kappa}}{1-\frac{P_{\text{Venturi,throat}}}{P_{\text{Venturi,inlet}}}} \right. \\ \left. \frac{1-\left(\frac{D_{\text{Venturi,throat}}}{D_{\text{Venturi,inlet}}}\right)^{4}}{1-\left(\frac{D_{\text{Venturi,throat}}}{D_{\text{Venturi,inlet}}}\right)^{4}\left(\frac{P_{\text{Venturi,throat}}}{P_{\text{Venturi,inlet}}}\right)^{2/\kappa}} \right]^{1/2}, \tag{D.8}$$

and the velocity of approach factor as:

$$M = \frac{1}{\sqrt{1-\left(\frac{D_{\text{Venturi,throat}}}{D_{\text{Venturi,inlet}}}\right)^{4}}}. \tag{D.9}$$

[tbp]

Table D.2 Large, medium, and small venturi meter diameters and discharge coefficients

$D \times 10^{-2}$ m					
Throat	Inlet	$a_{\mathrm{D0}} \times 10^{-1}$	$a_{\mathrm{D1}} \times 10^{-7}$	$a_{\mathrm{D2}} \times 10^{-12}$	$a_{\mathrm{D3}} \times 10^{-18}$
2.540	4.925	9.20	8.09	−3.28	4.29
1.587	3.246	9.26	7.81	−2.75	1.94
0.952	1.884	9.36	4.92	−0.08	−0.93

D.4 Water rotameters

Each rotameter's calibration data was plotted in terms of rotameter reading versus standard mass flow rate and compared with two sets of manufacturer's data from previous factory calibrations and also the matching rotameter from the alternate inlet with the exception of the largest rotameters, FP3/4-27-G-10/55, which no manufacturer calibration data was available for. A sample of these plots is shown in Fig. D.5. The calibrations were implemented through linear interpolations of the data similar to the air rotameters.

Calibration was carried out similarly to the air rotameters, but the mass was measured using the large weigh scale. The flow through the rotameter was controlled with the needle valve *after* the rotameter to avoid a large pressure change through the rotameter, which can cause bubbles of air to form due to the large pressure change, and thereby create an unsteady reading. Both the rotameter pressure and temperature were recorded as well as atmospheric conditions as a precaution, but the water density was treated as constant at $998\,\mathrm{kg\,m^{-3}}$. The mass flow rate is simply:

$$W = \frac{m}{t}. \tag{D.10}$$

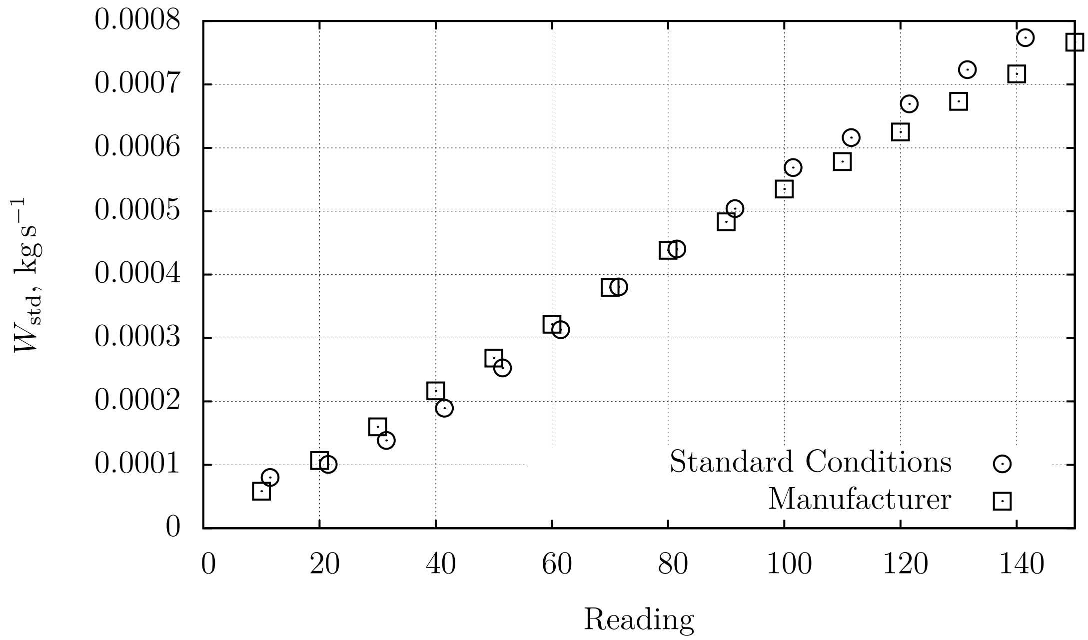

Figure D.5 Sample water rotameter calibration curve with manufacturer's data.

D.5 Pressure transducers

The transducers output a current which is passed through a resistor to give a voltage drop between (2–10) V that is monitored through the data acquisition system. For calibration, the voltage and pressure were monitored simultaneously. The pressure was measured with various water and mercury manometers depending on the range of the transducer being calibrated. Note that the small, backlit water manometer was of particular value for the smallest range transducers. The voltages were measured using the data acquisition system, and to ensure its accuracy, also measured using a multimeter set up directly from the resistor bank. The first calibration was done for each pair of the same range transducers simultaneously. After several months of use, some drift was noted (only noticeable on the smallest range transducers, and on the order of only (1–10) Pa) and future calibrations were done with all transducers simultaneously using the pressure manifolds as shown in Fig. D.6, and removing the lower range transducers as the pressure increased beyond their range. These later calibrations used only the water manometers to measure the pressure, and the data acquisition system to measure the voltage. A plot of the results for transducers 1 and 5 is shown in Fig. D.7. The results were implemented in the analysis program using linear interpolations between points.

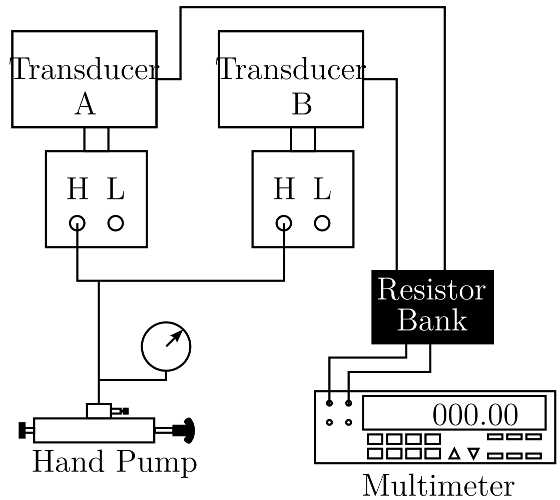

Figure D.6 Pressure transducer calibration setup.

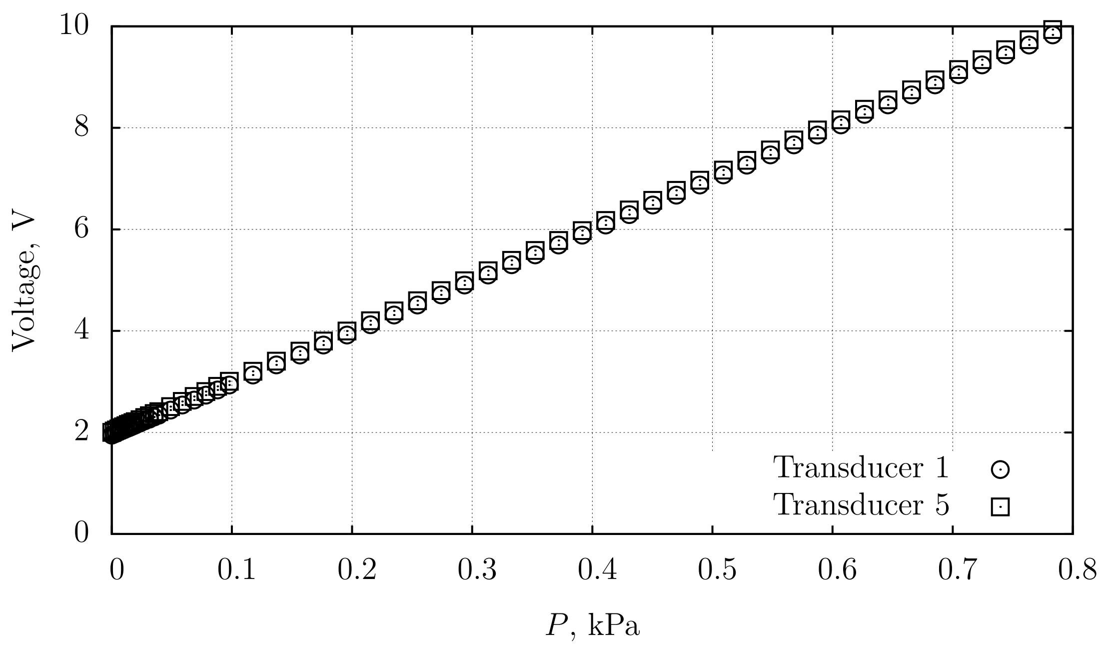

Figure D.7 Sample pressure transducer calibration data.

Appendix E

Uncertainty Analysis

E.1 Fixed uncertainties

All uncertainty analysis require an estimate of fixed errors for each measured parameter. Most of the fixed errors are estimates based on the calibration curves of the instruments. Table E.1 lists all of the values used in the analysis.

Figure D.7 on page 192 presents calibration data for the smallest range transducers, 1 and 5. The data forms an almost perfect linear regression with a calibration curve having much less than 1 % uncertainty; however, as a conservative estimate and allowance for the possibility of drift, a value of 1 % was adopted for all transducers. The barometer, PCL 200, and test section diameter uncertainties are taken from the manufacturers' data. The thermocouples, water rotameter pressure gauges, and rotameters uncertainties are based on their respective calibrations as well as an allowance for error in reading for both the pressure gauges and rotameters. The turbine meter calibration is given in terms of one of its calibration coefficients, a_0,

Table E.1 Fixed uncertainties associated with the apparatus.

Element	Uncertainty
Transducers	$\pm 1\,\%$ of reading
Thermocouples	$\pm 1\,°\mathrm{C}$
Barometer	$\pm 0.5\,\mathrm{kPa}$
PCL200	$\pm 0.5\,\mathrm{kPa}$
Dial-type pressure gauges	$\pm 2.1\,\mathrm{kPa}$
Test section diameter	$\pm 2 \times 10^{-4}\,\mathrm{m}$
Turbine meter calibration	$\pm 3\,\%$ of coefficient a_0 (see Eq. (D.4), page 186)
Rotameter	$\pm 2\,\%$ of reading

corresponding to the intercept value of the linear fit of the turbine meters' calibration data (see Eq. (D.4), page 186). When the data is plotted along with the calibration curve, all of the data fit within $\pm 0.03 \times a_0$ of the calibration curve. The generic value of 3 % was chosen for all turbine meters and all calibrations simply as a matter of convenience since they had bearings replaced often and were recalibrated each time, and it would have become tedious to define the exact limits for each data-set. All turbine meter calibrations were checked to be sure that the data fell within 3 % of a_0.

E.2 Pressure measurement uncertainty

Figure 4.1 on page 46 shows typical pressure loss data for a gas-liquid experiment. The fully developed flow data far from the junction forms a straight line consistent with fully developed pipe flow theory. The intercepts of the extrapolated fully developed lines to the junction centre provides the means for calculation of the junction pressure drops defined as:

$$\Delta P_{i\mathrm{C}} = P_i - P_{\mathrm{C}}, \text{ where } i = \mathrm{B, M}. \tag{E.1}$$

Calculation of the pressure drops in this fashion is standard, but it introduces two difficulties. The first is that use of the extrapolated lines results in the pressure drops being sensitive to the choice of curve-fitting method, and in fact, the uncertainty in the lines dominates the uncertainty in the calculated pressure drops. The second difficulty is that the extrapolated lines must use only fully developed data which requires some criteria be developed to determine where the data begins to deviate from fully developed. In order to deal with both difficulties, the analysis employs a statistical method, shown by Walpole and Myers [85], to develop the lines of best fit as explained in Section 4.2. Additionally, the total uncertainty for the pressure drops combines the curve fitting uncertainty with that of the pressure transducers and their calibrations.

Curve-fitting uncertainty

For a population of n values of a variable, say P, the statistical moment (MMT) of order k about some value c is:

$$\mathrm{MMT}_c^k(P) = \frac{1}{n}\sum_{i=1}^{n}(P-c)^k. \tag{E.2}$$

Using this definition, the uncertainty of the curve fit is calculated as follows:

$$(\delta P_i)_{\text{curve fit}} = \frac{\mathrm{t}_{0.95,n-2}\sqrt{\mathrm{MMT}^2_{P_\mathrm{r}}(P)\mathrm{MMT}^2_0(z)}}{\sqrt{n\mathrm{MMT}^2_{\mathrm{AM}(z)}(z)}}, i = \mathrm{B,\ M,\ C}, \tag{E.3}$$

where n is the number of points used for the regression, $\mathrm{t}_{0.95,n-2}$ is Student's t-statistic for a confidence interval of 95 % with $n-2$ degrees of freedom, and P_r is the value of the linear regression calculated for the experimental data. Using a 95 % confidence interval means that the odds are 20 to 1 the uncertainty will be within the calculated interval.

Transducer uncertainty

The uncertainty contribution to the pressure losses from the transducers and their calibrations follows from the basic uncertainty equation:

$$(\delta P_i)_{\text{transducer}} = P_i\left(\frac{\delta K}{K}\right), i = \mathrm{B,\ M,\ C}, \tag{E.4}$$

where $\delta K/K$ is the relative uncertainty in the transducers calibrations, in other words the uncertainty in each transducer's calibration curve.

Total pressure drop uncertainty

The value of the uncertainty in the branch, main, and combined's extrapolated pressures at the junction are found using the root-mean-sum method to combine the curve fitting, transducer uncertainties, and also the data reduction operations (see Section 4.2, page 43). If the reference line was in use the uncertainties are:

$$\delta P_i = \left((\delta P_i)^2_{\text{curve fit}} + (\delta P_i)^2_{\text{transducer}} + (\delta P_{\text{C1}})^2_{\text{transducer}}\right)^{1/2}, \; i = \text{B, M}, \tag{E.5a}$$

$$\delta P_{\text{C}} = \left((\delta P_{\text{C}})^2_{\text{curve fit}} + (\delta P_{\text{C}})^2_{\text{transducer}} + 2(\delta P_{\text{C1}})^2_{\text{transducer}}\right)^{1/2}, \tag{E.5b}$$

where δP_{C1} is the uncertainty in the measurement for tap C1. If the reference line was not in use the uncertainties are:

$$\delta P_i = \left((\delta P_i)^2_{\text{curve fit}} + (\delta P_i)^2_{\text{transducer}}\right)^{1/2}, \; i = \text{B, M}, \tag{E.6a}$$

$$\delta P_{\text{C}} = \left((\delta P_{\text{C}})^2_{\text{curve fit}} + (\delta P_{\text{C}})^2_{\text{transducer}} + (\delta P_{\text{C1}})^2_{\text{transducer}}\right)^{1/2}. \tag{E.6b}$$

The root-mean-sum method is again used to combine the intercepts uncertainty to calculate the final extrapolated pressure drops' uncertainty.

$$\delta(\Delta P_{i\text{-C}}) = \left((\delta P_i)^2 + (\delta P_{\text{C}})^2\right)^{1/2}. \tag{E.7}$$

E.3 Other uncertainties

The numerical method of sequential perturbation estimates the uncertainty in all of the other calculated parameters. The algorithm requires recalculating each output repeatedly, each time perturbing a different input by its estimated fixed error. As a result, the process requires calculating each output in terms of the most basic inputs which we have estimates of the fixed error for. Please note that while Moffat [86] suggests the use of sequential perturbation only where traditional analysis becomes difficult due to large numbers of variables, the current analysis employs it for all uncertainty calculations except pressures for simplicity of implementation in the analysis program. Hand calculations performed for select parameters show very good agreement between the traditional and numerical uncertainty analysis.

The sequential perturbation method is as follows.

1. Calculate the value of the variable using all nominal values. For example, W_G for an experiment using rotameters to measure the flow rate is calculated as a function of the measured parameters:

$$W_\mathrm{G} = f(T, P_\mathrm{B19}, P_\mathrm{rotameter}, K_\mathrm{rotameter}, D), \tag{E.8}$$

   where T is the temperature and K is the rotameter reading.

2. Recalculate the value of the variable using all except one nominal value, which is perturbed by its uncertainty value $+\delta i$. For example:

$$W_\mathrm{G}^{+\delta T} = f(T + \delta T, P_\mathrm{B19}, P_\mathrm{rotameter}, K_\mathrm{rotameter}, D). \tag{E.9}$$

3. Recalculate the value of the variable using nominal values except the one from step two, which is perturbed by value $-\delta i$. For example:

$$W_\mathrm{G}^{-\delta T} = f(T - \delta T, P_\mathrm{B19}, P_\mathrm{rotameter}, K_\mathrm{rotameter}, D). \tag{E.10}$$

4. Repeat steps two and three for each other dependant variable.

5. Calculate the combined effect of the positive perturbations with the root-sum-square method.

$$\delta W_\mathrm{G}^{+\delta} = \left(\sum (W_\mathrm{G} - W_\mathrm{G}^{+\delta i})^2\right)^{1/2}. \tag{E.11}$$

6. Repeat step five for the negative perturbations.

7. Calculate the total effect of both the positive and negative perturbations as the average of both.

$$\delta W_{\mathrm{G}} = \frac{\delta W_{\mathrm{G}}^{+\delta} + \delta W_{\mathrm{G}}^{-\delta}}{2}. \tag{E.12}$$

The averaging of the positive and negative perturbations attempts to compensate for non-linear effects. For example, consider some function, f, plotted against its dependant parameter, n, as shown in Fig. E.1. The positive and negative perturbations clearly result in differing amounts of change in f, but as the real uncertainty is uknown, the two are averaged to give an overall estimate.

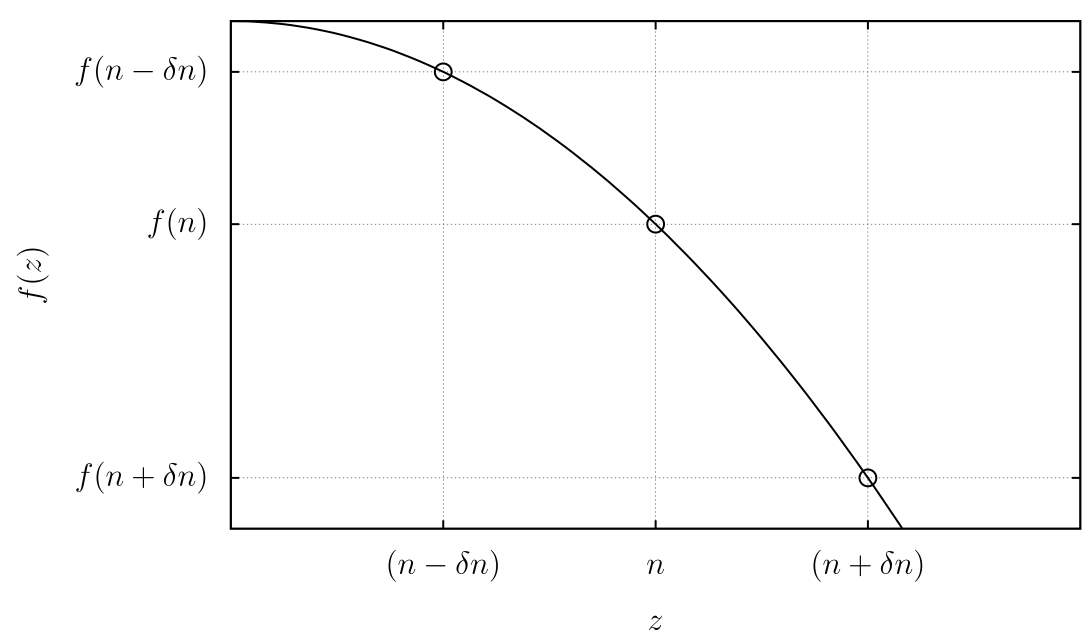

Figure E.1 Effect of averaging perturbations on non-linear uncertainty.

Appendix F

Experiment Data

Table F.1 Single-phase experiment results.

Test	Fluid	P_{junction}	W_{C}	λ	dP/dz_{M}	dP/dz_{B}	dP/dz_{C}	$\Delta P_{\text{M-C}}$	$\Delta P_{\text{B-C}}$
		kPa	$\mathrm{kg\,s^{-1}}$		$\mathrm{Pa\,m^{-1}}$			Pa	
01	Air	133.7	0.070	1.000	—	539.6 ± 36.7	642.8 ± 36.7	—	$1\,247.3 \pm 57.0$
02	Air	133.2	0.069	0.940	21.5 ± 17.7	479.3 ± 33.4	599.6 ± 26.3	$1\,770.1 \pm 53.7$	$1\,328.8 \pm 48.6$
03	Air	134.7	0.070	0.850	28.0 ± 11.2	416.5 ± 24.6	645.3 ± 43.6	$1\,797.3 \pm 53.4$	$1\,405.9 \pm 51.5$
04	Air	138.2	0.073	0.690	85.5 ± 6.0	289.6 ± 15.6	707.5 ± 42.0	$1\,867.7 \pm 52.3$	$1\,628.2 \pm 53.1$
05	Air	136.2	0.071	0.600	119.3 ± 5.6	224.5 ± 13.1	674.6 ± 32.7	$1\,649.4 \pm 43.4$	$1\,505.1 \pm 44.2$
06	Air	136.5	0.072	0.500	176.4 ± 12.6	166.3 ± 10.5	643.2 ± 33.3	$1\,572.6 \pm 44.5$	$1\,522.3 \pm 43.7$
07	Air	134.1	0.069	0.400	239.5 ± 11.0	105.6 ± 6.6	613.9 ± 30.0	$1\,298.6 \pm 39.8$	$1\,329.6 \pm 39.0$
08	Air	135.6	0.072	0.290	335.6 ± 16.1	69.7 ± 4.8	649.4 ± 31.0	$1\,105.7 \pm 41.6$	$1\,198.2 \pm 39.1$
09	Air	136.3	0.074	0.200	419.4 ± 20.5	33.9 ± 2.6	635.5 ± 34.8	806.7 ± 44.9	924.6 ± 40.6
10	Air	136.0	0.074	0.150	476.9 ± 27.2	21.9 ± 4.4	696.3 ± 56.3	583.2 ± 65.3	721.2 ± 59.9
11	Air	134.0	0.073	0.050	529.9 ± 31.4	1.1 ± 8.5	658.4 ± 42.7	213.1 ± 55.1	294.6 ± 46.3
12	Air	133.8	0.071	0.000	565.9 ± 32.4	—	621.1 ± 35.7	-11.0 ± 49.8	—
13	Air	135.2	0.036	0.930	1.5 ± 1.1	145.7 ± 7.2	183.3 ± 6.2	472.7 ± 10.1	349.8 ± 11.6
14	Air	135.0	0.036	0.800	12.1 ± 0.5	108.1 ± 4.3	182.5 ± 10.7	461.6 ± 13.2	373.7 ± 13.4
15	Air	136.8	0.037	0.700	20.1 ± 1.0	92.9 ± 3.7	194.0 ± 7.7	458.8 ± 11.1	388.5 ± 11.2
16	Air	134.5	0.036	0.590	33.7 ± 1.0	64.2 ± 2.2	180.4 ± 7.2	400.5 ± 10.2	364.7 ± 10.1
17	Air	135.5	0.036	0.500	52.3 ± 0.3	48.1 ± 1.4	182.3 ± 7.9	372.6 ± 10.5	360.5 ± 10.5
18	Air	136.1	0.036	0.410	68.0 ± 0.9	36.4 ± 2.8	185.0 ± 8.2	335.5 ± 10.6	336.8 ± 10.9
19	Air	136.7	0.036	0.310	89.6 ± 0.6	21.9 ± 0.4	182.1 ± 6.1	288.1 ± 8.7	306.0 ± 8.8
20	Air	137.0	0.036	0.210	111.0 ± 2.9	11.7 ± 0.3	187.5 ± 8.9	209.6 ± 10.9	232.6 ± 10.6
21	Air	135.8	0.038	0.150	161.5 ± 7.8	6.6 ± 1.1	222.1 ± 11.7	153.9 ± 15.2	200.6 ± 13.3
22	Air	134.8	0.036	0.070	161.3 ± 4.7	1.8 ± 0.1	194.6 ± 9.3	76.4 ± 11.4	98.5 ± 10.5
23	Air	135.8	0.038	0.050	187.4 ± 5.7	1.0 ± 0.7	216.6 ± 11.7	47.7 ± 13.9	79.2 ± 12.8
24	Air	136.1	0.036	0.000	182.5 ± 7.5	—	183.3 ± 7.5	11.6 ± 11.2	—
25-1	Water	100.7	0.260	0.000	24.0 ± 0.9	—	24.3 ± 0.4	-2.0 ± 1.1	—
25-2	Water	108.3	0.263	0.000	25.0 ± 0.3	—	24.9 ± 0.6	-2.0 ± 0.8	—
26	Water	107.0	0.263	0.120	19.9 ± 0.3	0.7 ± 0.1	25.2 ± 0.6	7.6 ± 0.9	2.8 ± 0.8
27	Water	107.7	0.257	0.210	15.8 ± 0.2	1.2 ± 0.1	23.8 ± 0.6	15.5 ± 0.9	10.2 ± 0.8
28	Water	107.1	0.263	0.300	11.7 ± 0.2	2.9 ± 0.1	23.3 ± 0.2	21.9 ± 0.7	15.1 ± 0.6

Continued on next page

Table F.1 – continued from previous page

Test	Fluid	P_{junction}	W_{C}	λ	dP/dz_{M}	dP/dz_{B}	dP/dz_{C}	$\Delta P_{\text{M-C}}$	$\Delta P_{\text{B-C}}$
		kPa	$\mathrm{kg\,s^{-1}}$		$\mathrm{Pa\,m^{-1}}$			Pa	
29	Water	107.4	0.266	0.400	10.2 ± 0.3	4.7 ± 0.2	24.3 ± 0.2	26.1 ± 0.8	20.5 ± 0.7
30-1	Water	107.1	0.264	0.500	7.5 ± 0.2	6.8 ± 0.1	24.0 ± 0.4	31.6 ± 0.9	23.7 ± 0.8
30-2	Water	103.7	0.264	0.500	6.8 ± 0.2	6.8 ± 1.4	23.0 ± 0.6	38.5 ± 1.1	35.8 ± 1.7
31	Water	108.4	0.263	0.590	5.2 ± 0.3	10.4 ± 0.5	23.5 ± 0.2	35.9 ± 0.9	25.1 ± 0.9
32	Water	108.1	0.264	0.700	3.3 ± 0.4	12.5 ± 0.1	24.1 ± 0.2	39.1 ± 0.9	27.8 ± 0.8
33	Water	108.0	0.264	0.790	1.3 ± 0.3	16.0 ± 0.1	24.4 ± 0.2	40.8 ± 0.9	27.2 ± 0.8
34	Water	110.3	0.269	0.890	0.8 ± 0.1	22.0 ± 0.1	24.6 ± 0.2	43.7 ± 0.9	23.9 ± 0.7
35	Water	110.5	0.266	1.000	—	24.7 ± 0.2	24.9 ± 0.2	—	23.9 ± 0.8
36	Water	144.4	0.366	0.370	19.5 ± 0.2	7.5 ± 0.2	42.9 ± 0.4	52.7 ± 1.4	46.1 ± 1.3
37	Water	153.0	0.449	0.500	18.7 ± 0.4	19.1 ± 1.1	62.0 ± 0.2	96.1 ± 2.1	82.1 ± 2.2

Table F.2 Two-phase results with annular flow in the combined side (St=stratified, W=wavy, A=annular, SA=semi-annular).

Test	P_{junction}	W_{C}	x_{C}	λ_{G}	λ_{L}	dP/dz_{M}	dP/dz_{B}	dP/dz_{C}	$\Delta P_{\text{M-C}}$	$\Delta P_{\text{B-C}}$	Flow regime		
	kPa	$\mathrm{kg\,s^{-1}}$				$\mathrm{Pa\,m^{-1}}$			Pa		M	B	C
01	150.2	0.106	0.535	0.503	0.500	216.9±7.4	234.0±33.2	1 100.5±29.2	1 179.5±45.8	1 110.6±55.8	W	W	A
02	149.7	0.052	0.523	0.000	0.000	204.8±7.9	—	204.9±10.6	1.8±14.1	—	W	—	W
03	149.3	0.056	0.899	0.302	0.193	192.3±3.2	42.0±5.1	404.2±6.0	509.0±15.2	534.1±15.9	W	St	SA
04	149.3	0.056	0.898	0.302	0.802	163.9±4.7	50.3±4.4	392.3±5.8	521.3±15.3	540.0±15.4	W	St	SA
05	150.4	0.056	0.898	0.698	0.193	40.8±6.7	184.6±10.4	420.8±4.6	780.2±18.2	612.3±18.7	St	W	SA
06	149.7	0.055	0.896	0.697	0.799	54.0±23.2	205.8±19.2	384.7±3.8	804.1±28.3	682.9±24.5	St	W	SA
07	150.1	0.102	0.304	0.000	0.200	370.0±14.2	2.8±2.5	359.8±8.6	−14.0±18.1	115.5±12.1	SA	—	SA
08	150.2	0.102	0.305	0.000	0.400	313.9±9.8	9.1±1.9	351.3±19.9	40.8±21.2	157.8±60.5	SA	—	SA
09	150.5	0.102	0.305	0.000	0.599	276.6±8.0	2.7±2.2	346.8±17.9	73.8±28.8	216.7±68.5	SA	—	SA
10	150.5	0.102	0.304	0.000	0.800	204.9±7.1	7.2±3.2	378.4±19.5	70.4±22.3	204.2±21.8	SA	—	SA
11	150.6	0.102	0.309	0.284	0.200	211.7±4.2	32.3±6.7	400.5±13.8	275.2±17.7	274.1±18.5	W	St	SA
12	149.9	0.102	0.308	0.284	0.400	173.5±8.0	14.1±5.2	418.3±21.1	256.0±24.9	314.2±24.4	W	St	SA
13	150.0	0.102	0.311	0.284	0.603	151.5±7.4	26.4±7.4	403.7±6.9	284.3±14.5	345.6±14.9	W	St	SA
14	150.3	0.104	0.303	0.288	0.805	110.4±8.0	31.2±7.0	402.8±21.1	296.5±25.0	385.1±25.0	W	W	SA
15	149.5	0.101	0.300	0.502	0.198	71.7±3.9	62.3±10.2	376.9±24.2	357.8±26.6	290.5±28.0	W	St	SA
16-1	150.2	0.101	0.298	0.500	0.399	65.5±10.1	79.4±5.4	351.3±15.8	385.1±21.4	339.7±19.4	W	W	SA
16-2	149.6	0.102	0.295	0.501	0.410	92.7±14.9	89.8±3.1	353.0±12.2	344.7±52.0	322.5±16.0	W	St	SA
17-1	150.3	0.101	0.299	0.499	0.599	52.2±7.0	89.1±6.5	346.4±15.5	384.1±19.8	355.2±19.5	W	W	SA
17-2	149.2	0.101	0.298	0.503	0.599	49.9±5.4	81.4±4.9	345.6±15.8	380.7±19.6	355.1±19.3	W	W	SA
18	150.5	0.103	0.293	0.497	0.805	27.5±5.2	117.7±13.9	377.4±14.8	396.3±19.1	340.9±22.8	St	W	SA
19	150.0	0.101	0.299	0.703	0.200	9.7±7.0	123.3±6.1	349.8±54.1	498.5±55.7	319.9±55.3	W	W	SA
20	150.5	0.101	0.301	0.703	0.399	23.7±9.6	172.0±25.2	328.0±71.1	530.4±72.6	367.8±76.8	W	W	SA
21	149.7	0.101	0.300	0.702	0.599	7.2±3.6	184.9±16.5	341.9±16.7	525.3±20.5	383.0±25.6	St	W	SA

Continued on next page

Table F.2 – continued from previous page

Test	P_{junction}	W_{C}	x_{C}	λ_{G}	λ_{L}	dP/dz_{M}	dP/dz_{B}	dP/dz_{C}	$\Delta P_{\text{M-C}}$	$\Delta P_{\text{B-C}}$	Flow regime		
	kPa	$\text{kg}\,\text{s}^{-1}$					$\text{Pa}\,\text{m}^{-1}$		Pa		M	B	C
22	150.0	0.101	0.299	0.702	0.800	13.1±2.2	217.3±22.8	370.7±18.4	503.2±21.9	377.8±31.2	St	W	SA
23	149.7	0.101	0.302	1.000	0.200	20.5±14.3	207.0±9.1	370.2±15.8	656.4±25.0	437.3±21.3	—	SA	SA
24	149.9	0.102	0.305	1.000	0.400	0.0±0.0	264.7±18.4	384.6±0.0	682.3±13.6	445.5±21.7	—	SA	SA
25	150.4	0.101	0.309	1.000	0.594	0.4±1.6	299.4±18.7	356.8±40.9	695.4±43.0	459.6±46.3	—	SA	SA
26	149.5	0.100	0.305	1.000	0.797	0.3±4.6	350.4±50.7	341.7±31.1	709.8±34.1	455.6±63.1	—	SA	SA
27	149.6	0.102	0.506	0.000	0.201	734.0±13.2	0.1±3.2	863.4±99.4	69.7±101.9	189.9±101.3	SA	—	A
28	149.3	0.102	0.505	0.000	0.399	663.9±15.5	5.5±2.6	858.7±83.7	99.9±87.1	246.8±86.0	SA	—	A
29	149.5	0.102	0.505	0.000	0.600	584.9±10.5	0.0±0.0	846.2±0.0	174.7±21.4	353.1±20.0	SA	—	A
30	149.9	0.102	0.504	0.000	0.800	461.5±0.0	0.0±0.0	928.9±33.0	85.7±38.4	274.9±39.1	SA	—	A
31	151.3	0.113	0.505	0.295	0.199	501.7±13.3	43.5±7.1	1 142.9±27.3	796.8±42.4	872.0±41.3	SA	St	A
32	151.5	0.113	0.504	0.295	0.400	440.9±17.4	73.5±11.8	1 115.4±215.7	879.2±38.5	929.1±48.1	SA	St	A
33	151.5	0.113	0.506	0.295	0.599	378.1±20.3	92.5±7.1	1 174.9±31.6	848.5±48.5	872.6±44.7	W	W	A
34-1	151.8	0.113	0.507	0.295	0.801	323.9±5.2	111.4±9.7	1 182.5±44.0	826.8±53.8	867.8±54.6	W	W	A
34-2	150.0	0.108	0.487	0.295	0.800	248.3±12.8	97.6±8.1	1 016.1±12.3	878.8±32.9	948.1±31.9	W	W	A
35	148.6	0.112	0.499	0.502	0.199	272.4±6.3	139.7±7.7	1 125.0±33.9	1 016.2±46.4	989.1±46.5	W	W	A
36	146.0	0.112	0.500	0.498	0.399	250.2±6.5	182.8±8.2	1 117.7±25.7	1 162.8±41.7	1 135.3±41.9	W	W	A
37	144.2	0.112	0.499	0.496	0.599	227.6±9.7	222.7±11.8	1 175.9±43.0	1 154.4±55.2	1 125.2±55.4	W	W	A
38	150.7	0.114	0.512	0.486	0.809	177.9±7.5	242.8±17.3	1 199.1±47.1	1 355.6±59.4	1 330.4±61.3	W	W	A
39	148.8	0.111	0.497	0.697	0.199	81.4±5.4	306.5±12.4	1 095.8±25.5	1 435.5±42.9	1 225.2±43.0	W	W	A
40	149.1	0.112	0.496	0.698	0.399	73.5±4.4	360.9±15.8	1 091.9±27.5	1 471.8±44.3	1 276.0±45.6	W	W	A
41	151.7	0.113	0.502	0.698	0.598	60.9±6.9	403.0±20.6	1 094.6±99.0	1 516.6±105.1	1 317.2±106.4	St	SA	A
42	151.3	0.112	0.501	0.702	0.802	39.5±5.5	441.0±22.3	1 099.1±37.8	1 530.0±51.9	1 331.8±55.1	St	SA	A
43	149.8	0.101	0.500	1.000	0.201	13.2±6.9	547.3±41.8	800.1±171.2	1 502.4±173.8	959.3±177.9	—	SA	A
44	150.4	0.101	0.500	1.000	0.399	−5.6±4.0	557.9±23.1	808.1±24.6	1 500.0±38.4	1 096.9±42.3	—	SA	A

Continued on next page

Table F.2 – continued from previous page

Test	P_{junction}	W_{C}	x_{C}	λ_{G}	λ_{L}	dP/dz_{M}	dP/dz_{B}	dP/dz_{C}	$\Delta P_{\text{M-C}}$	$\Delta P_{\text{B-C}}$	Flow regime		
	kPa	$\text{kg}\,\text{s}^{-1}$				$\text{Pa}\,\text{m}^{-1}$			Pa		M	B	C
45	150.2	0.101	0.498	1.000	0.600	2.1±6.3	638.1±90.1	717.3±65.6	1 620.1±71.8	1 233.1±259.8	—	SA	A
46	149.9	0.100	0.498	1.000	0.800	−8.0±6.7	709.0±30.5	771.2±41.1	1 540.5±50.6	1 145.2±57.1	—	SA	A
47	150.5	0.101	0.698	0.000	0.204	1 076.9±0.0	8.4±8.7	1 230.8±0.0	63.8±25.7	206.0±28.1	A	—	A
48	150.3	0.101	0.701	0.000	0.398	997.3±16.9	−3.3±2.4	1 275.3±27.8	39.2±41.9	228.3±39.4	A	—	A
49	150.2	0.100	0.698	0.000	0.602	864.8±12.9	4.2±6.7	1 276.8±25.7	112.5±39.4	296.0±38.8	SA	—	A
50	150.6	0.100	0.697	0.000	0.797	706.3±15.6	1.8±3.9	1 355.8±30.5	80.7±44.4	259.7±42.7	SA	—	A
51	165.9	0.113	0.700	0.298	0.197	670.7±22.9	71.3±13.1	1 479.7±22.4	1 156.2±50.8	1 271.0±48.0	SA	St	A
52	150.5	0.102	0.704	0.299	0.198	592.8±13.7	68.9±7.2	1 348.5±29.6	1 194.1±49.4	1 272.9±48.5	SA	St	A
53	167.4	0.112	0.698	0.295	0.402	619.8±26.1	91.0±7.6	1 460.0±77.3	1 258.3±90.8	1 387.5±87.8	SA	W	A
54	150.5	0.101	0.699	0.299	0.402	522.4±16.4	96.4±4.2	1 295.9±5.5	1 250.5±40.4	1 319.0±37.7	SA	St	A
55	149.9	0.101	0.700	0.299	0.601	440.0±12.8	120.9±8.2	1 306.0±20.7	1 212.3±43.7	1 255.4±42.9	SA	St	A
56	167.8	0.113	0.701	0.295	0.599	561.6±32.3	126.6±12.9	1 470.4±78.0	1 272.9±93.5	1 396.7±89.1	SA	W	A
57	149.3	0.104	0.670	0.299	0.826	317.0±11.2	127.5±6.9	1 335.0±17.3	1 213.3±42.3	1 256.6±41.7	SA	W	A
58	149.9	0.103	0.707	0.486	0.198	358.6±9.7	177.7±29.6	1 408.9±23.9	1 713.1±49.9	1 723.1±63.0	SA	W	A
59	150.4	0.103	0.707	0.490	0.402	333.9±13.7	288.8±28.2	1 497.6±76.9	1 685.3±89.8	1 604.8±92.8	SA	SA	A
60	149.8	0.103	0.706	0.489	0.601	277.7±17.4	300.2±12.4	1 398.4±27.6	1 868.4±54.8	1 808.3±53.0	SA	W	A
61	150.2	0.107	0.678	0.488	0.826	203.0±7.7	334.4±17.8	1 487.2±53.5	1 810.6±70.8	1 742.2±72.2	SA	W	A
62	149.7	0.102	0.705	0.682	0.198	74.3±38.3	396.7±40.6	1 436.8±39.6	2 045.0±71.9	1 680.4±71.2	W	SA	A
63	150.4	0.103	0.706	0.681	0.402	107.4±16.9	451.8±17.5	1 405.1±29.3	2 123.1±57.4	1 852.8±55.7	W	SA	A
64	150.1	0.103	0.706	0.680	0.601	116.6±9.2	548.6±62.2	1 407.3±28.1	2 109.0±54.9	1 792.7±80.9	W	SA	A
65	149.6	0.102	0.706	0.680	0.801	68.6±8.5	551.1±19.2	1 417.7±31.2	2 062.0±56.1	1 790.8±56.9	St	SA	A
66	150.4	0.101	0.699	1.000	0.204	15.7±2.7	731.0±0.0	1 311.8±33.8	2 267.4±57.0	1 616.8±52.3	—	SA	A
67	150.8	0.101	0.701	1.000	0.402	16.5±3.3	897.7±132.1	1 263.8±91.7	2 315.7±102.3	1 718.2±199.1	—	SA	A
68	150.2	0.101	0.701	1.000	0.598	1.3±11.2	1 000.0±0.0	1 115.4±215.7	2 549.8±220.6	1 964.4±219.3	—	A	A

Continued on next page

Table F.2 – continued from previous page

Test	P_{junction}	W_{C}	x_{C}	λ_{G}	λ_{L}	dP/dz_{M}	dP/dz_{B}	dP/dz_{C}	$\Delta P_{\text{M-C}}$	$\Delta P_{\text{B-C}}$	Flow regime		
	kPa	$\text{kg}\,\text{s}^{-1}$				$\text{Pa}\,\text{m}^{-1}$			Pa		M	B	C
69	150.6	0.101	0.700	1.000	0.797	−4.3±6.7	1 075.3±154.1	1 283.1±23.5	2 342.1±52.1	1 800.9±258.5	—	A	A
70	149.4	0.135	0.301	0.300	0.201	385.2±14.5	24.9±21.7	853.4±72.7	506.0±77.8	587.7±79.6	SA	W	A
71	149.4	0.136	0.300	0.300	0.801	293.6±8.6	71.5±8.2	836.4±45.7	616.2±52.4	762.1±52.9	SA	W	A
72	149.4	0.135	0.297	0.700	0.201	66.8±13.0	248.1±16.4	798.5±60.2	1 000.9±67.2	768.9±90.9	W	W	A
73	149.2	0.135	0.296	0.700	0.801	12.2±8.1	375.1±18.7	815.2±53.9	1 129.4±61.3	945.3±62.9	W	SA	A

Table F.3 Two-phase results with wavy flow in the combined side (St=stratified, W=wavy, SA=semi-annular).

Test	P_{junction}	W_{C}	x_{C}	λ_{G}	λ_{L}	dP/dz_{M}	dP/dz_{B}	dP/dz_{C}	$\Delta P_{\text{M-C}}$	$\Delta P_{\text{B-C}}$	Flow regime		
	kPa	$\text{kg}\,\text{s}^{-1}$				$\text{Pa}\,\text{m}^{-1}$			Pa		M	B	C
01	150.7	0.047	0.847	0.204	0.062	188.4±11.5	23.5±4.4	264.9±9.0	202.2±16.5	232.7±12.9	W	St	W
02	150.4	0.051	0.498	0.498	0.498	33.0±2.2	32.3±2.5	148.1±6.8	202.9±8.8	188.3±8.8	St	St	W
03	149.3	0.026	0.502	0.000	0.000	29.2±4.7	—	26.9±1.4	5.4±5.0	—	St	—	St
04	149.3	0.045	0.500	0.207	0.204	77.6±1.9	6.2±4.2	139.1±3.6	66.7±5.6	83.4±6.8	W	St	W
05	149.2	0.045	0.502	0.206	0.399	67.9±2.7	−0.1±3.3	133.9±4.8	78.0±6.6	116.7±7.1	St	St	W
06	149.4	0.045	0.502	0.206	0.602	53.6±3.2	−2.4±0.8	142.2±3.3	62.8±6.0	120.1±5.4	St	St	W
07	148.9	0.045	0.501	0.204	0.797	47.9±1.4	1.6±6.5	133.7±0.8	80.5±4.1	143.5±7.8	St	St	W
08	150.4	0.045	0.500	0.400	0.204	36.4±1.8	21.6±6.1	127.7±1.8	132.0±4.8	102.5±7.4	St	St	W
09	150.3	0.045	0.502	0.400	0.399	33.9±2.6	20.9±2.1	127.7±3.9	125.2±6.1	117.6±5.9	St	St	W
10	150.4	0.045	0.500	0.399	0.602	28.5±1.2	23.3±4.0	124.9±2.4	131.6±4.8	129.5±6.1	St	St	W
11	150.1	0.045	0.500	0.397	0.797	23.7±1.2	25.8±3.3	128.4±2.8	127.6±5.0	137.2±5.9	St	St	W
12	149.2	0.045	0.504	0.595	0.204	15.1±1.7	35.7±1.0	127.5±2.7	193.5±5.6	131.0±5.0	St	St	W
13	149.4	0.045	0.505	0.594	0.399	17.3±1.4	32.8±2.9	129.5±4.2	181.8±6.3	139.6±6.5	St	St	W
14	150.0	0.045	0.501	0.593	0.602	15.4±1.7	33.2±4.3	129.3±4.5	182.0±6.6	151.5±7.5	St	St	W
15	150.0	0.045	0.498	0.592	0.797	11.3±1.5	46.7±0.0	130.3±4.7	169.3±6.6	146.7±6.3	St	St	W
16	150.1	0.045	0.504	0.805	0.204	2.4±1.0	53.4±3.7	117.0±9.5	249.5±10.7	144.5±10.9	St	St	W
17	149.8	0.045	0.501	0.805	0.399	1.1±2.8	52.3±4.0	114.9±2.9	228.3±6.1	139.4±6.3	St	St	W
18	150.1	0.045	0.502	0.805	0.602	1.8±1.0	59.7±4.3	126.4±2.4	216.4±5.4	153.6±6.4	St	St	W
19	149.9	0.045	0.503	0.805	0.795	4.0±0.3	80.3±5.3	122.6±8.7	215.2±9.8	136.2±10.9	St	W	W
20	149.8	0.045	0.703	0.194	0.201	146.2±2.9	14.9±1.6	221.4±22.0	166.2±23.1	188.7±23.0	W	St	W
21	149.8	0.045	0.701	0.195	0.400	138.1±5.1	9.3±4.6	233.0±6.8	133.7±10.7	178.5±10.7	W	W	W
22	149.1	0.045	0.700	0.196	0.604	119.4±2.3	13.8±3.0	232.8±4.1	139.2±8.1	178.4±8.5	W	W	W
23	149.7	0.045	0.700	0.195	0.801	102.3±7.5	12.6±6.8	224.8±4.6	145.6±10.9	189.2±10.6	W	W	W

Continued on next page

Table F.3 – continued from previous page

Test	P_{junction}	W_{C}	x_{C}	λ_{G}	λ_{L}	dP/dz_{M}	dP/dz_{B}	dP/dz_{C}	$\Delta P_{\text{M-C}}$	$\Delta P_{\text{B-C}}$	Flow regime		
	kPa	$\text{kg}\,\text{s}^{-1}$				$\text{Pa}\,\text{m}^{-1}$			Pa		M	B	C
24	149.6	0.045	0.702	0.408	0.196	63.1±3.3	40.0±2.5	207.8±5.6	261.8±9.5	237.8±9.1	St	St	W
25	149.7	0.045	0.700	0.408	0.400	54.4±1.6	39.4±4.3	209.7±5.1	261.4±8.8	245.5±9.6	W	St	W
26	150.4	0.045	0.699	0.403	0.604	49.6±4.0	33.3±0.0	190.4±9.7	236.0±12.3	233.8±11.6	St	St	W
27	150.3	0.045	0.701	0.400	0.801	45.6±2.3	29.6±5.5	192.0±4.2	239.0±8.0	243.4±9.4	St	W	W
28	150.0	0.045	0.702	0.597	0.196	24.7±1.9	56.2±3.4	202.1±3.7	340.6±8.6	284.7±8.6	W	St	W
29	149.5	0.045	0.698	0.593	0.400	25.0±2.2	53.6±3.6	204.2±7.6	330.3±10.9	288.0±11.0	St	St	W
30	149.3	0.044	0.695	0.588	0.604	28.1±4.3	60.3±4.2	205.6±4.1	323.7±9.5	288.7±9.2	St	St	W
31	150.4	0.045	0.704	0.604	0.801	27.6±1.6	96.4±4.5	245.4±8.6	318.1±12.0	263.7±12.4	St	W	W
32	149.8	0.044	0.699	0.793	0.196	4.4±2.1	100.3±7.1	226.2±4.6	396.3±10.0	276.3±11.3	W	W	W
33	150.0	0.044	0.697	0.793	0.400	2.2±4.2	108.2±5.3	231.6±3.7	394.9±10.3	285.6±10.1	St	W	W
34	149.6	0.044	0.697	0.790	0.604	9.0±1.9	120.3±5.9	231.6±5.9	386.0±10.6	288.1±11.4	St	W	W
35	149.8	0.045	0.700	0.792	0.801	14.5±6.8	132.8±5.9	233.1±6.2	358.6±12.4	277.5±11.5	St	W	W
36-1	150.2	0.045	0.900	0.198	0.197	154.3±2.7	17.9±3.1	248.9±3.5	222.3±8.7	248.7±9.1	W	St	SA
36-2	149.7	0.045	0.899	0.214	0.197	157.0±2.0	22.1±3.0	250.8±1.8	228.6±8.1	259.1±8.6	W	St	SA
36-3	150.4	0.044	0.898	0.217	0.197	139.4±4.4	17.8±8.5	243.3±3.0	228.4±9.2	250.4±11.9	W	St	SA
36-4	149.6	0.046	0.901	0.212	0.197	153.4±2.9	14.6±3.7	253.6±6.7	236.2±10.7	268.6±11.1	W	St	SA
37	150.0	0.045	0.900	0.205	0.398	150.8±7.0	21.2±0.2	251.1±2.3	216.3±10.5	254.3±8.2	W	St	SA
38	149.8	0.044	0.899	0.192	0.599	145.3±1.0	20.7±2.3	241.8±3.5	203.9±8.1	240.5±8.6	W	St	SA
39	150.0	0.045	0.899	0.197	0.799	135.6±3.0	17.2±5.1	244.0±6.1	201.2±9.9	237.5±10.9	W	W	SA
40	151.8	0.045	0.901	0.300	0.198	136.2±3.2	34.1±3.4	269.4±4.5	306.9±10.3	321.8±10.5	W	St	SA
41	151.9	0.045	0.900	0.300	0.800	124.0±2.4	31.7±2.8	269.8±4.6	319.4±10.3	345.0±10.5	W	St	SA
42	150.0	0.045	0.901	0.394	0.198	110.9±1.7	43.1±3.2	272.0±4.0	400.7±10.5	403.4±10.9	W	St	SA
43	148.8	0.045	0.898	0.395	0.391	102.8±1.7	43.8±2.8	273.1±3.5	406.6±10.4	405.6±10.7	W	St	SA
44	148.9	0.044	0.896	0.407	0.604	109.3±3.5	44.7±4.5	275.9±3.1	392.7±10.7	403.3±11.1	W	St	SA

Continued on next page

Table F.3 – continued from previous page

Test	P_{junction}	W_{C}	x_{C}	λ_{G}	λ_{L}	dP/dz_{M}	dP/dz_{B}	dP/dz_{C}	$\Delta P_{\text{M-C}}$	$\Delta P_{\text{B-C}}$	Flow regime		
	kPa	kg s^{-1}				Pa m^{-1}			Pa		M	B	C
45	148.1	0.045	0.899	0.401	0.800	95.4±1.8	39.3±6.2	272.7±3.8	406.7±10.6	419.1±12.2	W	St	SA
46	150.6	0.045	0.900	0.600	0.197	35.4±2.1	103.5±10.3	259.6±5.2	524.8±11.9	435.5±15.0	St	W	SA
47	150.2	0.045	0.900	0.602	0.398	32.5±2.6	103.7±7.3	256.7±3.6	547.0±11.5	458.1±12.7	St	W	SA
48	149.8	0.045	0.900	0.601	0.599	40.8±2.6	110.9±7.3	265.4±2.7	519.4±11.2	435.0±12.5	St	W	SA
49	149.6	0.045	0.900	0.602	0.799	32.6±1.8	113.3±11.0	259.9±4.0	524.1±11.4	440.8±15.2	St	W	SA
50	149.8	0.045	0.900	0.796	0.197	6.9±1.5	145.8±6.2	262.3±4.8	578.2±12.1	434.8±12.5	St	W	SA
51	149.8	0.045	0.900	0.796	0.398	2.9±2.0	150.8±4.6	268.9±6.1	574.3±12.9	422.9±12.4	St	W	SA
52	150.2	0.045	0.900	0.797	0.599	3.2±3.2	154.7±6.8	252.4±5.5	602.3±12.7	463.1±13.1	St	W	SA
53	150.2	0.045	0.900	0.798	0.799	6.1±5.4	161.2±6.8	264.5±5.3	564.8±13.3	424.6±13.0	St	W	SA
54	150.0	0.045	0.504	0.500	0.500	21.3±2.3	25.6±3.9	125.4±2.3	149.3±5.2	128.2±6.0	W	W	W
55	149.3	0.055	0.493	0.213	0.200	150.1±4.0	−1.2±0.8	241.5±4.9	75.8±8.9	127.9±8.3	W	W	W
56	149.2	0.055	0.490	0.213	0.398	124.3±2.3	1.7±2.6	225.2±3.5	122.9±7.4	177.9±7.9	W	W	W
57	149.7	0.055	0.489	0.213	0.600	115.0±2.3	7.4±8.6	237.6±4.8	100.8±8.2	157.9±12.0	W	W	W
58	149.3	0.056	0.475	0.213	0.812	93.3±1.1	1.5±1.1	237.9±9.6	114.4±11.6	203.6±12.0	W	W	W
59	150.3	0.055	0.497	0.407	0.200	64.5±1.5	23.4±1.8	196.7±5.4	186.3±8.3	169.0±8.2	W	St	W
60	150.6	0.056	0.497	0.406	0.398	53.7±0.8	27.0±2.6	194.8±3.1	185.6±6.8	175.3±7.2	St	St	W
61	149.7	0.055	0.497	0.404	0.600	69.1±3.7	23.6±3.6	242.0±10.2	236.8±13.2	263.4±13.3	W	St	W
62	150.3	0.057	0.486	0.399	0.812	55.7±1.4	29.8±3.8	258.9±6.8	217.3±10.4	248.7±11.2	W	St	W
63	149.1	0.056	0.501	0.595	0.200	23.4±1.6	47.4±4.2	191.3±6.7	287.8±9.7	221.4±10.1	W	St	W
64	150.3	0.056	0.499	0.594	0.398	23.2±1.6	52.9±5.7	207.1±6.2	256.7±9.4	195.2±10.6	W	St	W
65	149.8	0.056	0.501	0.593	0.600	17.6±2.4	63.1±4.9	195.6±7.1	274.8±10.1	232.5±10.8	St	W	W
66	149.5	0.056	0.503	0.593	0.801	18.6±0.7	74.3±7.2	205.9±6.9	251.7±9.8	220.0±11.9	St	W	W
67	149.4	0.056	0.503	0.797	0.200	5.0±2.6	87.6±5.7	200.5±5.6	361.3±9.8	239.4±10.3	St	W	W
68	150.7	0.056	0.499	0.798	0.398	10.1±1.9	102.5±5.0	185.8±1.9	369.6±7.9	249.7±8.3	W	W	W

Continued on next page

Table F.3 – continued from previous page

Test	P_{junction}	W_{C}	x_{C}	λ_{G}	λ_{L}	dP/dz_{M}	dP/dz_{B}	dP/dz_{C}	$\Delta P_{\text{M-C}}$	$\Delta P_{\text{B-C}}$	Flow regime		
	kPa	$\text{kg}\,\text{s}^{-1}$				$\text{Pa}\,\text{m}^{-1}$			Pa		M	B	C
69	149.0	0.056	0.501	0.797	0.600	3.0±1.4	124.5±0.4	204.9±8.6	351.6±11.6	225.2±10.9	St	W	W
70	150.1	0.056	0.502	0.797	0.801	4.0±0.8	120.5±6.4	201.3±5.5	334.9±9.3	256.4±10.8	St	W	W
71	149.9	0.065	0.489	0.205	0.199	223.7±5.5	16.0±2.6	319.8±12.5	146.5±16.1	192.2±15.6	SA	St	SA
72	149.8	0.066	0.486	0.203	0.402	197.9±4.4	13.8±7.8	325.0±12.2	150.3±15.6	209.6±17.1	W	St	SA
73	149.6	0.066	0.487	0.206	0.599	160.1±13.8	12.9±1.5	310.8±14.0	195.1±21.5	266.9±16.9	W	St	SA
74	149.1	0.066	0.488	0.207	0.798	131.9±1.7	5.1±1.9	324.4±10.0	172.9±13.5	263.2±14.0	W	St	SA
75	150.8	0.067	0.500	0.397	0.198	148.6±4.2	26.0±4.7	351.1±2.6	368.1±12.2	390.0±12.5	W	St	SA
76-1	150.8	0.068	0.502	0.396	0.402	140.2±3.2	33.3±5.4	379.4±14.4	331.1±18.7	352.2±19.3	W	St	SA
76-2	149.6	0.069	0.507	0.394	0.402	117.3±5.0	48.6±6.7	374.9±16.6	342.4±20.8	359.1±21.3	W	St	SA
77	150.8	0.068	0.503	0.394	0.599	123.3±2.0	53.7±13.1	352.1±1.6	363.1±11.4	380.5±17.4	W	St	SA
78	150.8	0.068	0.504	0.395	0.798	101.3±4.0	44.5±4.8	375.1±27.6	340.4±30.1	379.9±30.4	W	St	SA
79	150.5	0.068	0.506	0.605	0.198	44.6±3.5	91.6±3.4	372.8±13.2	512.2±18.7	429.2±18.2	W	W	SA
80	149.6	0.069	0.507	0.608	0.402	37.3±4.2	133.9±14.6	381.1±10.5	531.9±17.4	418.5±21.7	W	W	SA
81-1	149.7	0.068	0.509	0.609	0.599	28.5±3.4	141.5±2.7	354.4±11.4	546.4±17.4	462.9±16.8	W	W	SA
81-2	151.1	0.067	0.497	0.601	0.589	26.5±3.2	120.8±11.3	369.0±14.6	518.2±19.7	461.4±22.2	W	W	SA
82	149.4	0.068	0.507	0.606	0.798	30.9±1.5	152.8±8.7	350.5±17.6	569.2±21.8	503.6±23.1	St	W	SA
83	149.2	0.067	0.498	0.792	0.198	6.2±4.0	143.0±5.8	342.7±14.8	583.3±20.0	413.3±19.5	W	W	SA
84	149.7	0.067	0.497	0.792	0.402	5.4±2.2	171.3±9.3	336.3±7.7	600.3±15.1	442.1±16.6	St	W	SA
85-1	149.6	0.067	0.498	0.792	0.599	9.8±2.6	221.2±34.9	327.3±31.4	607.9±33.9	432.2±48.2	St	W	SA
85-2	150.3	0.068	0.495	0.795	0.591	5.7±1.4	201.0±28.6	333.1±76.3	600.0±77.3	442.0±82.2	St	W	SA
86	149.6	0.067	0.499	0.793	0.798	10.3±4.6	220.2±11.5	325.6±11.6	593.4±17.7	482.4±20.0	St	SA	SA

Appendix G

Probability Density Functions

A stochastic, Gaussian process can be described entirely by its arithmetic mean and variance (VAR). For a sample of n measurements of P, the arithmetic mean and variance are defined as [89]:

$$\mathrm{AM}(P) = \frac{1}{n}\sum_{i=1}^{n} P_i, \tag{G.1a}$$

$$\mathrm{VAR}(P) = \frac{1}{n-1}\sum_{i=1}^{n}\Big(P_i - \mathrm{AM}(P)\Big)^2. \tag{G.1b}$$

For such a process, if an infinite number of measurements were taken a continuous distribution of the frequency of different measurements of the shape defined by:

$$f(P) = \frac{1}{\sqrt{2\pi\mathrm{VAR}(P)}}\exp\left[\frac{(P - \mathrm{AM}(P))^2}{2\mathrm{VAR}(P)}\right]. \tag{G.2}$$

will occur. In practice it is impossible to take an infinite number of measurements, and so a discrete approximation of the continuous curve with an associated error is used [90].

To illustrate, imagine a pipe flow experiment with P measured continuously and for an infinite amount of time. Figure G.1a shows a continuous curve that could be generated from such an experiment by plotting the resulting number of times each pressure value was measured and normalizing the value so that the area under the curve is one. This curve is called the probability density function, and is defined Eq. (G.2). In practice, of course, only a discrete number of measurements over a finite amount of time can be made. The approximate probability density function can be estimated from a histogram by grouping the data based on the magnitude of measurements into some number 'bins', say 100, finding the frequency by counting the number of measurements that fall into each bin, and then normalizing the frequency by dividing by the total number of samples and the width of each bin. A small sample size results in a histogram like Fig. G.1b, with the true (usually unknown) Gaussian distribution shown as a solid line. In this case, the arithmetic mean of the sample has a visible error in its estimate of the Gaussian distribution's mean (GM). On the other hand, a large sample size results in a histogram like Fig. G.1 where $\mathrm{AM}(P_{\mathrm{R}}) \approx \mathrm{GM}(P_{\mathrm{R}})$ has a much error in the estimate of the true average value.

Other types of distributions also exist, and can be used to diagnose experimental error like measurement hysteresis, measurement truncation, or other defects [90]. Skewed distributions with tails are often indicative of processes with multiple independent components and can be modelled by superposing several Gaussian distributions [90]. Slug flows in horizontal pipes have been shown to have this form of pressure distribution in previous studies [73, 91].

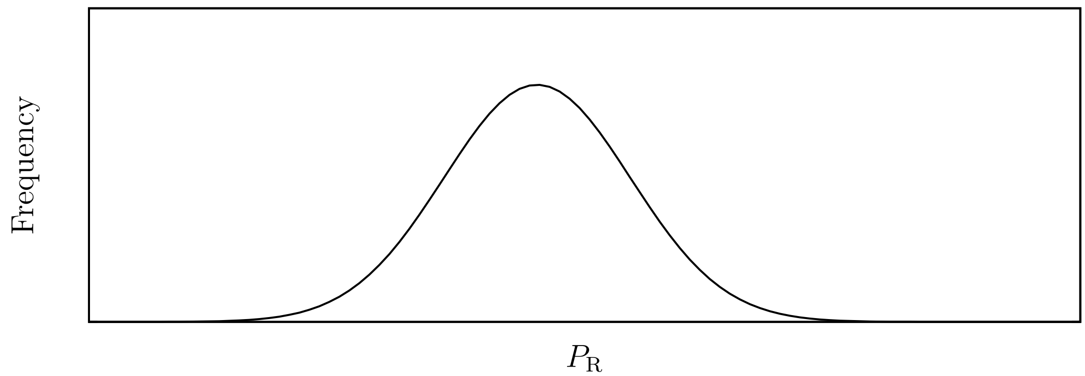

(a) The distribution for a Gaussian process

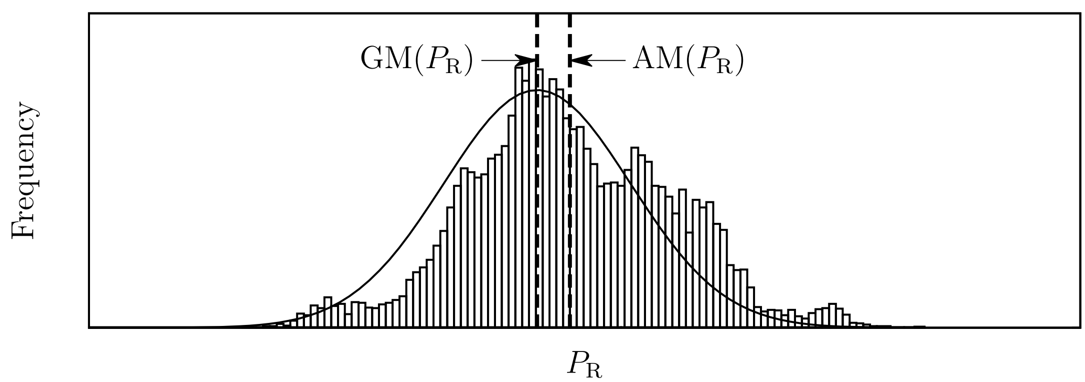

(b) Small n

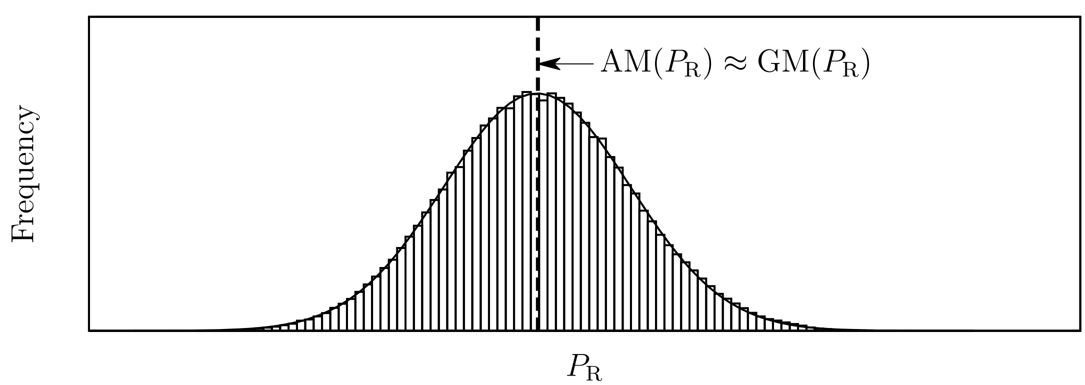

(c) Large n

Figure G.1 Sample histograms pressure data for small and large sample sizes.